University of West Bohemia

Faculty of Applied Sciences

Department of Physics

Ph.D. Thesis

submitted to acquire the degree of Doctor of Philosophy in the field
of Plasma Physics and Physics of Thin Films

Ing. Jakub Blažek

Pulsed reactive magnetron sputtering of thin films containing copper and characterization of their physical and mechanical properties

Supervisor:	prof. Ing. Jindřich Musil, DrSc.
Date of state doctoral exam:	5. 5. 2011
Date of submission:	1. 11. 2013

Plzeň 2013

Západočeská univerzita v Plzni

Fakulta aplikovaných věd

Katedra fyziky

Disertační práce

k získání akademického titulu doktor v oboru
Fyzika plazmatu a tenkých vrstev

Ing. Jakub Blažek

Pulzní reaktivní magnetronové naprašování tenkých vrstev obsahujících měď a stanovení jejich fyzikálních a mechanických vlastností

Školitel:	prof. Ing. Jindřich Musil, DrSc.
Datum státní doktorské zkoušky:	5. 5. 2011
Datum odevzdání:	1. 11. 2013

Plzeň 2013

Acknowledgements

There are many people whom I would like to thank at this point. No doubt the greatest thanks belong to prof. Ing. Jindřich Musil, DrSc. for numerous stimulating discussions and great amount of valuable comments and experiences related not only to the field of physics and science but also to life the way it is. I am also very grateful to prof. RNDr. Jaroslav Vlček, CSc. for giving me the opportunity to study a Ph.D. program at the Department of Physics and for his never-ending optimism, general support and fair attitude.

Undoubtedly this Ph.D. thesis would never have existed without the assistance of many colleagues who performed numerous analyses of the films or helped me conduct the experiments or consult my research and technical difficulties. These people include in particular but not exclusively Radomír Čerstvý, Karel Fajfrlík, Šárka Zuzjaková, Petr Stupka, Jiří Rezek, Tomáš Tölg, Jiří Houška and Richard Jílek. Besides I would like to acknowledge Petr Zeman and Pavel Baroch not only for helping me solve many technical problems encountered throughout my work but also for a plenty of stimulating ideas, suggestions and advice. Special thanks go to Šimon Kos who carefully went through the whole thesis and his kind assistance helped me improve the scientific, language and formal level of the work.

Out of the non-scientific community the greatest and deepest gratitude belongs to my parents, my brother and my whole family for everything they have done for me. I would also like to express many thanks to my friends and other exceptional people who supported me throughout my studies and who brought joy and happiness to my life. Last but not least very special thanks belong to two fantastic people from ODC Rokycany for showing me how to relax and recover my strength but also how to face challenges and push myself to the limits.

This work was supported in part by the Ministry of Education of the Czech Republic under Projects No. MSM 4977751302 and COST OC10045 and by the Grant Agency of the Czech Republic GACR under Project No. P108/12/0393.

Hereby I declare that I wrote the entire Ph.D. thesis myself using only results obtained during the whole study and works of other authors which are duly acknowledged in the text.

Plzeň 2013 ……………………………………

Contents

1. General introduction

Contemporary society is characterized by rapid technological development in various fields. This development is mainly driven by demands for high-quality products fabricated at low costs but with reduced negative impact on the environment. Surface treatment of materials by plasma-assisted processes represents one of such fields experiencing rapid progress. By applying a thin film on the surface of different products their mechanical, tribological, optical or functional properties can be significantly improved. Anti-fog and antireflective coatings on eyeglasses, self-cleaning and antimicrobial surfaces, wear-resistant coatings on cutting tools or thin films in photovoltaic cells represent just a brief list of examples where plasma technologies are used. Pulsed reactive sputtering with a dual magnetron is a sophisticated plasma processing technique characterized by a long-term stability of process parameters and capable of producing high-quality films in a wide range of elemental compositions. The non-equilibrium nature of this plasma processing technique makes it possible to fabricate unique materials such as nanocomposites or metastable structures.

From the point of view of designing new materials with unique properties, copper represents an interesting element. It has already been demonstrated that properly selected amount of copper in crystalline thin films can lead to formation of a nanocomposite structure with significantly enhanced mechanical properties. The ductility of metallic copper can also reduce the brittleness of the base material leading to formation of a tough yet still hard composite. Moreover since copper represents an effective antibacterial agent, addition of this element into the base material may introduce antibacterial effect.

This Ph.D. thesis deals with preparation of thin films of three different material systems containing copper using pulsed reactive magnetron sputtering utilizing a dual magnetron. The first part is focused on a systematic investigation of the effect of Cu addition into pure Al_2O_3 film with the aim to enhance its mechanical properties and resistance to cracking. The second study is devoted to fabrication of an antibacterial Cr-Cu-O film. In the last part of the work the advantages of both these materials are combined in an attempt to design and prepare a multifunctional Al-Cu-N film.

2. State of the art

This chapter summarizes the state of the art in fields relevant to the experimental part of the thesis. Since the topic of pulsed reactive magnetron sputtering has already been described in many scientific papers such as [1-4] and references therein, just a brief introduction to this techniques is given and only the dual magnetron is described in more detail. In the next sections one of the most important material characteristics – toughness - is introduced and the toughening mechanisms and toughness measurement methods are presented. A brief survey of antibacterial surfaces with special focus on those containing Cu as the antibacterial agent is also given. In the final section the reader is introduced to the basic properties and applications of selected materials studied in the thesis.

2.1 Magnetron sputtering process

Magnetron sputtering is a powerful technique for surface treatment of various products by deposition of a thin film. The rapid development of this technology was launched by the invention of the planar magnetron by Chapin [5], which significantly increased the low deposition rate of conventional diode sputtering systems. Magnetron sputtering and its modifications are currently used in a wide range of industrial applications such as cutting, milling and forming tools [6, 7], energy conversion [8], optical filters [9], decorative coatings [10] or microelectronics [11].

Compared to diode sputtering, the magnetron utilizes magnetic field to sustain the discharge close to the sputtered cathode (target). The drift of electrons in the vicinity of the target results in a significant increase of ionization probability of the process gas. The highly ionized plasma above the target makes it possible to operate the discharge at lower pressures and higher discharge currents resulting in a dramatic increase of deposition rate of the thin film. The deposition rate then becomes high enough to be competitive with other techniques of film deposition [1].

The wide variety of substrates together with the demand for low-cost and high quality coatings with specific microstructure, phase and elemental composition resulted in development of many modifications of the conventional magnetron sputtering process. These modifications include, for example:

- introduction of the reactive gas into the discharge (i.e. reactive sputtering) [2, 3]
- modification of the voltage waveform (DC, AC, DC pulsed, HiPIMS, MPP-MS) [12-14]
- modification of the magnetic field (conventional or unbalanced magnetron, mirror or closed magnetic field configuration of dual magnetron) [1,3]
- utilization of multiple magnetrons [3, 15]
- hybrid processes combining magnetron sputtering with other deposition techniques (e.g. ECR CVD, cathodic arc evaporation, sputtering pulsed laser deposition or cluster gun technique) [16-19]

2.1.1 Pulsed reactive magnetron sputtering

In the process of reactive magnetron sputtering a reactive gas (RG) such as oxygen, nitrogen, methane etc. is introduced into the deposition chamber. The atoms sputtered from the magnetron target react with atoms, molecules or ions of the reactive gas which makes it possible to form thin films based on nitrides, oxides, carbides or their combinations [3]. This significantly broadens the spectrum of materials that can be prepared compared to non-reactive magnetron sputtering alone. The possibility to produce ceramic films from metallic targets brings further technological advantages such as easy machinability of the targets, higher target purity, no need to use complex RF systems or more effective target cooling [2]. The introduction of the reactive gas into the deposition system however leads to interaction of the reactive gas with the condensing material on the chamber walls and also with the target surface. This brings several important problems that need to be taken into account.

First problem arises if the reactive gas and the sputtered metal form a dielectric compound such as Al_2O_3, MgO, ZrO_2, AlN etc. In this case the anode of the electric circuit (usually represented by the deposition chamber) is gradually covered with the dielectric film and ceases to operate properly or practically disappears leading to complete discharge extinction. The described phenomenon is called “disappearing anode“. In fact the anode does not need to be entirely covered with insulating film to have a serious impact on the deposited film. Just a partial coverage of the anode by an insulating layer leads to a change of the plasma spatial distribution, since the plasma is forced to find a lower resistance anode. This may result in a serious change of plasma parameters and deposition rate uniformity [20]. A very effective way to avoid the disappearing anode is utilization of the dual magnetron described in section 2.1.2.

Secondly, if the reactive gas forms a compound on the target surface (so called target poisoning), a significant decrease of deposition rate is observed, which is mainly attributed to lower sputtering yield of metal atoms from the compound on the target surface compared to pure metallic target. To keep the deposition rate sufficiently high, the working point needs to be properly stabilized in order to prevent complete coverage of the target by the compound. The methods proposed to provide stabilization of the working point include (1) increasing the pumping speed, (2) plasma emission monitoring (PEM), (3) voltage control or (4) successive plasma anodization or successive pulsed plasma anodization [2].

Another problem connected with formation of an insulating layer on the cathode is the formation of arcs. Based on the discharge power and partial pressure of the reactive gas either the whole target surface or only part of it is covered by the insulating layer. Due to the ion bombardment of the target a positive charge is accumulated on the surface of the insulating layer, actually forming a capacitor. If a critical charge is accumulated, electric arcs between different parts of the target and deposition chamber may occur.

A detailed investigation of the effect of process parameters on the generation of arcs during reactive magnetron sputtering of aluminum oxide films was performed by Koski et al. [21]. They divided the observed arcs into three arcing modes.

bipolar arcs	significant arcs between the target and the substrate or walls of the deposition chamber which represent serious instabilities of the deposition process
unipolar arcs	arcs between the metallic and insulating parts of the target
microarcs	small arc events in the form of sparks observed on the surface of the insulating layers of the target

The energy E released during the arc event depends on the particular arcing mode $E_{\mathrm{bipolar}}>E_{\mathrm{unipolar}}> E_{\mathrm{microarc}}$ and the detrimental effects of the arc generally become more serious with increasing energy. Strong arcing may result in reduction of target lifetime [22] increased film roughness, contamination of the surface of the growing film by metallic droplets, or even total shutdown of the power supply [21].

Common solutions for elimination of arcs in reactive magnetron sputtering of insulating films include 1) preventing the formation of the dielectric film on the target surface by moving the target relative to the magnet or vice versa 2) using of ”smart” power supplies capable of fast detection of the arc and its elimination by a short-term turn-off of the energy supply or 3) neutralizing the charge accumulation by pulsing the target voltage signal – i.e. pulsed magnetron sputtering [23].

In the pulsed reactive magnetron sputtering process a pulsed voltage signal is connected to the magnetron instead of direct current (DC) signal. During the pulse-on time (t_{on}) a high negative voltage is applied to the target, which is sputtered by positive ions as in the case of DC sputtering. In the pulse-off time (t_{off}) the positive charge accumulated on the surface of the insulating layers is discharged before the arcs occur thus providing a possibility to deposit defect free insulating films.

Depending on the value of the magnetron voltage in the pulse-off phase, there are two different types of pulsed sputtering regimes [2].

unipolar pulsed magnetron sputtering	the voltage in the pulse-off time is switched off and the charge accumulated on the insulating surface of the target is discharged through the plasma
bipolar pulsed magnetron sputtering	the voltage in the pulse-off time is positive and the charge accumulated on the insulating surface of the target is discharged as a result of electron bombardment

The term asymmetric bipolar pulsed magnetron sputtering refers to a magnetron voltage waveform where the absolute value of the negative magnetron voltage is not equal to the positive one. This case is very common since already positive voltage corresponding to 10% or 20% of the negative voltage is enough to fully discharge the charged regions and prevent arcing [24].

The asymmetric bipolar regime is considered more effective than the unipolar regime. Firstly the Ar^+ ions accumulated on the target surface are actively repelled by the reversed (positive) voltage on the target. Secondly the ions impacting on the dielectric parts of the target in the negative voltage pulse hit the dielectric surface with an additional energy since the plasma side of the dielectric layer is charged by electrons accumulated on its surface – this leads to a more intensive sputtering of the dielectric parts of the target.

Although pulsed magnetron sputtering provides a very efficient tool for preventing arc events the deposition parameters need to be properly selected. The frequency of arc events in pulse magnetron sputtering generally increases with decreasing pulsing frequency [2], pulse-off time [25, 26], total pressure [21, 26], target voltage [21] or with increasing target power density [26] and deposition time [21].

2.1.2 Dual magnetron

The dual magnetron provides a solution to the problem of disappearing anode and in combination with pulsed voltage signal represents an efficient tool for stable reactive magnetron deposition of insulating films such as AlN [27], TiO_2 [28], Al_2O_3 [29] etc. A typical system with dual magnetron consists of two magnetrons connected to outputs of a pulsed DC or AC power supply. During the sputtering process the voltage polarity of the magnetrons periodically changes from negative to positive and back. When one magnetron is at a negative potential acting as a source of the sputtered material i.e. temporary cathode, the other magnetron is at a positive potential representing the anode of the system. In the second phase of the pulse period the polarities of the magnetrons swap and possible insulating layer on the former-anode is now sputter-cleaned by the ion bombardment. This periodic sputter-cleaning of the anode surfaces fully eliminates the problem of disappearing anode. A schematic illustration of the voltage waveforms for the two individual magnetrons of the dual magnetron system is shown in Fig. 2.1.1. [3].

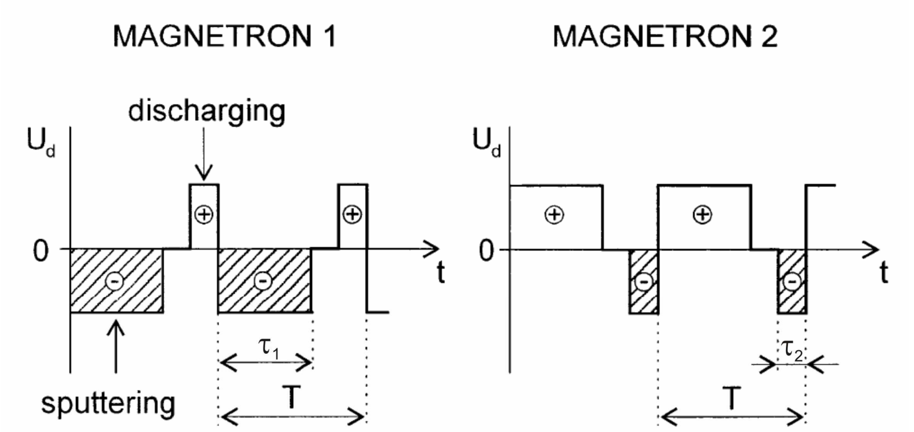

Fig. 2.1.1.: Schematic illustration of voltage waveforms on individual magnetrons of the dual magnetron in bipolar pulsed regime. Adapted from [3].

The presence of two magnetrons in the system makes it possible to change their mutual tilt angle or polarity of the magnets resulting in different spatial distribution of the plasma as shown in Fig 2.1.2.

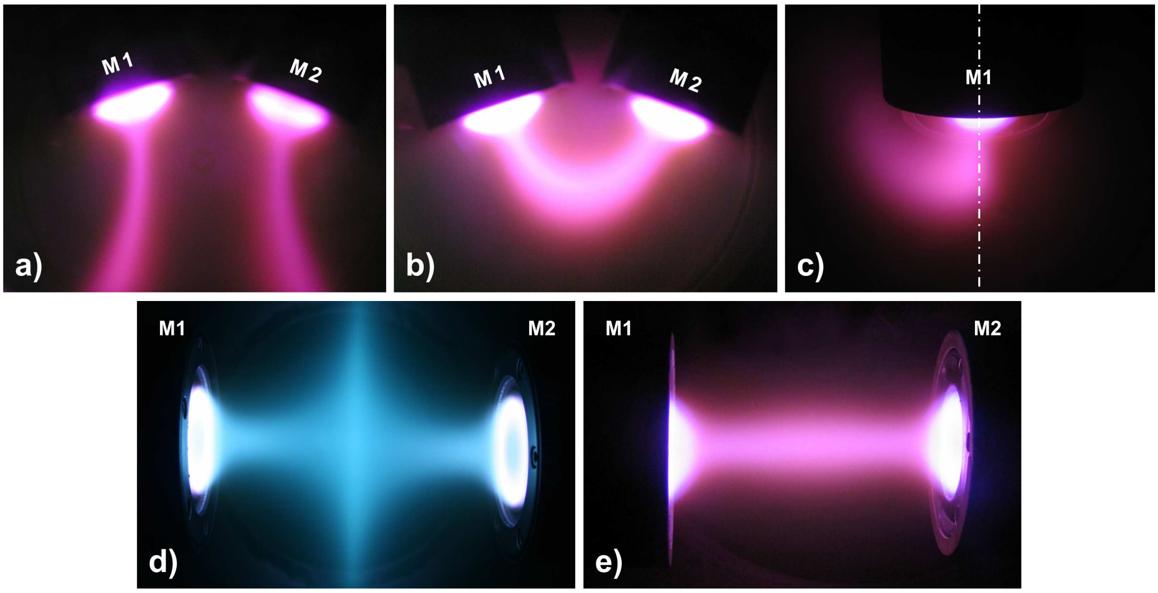

Fig. 2.1.2: Photographs of dual magnetron discharge with tilted magnetrons in a) the mirror field configuration, b) closed field configuration, c) closed field configuration in the side view. Dual magnetron in the face-to-face d) mirror field configuration and e) closed field configuration. Adapted from [30, 31].

In the closed field configuration the magnets of the opposing magnetrons have opposite polarity and the plasma discharge forms a closed loop (see Figs. 2.1.2. b) and e)). In the mirror field (sometimes also denoted as “open field“) configuration the opposing magnets have the same polarity which leads to mutual repelling of the plasma discharges (see Figs. 2.1.2 a) and d)). The asymmetric plasma distribution in Fig. 2.1.2 c) is a result of plasma drift in dual magnetron with tilted closed field configuration, which was reported by Baroch et al. [30]. Mutual tilting of the magnetrons forms a gradient of the *x*-component of the magnetic field **B.** This gradent has a positive *y*-component and lies in the plane perpendicular to the magnetic field lines as shown in Fig. 2.1.3. b). The cyclotron rotation of the charged particles in such inhomogeneous magnetic field results in a drift of plasma in the plane perpendicular to the magnetic field lines along the *z*-axis (see Figs 2.1.3 c) and 2.1.2. c)).

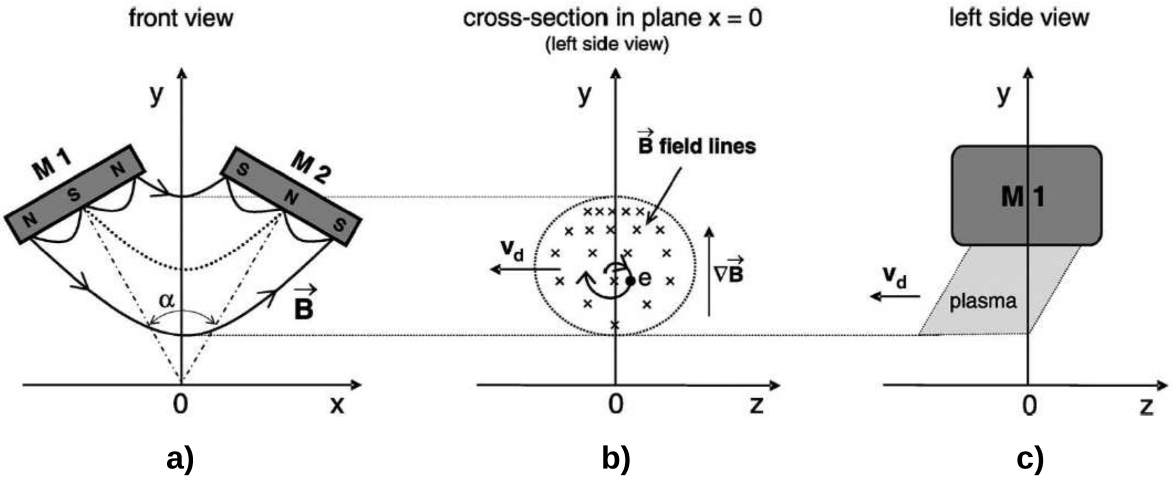

Fig. 2.1.3.: Schematic illustration of dual magnetron in closed magnetic field configuration. Adapted from [30].

The velocity of the plasma drift $\mathbf{v_d}$ along the *z*-axis is given by

$$\mathbf{v}_\mathrm{d} = -\frac{W_\perp}{qB_x^2}\nabla_\perp B_x \times \hat{x}\,, \tag{2.1}$$

where $W_\perp$ is the kinetic energy of the particle perpendicular to the field line, q is electric charge of the particle, B_x is the *x*-component of the magnetic induction $\boldsymbol{B}$ and $\hat{x}$ is the unit vector in the direction of the magnetic field line.

Depending on the particular power supply and the way it is connected to the system the dual magnetron can be either grounded (DG) or floating (DF) as illustrated in Fig 2.1.4 a). In the grounded configuration the power supply is electrically connected to the deposition chamber and the electric current may flow either onto the deposition chamber or onto the magnetron that temporarily represents the anode of the system. In the floating configuration the anode is represented by the magnetron that is in the pulse-off time only.

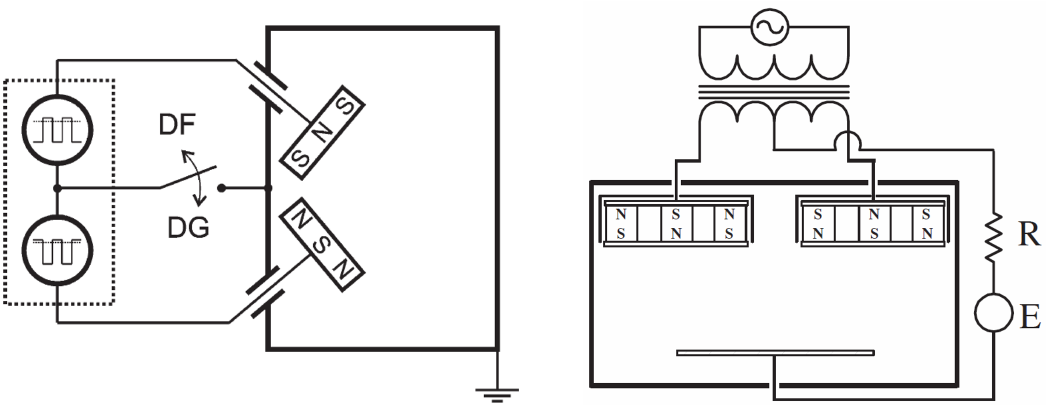

a) b)

Fig. 2.1.4: Schematic diagram of the deposition device with a) dual magnetron system with the grounded (DG) or floating (DF) power supply. Adapted from [28] b) dual magnetron system with substrate connection to the center tap of the secondary coil. Adapted from Belkind et al. [32]

The effect of different power supply connections on the deposition characteristics, ion flux characteristics and film structure during deposition of TiO_2 films using dual magnetron was investigated by Šícha et al. [28]. They observed two distinct phases in the reversed positive phase of the pulse cycle as shown in Fig 2.1.5. a): a short-lived (less than 1 μs) positive voltage overshoot followed by an almost steady-state positive low-voltage phase. These two phases were observed for a dual magnetron with a floating as well as with the grounded power supply. The same phases were also found for a dual magnetron with one magnetron switched off and a grounded power supply. They found that the voltage in the positive voltage overshoot and in the almost steady-state low-voltage phase is systematically lower for the dual magnetron with the floating power supply. The energy-resolved mass spectroscopy measurements presented in Fig. 2.1.5. b) showed that the maximum ion energy in the ion energy distribution function correlates well with the height of the voltage overshoot in the positive voltage phase. A much narrower ion energy distribution (maximum energy <50 eV) was observed for dual magnetron with the floating power supply compared to dual magnetron with the grounded power supply (maximum energy ≈100 eV). Such suppression of the high-energy ions in the flux onto the substrate resulted in formation of a low-temperature TiO_2 phase (anatase) and suppression of the high-temperature TiO_2 phase (rutile) in the growing film. This observation clearly illustrates the effect of the power supply connection to the dual magnetron on the structure of the growing film.

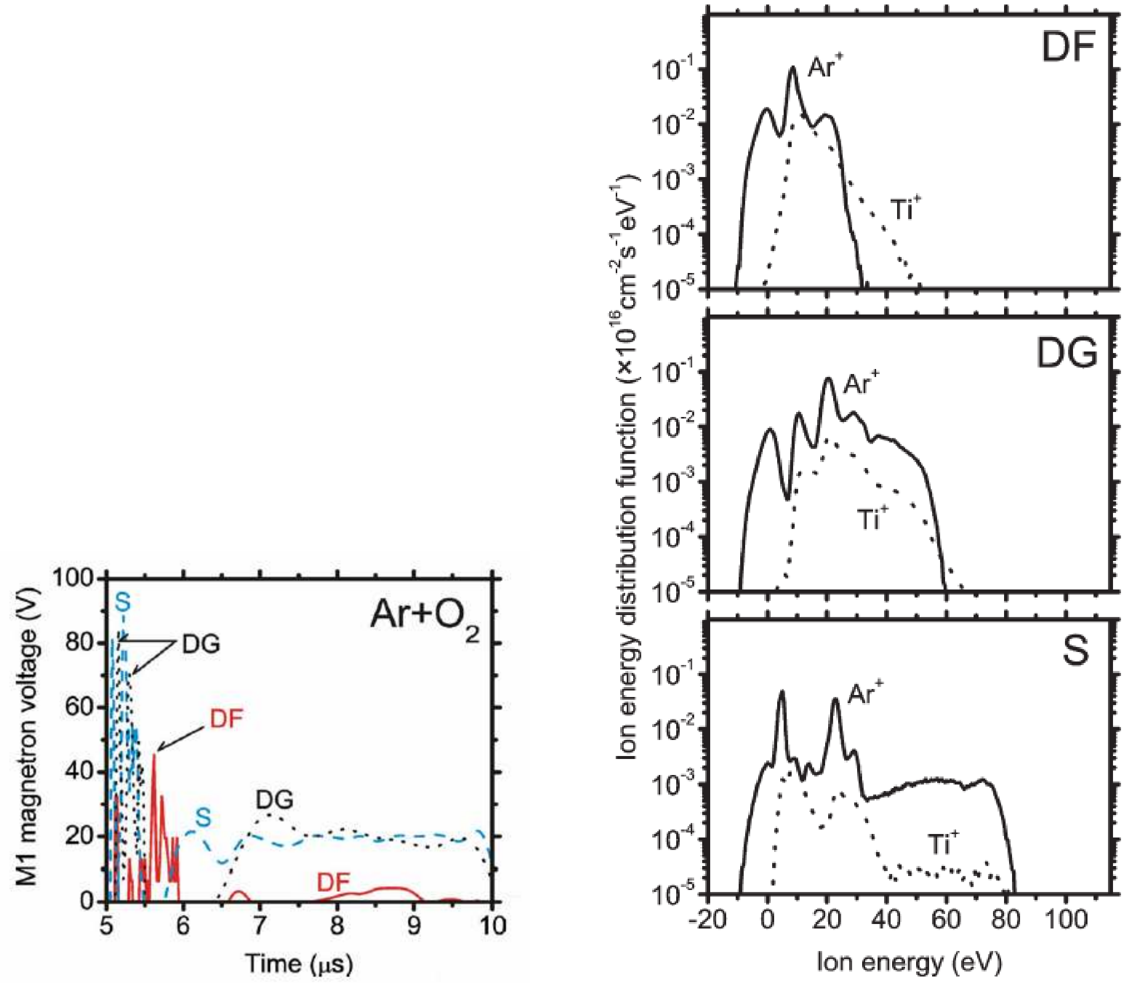

a) **b)**

Fig. 2.1.5: a) Time evolution of the magnetron voltage during positive phase of the pulses (t=5-10 μs) for floating (DF) and grounded (DG) arrangements of the dual magnetron and for single magnetron configuration (S) in Ar + O_2 mixture. The corresponding maximum values due to a short-lived positive voltage overshoot are indicated by arrows. b) Time-averaged energy distributions of titanium and argon ions at a substrate position of d=100 mm for floating and grounded arrangements of the dual magnetron and for a single magnetron configuration. Adapted from [28]

As can be seen from Fig 2.1.4 a) if a floating power supply is connected to a dual magnetron neither terminal of the power supply is connected to the ground. The absence of such electrical connection limits implementation of substrate biasing. To overcome this problem Belkind et al. developed a modified substrate circuitry, where the magnetrons were connected to the floating power supply through an isolation transformer. The substrate was connected to the center tap of the secondary coil of the transformer through a resistor and additional power supply as shown in Fig 2.1.4. b). Varying the resistance of the resistor made it possible to effectively change the ion bombardment and electron heating of the substrate and thus control properties of the growing film [32].

The effect of different pulse frequencies on structure and properties of alumina and titania films during dual bipolar pulsed magnetron sputtering was investigated by O’Brien et al. [33]. For comparison the same films were also prepared by DC magnetron sputtering. Compared to DC sputtering the pulsed sputtering process generally yielded a significant improvement of film quality in terms of defect density, roughness, coating adhesion and optical properties irrespective of the particular pulsed frequency used. Although increasing the pulse frequency from 100kHz to 350 kHz resulted in increase of plasma density, electron temperature and substrate heating, the effect on properties of the alumina and titania films was insignificant. The only parameter sensitive to the pulse frequency was the refractive index of alumina films, which increased with increasing pulse frequency.

Besides providing a long-term stability during deposition of insulating films, the dual magnetron has some other additional advantages particularly interesting from the industrial-applications point of view. Firstly the dual magnetron provides an easy way to control the elemental composition of the growing film without the need of modifying or changing the magnetron targets. This is realized by fitting the magnetrons with targets of different material and by changing the target power density on individual magnetrons [27, 34]. The process parameters that can be varied in order to change the target power density on individual targets include e.g. 1) discharge current [34] 2) pulse-on time [27] or 3) partial pressure of the reactive gas [27]. Another benefit can be seen if the overall deposition rate of pulsed dual magnetron is compared to the pulsed single magnetron. In case of the single magnetron the target is not continuously sputtered due to the period of reversed voltage (pulse-off time). This results in reduction of the deposition rate. In case of the dual magnetron system the pulse-off time on one magnetron is utilized to sputter the target on the other magnetron resulting in increase of the overall deposition rate compared to single magnetron systems [35]. The possibility to change mutual position of the magnetrons and their magnetic field polarity opens the door to new specific applications. An example of such a system is the dual magnetron in the mirror field face-to-face configuration presented in Fig. 2.1.2. d). In this case the same polarity of the opposing magnetrons forces the electrons and thereby also the ions to be transported radially away from the magnetron axis. Such configuration has been proposed by Aijaz et al. for sideways deposition of films inside tubular substrates [36].

2.2 Toughness of thin films

2.2.1 Toughness

Toughness can be defined as the amount of energy absorbed by a material before its fracture. [37]. In tensile testing of bulk materials toughness can be determined from the area under the stress-strain curve according to the following formula

$$\text{toughness} = \frac{\text{energy}}{\text{volume}} = \int_0^{\varepsilon_f} \sigma d\varepsilon \,, \qquad (2.2)$$

where σ, ε and ε_f represent stress, strain and strain at fracture, respectively. From Eq. 2.2 it is clear that neither the ability to withstand high stresses (stiff materials) nor the ability to withstand high deformations (ductile materials) alone result in high toughness. Instead an optimized combination of strength and ductility is necessary to obtain a tough material.

In contrast to toughness, resilience is the amount of energy a material is able to absorb under purely elastic deformation. After the load is removed from the resilient material the elastically stored energy is released again. If the stress-strain behavior of an uniaxially deformed material follows the linear Hooke's law, the resilience *R* can be calculated as follows

$$R = \frac{1}{2}\sigma_{\max}\varepsilon_{\max} = \frac{\sigma_{\max}^2}{2E}, \tag{2.3}$$

where $\sigma_{\max}$, $\varepsilon_{\max}$ and E correspond to the maximum stress for elastic conditions, elastic strain limit and Young's modulus of the material [38].

Achieving high toughness is a key issue in various applications where material reliability is of vital importance. These include for example total joint replacements [39], aerospace structural applications [40], power plant gas turbines [41] etc. Low toughness can result in a significant reduction in lifetime of various components due to sudden fracture. This can be illustrated in Fig. 2.2.1, which shows severely damaged gas turbine blades resulting from reduction of toughness of the alloy to 30 % of the original value. This toughness reduction is caused by segregation of carbides into the grain boundaries of the alloy during a long-term operation of the blades at high temperatures [41].

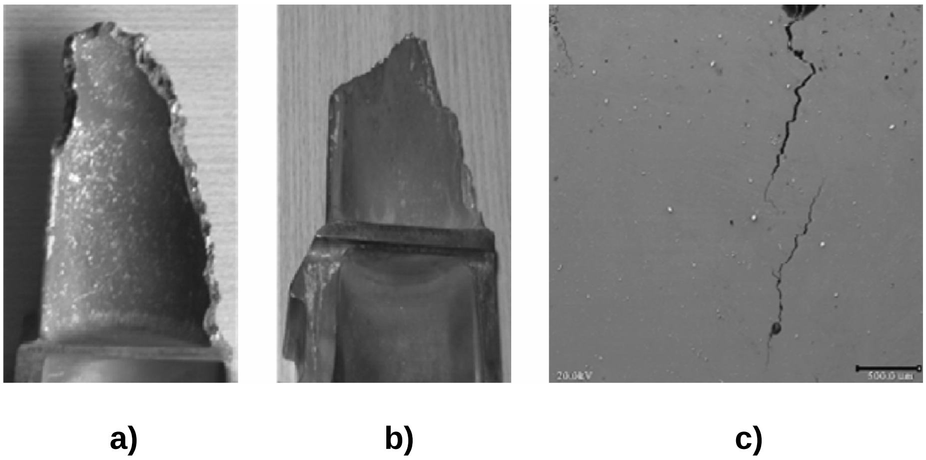

a) b) c)

Fig. 2.2.1: a) and b) examples of severely damaged gas turbine blades due to toughness reduction during long-term operation at high temperatures. c) SEM image of cracks observed on the surface of a damaged turbine blade. Adapted from [41].

2.2.2 Toughening mechanisms

From the safety, process effectiveness and cost savings points of view increasing the toughness of hard and brittle materials is an important issue. Up to now several principles of toughness enhancement of bulk materials as well as thin films have been described [42]. These principles are based either on increasing the energy neccessary for the formation of an initial crack in the material or on increasing the energy necceassary for a further propagation of an existing crack. For toughness enhancement the following mechanisms can be used:

(1) **Incorporation of a ductile phase** – there are two main mechanisms responsible for toughness improvement when a ductile phase is incorporated into a brittle material as illustrated in Fig. 2.2.2. (1) “crack blunting” i.e. relaxation of stresses in the frontal zone of the crack when the crack tip encounters the ductile phase which consequently plastically deforms thereby consuming the deformation energy (2) “crack bridging” i.e. binding of the opening crack in the bridging zone by the ductile phase which restrains the crack from further opening and reduces the driving force for crack propagation in the brittle material. The ductile phase is usually represented by Cu, Al, Ni, Ag etc. These mechanisms have been successfully employed for toughness enhancement of carbides [43, 44] borides [45], oxides [46, 47] etc.

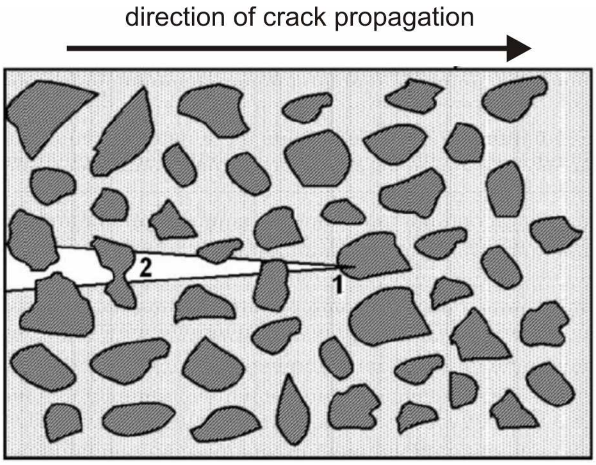

Fig. 2.2.2: Schematic illustration of toughening of brittle material by incorporation of a ductile phase. The crack blunting (1) and crack bridging (2) mechanisms are indicated. Adapted from [42].

(2) **Formation of a nanocomposite structure** – decreasing the grain size to a nanoscale level results in several consequences contributing to toughness enhancement. Firstly the magnitude of stress field around the crack tip is proportional to $\sqrt{a}$, where a is the crack length [38]. Since the size of the initial microcrack a in the material is often related to the grain size, decreasing the grain size results also in reduction of the effective stress at the crack tip. Smaller grain size also leads to frequent deflection and branching of the crack, which requires higher energy for its propagation. Furthermore the nanograins in a nanocomposite material are often surrounded by an amorphous phase which enables grain boundary sliding and thus further contributing to toughness enhancement [48, 49].

(3) **Formation of a multilayered structure** – a multilayered structure, often utilized in the form of a thin film, consists of alternating layers of at least two different phases. The crack propagating in a direction perpendicular to the planes of the alternating layers can either be deflected from its original direction at the interface of the two phases or, if one of the layers is made of a ductile material, crack bridging or crack blunting can also contribute to toughness enhancement of the overall system [50, 51]. Not only selection of suitable materials of the individual layers, but also their thickness is of significant importance. Too high thickness results in high stresses around the crack tip. This is because the magnitude of stress field around the crack tip is related to the crack length a (as noted in point (2) above) and thus to the thickness of the individual layer. Too low thickness on the other hand leads to a limited ability of the ductile phase to plastically deform and blunt the crack tip [51].

(4) **Gradient coating** – good adhesion of a thin film to the substrate is a key issue for achieving high toughness. A common approach to improve the adhesion is either to introduce an interlayer between the film and the substrate or to gradually change the structure or the elemental composition of the film to avoid a sharp step change in properties at the film-substrate interface. The importance of matching the mechanical properties of the film to the mechanical properties of the substrate was illustrated by Leyland et al. [52]. Using reactive magnetron sputtering at various N_2 partial pressures they prepared Cr-N coatings with different nitrogen concentrations. The structure of the coatings gradually shifted from metallic Cr via metallic Cr(N) solid solution to chromium nitrides (CrN and Cr_2N). The ball-on-plate impact wear tests showed that the highest wear resistance, i.e. no cracks in the film and low impact wear volume, was achieved for films that did not exhibit the highest hardness but those that exhibited intermediate hardness and Young's modulus close to the Young's modulus of the steel substrate. Wu et al. prepared composite Ni-WC coatings on low carbon steel substrate by means of laser cladding in three consecutive steps. In these steps the volume fraction of the WC phase was set from 20 % to 40 % and 80 %, respectively, resulting in a gradient coating with WC phase concentration increasing from the film-substrate interface to the film surface. In a subsequent abrasive wear test, no cracks and fatigue failures were observed in this coating in contrast to a film with 50 % volume fraction of WC phase prepared in a one step procedure [53].

(5) **Incorporation of nanofibers** – similarly as for bulk materials the toughness of thin films can be enhanced by incorporation of fibers into the matrix phase. With a typical thickness of thin films ranging from 0.1 μm to 10 μm, the size of the fibers needs to be relatively small. This requirement is met if the reinforcing fiber is in the form of a carbon nanotube (CNT). The toughening mechanisms observed in CNT reinforced ceramics include (i) crack deflection at the CNT/matrix interface, (ii) crack bridging by the CNTs and (iii) fiber pullout. Crack bridging and crack deflection mechanisms have already been described in points (1) and (3) above. In case of the fiber pullout mechanism the fibers bridging the crack are eventually pulled out from the crack plane. The work required to pull the embedded fibers out from the matrix represents additional energy that contributes to the overall toughness of the composite. The toughness enhancement by incorporation of CNTs was observed e.g. in case of alumina or yttria-stabilized zirconia ceramics [54, 55]. The crack bridging and fiber pullout phenomena can be observed by the FESEM technique as shown in Fig. 2.2.3.

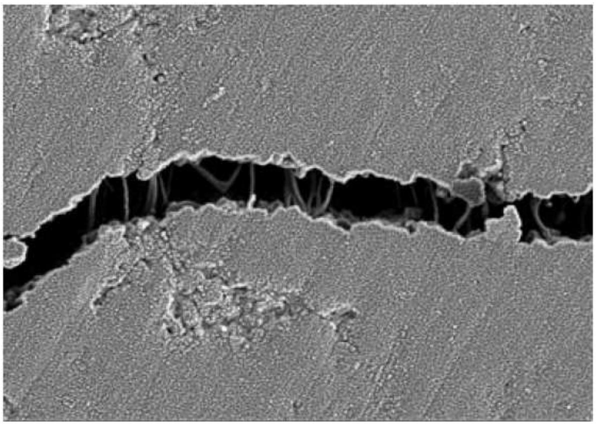

Fig. 2.2.3: Field emission scanning electron microscope (FESEM) micrograph of indentation induced crack morphology in 1 wt.% single wall carbon nanotube (SWCNT) added ZrO_2 composite ceramic. Adapted from [55].

(6) **Transformation toughening –** this toughening mechanism is related mainly to zirconia-based ceramics containing the tetragonal-zirconium dioxide phase (t-ZrO_2). If a crack propagates through such material the t-ZrO_2 phase undergoes a stress-driven phase transformation from the tetragonal to the monoclinic (m-ZrO_2) phase. This transformation is accompanied by a volume increase resulting in generation of compressive stresses around the crack and counteracting its further propagation. By optimizing the microstructural parameters of the material such as grain size, elemental or phase composition the extent of the transformation can be enhanced in order to increase the toughening effect [56].

(7) **Residual stress toughening** – the effect of magnitude and type (compressive or tensile) of residual stress on formation of cracks in thin films has been described by several authors using different testing methods. Generally speaking the tensile stresses favor the formation of cracks whereas the compressive stresses help to close the cracks thus increasing the toughness of the material [57]. Zhang et al. investigated the effect of residual stress in SiO_x films on film strength, fracture energy and interfacial shear strength (IFSS) using a tensile testing method. They found that all the quantities i.e. film strength, fracture energy and interfacial shear strength were proportional to the compressive residual stress in the film [58]. The beneficial effect of compressive residual stress on suppression of indentation induced cracks in thin films was reported for different material systems such as Zr-Cu-O or TiC-Al [59, 60]. Too high compressive stresses can however lead to reduced wear resistance and adhesion of the film to the substrate [61, 62]. Since adhesion also represents an important factor affecting the toughness of the film-substrate system (see point 4), an optimum value of compressive stress needs to be found in order to obtain films, where the compressive stress increases the toughness but does not lead to significant reduction of adhesion of the film to the substrate.

2.2.3 Quantification of toughness of thin films

The most frequent quantity used for determination of material toughness is the fracture toughness denoted as K_c. The fracture toughness represents the critical value of stress-intensity factor K that causes fracture [38]. While in case of bulk materials the fracture toughness is commonly used for comparison of toughness of different materials, the same approach is rather complicated in case of thin films. Firstly the fracture toughness calculation requires meeting the plane strain condition, which needs to satisfy the following inequality

$$h \geq h_{\min} = 2.5\left(\frac{K_{Ic}}{\sigma_y}\right)^2, \tag{2.4}$$

where $h_{\min}$, K_{Ic} and σ_y represent minimum film thickness, fracture toughness in the opening mode (denoted by the “I” subscript) and yield stress, respectively. For brittle thin films with thickness typically ranging from hundreds of nanometers to several microns this condition is however not met [63]. Secondly, the fracture toughness determination requires an existence of a predefined flaw in the material, which might be quite complicated to realize in case of a 100 nm to 10 μm thin film. Moreover the fracture toughness itself represents critical stress-intensity factor necessary for crack propagation, but does not include the energy necessary for formation of the initial crack which also contributes to the overall toughness of the material. To overcome these difficulties different authors proposed different measurement techniques and quantities for toughness determination of either stand-alone films or films deposited on various substrates. The toughness measurement methods can be divided into the following groups based on the type of loading:

1) Bending [50, 64-69]
2) Buckling [70, 71]
3) Scratching [63]
4) Indentation [43, 49, 59, 72-77]
5) Tensile testing [51, 63, 78]
6) Impact testing [52, 79]

Most of these toughness measurement methods have already been thoroughly described in [42, 63, 80]. With respect to the experimental part of this thesis only indentation and bending methods are described in more detail.

2.2.3.1 Indentation methods

Indentation belongs among the most common methods used for toughness evaluation of thin films. This is mainly due to its simplicity and availability. It can be easily realized using the micro- or nanohardness measurement systems that are widely used for determination of mechanical properties of thin films. Based on the indenter load, type of film failure, specific film or substrate post-deposition processing etc. different methods and quantities were proposed for toughness evaluation of thin films from indentation measurement.

Plasticity

In the instrumented indentation a diamond indenter is pressed into the tested material while the applied force (load) and position of the indenter (displacement) are simultaneously recorded. The output of this measurement is the load vs. displacement curve as illustrated in Fig. 2.2.4.

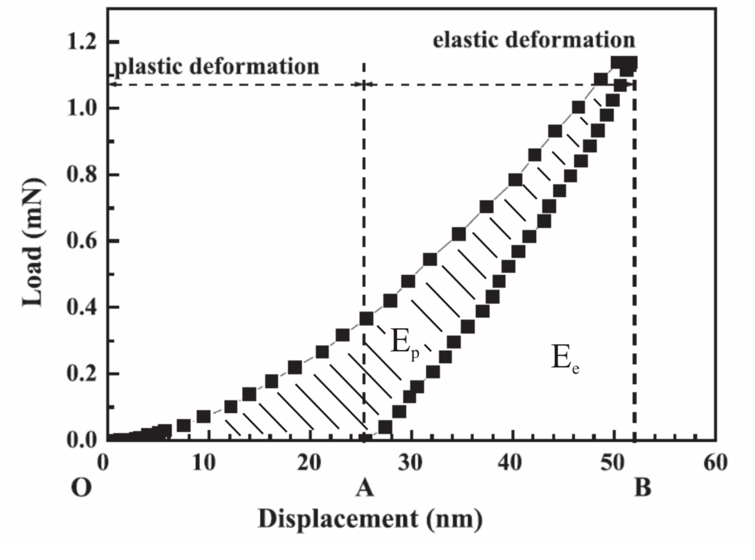

Fig. 2.2.4: Schematic plot of a load-displacement curve obtained from nanoindentation. Adapted from [80].

The plasticity can be calculated as the ratio of the plastic displacement (OA) over the total displacement (OB) according to

$$plasticity = \frac{OA}{OB} . \tag{2.5}$$

High plasticity, as defined above, has been associated with high toughness of e.g. DLC or TiC/a-C films [48, 81]. Similarly Fox-Rabichovich expressed plasticity as the ”microhardness dissipation parameter“ MDP defined by

$$MDP = \frac{E_p}{E_t} = \frac{E_p}{E_p + E_e}, \tag{2.6}$$

where E_p, E_t, E_e represent the plastic, total and elastic components of the indentation work, respectively (see Fig. 2.2.4) [82]. Although incorporation of a ductile (i.e. plastic) phase can improve the material toughness as stated in section 2.2.2, plasticity does not represent the same quantity as toughness. This has been illustrated e.g. by Jirout et al. who showed a completely opposite correlation between MDP and toughness of thin Zr-Cu-O films. They observed that the size and number of indentation-induced radial cracks in Zr-Cu-O films gradually increased with increasing MDP i.e. with increasing plasticity [59].

Fracture toughness

Since the correct determination of fracture toughness requires formation of a pre-crack with a defined length and geometry as well as controlled loading conditions, implementation in the case of thin films remains a difficult task. Tsui et al. proposed a method for determination of fracture toughness of thin hard films on soft substrates on the example of nickel phosphorous (NiP) or multilayered Ti/Al films deposited on Al substrate [83]. Using a focused ion beam a pre-crack is fabricated in the film. A Knoop indenter is then forced into the film parallel to the pre-crack at a given distance as shown in Fig. 2.2.5. The indentation sink-in effect, which was reported for hard films on soft substrates, generates tensile stress in the vicinity of the pre-crack leading to further crack extension.

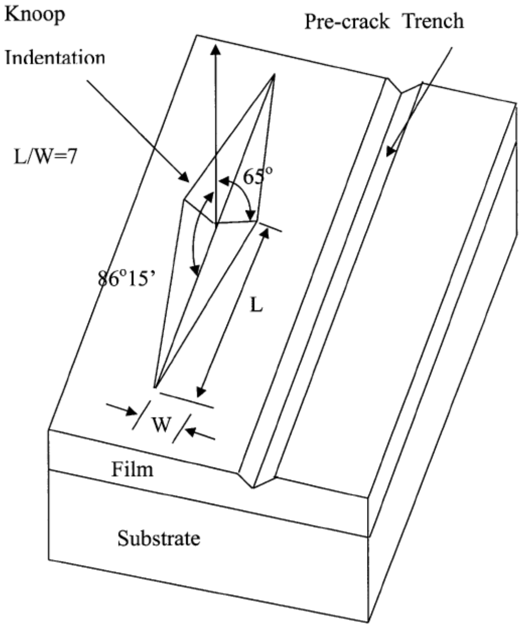

Fig.2.2.5: A schematic drawing showing the orientation of the Knoop indentation relative to the pre-crack trench. Adapted from [83].

Using the crack tip opening displacement model (CTOD) the fracture toughness K_{Ic} of the film can be determined according to

$$K_{Ic} = \sqrt{m\delta\sigma_Y E}\ , \tag{2.7}$$

where m represents a dimensionless parameter approximately equal to 2.0 under the plane strain condition and E and σ_Y are Young's modulus and yield stress of the film, respectively. δ is the crack tip opening immediately before the 'catastrophic' failure, which can be measured using a scanning electron microscope after cross-sectioning the trench by focused ion beam milling technique. Although this method represents a rigorous approach to fracture toughness determination, its main limitations are a demanding and time consuming fabrication of the pre-crack trench, post-indentation ion milling to obtain the cross section of the film and a subsequent SEM analysis.

In order to avoid a complicated fabrication of a pre-crack, several methods for determination of fracture toughness of thin films have been developed, that combine only indentation of the thin film and subsequent evaluation of the indenter imprint and crack geometry or the load-displacement curve. Three different types of crack patterns can be observed in thin films after indentation:

1) radial cracks
2) circumferential cracks (often accompanied by spallation of the film)
3) channel cracks

Determination of fracture toughness of thin films from the radial crack pattern has originally been proposed for bulk materials [84]. Several authors subsequently adopted this approach for thin films [72, 74, 76]. The relation between fracture toughness and radial cracks is given by

$$K_{Ic} = \alpha\left(\frac{E}{H}\right)^{1/2}\left(\frac{P}{c^{3/2}}\right), \tag{2.8}$$

where α is an empirical constant dependent on the indenter geometry being 0.016 for the Vickers and Berkovich indenter. P, c, E, H represent applied load, crack length, Young's modulus and hardness of the film, respectively. In order to fulfill the criterion for a well-defined radial and median crack pattern (i.e. "half-penny" pattern) it is required that

$$c \geq 2a\,, \tag{2.9}$$

where a is half of the indenter imprint diagonal as illustrated in Fig. 2.2.6 b).

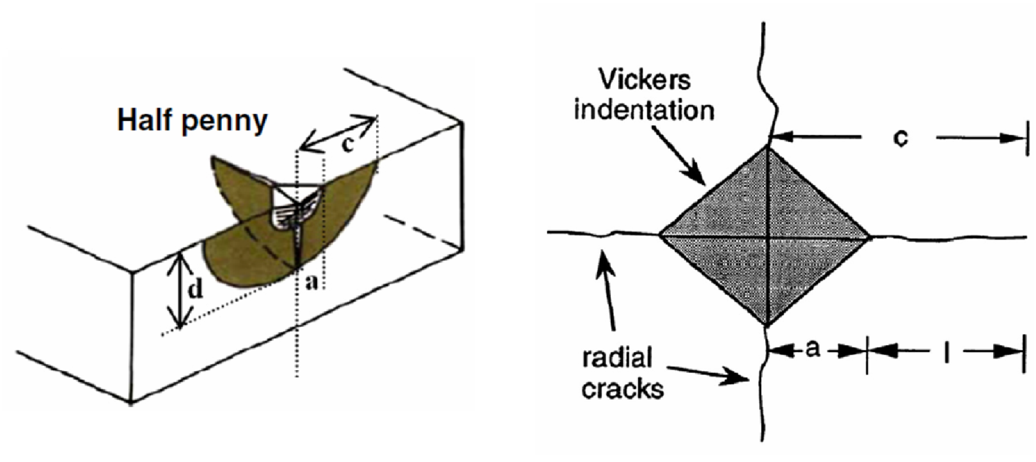

a) b)

Fig.2.2.6: a) “Half-penny” crack pattern (i.e. combination of radial and median crack pattern) and b) top view of radial crack pattern upon Vickers indentation [85, 86].

Since residual stress in the film acts as another crack propagation driving or retarding force, a modification of Eq. (2.8) is used for films with residual stress σ to calculate the fracture toughness [87].

$$K_{Ic} = \alpha\left(\frac{E}{H}\right)^{1/2}\left(\frac{P}{c^{3/2}}\right) + Z\sigma c^{1/2} \tag{2.10}$$

The parameter Z in Eq. (2.10) is the crack shape factor, which depends on the crack pattern geometry. For an idealized half-penny where $d=c$ (see Fig. 2.2.6), Z=1.26.

Since this method is adopted from toughness measurement of bulk materials the calculation does not account for interaction with the underlying substrate. In practice this means that the depth d of the half-penny crack (see Fig. 2.2.6. a)) needs to be less than 10 % of the film thickness. Taking this into consideration the indentation depth (which is smaller than d) needs to be significantly lower that 10 % of the film thickness. For Vickers and Berkovich indenters the threshold load necessary to induce radial cracks in ceramic material is usually 250 mN or higher, resulting in indentation depth in the range of several micrometers. Since typical thickness of thin films ranges from 100 nm to 10 µm, the condition above is not fulfilled and the value of fracture toughness depends on the thickness of the film. This effect has been illustrated for example by Kodali et al. [74]. They prepared DLC films with thickness ranging from 0.7 µm to 7.0 µm on Si(100) substrate using pulsed bias deposition and found that the apparent fracture toughness of the films increases with increasing film thickness (see Fig. 2.2.7). In case of the film with the highest thickness of 7.0 µm no cracks were observed even for very high indenter load of 30 N. This illustrates that the underlying substrate may influence the calculated value of fracture toughness very significantly. The threshold load necessary to induce radial cracks in the film can be reduced by one to two orders of magnitude if a sharper cube-corner indenter is used [85]. Yet even with the cube corner indenter the threshold load and corresponding indentation depth for many ceramic materials remain too high to meet the 10 % rule.

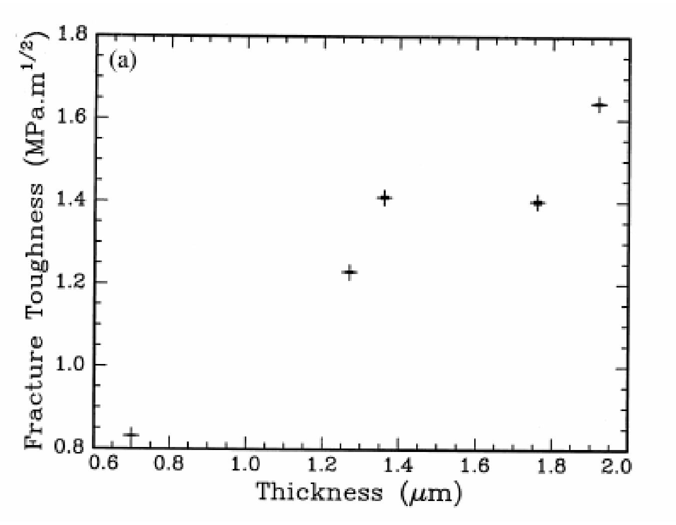

Fig. 2.2.7: Dependence of apparent fracture toughness on thickness of DLC films [74].

In order to avoid the effect of the underlying substrate on the calculated fracture toughness, a substrate indentation method was suggested by Xia et al. [88]. In this method the radial crack pattern is introduced in the uncoated substrate in a close vicinity of the film as shown in Fig. 2.2.8. The radial crack propagates from the substrate into the film and the fracture toughness is calculated from the geometry of the imprint and crack dimensions according to

$$K_{Ic} = \left\{ K_s^2 \left[1 + \lambda \frac{(\phi b - a)}{h} \sqrt{\frac{E_f}{E_s} \frac{(1-\nu_s^2)}{(1-\nu_f^2)}} \right]^2 \pm \left[2\psi_c \sigma \sqrt{h} \sqrt{\frac{E_f}{E_s} \frac{(1-\nu_s^2)}{(1-\nu_f^2)}} \right]^2 \right\}^{1/2}, \qquad (2.11)$$

where a and b are crack lengths as displayed in Fig. 2.2.8 and E, ν, h, σ and K_s are Young’s modulus, Poisson’s ratio, thickness and residual stress of the film and fracture toughness of the substrate, respectively. The subscripts s and f in Eq. 2.11 correspond to the characteristics of the substrate and the film, respectively. λ and ψ_c represent dimensionless parameters obtained from a finite element model and ϕ is the slope of a versus b.

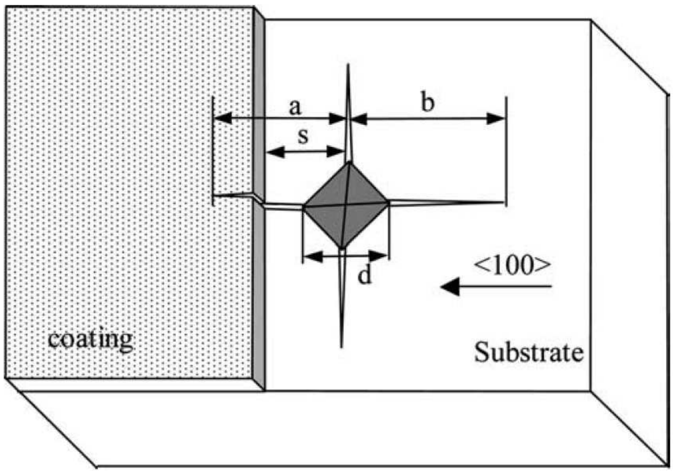

Fig. 2.2.8: Schematic illustration of the indentation geometry for substrate indentation method [88].

Depending on the particular substrate and film material circumferential cracks or even total spallation of the film can be observed around the indentation imprint as illustrated in Fig. 2.2.9 a). The circumferential through-thickness cracking and spallation formed in the third stage of the indentation fracture result in a sudden step in the load- displacement curve schematically shown in Fig. 2.2.9 b).

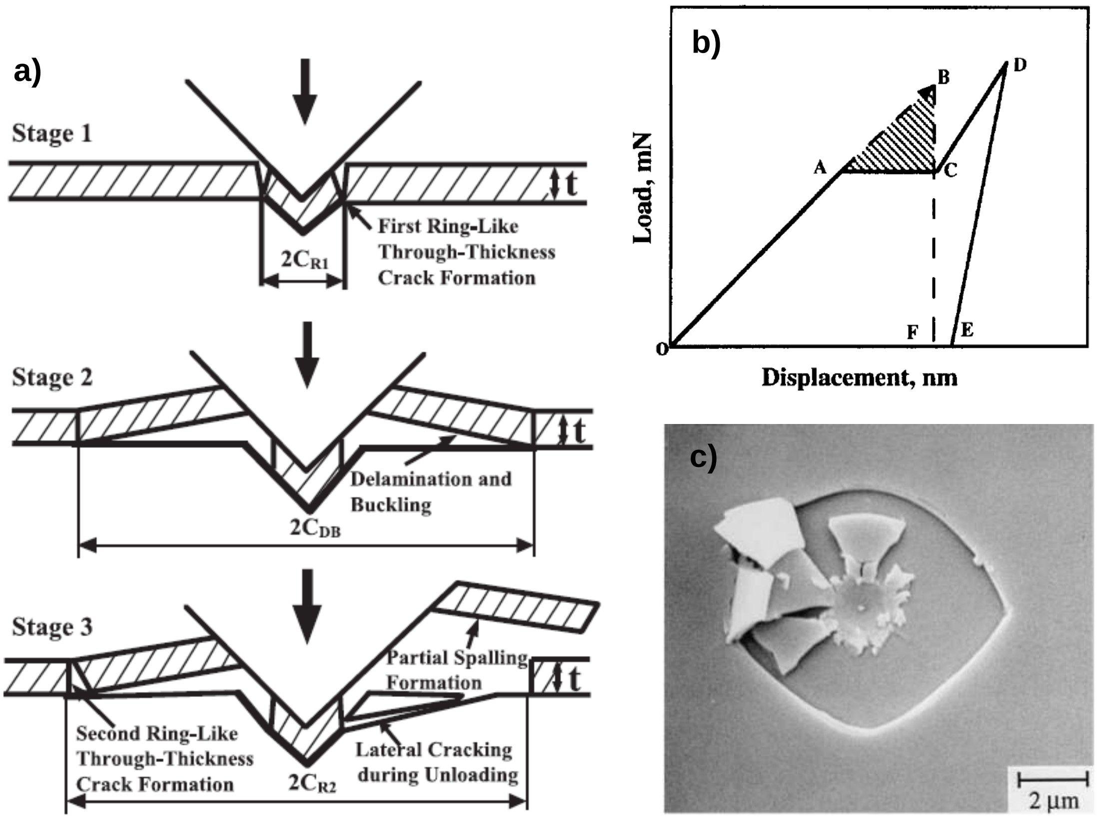

Fig. 2.2.9: a) schematic of various stages of nanoindentation fracture for the film/substrate system and b) schematic of a load-displacement curve, showing a step during the loading cycle and associated energy release [89]. c) SEM micrograph of an indentation imprint of a conical indenter in a carbon film on a silicon substrate with a typical delamination and buckling pattern [90].

As proposed in Li et al. the area enclosed by points ABC in Fig. 2.2.9 b) represents the energy U dissipated upon the film cracking and can be used for determination of fracture toughness according to

$$K_{Ic} = \left[\frac{E}{\left(1-\nu^2\right) 2\pi C_R} \left(\frac{U}{h} \right) \right]^{1/2}, \tag{2.12}$$

where $A = 2\pi C_R h$ represents the crack area calculated using the film thickness h and radius of the circumferential crack C_R and E and ν are Young’s modulus and Poisson’s ratio of the film [89]. The most controversial issue in calculating the fracture toughness using this method is determination of the fracture energy U. One of the fundamental questions is which part of the load-displacement curve does the fracture energy U actually correspond to [91]. The contributions of other factors to the step also remain unclear. These include for example the contribution of cracking and spallation of the substrate, dislocation nucleation and phase transformation of the substrate. [63]. In a recent paper Zhang et al. scrutinized several scientific papers dealing with the step in the load –displacement curve and concluded that the step corresponds to a freefall of the indenter after the film fracture. During this freefall the load is zero and the indenter does not do any work that could be related to fracture energy. The use of this approach is therefore doubtful and not recommended [92].

The third type of indentation-induced crack patterns are channel cracks. The channel cracks represent cracks that extend through the whole thickness of the film down to the substrate. This through-thickness profile of the crack is maintained during further propagation of the crack virtually forming a “channel”. The channel cracks in thin films can be generated using different methods such as bending [65], indentation [93] or thermal straining [94].

Using the indentation method a system of radial channel cracks can be generated if a hard film is deposited on a rigid substrate. For low indenter loads a hemispherical (“half-penny”) plastic zone is formed under the indenter and the radial cracks penetrate only part of the film thickness (see Fig. 2.2.10 a)). If the indenter load is further increased the plastic zone reaches the film/substrate interface, transforms into a cylindrical shape and through-thickness channel cracks are formed in the film (see Fig. 2.2.10 b)).

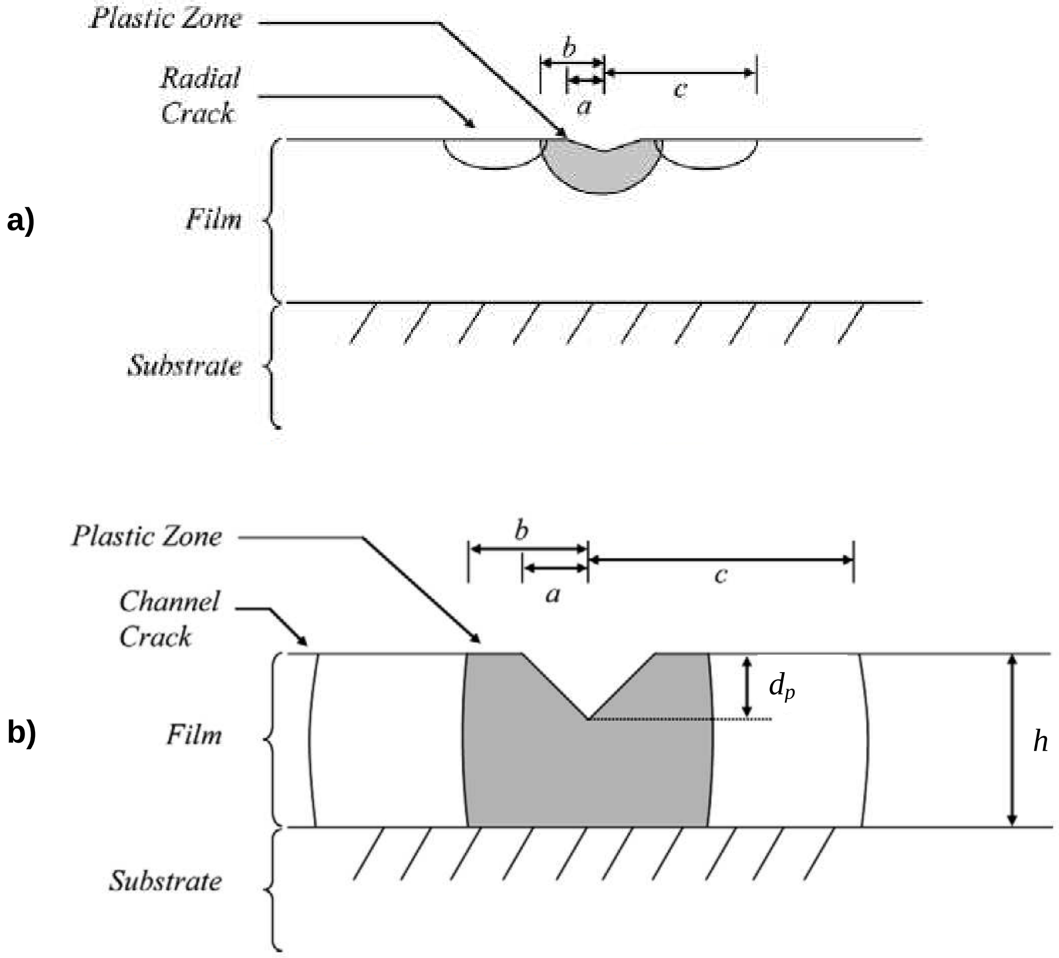

Fig. 2.2.10 : Schematic cross-section of indentation induced a) partial-penetration fracture in a mechanically thick film and b) channel cracking in a mechanically thin film [93]. Parameters a, b, c, d_{p} and h represent radius of the indentation, radius of the plastic zone, crack length, residual plastic displacement and film thickness, respectively.

If the substrate material is harder and tougher than the film, it can be assumed that the indented volume is accommodated by the film material only and the fracture toughness can be calculated according to

$$K_{Ic} = \lambda' V^* \left(\frac{E}{H} \right)^{1/3} \frac{1}{h} \frac{P}{c^{1/2}} + \psi' \sigma h^{1/2}, \tag{2.13}$$

where *λ'* is a constant that can be calculated from the indenter shape, geometry and Poisson's ratio and *ψ'* is related to Dundrun's parameters that depend on the elastic mismatch between the film and the substrate [93]. The parameter V^* in Eq. 2.13 is used to exclude the portion of plastic displacement accommodated by the substrate in case the indenter penetrates through the film into the substrate. The parameter V^* is defined as

$$V^* = \begin{cases} 1 & d \le h \\ 1 - \dfrac{(d-h)^3}{h^3} & d > h \end{cases}, \tag{2.14}$$

where d and h represent indentation depth and film thickness, respectively. Other parameters in Eq. 2.13 are the same as in case of Eqs. 2.8 and 2.10. Similarly as in Eqs. 2.10 or 2.9 the second term on the right-hand side of Eq. 2.13 accounts for the film residual stress which represents an additional driving or retarding force for the crack propagation.

*H/E** ratio

Since hardness H and effective Young's modulus E^* belong to the most common material parameters measured by micro- or nanoindentation method, calculation of H/E^* ratio is very simple and straightforward. The effective Young's modulus E^* is related to Young's modulus E according to

$$E^* = \frac{E}{\left(1 - \nu^2\right)}, \tag{2.15}$$

where ν represents the Poisson's ratio.

Based on the modern theories of wear the H/E^* ratio is more important for the wear resistance of the material than hardness alone [52]. Some authors also attribute the enhanced resistance to cracking (i.e. enhanced toughness) of thin films to increased H/E^* ratio. Correlations between increased H/E^* and enhanced resistance to cracking have been shown for thin films of different material systems such as Al-O-N [67], Zr-Al-O [66], TiC/a-C:H [95] or W-DLC [96].

The qualitative explanation for enhanced toughness of films exhibiting high H/E^* can be given as follows. A sufficiently high hardness is obviously essential for satisfactory performance of films in different applications (e.g. protective or tribological). A low effective Young's modulus E^* enables to distribute the locally applied load to a larger volume of the film, which leads to a delay of the plastic deformation of the underlying substrate. The plastic deformation of the substrate is connected with generation of tensile stresses on the film side close to the film/substrate interface and subsequent formation of cracks as illustrated in

Fig. 2.2.11. From this figure it is clearly seen that a significantly lower plastic deformation of the steel substrate occurs in case of film with lower hardness, lower effective Young's modulus and higher *H/E** ratio (see the curved indenter imprint profile in Fig. 2.2.11 d) which is due to higher elasticity i.e. lower plastic deformation of the film compared to Fig. 2.2.11c))[95].

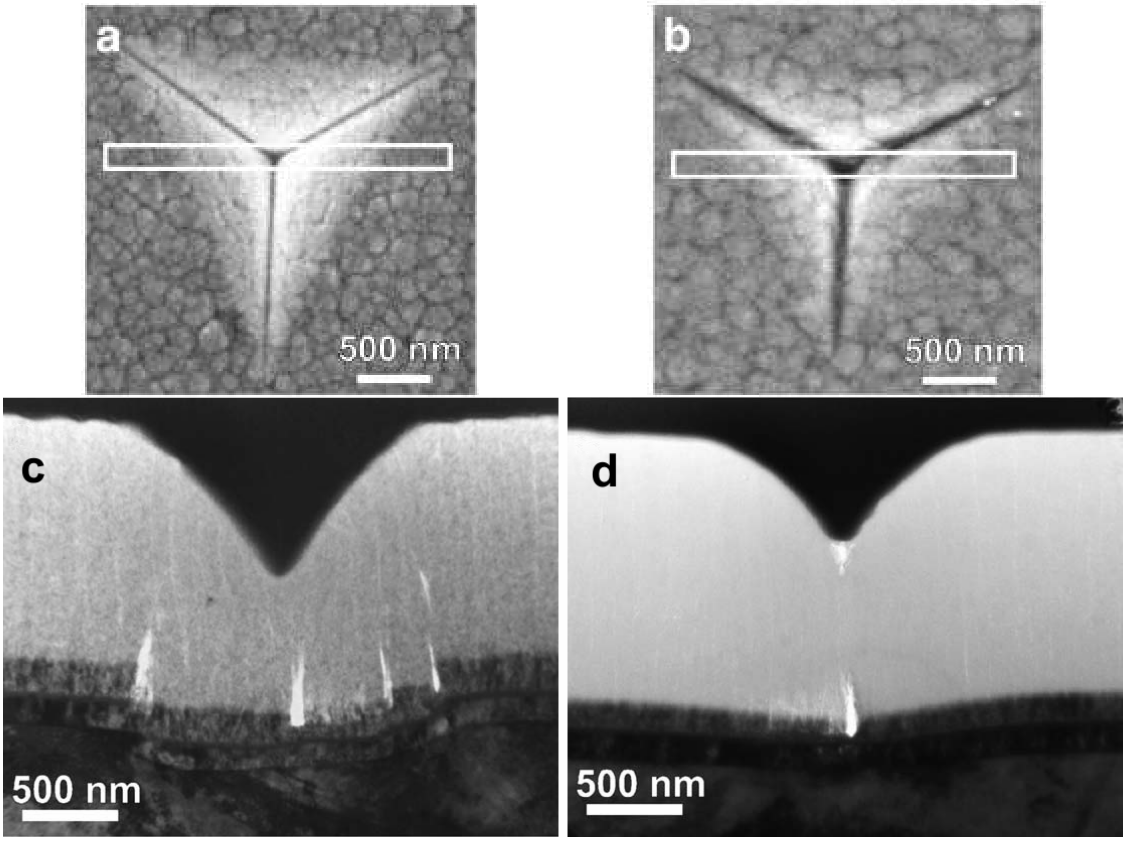

H= 20.0 GPa, E*=237.1, H/ E*=0.087 **H= 15.6 GPa, E*=141.2, H/ E*=0.114**

Fig. 2.2.11: Cube corner indenter imprints in 1400 nm thin TiC/a-C:H films with a) low and b) high H/E^* ratio after indentation into a constant depth of 1000 nm. A focused ion beam (FIB) technique was employed to cut samples from the areas indicated by the white boxes in Figs a) and b). TEM micrographs of the cut samples are shown in Figs c) and d) [95].

Since in plenty of applications the substrate material is often stainless steel or other metal (with low E^*) decreasing the effective Young's modulus is also required to match the mechanical properties of the hard film to those of the substrate. The beneficial role of low E^* close to that of the steel substrate in enhancement of the toughness of the film/substrate system was shown by Leyland et al. [52].

H^3/E^{*2} ratio

Some authors investigated correlations between resistance to cracking of thin films and their H^3/E^{*2} ratio [59, 77, 97]. This parameter originates from the estimated the load P_y necessary to initiate plastic deformation when a rigid sphere of radius r is pressed into an elastic/plastic substrate [98].

$$P_y = 0.78 r^2 \frac{H^3}{E^{*2}} \tag{2.16}$$

From Eq. 2.16 it is seen, that the material's resistance to plastic deformation is proportional to the H^3/E^{*2}. A correlation between H^3/E^{*2} and increased resistance to cracking of magnetron sputtered films was demonstrated for different material systems such as Zr-Cu-O [59, 77] or W-C:H [97].

Similarly as in the case of simple H/E^* ratio the H^3/E^{*2} ratio also increases with increasing hardness and decreasing effective Young's modulus. Whereas the H/E ratio is generally recognized as an indicator of wear resistance [52] the H^3/E^{*2} ratio describes the resistance to plastic deformation [98].

Based on the works of different authors dealing with correlations between both H/E^* and H^3/E^{*2} ratios and resistance to cracking of thin films, it is clear that the materials with higher hardness and lower effective Young's modulus exhibit enhanced resistance to cracking i.e. enhanced toughness [59, 77, 66, 67, 95-97]. Some open questions however still remain such as: Which of these parameters more precisely describes the films' resistance to cracking? Is there any value of these parameters that represents a sufficient condition to prevent formation of cracks in the film? How do other properties such as film thickness, macrostress or substrate material affect mutual interrelationships between these ratios and resistance of thin films to cracking?

Critical indentation load

Low thickness of the film and deformation of the underlying substrate represent major limitations in determination of fracture toughness of thin films from radial cracks. The indentation load can be reduced if the cube corner indenter is used. However materials with high toughness still require relatively high loads to induce cracks that are essential for calculation of the fracture toughness K_{Ic}. In some cases the resulting indentation depth may even exceed the film thickness. Galvan et al. used focused ion beam (FIB) technique to cut samples in the vicinity of cube-corner indenter imprints in TiC/a-C:H films [95]. This made it possible to investigate the cross section of the film containing typical radial cracks developing from corners of the indenter imprints (see Fig. 2.2.12). The indentation depth in this case exceeded the film thickness, which was 1.4 μm. From Fig. 2.2.12 it is clearly seen that the cracks initiate in the brittle silicon substrate and a further propagation of the crack through the film depends on the film's toughness. From these observations it is clear that quantification of fracture toughness from the length of the radial cracks assuming no interaction with the substrate would be incorrect. The authors however used this phenomenon to detemine another quantity that is related to fracture toughness and that provides a qualitative comparison of films' toughness. Instead of the length of the radial cracks their method relies on observation of the number of cracks that form in the film. In this method sets of 5 indentations are introduced in the film using different loads. The loads range from low values that do not result in formation of radial cracks to high values that lead to radial cracking in most corners of the indentation imprints. Subsequently the average number of cracked corners is calculated for each load and the percentage of cracked corners is plotted as a function of applied load as shown in Fig. 2.2.13. The data for a given material are then fitted by a sigmoidal curve and the critical indentation load L_r is determined. The critical indentation load represents a threshold load that results in formation of cracks in 50 % of the indentation imprint corners. Since the cracks initiate from the underlying silicon substrate the number of cracked corners will obviously depend on thickness of the film and a possible interlayer. For that reason thickness of the film and the interlayer should be kept constant for proper comparison of the materials [95].

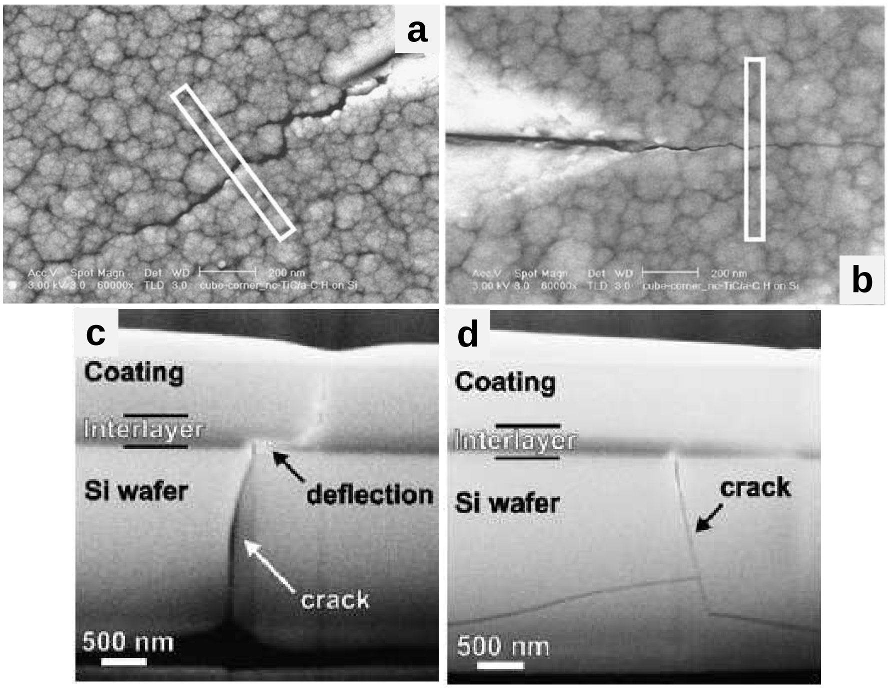

Fig. 2.2.12: SEM images of cracks propagating from the edge of cube-corner indentations in TiC/a-C:H films with a) low and b) high toughness. A focused ion beam (FIB) technique was employed to cut samples from the areas indicated by the white boxes in Figs a) and b). SEM micrographs of the cross section of the cut samples from figures a) and b) are shown in figures c) and d), respectively [95].

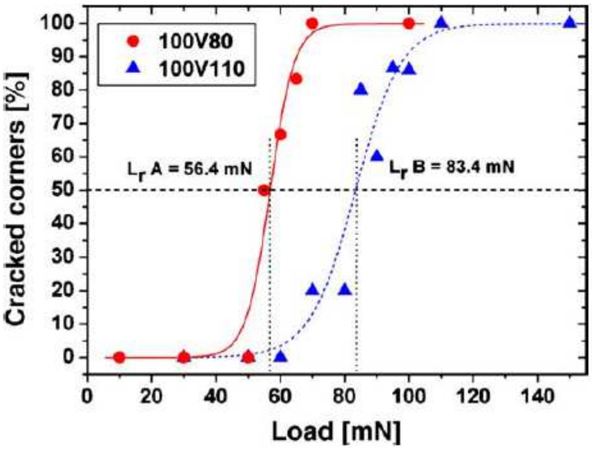

Fig. 2.2.13: Sigmoidal curves of the percentage of cracked corners as a function of the indentation load for films with low (red) and high (blue) toughness [95].

Visual comparison of crack patterns

Although not giving an exact quantity, comparison of the crack patterns is a simple technique providing an easy way to evaluate the coating's resistance to formation of cracks i.e. film toughness. Compared to the calculation of the critical indentation load L_r (see above) the direct observation of crack patterns takes into consideration not only the number of cracks but also their size. This is reasonable since the crack size (e.g. length of radial cracks or diameter of circumferential cracks) provides additional information about the film's resistance to cracking. Even if the cracks are initiated in the underlying substrate, a film with higher toughness will obviously lead to a smaller crack length compared to a film with lower toughness. Since no specific quantity is calculated in this method, it is appropriate to use the general term toughness to refer to the film's ability to resist the formation of cracks. A detailed investigation of different factors affecting the formation of cracks in sputtered films using direct observation of crack patterns is provided in references [42, 59, 77]. Based on these works several issues need to be taken into consideration when comparing the crack patterns in thin film.

Firstly the crack pattern may form in the thin film with a certain time delay after the indentation. For that reason the crack pattern does not necessarily need to be accompanied by the typical step feature on the corresponding loading-unloading curve. It was observed that the characteristic radial cracks formed >10 s after the removal of the indenter [42].

The substrate material represents another factor that significantly affects the crack pattern. As shown in Fig. 2.2.14 indentation of Zr-Cu-O film (H=10 GPa, E^*= 120 GPa) deposited on a steel substrate (H=2.9 GPa, E^*= 212 GPa) results in formation of circumferential cracks surrounding the indentation imprint. The same film deposited on Si(100) wafer (H=12.6 GPa, E*= 132 GPa) exhibits radial cracks while on soda-lime glass (H=7.1 GPa, E*= 69 GPa) only point defects are observed [42, 59]. This can be explained by different response of the film to the deformation of the underlying substrate. A significant plastic deformation of the soft steel substrate generates high shear stresses that are symmetrically distributed with respect to the indenter axis, which leads to formation of circumferential cracks. The hard silicon substrate represents a stiff support where most of the deformation is absorbed by the film leading to generation of high lateral stresses and formation of radial cracks. The glass substrate has a higher hardness compared to steel and a lower effective Young's modulus compared to the silicon substrate. This leads to a lower plastic deformation of the substrate and redistribution of the applied load over a larger area thus decreasing the local stress maxima and increasing the toughness of the overall system. These results indicate that it is not possible to evaluate the toughness of thin films from the size of the crack pattern if the films are deposited on different substrates. Out of these three substrate materials the Si wafer seems most suitable since the deformation work is absorbed predominantly by the film and the length and number of the radial cracks can be easily determined [42].

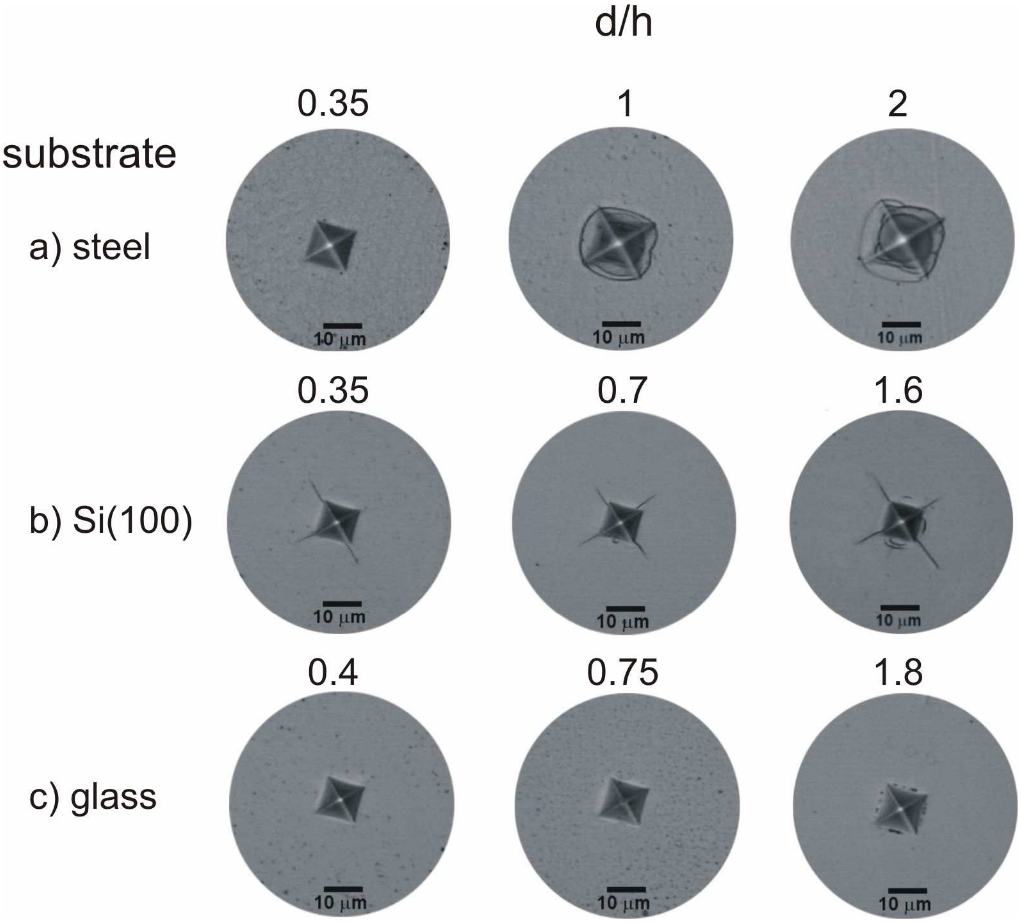

Fig. 2.2.14: Imprints of a Vickers diamond indenter into a Zr-Cu-O film with different thickness deposited on a) ČSN 15330 steel, b) Si(100) wafer and c) soda-lime glass. The film thickness ranged from 2 µm – 10 µm and the indentation load was L=1 N resulting in different d/h ratio. Mechanical properties of the film are: H=10 GPa, E^*= 120 GPa, W_e=50 %, H/E^*= 0.083, H^3/E^{*2}= 0.0694 GPa [42].

Fig. 2.2.14 also illustrates the effect of film thickness on the formation of crack pattern. The film thickness is expressed in terms of a dimensionless d/h ratio where d is the indentation depth and h is the film thickness. The indentation load of 1 N was applied to films with h ranging from 2 µm -10 µm deposited on steel, Si(100) wafer and glass substrates. In case of a steel substrate (Fig. 2.2.14) the size and number of circumferential cracks increases with a increasing d/h ratio (i.e. with decreasing film thickness). Films deposited on a glass substrate (Fig. 2.2.14 c)) exhibit small point defects for high d/h only i.e. for low thickness. The crack patterns in films deposited on silicon substrate do not vary significantly with the film thickness – only a slight increase is observed for films with lower thickness i.e. high d/h. Based on the presented results the silicon substrate was suggested as most suitable for the toughness evaluation from direct comparison of crack patterns. The main reasons were a clear crack pattern and relative independence of the crack pattern on the film thickness [42, 77]. With respect to observations of Galvan et al. showing that the cracks are initiated in the substrate and further propagate through the film, the thickness might play a role in case of films with high toughness and thickness <2 microns [95]. For that reason the film thickness should be kept constant in direct comparisons of the crack patterns even if the silicon wafer is used as the substrate material.

In summary the direct observation of indentation crack pattern is a useful method for qualitative comparison of toughness of thin films especially where interaction with the underlying substrate is inevitable. In order to avoid uncertainties in the evaluation of film toughness from visual comparisons of the crack patterns, the following requirements should be met:

1) delay between indentation and observation of crack pattern >10 s
2) substrate material that results in formation of clear crack pattern (e.g. silicon wafer)
3) comparison of films on the same substrates
3) constant thickness of the films that are compared

In general it can be concluded that for thin films where the depth of the plastic zone during indentation exceeds 10 % of the film thickness, interaction with the substrate can not be excluded. In this case determination of toughness of thin films using the fracture toughness parameter is doubtful and qualitative comparison of films with similar thickness deposited on the same substrates represents an easy and straightforward alternative. This can be practically realized either using direct comparison of the crack patterns or by calculating the radial critical load.

2.2.3.2 Bending methods

Another relatively simple method used for determination of toughness of a thin film is bending. Information from this type of loading is especially useful for applications such as flexible electronics, solar cells, food packaging etc. Similarly to the case of indentation, different methods and quantities were proposed to quantify toughness of thin films from bending.

Fracture toughness

Even in the case of bending methods the fracture toughness represents a frequent parameter for toughness evaluation. Some of these methods are however difficult to implement for different reasons such as a complicated procedure, need for substrate etching or applicability to freestanding films only, which are very difficult to handle if their film thickness is just several microns or even hundreds of nanometers [99, 100].

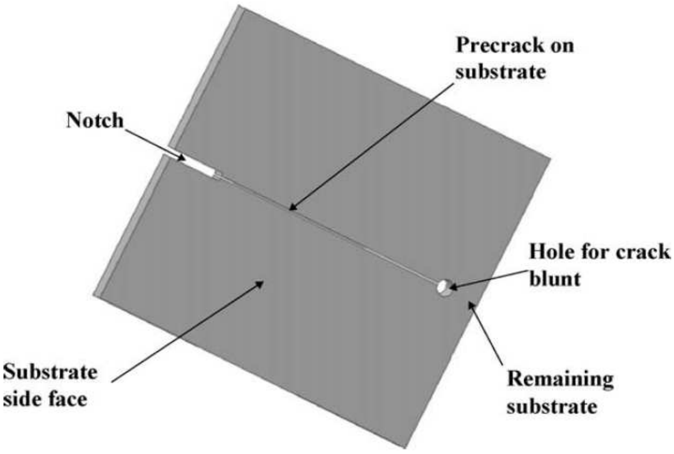

Fig. 2.2.15: Steel substrate with a precrack for toughness measurement of hard thin films using four-point bending. The film is deposited on the side face [80].

Jaeger et al. proposed an ingenious method that solves the difficulties with fabrication of pre-crack and handling of thin freestanding films [101]. A notch and a hole were first fabricated in a steel substrate as shown in Fig. 2.2.15. This substrate was fatigued to generate a crack that extends from the notch to the whole. Subsequently the film is deposited on both sides of the substrate. Two four-point bending tests are then performed and the corresponding load, displacement and crack opening are recorded. In the first test a load is applied on the specimen until a crack forms in the film and extends to the hole. In the second bending the specimen with the cracked film is loaded again until the same displacement is obtained as in the case of the first bending. The difference in the applied load is considered as the load necessary for crack propagation in the film. For a plane stress condition the fracture toughness K_{Ic} can be calculated using

$$K_{Ic} = \sqrt{G_c \cdot E^*}\ , \tag{2.17}$$

where G_{c} and E^* are critical energy release rate and effective Young's modulus, respectively. The critical energy release rate in Eq. (2.17) can be calculated from

$$G_c = \frac{1}{4ha}\int_0^\infty F^2 \mathrm{d}C\,, \tag{2.18}$$

where h and a are the film thickness and total crack length, respectively, and the functional dependencies of film load F and film compliance C are recorded during the bending test. Besides the fracture toughness this method also enables to calculate the ultimate tensile strength of the material from the maximum load. There are however several limitations of this method. Firstly the energy measurement requires a purely elastic deformation of the substrate. Thus the calculated fracture toughness would be incorrect if plastic deformation occurred. Secondly the existence of the pre-crack in the substrate may influence the growth of the film and thus its fracture toughness [101].

A multi-strain flexure test for determination of fracture toughness of ceramic films deposited on ductile substrates was proposed by Leung et al. [102]. In this method 100 μm strips of the film are sputter-deposited on a side face of a substrate beam using a mask. The orientation of the strips is parallel to the beam axis and the beam thickness is $2b$ (see Fig. 2.2.16). A four-point bending method is applied in order to strain the beam. The maximum strains ε_{max} generated on the top and bottom sides of the beam are monitored by strain gauges. During bending different strips experience different strains ε depending on the distance z of the particular strip from the neutral plane. Film strips that are subjected to strains higher than the critical value fracture. From the position of the cracked strips the critical strain of the film material can be determined. Assuming a purely elastic deformation the Hooke's law makes it possible to calculate the critical stress σ_{c}.

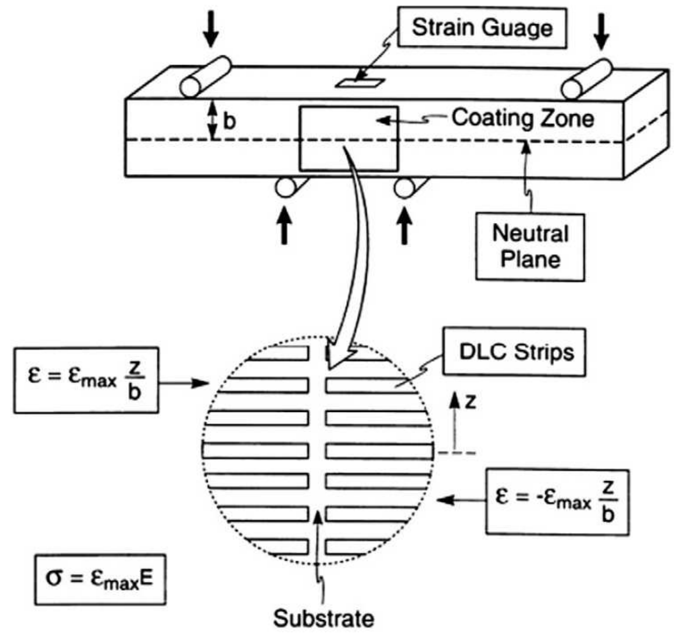

Fig. 2.2.16: Schematic illustration of the multi-strain flexure specimen and test configuration [102].

Knowing the value of critical stress σ_c the fracture toughness of the film can be calculated using

$$K_{Ic} = \sigma_c \left(\frac{1-\nu^2}{2} \pi h g \right)^{1/2}, \tag{2.19}$$

where υ and *h* are Poisson‘s ratio and thickness of the film, respectively. The *g* parameter in Eq. (2.19) contains the substrate effect and is a function of the applied stress, the yield stress, the strain hardening coefficient of the substrate and the Dundurs parameters that describe the elastic mismatch between the film and the substrate [63]. Beside fracture toughness the multi-strain flexure test also provides information about the film’s critical strain ε_c, i.e. “cracking resistance“, which is discussed below.

Cracking resistance

Bending tests can also be used to determine the film’s “cracking resistance“, which can be related to fracture toughness of the thin films [69, 50]. The cracking resistance represents the threshold strain over which the density of cracks sharply increases.Wiklund et al. proposed a small bending device that can be installed into a scanning electron microscope to enable in situ observation of crack patterns in thin films deposited on high speed steel (HSS) [69]. A schematic view of the central part of the device based on the four-point bending method is shown in Fig. 2.2.17.

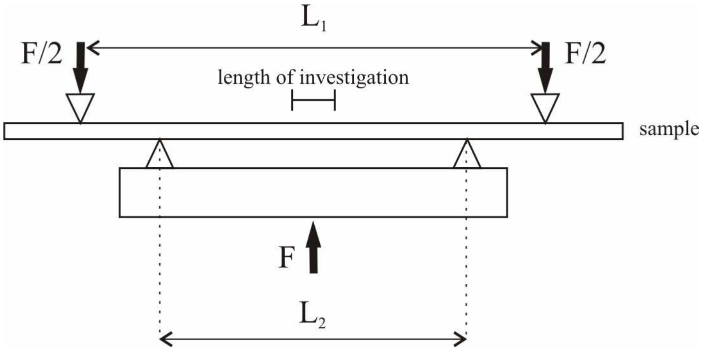

Fig. 2.2.17: Schematic view of the central part of the bending device [69].

In the case of four-point bending (Fig. 2.2.17) the upper part of the test sample is exposed to tensile forces. If the strain in the upper fibre of the sample, i.e. where the film is deposited, exceeds the threshold value for crack nucleation, a crack is formed in the film. As the applied force further increases the crack density increases as well. If the substrate thickness h_s is significantly higher than the film thickness h ($h_s \gg h$), the strain ε_s in the upper fiber, i.e. on the film surface, can be approximated by

$$\varepsilon_s = \frac{3F(L_1 - L_2)}{2E_s b h_s^{\,2}}, \tag{2.20}$$

where F, E_s, b, L_1, L_2, represent the applied load, the Young's modulus of the substrate, the width of the substrate and distances between the outer and the inner supports, respectively. Since PVD films often exhibit residual stresses leading to certain residual strain ε_{res}, the actual strain in the film ε_c is a sum of the residual strain and the strain generated due to bending of the sample.

$$\varepsilon_c = \varepsilon_s + \varepsilon_{res}, \quad \varepsilon_{res} < 0 \tag{2.21}$$

In case of compressive residual stress, which is a frequent situation in sputtering, the actual strain in the film ε_c is lower than ε_s, because a certain strain is necessary in the beginning of bending to compensate for the compressive residual stresses (i.e. residual strains). The residual strains of the as-deposited films can be calculated e.g. using the deflection method or the $\sin^2\psi$ X-ray diffraction method [50]. The number of cracks generated in the film during bending can either be determined from visual inspection of the film surface in SEM or by an acoustic emission method. The crack formation produces an acoustic signal that can be measured using an acoustic detector. The acoustic emission is then used as a measure of crack density. Compared to visual observation the acoustic emission method provides data with the same accuracy (see Fig. 2.2.18) but is easier and faster. The crack density is then plotted as a function of film strain and the threshold strain, over which the crack density sharply increases, represents the cracking resistance of the film.

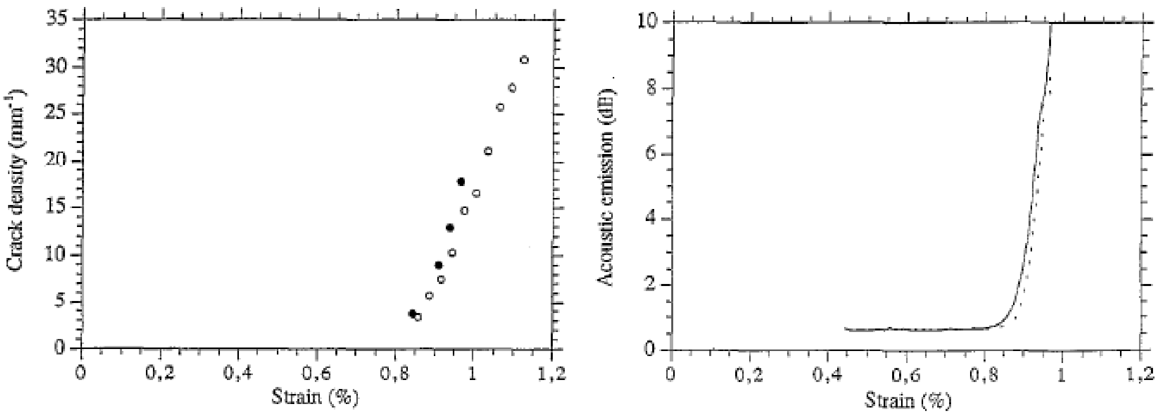

a) **b)**

Fig. 2.2.18: a) Density of cracks vs. coating strain ε_c for two different TiN coatings. b) The average amplitude of acoustic emission, resulting from crack initiation and growth for two different TiN coatings as a function of coating strain [69].

Fracture stress

While the fracture toughness K_{Ic} represents the ability of a material to resist propagation of a crack that already exists, the fracture stress is defined as the tensile stress that must be applied in order to create a first crack in the material. An experimental method for determination of fracture stress of ceramic films was suggested by Carneiro et al. [64]. In this method an Yttria-stabilized Zirconia (ZrO_2-Y_2O_3) film sputter-deposited on a Ni-alloy substrate was bent in a four-point bending apparatus shown in Fig. 2.2.19 a). For a thin film on a thick substrate where $h_s \gg h$ the nominal stress in the film σ_N can be estimated using

$$\sigma_N = \varepsilon_{\max} \frac{E}{(1-\nu^2)} = \varepsilon_{\max} E^*, \tag{2.22}$$

where $\varepsilon_{\max}$, υ, E and E^* represent the maximum strain that occurs in the outer fibre of the beam bent (i.e. in the film), Poisson’s ratio, Young’s modulus and effective Young’s modulus of the film, respectively. The maximum strain ε_{max} can be calculated from the geometry of the bending apparatus, applied force, geometry of the substrate and Young’s modulus of the substrate using the classic Euler-Bernoulli beam theory (for details see ref. [64]). If the residual stress σ in the film is calculated using the Stoney‘s equation [103], the predicted stress σ_P is given by a simple sum

$$\sigma_P = \sigma_N + \sigma. \tag{2.23}$$

During bending of the film+substrate system a typical crack pattern with parallel cracks running perpendicular to the bending direction is formed. Using the Swanson model the stress distribution along an uncracked segment with the width of λ can be calculated [104]. This stress (denoted as actual stress) reaches the maximum value $\sigma_{\max}$ in the center of the uncracked segment. If at least two bending tests are performed yielding two different values of predicted and maximum actual stresses, the fracture stress can be determined from the intercept of the σ_P (u) *and* $\sigma_{\max}(u)$ functionalities, where u represents total deflection of the beam (see Fig. 2.2.19 b)).

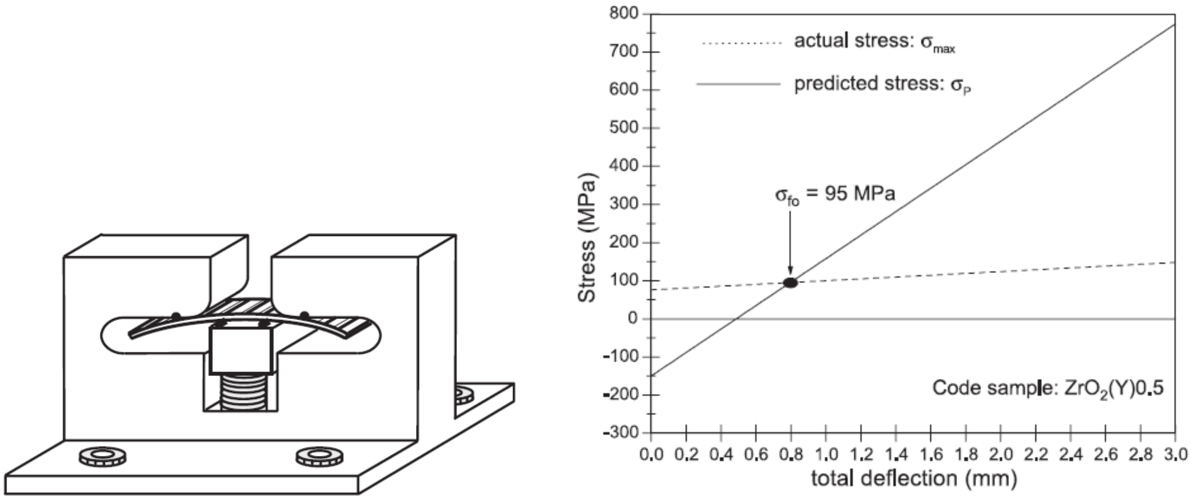

a) **b)**

Fig. 2.2.19: a) Scheme of the four-point bending apparatus b) determination of the fracture stress σ_{f0} of a 0.5 µm thick ZrO_2-Y_2O_3 film from the interception between the actual stress and the predicted stress values [64].

The same authors also investigated the effect of film thickness on fracture properties of the films. They observed that the fracture stress significantly increased with a decreasing film thickness. In their explanation they suggest that the fracture stress of the film depends on the size of large defects only. As the probability to incorporate larger defects is obviously higher for larger volumes, films with higher thickness exhibit lower fracture stress [64].

Visual comparison of cracks after bending

Visual observation of film surface after bending represents a qualitative method that enables to compare resistance to cracking of thin films. Musil et al. proposed a simple bending apparatus and investigated resistance to cracking of different films prepared by magnetron sputtering [66, 67, 105]. In their work the authors bent films deposited on molybdenum strips over a cylinder with a diameter of 25 mm and the presence of cracks was observed using a scanning electron microscope or light optical microscope. Since no specific quantity was calculated from the visual observations, the films were simply denoted as crack resistant if no cracks were observed after bending.

2.2.4 Cu-containing films with enhanced toughness

From the point of view of architure of nanocomposite thin films with enhanced toughness copper represents an interesting element. Since copper nitride Cu_3N is decomposed to pure Cu at relatively low temperatures (≈450°C) [106], reactive co-deposition of copper and other metals in the presence of nitrogen at elevated temperatures results in formation of MeN and pure Cu [73, 107, 108]. Such a mixture of metallic Cu and a hard nitride phase MeN, belongs to one group of hard and superhard nanocomposites denoted as nc-MeN/soft phase, representing a two phase nanocomposite composed of a nanocrystalline hard nitride and a soft metallic phase such as Cu, Ni, Y, Ag, etc. [109]. The presence of metallic Cu in the film has several beneficial effects on its toughness. Firstly Cu alone represents a ductile phase, which may improve the toughness of brittle materials by mechanisms described in section 2.2.2.

Secondly as an insoluble additive Cu may restrict the grain growth and reduce the grain size of the second hard phase to a nanoscale level as described by the Barna-Adamik structural zone model [110]. The formation of a fine-grained nanocomposite structure represents another toughening mechanism.

However the Cu-induced enhanced toughness is not exclusively connected with thin films containing a nitride phase. An increased toughness has also been reported for films based on carbides [42, 60], DLC [111] or metallic multilayers [51, 112]. Moreover pure metallic copper films also exhibit variations in toughness due to the size effect [113]. Tab. 2.1 summarizes papers reporting on enhanced toughness of Cu-containing films. Besides the deposition method, specification of the toughened material and the method or quantity that indicated toughness enhancement, the table also briefly describes explanation of the toughening effect provided by the authors. As can be seen from Tab. 2.1 in case of all films copper exists in a metallic form and does not form a nitride or an alloy with the other elements. The optimum Cu content that results in maximum toughness differs depending on the other elements in the carbide- or nitride-based films. Apparently the other co-existing phases are able to accommodate some copper atoms in their structure and when their solubility limits are reached, agglomerates of pure Cu are formed. Different solubility limits of different phases then result in films with maximum toughness at different Cu contents. Moreover the non-equilibrium nature of the deposition process needs to be taken into account, which may result in formation of non-stoichiometric phases with somewhat higher solubility limits. Based on the studies listed in Tab. 2.1 the main mechanisms of toughness enhancement in Cu-containing films can be summarized as follows:

1) Crack tip blunting by the ductile phase – The ductile Cu agglomerates or interlayers are able to blunt the tip of the propagating crack and dissipate the deformation energy [51, 113].

2) Formation of a nanocomposite structure – Cu restricts grain growth and stimulates nucleation of new grains, which leads to formation of a fine-grained nanocomposite. As the initial crack size is related to the size of the grains, decreasing the grain size or layer thickness in multilayered films results in reduction of the size of a potential crack and thus to reduction of the stress intensity factor when external load is applied [51, 60, 73]. Having different thermal expansion than the matrix phase, the Cu agglomerates also change the stress fields in their surroundings causing deflection of the propagating crack and increase of the crack path [60]. Furthermore the formation of a nanocomposite structure is often accompanied by a hardness enhancement, which reduces deformation of the material when constant indentation load is applied [107, 112].

3) Reduction of high compressive stresses – presence of Cu is able to reduce compressive stress that may result in film delamination. Such delamination may occur either immediately after the deposition or in the impact indentation tests, where additional compressive stresses are generated in the contact area between the indenter and the film [42, 111].

4) Grain-matrix sliding – weak bonds between the hard phase and the soft Cu phase enable grain-matrix sliding [111]

It is however important to note, that mechanisms described in points 1) and 2) are antagonistic. High content of the ductile Cu phase would be beneficial for enhanced energy absorption, but on the other hand it would lead to a significant decrease of hardness, increase of the grain size of the Cu phase and thereby also to an increase of the size of the potential initial crack. On the other hand too small size of the Cu particles results in a limited ability to accommodate dislocation activities and dissipate the deformation energy. These two counteracting phenomena lead to an enhanced toughness of nanocomposite films with a relatively low optimum Cu content approximately in the range of 1.4 ÷ 11 at.% [42, 60, 73, 107, 111] or a relatively low thickness of Cu layers (h_{Cu}≈25 nm) in multilayered films [51].

Tab. 2.1: Summary of various Cu-containing thin films with enhanced toughness.

preparation method	material	material description	method/quantity indicating enhanced toughness	explanation of enhanced toughness	Ref.
ion beam assisted magnetron sputtering	Cr-Cu-N	CrN+Cr+Cu, Cu$\leq$ 5 at.%	fracture toughness	formation of fine grained microstructure due to addition of Cu, coarse columnar structure is restricted	[73]
DC magnetron sputtering	Cr/Cu	Cr/Cu nanostructured multilayered film, λ=50 nm	fracture toughness	intermediate bilayer period (λ=50 nm) is low enough to reduce the stress intensity factor but high enough to blunt the crack tip	[51]
reactive DC magnetron sputtering	DLC/Cu	Cu particles embedded DLC matrix, Cu=11 at.%	Rockwell indentation test	Cu reduces high compressive stress, weak bonds between Cu and DLC enable grain-matrix sliding, introduction of ductile phase	[111]
reactive magnetron co-sputtering + RTA	TaN-Cu	TaN+Cu nanocomposite, Cu=1.4 at.%	indentation test, H^3/E^{*2}	formation of Cu network phase surrounding TaN columns	[107]
reactive magnetron co-sputtering,	Cu/Ni	Cu/Ni nanostructured multilayered film, λ=200 nm	repeated indentation test	intermediate bilayer period (λ=50 nm) results in enhanced hardness, deformation is reduced by many interfaces	[112]
electron beam evaporation	Cu	freestanding Cu film	fracture toughness	thick films exhibit higher toughness, increased probability of dislocation annihilation in thin films results in smaller plastic zone in the crack tip leading to reduced ability to dissipate deformation energy	[113]
DC magnetron sputtering	TiC/Cu	TiC+Cu+C, Cu= 5-9 at.%	indentation toughness	grain size refinement, crack deflection and meandering between the Cu agglomerates	[60]
DC magnetron sputtering	ZrC/Cu	ZrC+Cu, Cu= 2-10 at.%	indentation test	incorporation of Cu improves film adhesion by reducing the high compressive stress , high hardness is preserved	[42]

RTA = rapid thermal annealing

2.3 Antibacterial surfaces

The term antibacterial surface generally refers to a surface containing an antibacterial agent, which is able to destroy the bacteria or reduce their ability to grow or reproduce. The rather broad term antibacterial agent can further be divided into two groups [114].

Bacteriostatic agent – prevents the growth of bacteria - i.e. it keeps them in the stationary phase of growth - but does not necessarily lead to death of the bacterial cell and after removing the agent the bacteria are able to reproduce again

Bactericidal agent **–** kills the bacteria

Antibacterial surfaces have attracted considerable scientific attention in recent years. This is mainly due to the fact that application of such surfaces into hospitals settings (door handles, bed rails, call buttons, toilet seats etc.) and other public settings can provide a way to deal with the widespread nosocomial infections [115] and emerging multi-drug resistant bacteria [116]. Examples of such modern multi-drug resistant bacteria include *Methicilin-resistant staphylococcus aureus* [117], *Streptococcus pneumoniae* [118], *Mycobacterium tuberculosis* [119], *Escherichia coli* [120], *Vancomycin-resistent enterococcus* [121] and others. Another important application of antibacterial surfaces is modification of surface of biomedical materials for implants in order to reduce the risk of inflammatory processes [122].

The most common antibacterial agents used for fabrication of antibacterial surfaces include copper [123, 124] , silver [125], titanium dioxide [126], antimicrobial peptides [127], N-halamine [128], ammonium or phosphonium salts [129] and some oher polymeric materials [130]. The effectiveness of killing various species of bacteria differs depending on the particular bacteria and antibacterial agent used. For that reason fabrication of surfaces or nanoparticles containing more than one antibacterial agent was proposed in order to broaden the spectrum of bacteria the surface is able to eliminate. Examples of surfaces containing more antibacterial agents include combination of Ag/Cu [131-133], TiO_2/Ag [134, 135] or TiO_2/Cu [136].

2.3.1 Quantification of antibacterial properties of thin films

In order to compare the antibacterial properties of different surfaces the antibacterial effect needs to be properly quantified. The most common method used for quantification of the antibacterial properties of thin films is the plate counting method adopted from the 22196; 2007 ISO standard [137] which has been utilized for instance by Chiu et al. [138].

Plate counting method

The film is first washed with a disinfectant to kill any bacteria on the surface. After drying the sample a certain volume of a solution containing bacteria is applied onto the surface of the thin film and held in close contact by a sterilized glass. The samples are incubated for a given contact time *t* at a given temperature. Afterwards the samples are washed with a physiological solution and a certain volume of the wash-away solution is abstracted and used for inoculating the bacteria onto Petri dishes containing nutrient agar. After 24 hours of cultivation at 37 °C the bacterial colonies are visible and can be counted. The antibacterial properties are quantified by means of antibacterial efficiency E (sometimes also denoted as antibacterial ratio, antibacterial rate or antibacterial effect) which is given by the following formula

$$E = \frac{(A - B)}{A} \cdot 100\,\%, \tag{2.24}$$

where A is the number of colonies on the control sample (uncoated substrate) and B is the number of colonies on the sample corresponding to the film tested.

Alternatively the whole specimens (substrate with film) can be immersed into the nutrient broth containing bacteria for 24 hours at 37 °C. After the end of incubation the nutrient broth is diluted by deionized water and inoculated onto a Petri dish containing nutrient agar. After incubation for 24 hours at 37°C, the number of bacterial colonies is counted as described above [139].

Dry method

In order to mimic the dry surfaces in health care environments a „dry“ method of testing antibacterial surfaces was developed. In this method a small volume of bacterial solution is streaked out on the tested surface using a sterile cotton swab. The thin liquid film evaporates within a few seconds leaving the bacterial cells in direct contact with the surface. After incubation for a given time the sample is vortexed in an ice-cold phosphate-buffered saline (PBS) with glass beads. The vortexed solution is further diluted in PBS buffer and plated on lysogeny broth (LB) agar. After incubation the surviving bacterial colonies are counted and antibacterial efficiency can be determined [140]

Besides the quantitative evaluation of antibacterial properties of thin films, there are also other tests related to fabrication of antibacterial materials but not necessarily connected with killing the bacteria. These methods include for example the fluorescence staining method used for evaluating of retention of bacteria on a particular surface [122, 141] or the MTT test where the biocompatibility of the antibacterial surface is investigated using human tissue cells [141].

For the evaluation of antibacterial properties of thin films various species of bacteria are used. The most common are *Escherichia coli* [132, 142, 143] and *Staphylococcus aureus* [122, 132, 143, 144]. However some other bacterial species like P*seudomonas aeruginosa* [142], *Methycilin-resistant staphylococcus aureus – MRSA* [142], *Staphylococcus epidermidis* [145] or *Actinobacillus actinomycetemcomitans* [122] are also used. Depending on the particular species used for the antibacterial test, different antibacterial efficiency E can be achieved as reported by Foster et al. [142]. These differences are often attributed to different thickness and composition of the cell wall and the ability of the antibacterial agent to penetrate it [146]. The structure of the cell wall in Gram-negative and Gram-positive bacteria is schematically shown in Fig 2.3.1. The thickness of the peptidoglycan layer of the gram-negative *Escherichia coli* is very small (approximately 2–3 nm) while for gram-positive *Staphylococcus aureus* the thickness is significantly larger (10–100 nm).

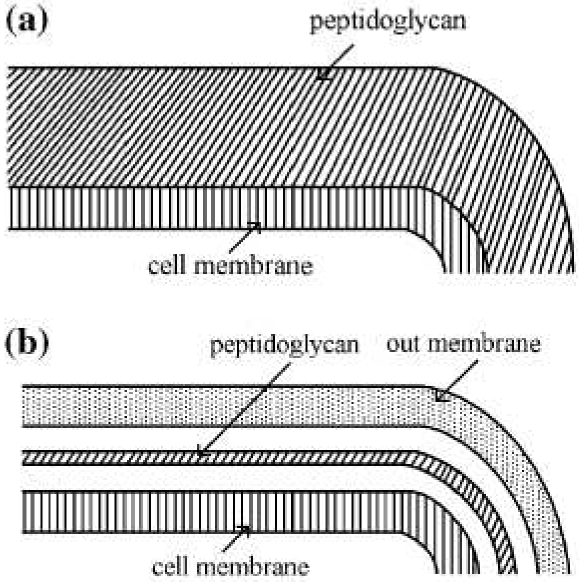

Fig. 2.3.1: The structure of the cell wall of (a) gram-positive bacteria and (b) gram-negative bacteria [146].

2.3.2 Antibacterial properties of Cu-containing surfaces

The first medical use of copper is reported in the Egyptian Smith Papyrus which dates back between 2600 and 2200 B. C. and describes application of copper for sterilization of chest wounds and drinking water. Other ancient civilizations like the Greeks, Romans or Aztecs utilized copper for example for treating headaches, burns, intestinal worms or ear infections. In the early 20th century the use of copper products was common in treatment of a variety of ailments [124]. After the discovery of antibiotics and their mass expansion after Second World War the use of copper- as well as silver-containing products in medicine gradually decreased. However the emerging multi-drug resistant bacteria, nosocomial infections and modern implant surgery attract increasing scientific and industrial attention to copper-containing antibacterial surfaces as demonstrated by many recent scientific papers. [122, 132, 136, 138, 142, 146-154].

In the field of magnetron sputtering of thin films incorporation of silver or copper is often used to provide the antibacterial effect. Such approach has been utilized for example for sputter-deposition of antibacterial films based on oxides [122, 135, 136, 138, 139, 155], nitrides [132, 141, 147, 150, 156, 157], oxynitrides [158], a-C:H [151, 159], multilayers [152], inter-metalic films [149] or pure metals [143, 148, 160]. The published papers show that the antibacterial effect of the films depends on many parameters including contact time of bacteria with the film [132, 150], post-deposition annealing [132, 158], concentration of Cu [136, 147, 148, 150, 151] or Ag [141, 156, 158] in the film, density [148] and size [156, 157] of the antibacterial metallic particles, ability to release metallic ions [155], presence of other elements in the film [157], sputtering time of individual layers in multi-layer films [152], additional effect of radiation-induced photocatalytic activity of the matrix phase [135], film thickness [138, 157, 160], particular magnetron sputtering method [149, 160], form of bacteria i.e. biofilm vs. planctonic [149] or number of antibacterial tests performed [148].

While silver does not have any physiological function in human organism [161] and the use of silver products may lead to toxicity such as irreversible argyria [161, 162], copper is an essential trace element for human metabolism [123] and after the metabolic requirements are met the excess of copper is released into the bile or excreted in the feces [163]. The relative harmlessness of copper can be demonstrated e.g. by the use of copper wrist bangles [164], intrauretine devices [165] or anti-inflammatory implants [166]. Together with the lower cost compared to silver this makes copper a more attractive element for fabrication of antibacterial surfaces.

The effectiveness of Cu-containing surfaces in reducing the number of bacteria in a real hospital setting has already been demonstrated in several trials. In a study conducted by Casey at al. copper containing toilet seats, tap handles and entrance door push plates were sampled for the presence of micro-organisms and compared to equivalent non-copper-containing items on the same ward. They observed that the median numbers of microorganisms harbored by the copper-containing items were between 90% and 100% lower compared to the non-copper-containing control equivalents [167]. A similar study was performed on an oncological/pneumological and geriatric ward in Hamburg. The numbers of aerobic, heterotrophic colony-forming units were determined on door knobs, door push plates and light switches made of copper alloys and the results were compared to aluminum or plastic items in control rooms. The number of colony-forming units on metallic copper-containing surfaces was reduced by one third compared to the control surfaces. Moreover after disinfection by common desinficant the repopulation of the surfaces was delayed in case of copper alloys [168].

2.3.3 Mechanisms of antibacterial action of Cu

Copper is a ductile metal with high thermal and electrical conductivity and atomic number of 29. Since completely filled orbitals represent a state of low energy, the actual electronic configuration of copper is Ar $4s^1$ $3d^{10}$, which results in the following important chemical and biochemical consequences [168]:

1) Copper cations are stable in the Cu(I) and the Cu(II)oxidation states in water.

2) The standard redox potential of the Cu(I)/Cu(II) couple at $pH=7$ and 25 °C is $E_0'=-261$ mV, falling within the range of standard redox potential of water constituents i.e. molecular hydrogen ($E_0'=-414$ mV) and molecular oxygen ($E_0'=+815$ mV).

3) In contrast to manganese (Mn) copper-involving redox reactions are one-electron transfers.

4) The electron transfer from Cu(I) to molecular oxygen is thermodynamically twice as favorable as that from Fe(II) (−104 kJ/mol versus −44.2 kJ/mol, respectively), making Cu(I) and exceptionally good redox reaction partner for O_2.

5) Copper cations are able to form stable complex compounds.

6) Copper cations have higher affinity to first shell ligands of periods 2 and 3 compared to other metals of the first transition period.

Due to the features listed above the copper ions are (1) essential for a variety of biochemical reactions on one hand but (2) potentially toxic to microorganisms on the other hand. Several redox reactions leading to potential copper cytotoxicity have been proposed. In the Fenton-type reaction (Eq. 2.25) copper ion and hydrogen peroxide produce reactive hydroxyl radical (·OH) which can participate for example in oxidation of cellular lipids, proteins, DNA or other biomolecules.

$$Cu^{+} + H_2O_2 \longrightarrow Cu^{2+} + OH^{-} + OH\cdot \qquad (2.25)$$

Cycling between reactions (2.26) and (2.27) can lead to depletion of sulfhydryls, which represent a biologically very important functional group.

$$2Cu^{2+} + 2RSH \longrightarrow 2Cu^{+} + RSSR\ 2H^{+} \qquad (2.26)$$

$$2Cu^{+} + 2H^{+} + O_2 \longrightarrow 2Cu^{2+} + H_2O_2 \qquad (2.27)$$

Here the term RSH indicates a thiol i.e. an organosulfur compound that contains a carbon-bonded sulfhydryl and RSSR is an organic compound containing a disulfide bond. Another route of copper toxicity is the ability of copper ions to compete with zinc or other essential metals for their binding sites in proteins [124].

The main mechanisms of toxicity of copper to microorganisms include copper mediated cell membrane damage, interaction with nucleic acids and copper mediated protein damage as illustrated in Fig. 2.3.2.

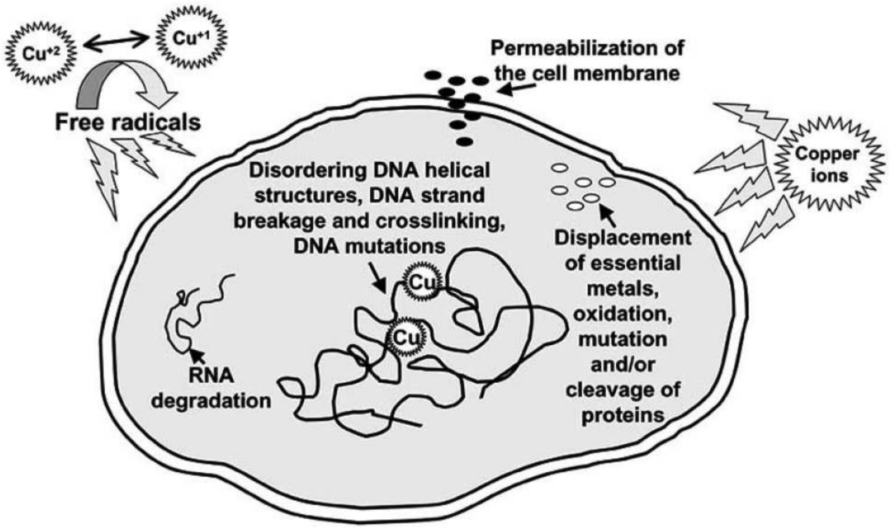

Fig. 2.3.2: Mechanisms of toxicity of copper to microorganisms [123].

An extensive disruption of membrane integrity followed by leakage of mobile cellular solutes from the cell interior inevitably leads to cell death. But the term copper mediated cell membrane damage also includes relatively small alterations in physical properties of the membrane, which however lead to significant changes in essential membrane-dependent functions of the cell. The DNA damage is caused mainly by Cu^{2+} ions and Fenton-type reaction-generated ·OH radicals. While the Cu^{2+} ions have a specific affinity to DNA and are able to bind to the DNA or crosslink the DNA strands, the highly reactive ·OH radicals are able to cause a multiple damage to the nucleic acids. The copper mediated protein damage includes processes described by reactions (2.26) and (2.27), displacement of essential metals from their binding sites or cleavage of proteins due to a free radical attack [123].

After exposure of the bacteria to copper, several scenarios may follow:

1) necrosis = the microbial cell loses membrane integrity and dies rapidly as a result of leakage of mobile cellular solutes from the cells interior.

2) decrease of cell viability = the cell stops actively growing and dividing.

3) apoptosis = the cell activates a genetic program of controlled cell death.

It time bacteria have developed resistance mechanisms to fight copper toxicity. Such mechanisms include for example (1) exclusion of copper by a permeability barrier, (2) active transport of copper away from the microorganism (3) intracellular and/or extracellular sequestration (4) enzymatic detoxification of a copper ion to a less toxic form or (5) decrease of the sensitivity of essential cellular components to copper [123].

2.4 General characterization of selected materials

This chapter summarizes general properties and structure of materials that are related to the experimental part of this thesis. Current state of the art of their preparation in the form of thin films and their applications are also briefly discussed.

2.4.1 Al-Cu-O system

Al_2O_3

Aluminum oxide (alumina) is known for its chemical inertness, optical transparency, low electrical conductivity and high hardness that are retained even at elevated temperatures. These properties make this material attractive e.g. for abrasives, cutting tools, microelectronics or joint replacements [169-173]. Due to their high surface area some polymorphs of alumina are also used as catalysts, catalyst supports or adsorbents.

Aluminum oxide forms many metastable polymorphs and one thermodynamically stable phase (α-Al_2O_3) with a corundum structure. The metastable phases can roughly be divided into two categories depending on the arrangement of oxygen anions in the crystal lattice. These are either face-centered cubic (e.g. γ-, η-, θ-, δ-Al_2O_3) or hexagonal close-packed (e.g. κ, χ-Al_2O_3). The particular distribution of Al cations in the oxygen sublattice determines the resulting polymorph. Transformation of the metastable phases to the thermodynamically stable α-Al_2O_3 phase is irreversible and occurs in the temperature range of 800 °C–1000 °C [174]. This transformation is accompanied by a volume contraction leading to formation of cracks which limits the utilization of the metastable phases at higher temperatures [170, 175, 176]. The most common phases observed in thin alumina films are α, κ, γ and θ-Al_2O_3 phases and amorphous Al_2O_3, out of which the amorphous Al_2O_3, γ-Al_2O_3 and α-Al_2O_3 phases usually form if PVD methods are used [29, 177-180].

α-Al_2O_3 adopts the rhomboedral lattice system with lattice constants a=4,758 Å and c=12,991 Å. Its crystal structure can be described as a sublattice of oxygen anions in a hexagonal closed-packed (hcp) arrangement, where 2/3 of the octaedral interstitial sites are occupied by the Al cations [181]. The distribution of the Al cations in one layer of the hcp sublattice of oxygen anions is shown in Fig. 2.4.1 a) [182]. The unit cell of α-Al_2O_3 within an idealized Al cation sublattice is illustrated in Fig. 2.4.1 b) [183].

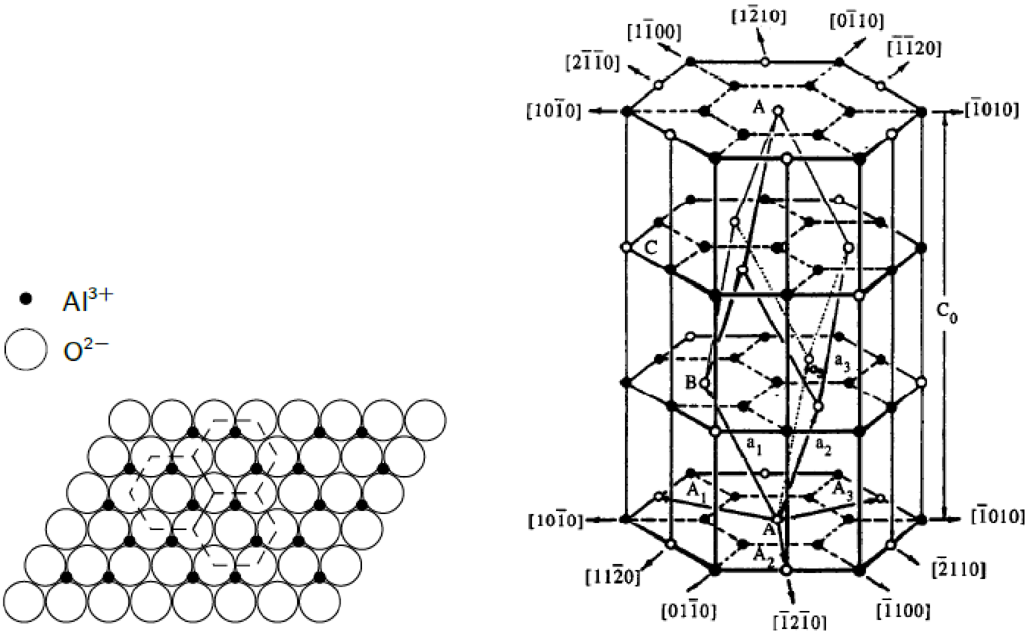

a) **b)**

Fig. 2.4.1: a) Top view of one layer of the hexagonal close-packed sublattice of oxygen anions with Al cations distributed in 2/3 of interstitial sites [182]. b) Unit cell of α-Al_2O_3 with the idealized Al cation sublattice. In Fig. b) only Al cations (full circles) and vacant interstitial sites (open circles) are shown without the oxygen anion sublattice. [183].

The exact structure γ-Al_2O_3 still remains a matter of debates, which is mainly due to the impossibility to obtain a pure single crystal of this phase. The traditionally accepted structure model of γ-Al_2O_3 is a defective cubic spinel with a lattice constant a=7.911 Å. The ideal spinel is described by a general formula AB_2O_4, where the cations A occupy 1/8 of the tetrahedral sites and the cations B occupy 1/2 of the octahedral sites in a face-centered cubic oxygen sublattice. The defective spinel can be obtained by stacking 3 unit cells of ideal spinel (shown in Fig. 2.4.2) containing 14 atoms (Al_6O_8) on top of each other obtaining a cell with 18 Al atoms and 24 O atoms. In order to meet the correct stoichiometry of Al:O=2:3, two Al atoms are removed achieving $Al_{16}O_{24}$=8 Al_2O_3 leading to a partial distortion of the crystal structure i.e. defective spinel [184].

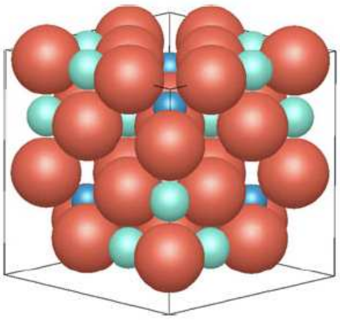

Fig. 2.4.2: General structure of spinel AB_2O_4. Big red spheres=O atoms, small blue spheres=A atoms in tetrahedral sites, small green spheres=B atoms in octahedral sites [185].

Besides the defective spinel other models describing the structure of γ-Al_2O_3 have been investigated recently. These include the nonspinel models with the space groups $Fd\bar{3}m$ and $I4_1/amd$ proposed by Paglia et al.[186, 187] and the $S_{0,25}$ model proposed by Krokidis et al [188]. Out of these models the $I4_1/amd$ provided the best fit to the nuclear resonance data suggesting that the traditional defective spinel model should be revised. Moreover Ching et al. used ab initio calculations to determine the physical properties of non-cubic γ-Al_2O_3 and concluded, that the structure of γ-Al_2O_3 should be described as amorphous network-like structure with well defined local order [189]. The latter is supported by many experimental observations showing that γ-Al_2O_3 can only be prepared in the nanocrystalline form with broad X-ray diffraction patterns. No sharp and narrow diffraction peaks indicating large crystallites can be observed even if high substrate temperatures or high post-deposition annealing temperatures are used [179, 190].

Tab. 2.2: Structure and properties of γ-Al_2O_3 and α-Al_2O_3.

	γ-Al_2O_3	α-Al_2O_3
lattice system	cubic a=7.911 Å [184]	rhomboedral a=4.758 Å, c=12.991 Å [181]
density ($g\cdot cm^{-3}$)	3.6÷3.65 [174]	3.96÷3.98 [181]
melting point (K)	1248-1373 [175, 176, 190]	2324±9.7 [181]
hardness (GPa)	8÷20 [179], 25.8 [191] 4)	22 [192], 27 [193]
effective Young's modulus (GPa)	≈305 [191]4)	306 [193]
electrical resistivity (Ωm)		10^{11}[181]1)
refractive index	1.749 [194]	1.768 [181]2)
band gap (eV)	7.2 [195]	8.8 [195]
enthalpy of formation ($kJ\cdot mol^{-1}$)	1653 [196]	1675 [197]
coef. of therm. expansion ($10^{-6}K^{-1}$)	7.8÷8.5 [198]	5.5 [197] 3)
heat capacity ($J\cdot g^{-1}K^{-1}$)		0.753 [197] 3)
thermal conductivity ($J\cdot cm^{-1}s^{-1}K^{-1}$)		0.46 [197] 3)
surface energy ($J\cdot m^{-2}$)	1.67[199]	2.64[199]

Table 2.2 summarizes structure and properties of the γ-Al_2O_3 and α-Al_2O_3 phases. Although both phases are transparent chemically inert insulators, differences can be found mainly in their structure, density, thermal stability, hardness, thermal expansion and surface energy. The significantly lower surface energy of γ-Al_2O_3 makes it possible to form fine grained nanocomposites or powders with very small particle sizes that are often used as catalyst supports [200]. The large interval of hardness measured for γ-Al_2O_3 is due to the fact that alumina films with γ-Al_2O_3 structure often contain various amount of the amorphous phase. Generally it holds that the hardness of aluminum oxide containing a mixture of amorphous and crystalline γ-Al_2O_3 phases increases with an increasing content of the crystalline phase [179].

One of the principal advantages of the α-Al_2O_3 phase is that, once formed, it is thermally stable up to the melting point of aluminum oxide (≈2047°C)[181] and no other phase transformations occur during subsequent heating or cooling. The main limitation is however the fact that fabrication of films with the α-Al_2O_3 structure typically requires relatively high substrate temperatures ≥1000 °C [201]. In recent years, a great effort has been devoted to the deposition of thin Al_2O_3 films with the thermodynamically stable α-Al_2O_3 structure at low substrate temperatures. This effort originates from the potential benefit of depositing the hard, chemically inert, thermally stable and wear-resistant α-Al_2O_3 film on cutting tools made of high-speed steel which does not allow to exceed 550 °C due to its thermal degradation.

Up to now several approaches have been investigated to produce the α-Al_2O_3 phase at reduced substrate temperatures: (1) the formation of α-Al_2O_3 films at low substrate temperatures under ion bombardment of the growing film [202], (2) the epitaxial growth of α -Al_2O_3 films on an α-Cr_2O_3 template which crystallizes isostructurally to the α-Al_2O_3 phase [193, 203-206] and (3) stabilization of the corundum α-Al_2O_3 structure in a solid solution - typically $(Cr,Al)_2O_3$ [207-210].

An alternative approach to depositing the α-Al_2O_3 films at low substrate temperatures is to increase the thermal stability of the metastable phase. This way the degradation of the film by transformation-induced cracking can be shifted to higher temperatures. Jiang et al. investigated the effect of different additives on the stability of γ-Al_2O_3 structure relative to α-Al_2O_3. Using ab-initio calculations they found that addition of Si stabilizes the γ-Al_2O_3 structure, which might lead to an increase of the thermal stability and potential utilization of this phase for high-temperature applications [211]. Experimental verification of these calculations is however missing.

Although it has been demonstrated that deposition of alumina films with the α-Al_2O_3 structure at substrate temperatures below 550°C is possible, the deposition rates especially in the case of epitaxial growth are rather low (0.7 - 5.0 nm/min) [193, 203, 205, 206]. Moreover the cutting performance of tools coated with γ-Al_2O_3 was reported to be comparable to those coated with α-Al_2O_3 or κ-Al_2O_3 [212]. For that reason alumina films with the γ-Al_2O_3 structure are still frequently used as protective and wear-resistant coatings on cutting tools [176] and remain in the focus of recent scientific papers.

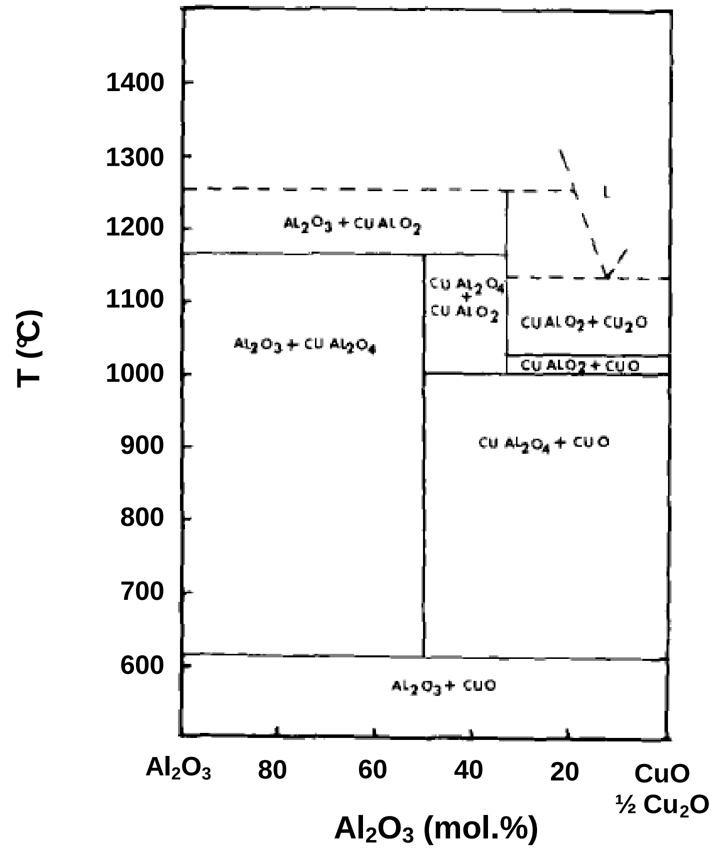

Fig. 2.4.3: Isobaric section of the ternary CuO-Cu_2O-Al_2O_3 system [213].

The phase equilibrium diagram of CuO-Cu_2O-Al_2O_3 is displayed in Fig. 2.4.3. Here the Al_2O_3 is the thermodynamically stable α-Al_2O_3 phase. As can be seen below 612 °C a mixture of binary oxides CuO and Al_2O_3 is formed and no or very small solubility of Cu atoms in the structure of α-Al_2O_3 can be expected. At higher temperatures copper oxide and alumina form two ternary compounds – copper aluminate $CuAl_2O_4$ and cuprous aluminate $CuAlO_2$. The $CuAl_2O_4$ phase forms at $T \geq 612$°C irrespective of the initial concentration of Al_2O_3. Depending on the relative content of Al_2O_3 (atomic ratio of Cu/Al is lower or higher than 0.5) the $CuAlO_2$ phase starts to crystallize either at 1171 °C (Cu/Al<0.5) or at 1003 °C (Cu/Al>0.5).

The Cu-Al-O system has been intensively investigated after Kawazoe et al. discovered that films with the delafossite-$CuAlO_2$ structure exhibit p-type conductivity combined with good optical transparency representing a potential candidate for new p-type transparent conducting oxides [214]. The subsequent research activities were focused mainly on investigations of the effects of structure, elemental composition or post-deposition processing on the electrical and optical properties of the Cu-Al-O films [215-218]. It was found that the Cu/Al ratio is a significant parameter that controls the relative abundance of phases, transmittance, resistivity and band gap of reactively sputtered films [216, 218].

$CuAl_2O_4$

$CuAl_2O_4$ is a semiconductor with a relatively narrow band gap (2.1 eV [219], 1.77 eV[220]). This enables an effective utilization of visible and UV radiation and makes $CuAl_2O_4$ an interesting material for a variety of catalytic reactions such as photodegradation of methyl orange [220, 221], hydrogen generation [222] or dehydrocoupling of methanol [223]. The cubic structure of spinel $CuAl_2O_4$ also proved useful for improving the adhesion of superconducting cuprate films or metallic Cu films to alumina substrates [224, 225]. Moreover a $CuAl_2O_4$ interlayer acts as an effective barrier preventing reaction of Al from the alumina substrate with the superconducting film [224]. Among CuO, Cu_2O and $CuAlO_2$ the spinel $CuAl_2O_4$ exhibits the lowest leachability of Cu in an acidic environment, which makes it a potential candidate for the product of stabilization of copper-laden sludge by thermal treatment [226].

According to the CuO-Al_2O_3 phase equilibrium diagram the $CuAl_2O_4$ phase forms at 612°C as a reaction product of α-Al_2O_3 and CuO and depending on the initial concentration of α-Al_2O_3 it transforms into $CuAlO_2$ at 1171 °C or 1003 °C (see Fig. 2.4.3). $CuAl_2O_4$ has a cubic spinel structure ($a_{CuAl2O4}$=8.075 Å [227]) described in Fig. 2.4.2 where *A* atoms (small blue spheres) represent Cu and *B* atoms (small green spheres) represent Al.

2.4.2 Cr-Cu-O system

The isothermal section of the Cr-Cu-O ternary phase diagram for T=700÷1100 °C is shown in Fig. 2.4.4 a) [228]. It can be seen that depending on the particular elemental composition, Cr, Cu and O form two binary oxides of chromium (Cr_2O_3, CrO_3), two binary oxides of copper (CuO, Cu_2O) and three ternary oxides ($CuCr_2O_4$, $CuCrO_2$, $CuCrO_4$). For low concentrations of oxygen metallic copper and chromium are also present and oxygen predominantly binds to chromium, which can be explained by a much lower oxygen affinity for Cu compared to that for Cr ($\Delta H_f^o(Cr_2O_3)$= -1139.7 kJ/mol, $\Delta H_f^o(CuO)$=-157.3 kJ/mol, $\Delta H_f^o(Cu_2O)$= -168.6 kJ/mol [196]). The isobaric section of of the Cu_2O-CuO-Cr_2O_3 phase diagram is illustrated in Fig. 2.4.4 b) and exhibits analogous behaviour to the Cu_2O-CuO-Al_2O_3 system shown in Fig. 2.4.3

above. Again two ternary oxides are observed - cupric chromite $CuCr_2O_4$ and cuprous chromite $CuCrO_2$ where formation of the latter one is favoured at higher temperatures and higher concentrations of Cu. Due to its application potential and relation to the experimental part of this thesis the $CuCrO_2$ compound will be discussed in more detail.

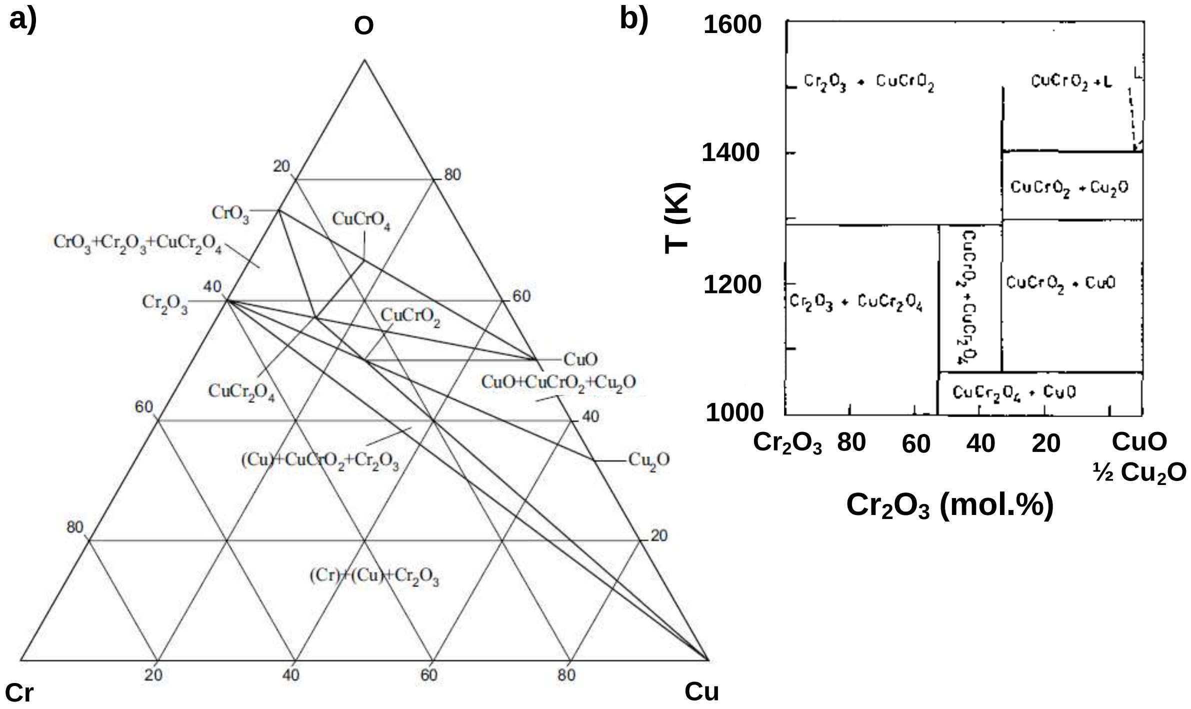

Fig. 2.4.4: a) isothermal section of the Cr-Cu-O ternary phase diagram in the temperature range 700 °C÷1100 °C [228] and b) isobaric section of ternary system Cu_2O-CuO-Cr_2O_3 [229].

$CrCuO_2$

Cuprous chromite $CuCrO_2$ is a ternary oxide of copper and chromium that exists in two crystalographic modifications. The rhomboedral 3R-$CuCrO_2$ is a stable polymorph with a delafossite structure and lattice parameters *a*=2.975 Å and *c*=17.096 Å. Its crystal structure is illustrated in Fig. 2.4.5. A different stacking of oxygen layers along the c-axis as compared to that provided in Fig. 2.4.5 results in formation of a metastable 2H-$CuCrO_2$ polymorph. 2H-$CuCrO_2$ has a hexagonal lattice with lattice parameters *a*=2.974 Å and *c*=11.400 Å and can be obtained e.g. by quenching of $CuCrO_2$ from 1100°C [228, 230].

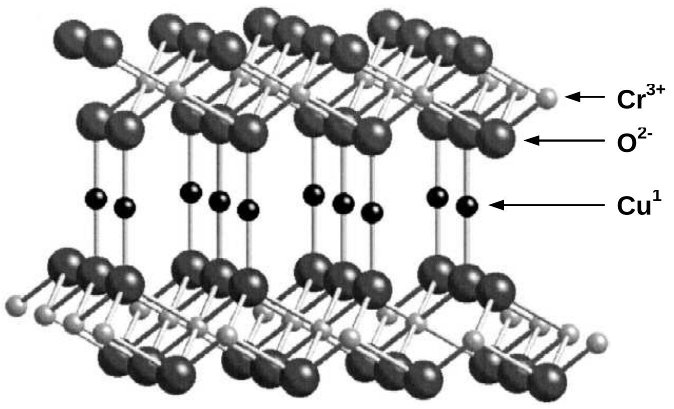

Fig. 2.4.5: Crystal structure of delafossite $CuCrO_2$. Adapted from [231].

Delafossite 3R-$CuCrO_2$ is a chemically stable semiconductor with a narrow band gap of ~1.3 eV resulting in absorption in the entire visible spectrum [232]. 3R-$CuCrO_2$ together with other materials with the delafossite structure is known to be a p-type conducting oxide [231]. It is also a versatile catalyst used e.g. for photocatalytical reduction of potentially harmful metal ions [233] or inorganic pollutants [232] or for enhancement of burning rate in solid propellants [234]. Due to its magnetic and electric properties $CuCrO_2$ is also a potential candidate in some multiferroic applications [235].

Recent scientific efforts have focused predominantly on doping of the pure delafossite $CuCrO_2$ by Mg or N in order to realize a stable conducting *p*-type oxide with a high transparency in the visible range [231, 236-238]. Lately it has been shown that single-phase delafossite $CuCrO_2$ thin films exhibit antibacterial behavior against *E. coli* bacteria [138]. No artificial UV irradiation was necessary to induce the antibacterial effect which represents a significant advantage compared to well-known UV light active TiO_2 films [239]. However to obtain the $CuCrO_2$ phase a post-deposition annealing of as-deposited films was necessary. The formation temperature of the delafossite $CuCrO_2$ phase can be reduced from ≈ 800 °C as presented in the phase equilibrium diagram (see Fig. 2.4.4 b)) [229] down to 700°C if annealing in inert gas is applied [236, 240] or even to 500°C if two-step annealing in forming gas and nitrogen is used [237].

2.4.3 Al-Cu-N system

AlN

AlN is a wide band gap insulator transparent in near UV, visible and near infrared spectrum. It is especially valued for its high thermal conductivity comparable to metals and high insulating properties comparable to best ceramics. These properties make AlN attractive in the field of ultraviolet optoelectronics, electronics with high integration density, cooling systems etc. [241]. Thanks to its piezoelectric properties and high surface acoustic velocity AlN represents an important material for fabrication of piezoelectric sensors and actuators [242, 243]. AlN-based piezoelectric devices can also be used for micro-energy harvesting from ambient vibrations [244].

Tab. 2.3: Structure and properties of AlN.

lattice system	hexagonal, *a*=0.3111 nm and *c*=0.4979 nm [250]
density (g·cm^{-3})	3.26 [196]
melting point (K)	2473 [249]a)
hardness (GPa)	12 [249], 25 [248]b)
effective Young's modulus (GPa)	≈224 [248]b)
electrical resistivity (Ωm)	10^{11}[249]
refractive index	2.0 [251]
band gap (eV)	6.28[249]
enthalpy of formation (kJ·mol^{-1})	318 [196]
coef. of therm. expansion ($10^{-6}K^{-1}$)	2.7 [249] c)
thermal capacity (J·g^{-1}K^{-1})	0.7÷0.9 [249] c)
thermal conductivity (J·cm^{-1}s^{-1}K^{-1})	up to 3.20 [249]d), 1.34 [252]e)
surface acoustic velocity (km·s^{-1})	6.0-6.2 [249]

a) in N_2 atmosphere
b) thin film, Berkovich nanoindentation
c) at 25 ℃
d) monocrystal
e) RF sputtered thin film

Compared to other nitrides the hardness of bulk AlN is relatively low (≈12 GPa) being comparable to Si. However depending on the particular measurement and deposition techniques and film structure AlN films with significantly higher hardness reaching up to 24 GPa have been reported [245-248]. AlN dissolves in acids and alkalis and also slowly hydrolyzes in water resulting in formation of aluminum hydroxide and ammonia [196]. It is stable in inert atmosphere up to 2200°C. In air a 5-10 nm thick surface oxide layer is formed protecting the material from further oxidation up to cca 1350°C [249]. Above this temperature a bulk oxidation occurs. Selected properties of the stable hexagonal polymorph of AlN are summarized in Tab. 2.3.

AlN exists in three polymorphs. The stable AlN polymorph adopts hexagonal lattice system with lattice parameters a=0.3111 nm and c=0.4979 nm [250]. It has the wurtzite crystal structure (denoted as w-AlN, α-AlN or h-AlN) where atoms of both elements form a hexagonal close-packed (hcp) sublattice with each atom tetrahedrally coordinated (see Fig. 2.4.6).

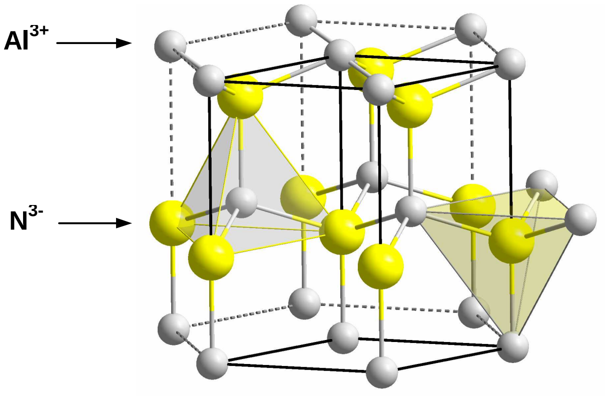

Fig 2.4.6: Crystal structure of wurtzite AlN with coordination polyhedra [253]

The two remaining polymorphs of AlN are metastable and both have a cubic structure (denoted as c-AlN or β-AlN) with different lattice parameters - a=0.4045 nm for the NaCl type c-AlN and a=0.7913 nm for the zincblende type c-AlN [254]. Powder c-AlN is commonly produced by carbothermal reduction of Al_2O_3 in N_2 atmosphere [255, 256]. Thin films with c-AlN structure can be prepared e.g. by RF magnetron sputtering with reactive gas timing [257] or by pulsed laser deposition using epitaxial growth on $SrTiO_3$ or MgO [258, 259]. Thanks to their higher symmetry the cubic AlN polymorphs are expected to exhibit higher thermal conductivity, electrical resistivity, hardness and acoustic velocity compared to the hexagonal wurtzite-type AlN [254, 255]. Due to its metastable nature it is however difficult to prepare a pure c-AlN phase and usually a mixture of c-AlN and w-AlN is obtained [255, 256].

Al-Cu-N films

Al-Cu-N films were first studied by Musil et al., who investigated the possibility to prepare this new material in the form of nc-MeN/soft phase nanocomposite [260]. Here nc- denotes the nanocrystalline phase, Me are the elements forming nitrides (Me=Ti, Zr, W, Cr, Mo, Al, etc) and soft phase is represented by Cu, Ni, Y, Ag, etc. [109]. The authors used reactive DC magnetron sputtering and investigated the effect of various deposition parameters on structure and properties of the films. They found that by optimizing the partial pressure of N_2, the substrate bias, the substrate temperature and the Cu content in the film (< 10 at.%) it is possible to prepare dense, fine-grained substoichiometric (N/Al≈0.77) superhard films (hardness up to 48 GPa) with low compressive stress ($\sigma\approx$-0.5 GPa) [260]. Compared to superhard Zr-Cu-N nanocomposite films the Al-Cu-N films exhibited the same hardness but significantly lower effective Young’s modulus enabling to prepare superhard films with high values of H/E^* and H^3/E^{*2}. These ratios are indicative of films with enhanced resistance to cracking and resistance to plastic deformation as already discussed in section 2.2.3.1.

Tian et. al investigated thermal properties of bulk AlN-Cu composites prepared by hot pressing of AlN (with 6 wt%. of Y_2O_3 as sintering aid) and Cu powders. Samples with different volume fractions of AlN and Cu were prepared and their thermal conductivity and coefficient of thermal expansion were determined. The main aim of their investigation was to improve the thermal conductivity of polycrystalline AlN (due to addition of Cu) while maintaining the coefficient of thermal expansion (CTE) low. They found that both the thermal conductivity and the coefficient of thermal expansion decrease with an increasing volume fraction of AlN and achieved thermal conductivity of 235 $W \cdot m^{-1} \cdot K^{-1}$ and CTE of 12.6×10^{-6} K^{-1} for 40 vol. % of AlN [261].

Ran et al. deposited AlN films doped with 3.2 at.%÷8.2 at.% of Cu by helicon magnetron sputtering and observed that this material exhibits anisotropic ferromagnetic properties. This finding opens up new possibilities for application of Al-Cu-N films in spintronics devices based on diluted magnetic semiconductors (DMSs). They found that the room-temperature saturation magnetization decreases with increasing Cu concentration [262] and that the easy axis of magnetization is along the [0002] AlN direction [263].

In order to prepare amorphous superhard films Musil et al. investigated the effect of Si addition into reactively DC-sputtered Al-Cu-N films on their structure and mechanical properties. The Al-Si-Cu-N films with 5÷9 at.% of Si and 2÷12 at.% of Cu easily formed a disordered structure characterized either by broad, low-intensity X-ray reflections of hexagonal h-AlN phase or by X-ray amorphous structure. Compared to silicon-free Al-Cu-N films, incorporation of low amount of Si resulted in increase of the film stoichiometry i.e. N/(Al+Si) ratio. This was explained by formation of amorphous Si_3N_4 phase that has a higher enthalpy of formation ($\Delta H_f^o(Si_3N_4)$=-745 kJ/mol^{-1}) compared to AlN and is able to accommodate more nitrogen in its structure. In general the mechanical properties of Al–Si–Cu–N films were similar to those of Al–Cu–N films. However for specific deposition conditions (p_{N2}=0.13 Pa) the Al–Si–Cu–N films exhibited an additional improvement of hardness up to ≈59 GPa [264].

Based on the observations of Musil et al., showing that the Al-Cu-N films exhibit high H/E^* ratio, an enhanced resistance to cracking could be expected in case of this material. Besides, the presence of copper in the Al-Cu-N nanocomposite film could induce antibacterial properties similarly as in the case of some other metal nitride/Cu nanocomposite films such as TiN-Cu [152], TaN-Cu [150] or Cr-Cu-N [147]. Up to now no report on the antibacterial properties or resistance to cracking of Al-Cu-N nanocomposite films has been presented.

3. Goals of the thesis

In recent years a great progress has been made in the development of new nanocomposite materials. It has been shown, that alloying of thin films based on binary oxides [42], nitrides [260, 265] or carbides [60] by copper may result in a significant improvement of their hardness or toughness if the process parameters are correctly selected. Moreover the presence of copper in thin films may provide an antibacterial effect as already described in chapter 2.3. This Ph.D. thesis is devoted to preparation and investigation of thin films of three different material systems containing copper. The films are prepared by means of pulsed reactive magnetron sputtering using a dual magnetron system. The main attention is focused on understanding the effect of process parameters and copper concentration on structure, mechanical properties and antibacterial properties of the films as well as their resistance to cracking.

The main goals of the Ph.D. thesis are the following:

1. To develop nanostructured Al-Cu-O films with the aim to enhance their mechanical properties and resistance to cracking compared to pure Al_2O_3 films.

2. To investigate the effect of copper content and phase composition on the antibacterial efficiency of Cr-Cu-O films. Based on the obtained results prepare protective Cr-Cu-O films killing *E. coli* bacteria in the daylight and in the dark without the need for an additional irradiation.

3. To develop antibacterial Al-Cu-N films with enhanced hardness and enhanced resistance to cracking.

4. Experimental details

The following chapter describes the deposition system and analytical methods used for preparation and characterization of the films.

4.1 Deposition system

The main components of the deposition system are the deposition chamber, the pumping system, the power supplies, the magnetrons, the magnetron targets and the appliances for control and measurement of different process parameters (e.g. substrate temperature, bias, pressure, gas flow etc.). A more detailed description of these components is provided in the following sections.

4.1.1 Pumping system and deposition chamber

The deposition chamber with the pumping system is schematically shown in Fig. 4.1.1. In order to obtain a sufficiently low base pressure and sustain a stable total pressure during deposition, a two stage pumping system is employed. A rotary vane pump is able to pump the system from atmospheric pressure down to ≈1 Pa. It also serves as a fore-pump to provide a sufficiently low pressure for a proper operation of the turbomolecular pump, which requires a maximum pressure at the output <1300 Pa. Technical details of both pumps are listed in Tab. 4.1. Depending on the pumping time, substrate holder temperature and deposited materials, such two-stage system is able to reach a base pressure of $p_0 < 1\times10^{-3}$ Pa. During depositions both pumps were set in operation and prior to each deposition the system was evacuated to a base pressure of $p_0 < 2\times10^{-3}$ Pa.

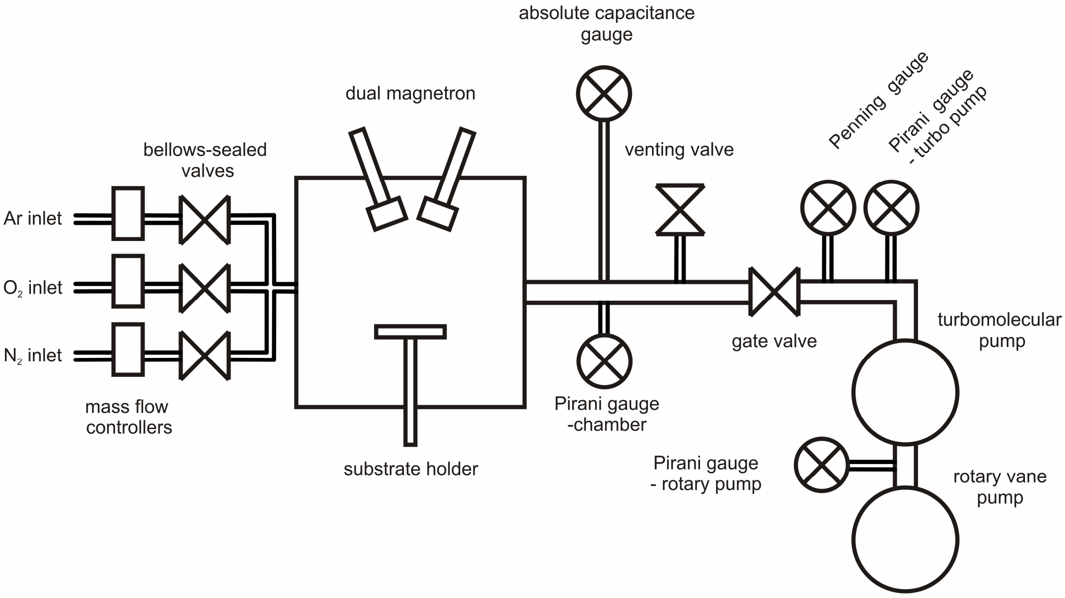

Fig. 4.1.1: Schematic illustration of the pumping system.

For monitoring the pressure before and during the deposition, various types of pressure gauges are used. Three Pirani gauges are mounted in different parts of the system to indicate pressure in the deposition chamber, between the gate valve and the turbopump and between the turbopump and the rotary pump. These gauges operate in the range from atmospheric pressure down to $5\cdot10^{-2}$ Pa. Their accuracy however significantly decreases below 0.1 Pa. The

Pirani gauges are factory calibrated to operate in Air, O_2, N_2 and CO and thus can not be properly used after the mixture of Ar and reactive gas is introduced into the system. The air-calibrated Penning gauge measures the pressure below the range of the Pirani gauges and is used to calibrate the capacitance Baratron gauge. Once a sufficiently low base pressure is achieved, the Baratron gauge is calibrated to a zero value and different gases may be introduced into the system. Since the Baratron gauge is a capacitance gas-independent gauge, it is suitable for monitoring the total pressure during deposition. Technical specifications of the pressure gauges used in the system are provided in Tab. 4.2.

Tab. 4.1: Declared technical specifications of vacuum pumps.

pump type	pumping speed (l/s)	ultimate pressure (Pa)	max. pressure at output (Pa)
rotary vane pump (LAVAT VRO 25-23)	6.9	$< 5\cdot10^{-2}$	$1.5\cdot10^{5}$
turbomolecular pump (Pfeiffer Vacuum TMH 521 P)	290	$< 5\cdot10^{-8}$	1300

Tab. 4.2: Declared technical specifications of pressure gauges.

gauge type	calibrated to operate in	pressure range (Pa)
Pirani (Pfeiffer Vacuum, TPR 280)	Air, O_2,N_2,CO	$5\cdot10^{-2}$ - 10^{5}
Penning (Pfeiffer Vacuum, IKR 251)	Air, N_2	$2\cdot10^{-7}$ - 1
capacitance (MKS Baratron 627A)	gas independent	$1.33\cdot10^{-3}$ - 6.65

The flow of the working gas (Ar, 99.999 %) and reactive gases (N_2, 99.999 % and O_2, 99.995 %) is controlled by mass flow controllers (MKS Mass-Flo Type 1179A) with maximum flow rates of 139 sccm, 100 sccm and 19.9 sccm for argon, nitrogen and oxygen, respectively. Bellows-sealed valves are installed between the mass flow controllers and the deposition chamber for the ease of maintenance and to avoid possible contamination of the gas mixture by gases that are not currently used. The mass flow controllers are controlled by a multi gas controller (MKS 647 C) unit. This unit enables to control the flow rates of up to four different gases using various modes. For introducing argon, an independent mode was used in all experiments. In this mode the flow rate is simply set to the setpoint value. Unless explicitly specified in the text the flow rate of the reactive gas was controlled using the feedback PID mode in a procedure described as follows. Firstly the flow rate of Ar (ϕ_{Ar}) is manually set to a constant value that corresponds to a desired partial pressure of Ar (p_{Ar}). The multi gas controller compares the setpoint value of the total pressure with the actual pressure measured by the Baratron capacitance gauge. Using a PID feedback control algorithm the flow rate of reactive gas (N_2 or O_2) is adjusted in order to achieve the setpoint value of the total pressure p_T. Such procedure is repeated continuously and automatically so as to maintain the desired total pressure during the whole deposition. In this way, the partial pressure of the reactive gas p_{RG} (RG=O_2 or N_2) can be calculated as a simple difference between the total pressure p_{T} and the partial pressure of argon p_{Ar} measured before introducing the reactive gas. The total pressure as well as the partial pressures of working and reactive gases may also be regulated by a control gate valve (VAT 64244-PE52). The cross section of this gate valve can be varied in 1000 discerete steps ranging from fully open to fully closed. This makes it possible to adjust the pressure value while keeping the gas flow rates constant.

The grounded deposition chamber is schematically illustrated in Fig. 4.1.2. It is made of stainless steel with duraluminum flanges and has a cylindrical shape with a diameter and a height of 500 mm and 400 mm, respectively. The dual magnetron is mounted in the top flange of the deposition chamber and consists of two magnetrons in the closed field configuration tilted with respect to the vertical axis at the angle of 20° and equipped with permanent magnets of 50 mm in diameter. Various compact or composed water-cooled metallic targets were used for deposition of the films. A detailed description of the targets is further provided in section 4.1.3. The substrate holder is installed in the bottom flange of the chamber and can be ohmically heated up to 500 °C (the substrate temperature is monitored by a K-type NiCr-NiAl thermocouple), shifted in the vertical direction and biased using an external power supply. The substrate-to-target distance $d_{\text{s-t}}$ was set to 110 mm for deposition of Al_2O_3, Al-Cu-O and Cr-Cu-O films. Al-Cu-N films were prepared at $d_{\text{s-t}}$=80 mm.

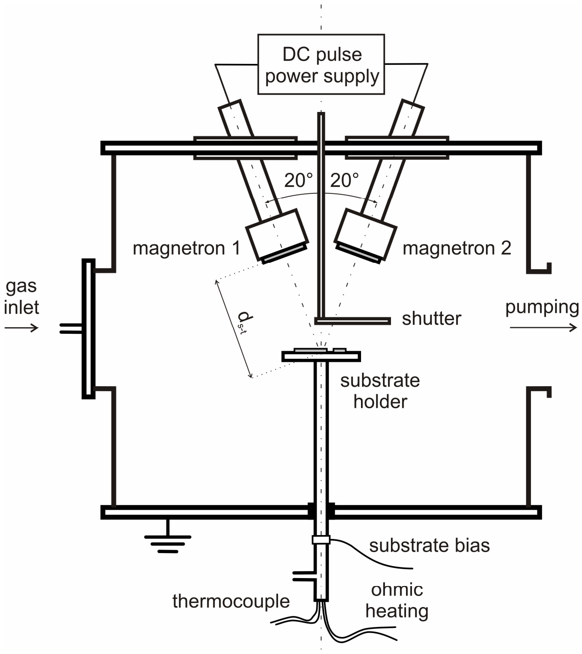

Fig. 4.1.2: Schematic illustration of the deposition chamber

4.1.2 Power supplies

For the experiments described in this thesis two different power supplies were used: (1) pulsed DC power supply RMP 10 (Huttinger Elektronik) for powering the dual magnetron and (2) pulsed DC power supply IAP 1010 (EN Technologies) for biasing the substrate .

RMP 10 (Hüttinger Elektronik)

Huttinger Elektronik RMP 10 is a floating pulsed DC power supply designed for PVD surface treatment technologies. It consists of two DC power sources and a MOSFET-switch based section responsible for modulating the DC output signal to a desired shape (DC, rectangular or trapezoidal). It is able to supply a maximum power of 10 kW providing a maximum current of either 12.5 A (at 800 V) or 25 A (at 400 V). The power supply can operate in three different regimes depending on which output parameter is set to a constant value - constant current/voltage/power. The pulse repetition frequency can be set to 4÷100 kHz and the duty cycle (i.e. the ratio of negative voltage pulse length τ and the pulse period T) can be varied from 20 % to 80 %. The dual magnetron operates either in a single or a dual magnetron regime [266]. In the single magnetron regime only one magnetron target is sputtered by a DC or pulsed signal whereas in the dual magnetron regime the voltage polarity periodically changes and both magnetron targets are sputtered as described in section 2.1.2. For deposition of Al_2O_3, Cr-Cu-O and Al-Cu-N films the dual magnetron regime with fixed duty cycle of τ/T=0.5=50% was used. In the case of Al-Cu-O the duty cycle was varied from 20 % to 80 % in order to control the elemental composition of the films by changing the sputtering time of two targets of different compositions (see Fig. 4.1.3). Since the duty cycles on outputs 1 and 2 of the power supply are mutually coupled to give 100% in total, as the duty cycle on magnetron 1 is increased the duty cycle on magnetron 2 is decreased and vice versa. This way the pulse length of the composed Al/Cu target can be simply expressed using the pulse length of the pure Al target (e.g. for repetition frequendcy of f_r=20 kHz i.e. pulse period of T=40 μs the pulse length on the composed Al/Cu targets is $\tau_{Al/Cu}$ [μs] = 40 μs - τ_{Al} [μs]).

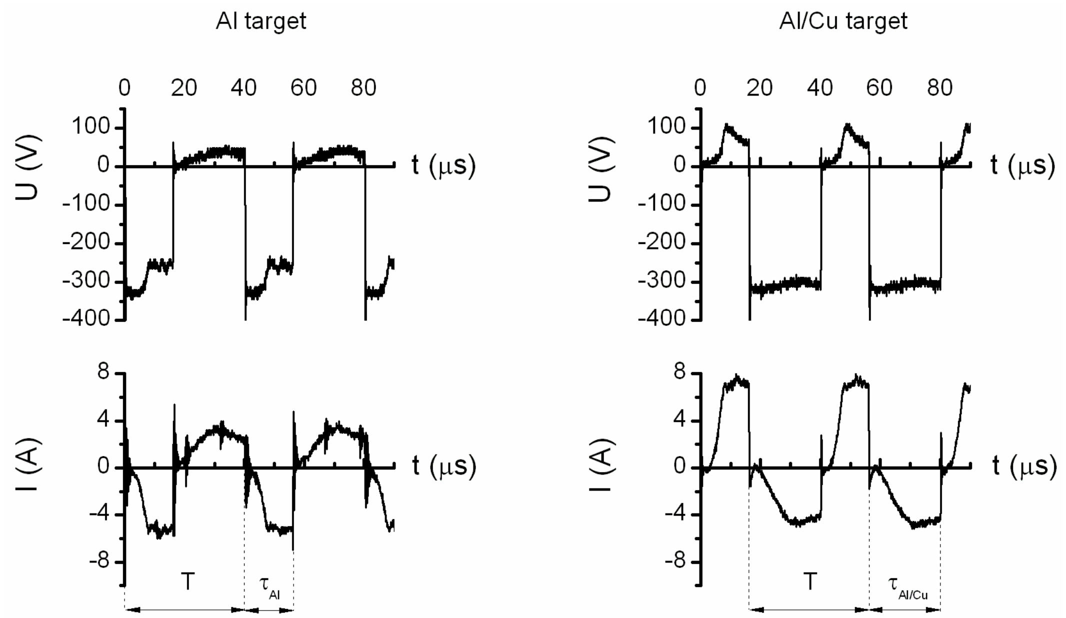

Fig. 4.1.3: Current (I) and voltage (U) waveforms of a dual magnetron equipped with a compact Al target on one magnetron and a composed Al/Cu targets on the second magnetron. The repetition frequency is 25 kHz and duty cycles on the Al and Al/Cu targets correspond to τ_{Al}/T=40% and $\tau_{Al/Cu}/T$=60%, respectively.

The process parameters quoted in the thesis are defined as follows. I_d represents the average cathode current in the pulse on time. U_d represents the average potential difference (i.e. average voltage) between magnetron 1 and magnetron 2 in the pulse on time. For simplicity these two parameters are simply referred to as discharge current and discharge voltage throughout the thesis. The average target power in pulse P_d can be approximated by a simple multiplication of I_d and U_d (i.e. $P_d \approx I_d \cdot U_d$). The target power loading can also be expressed in terms of average target power density in pulse $W_d = P_d/S$, where S=19.63 cm^2 represents surface area of the target.

IAP 1010 (EN Technologies)

The pulsed DC power supply IAP 1010 was used for biasing the substrates during depositions of Al-Cu-N films. Due to one output only this power supply can not be utilized for powering the dual magnetron. However, thanks to its wide range of variable parameters (see Tab. 4.3) it is suitable for providing power to single magnetrons or for biasing the substrates.

For depositions of Al-Cu-N films a bipolar DC pulse substrate bias with a pulse frequency of f_s=20 kHz was applied. The selected negative bias $U_{s-} \equiv U_s$ was applied for 50 % of the pulse period whereas the positive bias of $U_{s+} = +10\ V$ was applied for 45 % of the pulse period. The current waveforms were monitored and recorded using a Tektronix TPS 2024 oscilloscope with a Tektronix TCP A 300 current probe. The average substrate ion current in the negative pulse I_s was estimated from the current waveforms. Knowing surface area of the top side of the substrate holder (S_s=78.5 cm^2) the average substrate ion current density in the negative pulse i_s was calculated as I_s / S_s. For simplicity, the i_s parameter is simply denoted as "substrate current density" in the text below.

Tab. 4.3: Specifications of the IAP 1010 (EN Technologies) pulse power supply used for substrate biasing [267].

output voltage	100÷1000 V
output DC current	0÷10 A
output pulse current	0÷20 A (duty 50 %)
maximum output power	10 kW
regulation modes (constant parameter)	voltage/current/power
modes of operation	DC, bipolar, unipolar
frequency	5÷50 kHz
duty cycle	2÷90 %

4.1.3 Magnetron targets

For deposition of thin films presented in this work, four types of metallic targets were used. Their geometries and dimensions are presented in Figs. 4.1.4 to 4.1.7. The targets were fabricated of bulk metals with the following purity – Al (99.5 at.%), Cu (99.9 at.%), Cr (99.9 at.%). All targets were directly cooled by flowing tap-water and they were screwed to the body of the magnetron. Position of the permanent magnets of the magnetron is shown in Fig. 4.1.4 (shaded fill pattern). For deposition of Al_2O_3, Cr-Cu-O, AlN and Al-Cu-N films identical targets were mounted on both magnetrons. In the case of Al-Cu-O films, one magnetron was equipped with a pure Al target (Fig. 4.1.4) while the second magnetron with a composed Al/Cu target (Fig. 4.1.5) so that the Cu content in the film could be controlled by changing the duty cycle on the magnetrons without the need to unmount the targets. To prepare Cr-Cu-O and Al-Cu-N films with various Cu contents a different approach was adopted. Here identical composed targets were fixed to both magnetrons and the Cu content was controlled by changing the inner diameter ($Ø_{in}$) of the Cu fixing ring in the ranges of 28 mm÷34 mm and 28 mm÷36 mm for Cr-Cu-O and Al-Cu-N films, respectively.

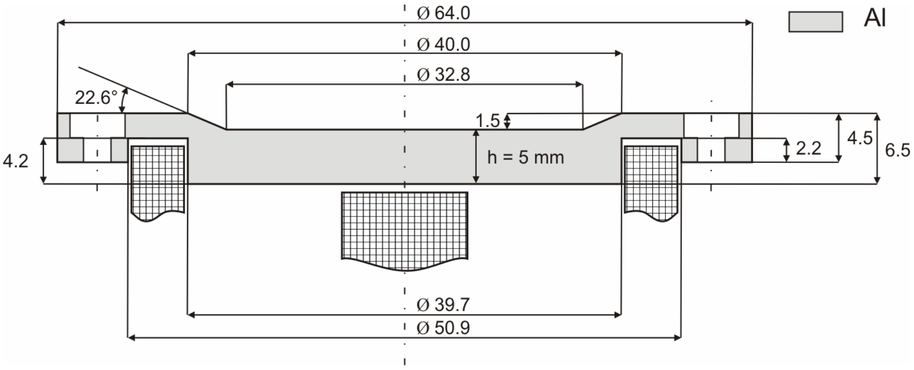

Fig. 4.1.4: Geometry and dimensions of a directly cooled Al target used for deposition of Al_2O_3, AlN and Al-Cu-O films. The shaded fill patterns indicate the position of permanent magnets.

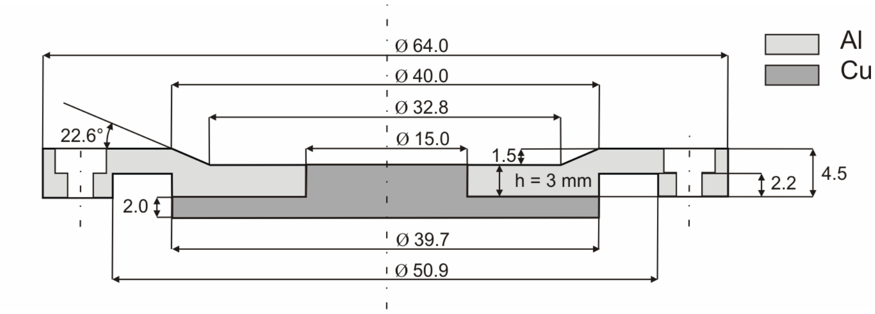

Fig. 4.1.5: Geometry and dimensions of a directly cooled composed Al/Cu target used for deposition of Al-Cu-O films.

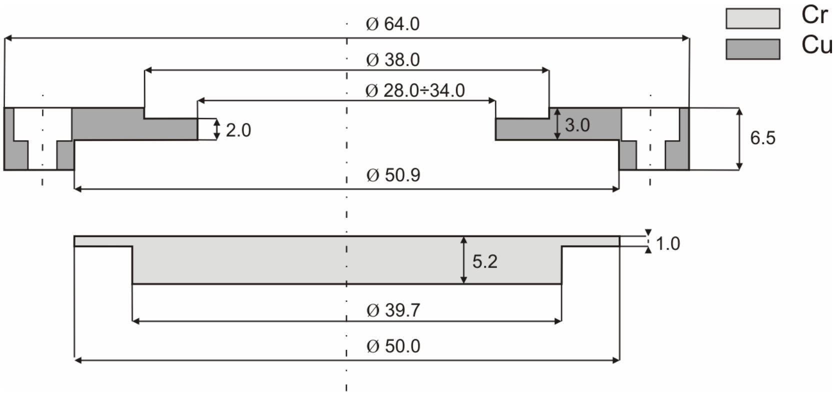

Fig. 4.1.6: Geometry and dimensions of a directly cooled composed Cr/Cu target used for deposition of Cr-Cu-O films.

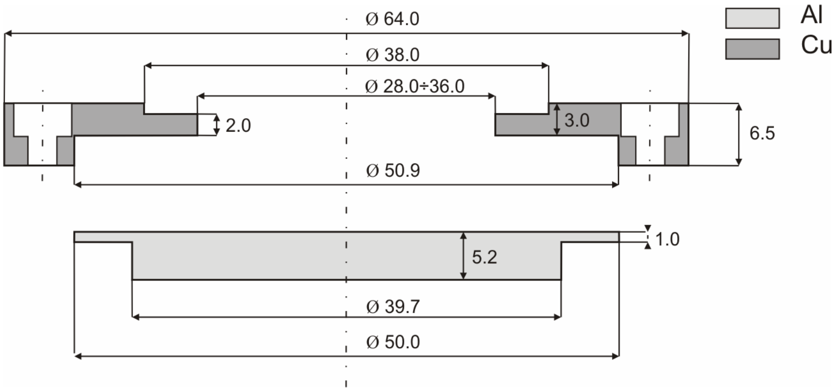

Fig. 4.1.7: Geometry and dimensions of a directly cooled composed Al/Cu target used for deposition of Al-Cu-N films.

4.2 Substrate preparation and post-deposition processing

For evaluation of different properties of the films various substrate materials of different dimensions were used. A list of these is provided in Tab. 4.4. Most of the analyses were performed with the square 20×20 silicon monocrystals. The 35 mm long silicon strip is suitable for calculation of residual stress by means of the bending plate method (see section 4.3.1). The soda lime microscope glass slides and molybdenum strips were used for determination of optical transmittance and resistance to cracking in bending, respectively. To exclude the influence of silicon substrate on their structure, Al_2O_3 and Al-Cu-O films were also deposited on thin aluminum foils and a fine powder was obtained using the following procedure. The film on the foil was immersed into a solution of distilled water and hydrochloric acid with a concentration of 19%. After several hours the Al foil was chemically etched and after filtering, washing in water and drying, freestanding fragments of the film were obtained. These fragments were mechanically ground in an agate mortar to provide a fine powder.

Tab. 4.4: Materials and dimensions of substrates used for deposition of thin films.

substrate	dimensions (mm)
monocrystalline Si (100)	35×5×0.38
monocrystalline Si (111)	35×5×0.53
monocrystalline Si (100)	20×20×0.38
monocrystalline Si (100)	20×20×0.63
rolled aluminum foil	55×55×0.1
amorphous soda lime glass	26×19×1
molybdenum	55×9×0.15

Prior to deposition all substrates were washed thoroughly by a wood-pulp wipe with isopropylalcohol, placed into an ultrasonic bath with acetone for 10 minutes, wiped by acetone again and left to air-dry.

4.3 Thin film characterization

This chapter describes the analytical methods and specific conditions used for characterization of the thin films.

4.3.1 Thickness, surface roughness and macrostress

The film thickness, deposition rate, surface roughness and macrostress (i.e. residual stress) were determined by means of Dektak 8 stylus profiler (Veeco Metrology Group). The profiler uses a diamond tipped stylus to scan the surface of the film with a declared vertical resolution as low as 1 nm [268]. During every deposition part the silicon substrate was covered by a small silicon fragment. After the deposition this fragment can be easily removed forming a step between the coated and uncoated part of the substrate. A scan across the step at 3 different locations is performed and the film thickness h is calculated as the arithmetic mean. Once the film thickness is know the deposition rate a_D can be calculated as $a_\mathrm{D}=h/t$, where t represents the deposition time. The arithmetic average surface roughness R_a was determined as the mean of three 2 mm long scans performed at different positions on the film surface.

In order to calculate the film macrostress a pre-deposition scan of uncoated silicon substrates was performed prior to deposition. After the deposition the coated substrate was scanned again and the film macrostress σ was calculated using the manufacturer-provided software according to

$$\sigma = \frac{1}{6}\left(\frac{1}{R_{post}} - \frac{1}{R_{pre}}\right)\frac{E_s}{(1-\nu_s)}\frac{h_s^2}{h_f}, \tag{4.1}$$

where R_pre, R_post, h_f, E_s, ν_s, h_s represent pre- and post-deposition radii of curvature of the sample, film thickness and Young’s modulus, Poisson’s ratio and thickness of the substrate, respectively. The radii of curvature in eq. 4.1 are calculated using the first and second derivatives of the scan profiles [269]. A negative value of σ (i.e. $\sigma<0$ GPa) corresponds to compressive macrostress in the film while $\sigma>0$ GPa represents tensile macrostress. The particular scan parameters used for determination of film thickness and macrostress are summarized in Tab. 4.5.

Tab. 4.5: Measurement parameters used for determination of film thickness and macrostress.

quantity	stylus radius (μm)	stylus force (mg)	scan length (mm)	scan duration (s)	vertical resolution (nm)
thickness h	12.5	15	2	10	1
macrostress σ	12.5	15	27	50	4

4.3.2 Mechanical properties

Mechanical properties and parameters characterizing mechanical behavior of the films were measured using a computer controlled microhardness tester Fischerscope H100 with a Vickers diamond indenter. During the measurement the diamond indenter is gradually pressed into the test material with an increasing load. A certain hold on time (creep) can be applied at the maximum load and then the indenter load is decreased again. During the whole process the indenter depth-load dependence is recorded in the form of a load-displacement curve (see Fig. 4.3.1).

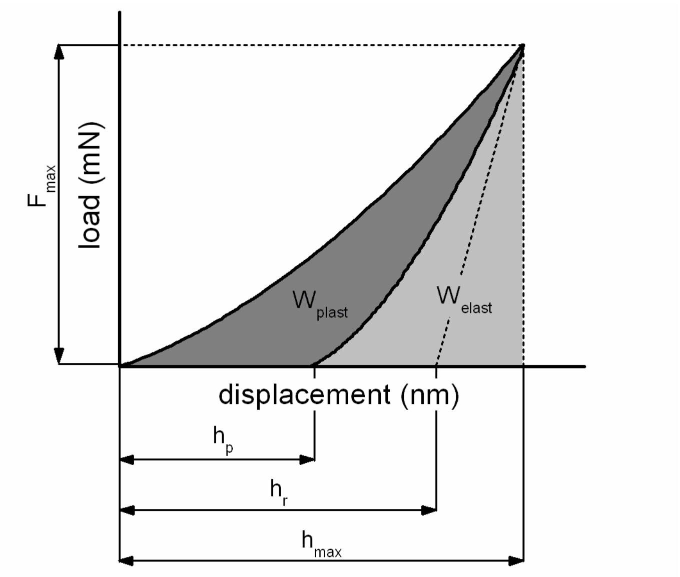

Fig. 4.3.1: Schematic illustration of load-displacement curve with selected important parameters. h_p represents permanent indentation depth after removal of the test force.

Based on the data obtained from the load-displacement curve the indentation hardness H can be calculated using

$$H = \frac{F_{\max}}{A_p}, \tag{4.2}$$

where $F_{\max}$ and A_p are the maximum applied force and the projected area of contact between the indenter and the test piece, respectively. The projected area A_p is obtained from

$$A_p = 24.50 \cdot h_c^2, \tag{4.3}$$

$$h_c = h_{\max} - \varepsilon(h_{\max} - h_r), \tag{4.4}$$

where ε, $h_{\max}$, h_c and h_r are the correction factor for indenter geometry (0.75 for Vickers indenter), the maximum indentation depth at the maximum indentation load $F_{\max}$, the depth of contact of the indenter with the test piece at $F_{\max}$ and the point of intersection of the tangent to the unloading curve at $F_{\max}$ with the indentation depth axis, respectively [270].

The film stiffness can be expressed by means of the effective Young's modulus E^*, which is calculated using

$$E^* = \frac{E_{IT}}{1-\nu_f^2} = \frac{1}{\frac{1}{E_r} - \frac{1-\nu_i^2}{E_i}}, \tag{4.5}$$

$$E_r = \frac{\sqrt{\pi}}{2C\sqrt{A_p}}. \tag{4.6}$$

The parameters in Eqs. (4.5) and (4.6) are defined as follows:

E_{IT}	indentation modulus of the film (is comparable with its Young's modulus)
ν_f	Poisson's ratio of the film
ν_i	Poisson's ratio of the indenter
E_r	reduced modulus of the indentation contact
E_i	modulus of the indenter
C	compliance of the contact, i.e. dh/dF at maximum test load
A_p	projected contact area

Having the $F=F(h)$ functionalities for loading and unloading it is possible to calculate the plastic (W_{plast}) and elastic (W_{elast}) components of the total indentation work (W_{total}). The ratio of the elastic deformation work to the total deformation work is denoted as the elastic recovery W_e and provides information about the extent of the elastic deformation of the material.

$$W_e = \frac{W_{elast}}{W_{total}} = \frac{W_{elast}}{W_{elast} + W_{plast}}, \tag{4.7}$$

From the literature survey provided in section 2.2.3.1. ("Indentation methods") it is seen that not only H and E^* but also W_e, H/E^* and H^3/E^{*2} represent important parameters that describe the mechanical behavior of thin films. For that reason these parameters are also given in the results part of the thesis.

In all measurements the indenter load of 20 mN was used and in most cases the indentation depth to film thickness ratio (d/h) did not exceed 0.1. Only in the case of some Cr-Cu-O films with hardness typically ≤4 GPa the d/h ratio exceeded 0.1. However the measured hardness vs. indentation load functionality $H=H(L)$ presented in section 5.2.5 indicates that there is no significant difference in the value of hardness of Cr-Cu-O films obtained with L=20 mN (d/h>0.1) and L=5 mN (d/h<0.1). The load increase as well as load decrease times were set to 10 s, no creep was applied and 25 indentations were performed on each sample. The indentation curves with inappropriate shapes or those that did not satisfy the Grubb's test for outliers with a significance level of α=0.05 were expelled from the evaluation and average values of mechanical properties were calculated from the remaining dataset.

4.3.3 Resistance to cracking

In this study the general term "resistance to cracking" refers to the film's resistance against formation and propagation of cracks when an external load is applied. Two methods were used to evaluate the films' resistance to cracking. In the indentation test the films are subjected to a predefined constant load. The bending test was used to determine the films' "cracking resistance" which is used instead of the critical load to represent the critical strain before film's fracture.

Indentation test

A direct comparison of crack patterns generated in the film in the indentation test was shown to be a simple and useful technique for a qualitative comparison of toughness of thin films [42, 59, 77]. The indentation test was carried out using the Fischerscope H100 microhardness tester with a Vickers diamond indenter. Since the indentation depth to film thickness ratio is significantly higher than 0.1 and sometimes even exceeds 1.0, interaction with the substrate is inevitable. Calculation of the fracture toughness in such case would not correspond to the film material itself but rather to the whole film-substrate system. Instead the crack patterns (mainly size and number of cracks) in films deposited on Si(100) monocrystal were qualitatively compared. In order to generate radial cracks, high indenter loads ranging from 250÷1000 mN were used. If the indentation of different films resulted in similar crack patterns additional indentations at lower loads were performed. When different film thicknesses complicated interpretation of the results, not only indentation at a constant load (L=const.) but also indentations to a constant depth (d/h=const.) or constant distance from the film substrate interface (h-d=const.) was used. All measurements were carried out with the overall loading-unloading time of 20 s (10 s loading, no creep, 10 s unloading) and indentation at a given load was repeated 3 times to make sure the crack pattern is reproducible. The position of each indentation was selected individualy at a plain and clear spot to avoid an interaction of the propagating crack with surface defects.

Bending test

Cracking resistance (i.e. critical film strain) as a measure of the film toughness was introduced by Wiklund et al. [50, 69]. In this thesis the resistance of the films to cracking was investigated in a bending test which utilizes a bending apparatus schematically shown in Fig. 4.3.2 a) developed at the Department of Physics (FAV, ZČU). In this test the molybdenum substrate with the film on the top side is placed between two cylinders and one of its ends is fixed. One cylinder (indicated by subscript „mc“) is moved around the other fixed cylinder of a given diameter ($Ø_{fc}$) and guides the molybdenum strip with the film to follow the radius of the fixed cylinder.

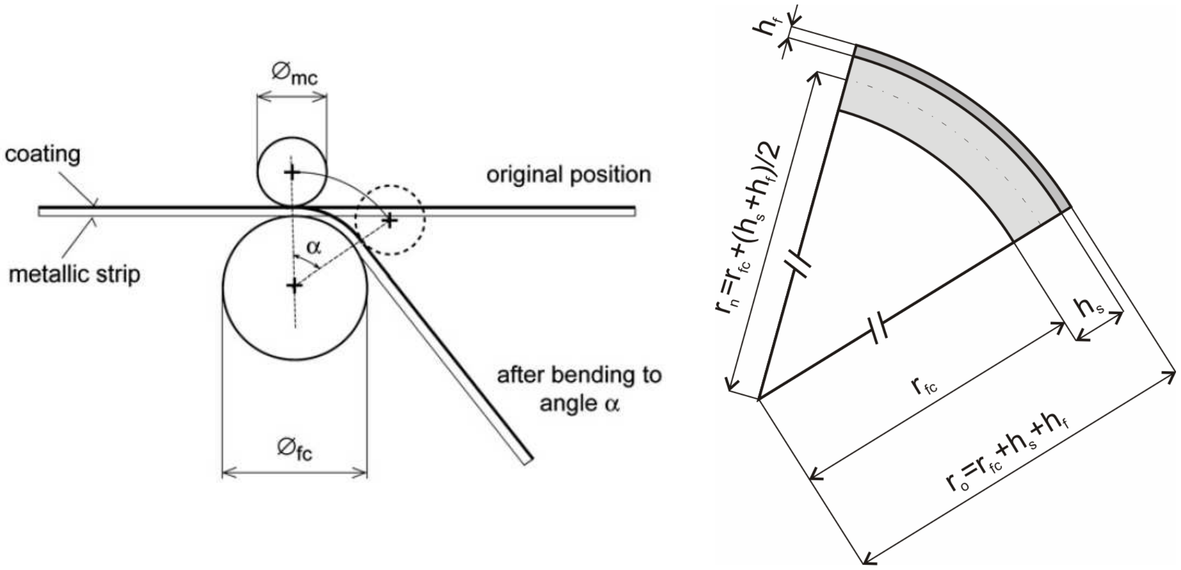

a) b)

Fig. 4.3.2: a) Schematic illustration of bending test. $Ø_{mc}$ and $Ø_{fc}$ are diameters of the moving and fixed cylinders, respectively [105]. b) Detail of the film-substrate geometry during bending.

Under the assumption that the substrate thickness ($h_s=150\ \mu m$) is much higher that the film thickness ($h_f \approx 1 \div 3\ \mu m$) the film strain ε can be calculated from the bending geometry in Fig 4.3.2 b) according to

$$\varepsilon = \frac{r_{fc} + h_s + h_f - \left(r_{fc} + \dfrac{h_s + h_f}{2} \right)}{r_{fc} + \dfrac{h_s + h_f}{2}} = \frac{1}{\dfrac{2r_{fc}}{h_s + h_f} + 1} = \frac{1}{\dfrac{\O_{fc}}{h_s + h_f} + 1}, \tag{4.8}$$

where $r_o = r_{fc} + h_s + h_f$ is the radius of the outer fiber, $r_n = r_{fc} + (h_s + h_f)/2$ is the radius of the neutral axis of the substrate+film system and r_{fc} is the radius of the fixed cylinder. Since the substrate thickness is constant and the film thickness is much smaller than h_s, the diameter of the fixed cylinder $\O_{fc}$ represents a variable parameter that determines the film strain ε. In the measurements presented below films deposited on molybdenum substrates were bent over fixed cylinder with $\O_{fc}$=25 mm, 20 mm, 15 mm and their surface morphology was investigated in-situ by an optical microscope or ex-situ by a scanning electron microscope. The sample is bent in the direction parallel to the surface texture of the molybdenum substrate. When a critical strain is reached a set of cracks is formed which are perpendicular to the direction of bending i.e. to the surface texture (see Fig. 4.3.3). This way it is possible to distinguish the cracks from the texture features.

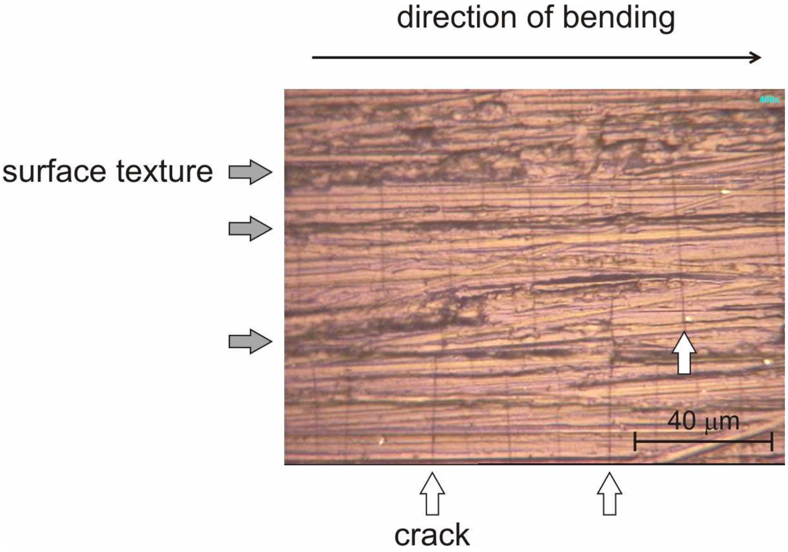

Fig. 4.3.3: Optical microscope (OM) image of the surface of Al-Cu-N/Mo film after bending over the fixed cylinder with a diameter of $\O_{fc}$=15 mm. The white arrows indicate cracks formed due to straining the film in bending while the grey arrows indicate surface texture of the molybdenum substrate.

4.3.4 Structure and phase composition

Structure of the films was characterized by X-ray diffraction technique using a PANalytical X'pert PRO spectrometer utilizing CuK$_\alpha$ radiation (λ=1.54187 Å). The obtained data were analyzed by X'Pert HighScore Plus software. Two different diffraction geometries were employed. The standard θ-2θ (Bragg–Brentano) configuration was used for characterization of Al-Cu-N and Cr-Cu-O films while the glancing incidence XRD (GIXRD) configuration was employed for investigation of Al_2O_3 and Al-Cu-O films. A schematic illustration of the goniometer in the Bragg–Brentano configuration is provided in Fig. 4.3.4 a). During the measurement the X-ray tube is stationary, the sample moves by an angle θ and the detector (semiconductor detector X´Celerator) moves simultaneously by the angle 2θ. Since the angle between the sample and the incident beam is the same as the angle between the sample and diffracted beam, the Bragg's law is fulfilled for crystal planes that are oriented parallel to the sample surface only. Crystal planes non-parallel with the sample surface are not detected.

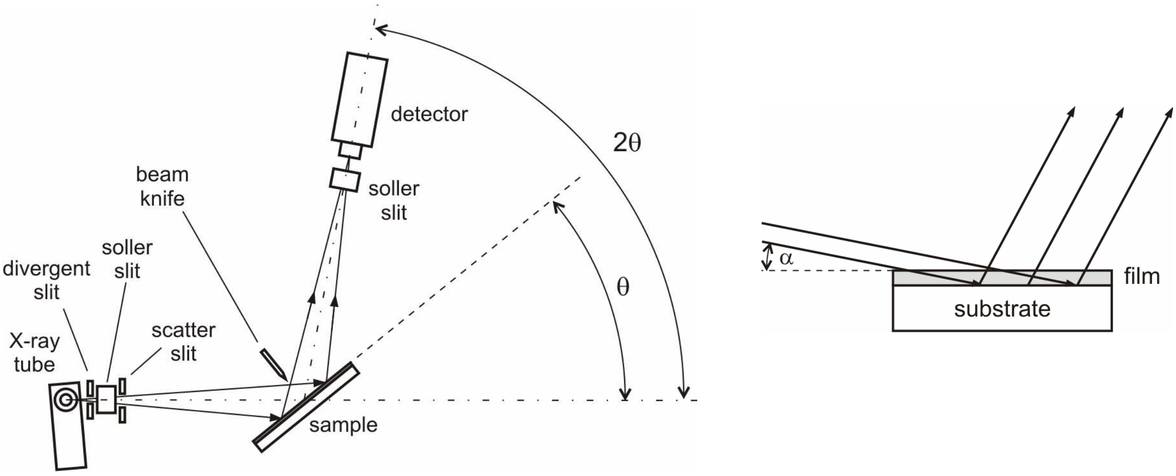

a) **b)**

Fig. 4.3.4: a) Schematic illustration of the goniometer in a standard Bragg-Brentano X-ray diffraction configuration [271]. b) Detail of the substrate and beam geometry in a glancing incidence X-ray diffraction (GIXRD) configuration. α represents the fixed incidence angle. Adapted from ref. [272].

In order to reduce the signal from the substrate and increase the signal-to-noise ratio, the Al_2O_3 and Al-Cu-O films were characterized by the glancing incidence X-ray diffraction (see Fig. 4.3.4 b)) at an incidence angle of 0.75°. In this configuration the incidence angle is fixed, so is the position of the sample and a proportional detector scanned the 2θ range. Since the GIXRD geometry is asymmetric the crystalline planes that contribute to the diffraction signal are inclined with respect to the sample surface and the angle of inclination changes as the detector is scanned [272]. The crystallite size and the lattice constant of Al_2O_3 and Al-Cu-O powders were determined using Williamson-Hall and Nelson-Riley plots, respectively.

4.3.5 Elemental composition

Elemental composition of the films was determined by two different analytical methods – the X-ray fluorescence (XRF) and the Rutherford backscattering spectroscopy (RBS). In the both cases films deposited on Si(100) substrate (20 mm×20 mm×0.63 mm or 20 mm×20 mm× 0.38 mm) were analyzed.

X-ray fluorescence (XRF)

In the XRF method the film is irradiated by X-rays that are energetic enough to expel electrons from inner orbitals of the atom. As a result electrons from higher orbitals deexcite to fill the unoccupied holes in the inner orbitals and emit photons of specific energies (wavelengths). The emitted photons are characteristic of the atom present and can be used for identification of the material. The XRF analysis of films presented in the thesis was conducted by a PANalytical X-ray fluorescence spectrometer MagiX PRO. A 4 kW rhodium X-ray tube was used as an X-ray source and SuperQ 4.0 and FP-MULTI softwares were utilized for data colection and processing. The quantitative XRF analysis of Al-Cu-O, Cr-Cu-O and Al-Cu-N films had been calibrated using the following combinations of standards: Cu film+Al_2O_3 standard, Cu film+Cr_2O_3 film and Cu film+AlN film, respectively. Based on the known value of the film thickness (as determined by profilometry) the film density was also calculated using the FP-MULTI software.

Rutherford backscattering spectroscopy (RBS)

In the RBS method the sample is bombarded by ions or protons accelerated to high energies (typically in the MeV range) and the angle and energy of elastically backscattered projectiles is recorded by energy sensitive detectors. Since the energy of the backscattered projectile particle depends only on the mass of the projectile and target particles and the backscattering angle it is relatively easy to identify the target particle (i.e. determine the elemental composition of the film). In this work the RBS analyses was performed using protons with the energy of 2.6 MeV. The results were further verified using protons with energies of 1.74 MeV and 2.2 MeV and alpha particles with the energy of 3.04 MeV. The principal advantage of the RBS method is that it does not require any reference standard to provide quantitative information about the elemental composition. Thus several Al-Cu-O and Cr-Cu-O films were selected, analyzed by the RBS method and the results were compared with the XRF method. The error bars in the elemental composition of the films represent a maximum relative error of the XRF method with respect to RBS.

4.3.6 Surface morphology

A preliminary analysis of the surface morphology of the films was performed by an optical microscope, which is a part of the Fischerscope microhardness tester (described in section 4.3.2). When higher magnification or resolution was necessary a scanning electron microscope (SEM) or atomic force microscope (AFM) were used.

Surface morphology of the films after the indentation or bending tests was examined by scanning electron microscopy (SEM). The SEM utilizes an accelerated focused electron beam that scans the sample surface. The interaction of the beam with the sample results in generation of secondary electrons, backscattered electrons or emission of electromagnetic radiation each of which can be analyzed by specialized detectors. These signals provide useful information about the surface morphology, material contrast or elemental composition. The scanning electron micrographs of presented films were obtained using FEI Quanta 200 scanning electron microscope (by FEI Company) with thermal emission of electrons and accelerating voltage of 30 kV. Due to their non-conductive nature the Al_2O_3, Al-Cu-O and AlN films were examined in the environmental SEM regime (ESEM). In this regime water vapor is introduced into the measurement chamber and its molecules are ionized by the electron beam. The ionized gas effectively discharges the electrons accumulated on the non-conductive surface and this way imaging of insulating films is possible. The micrographs shown in this work represent backscattered electron (BSE) images, since they yielded the best contrast of the crack patterns on the film surface.

Morphology of the *E. coli* bacterial cells after exposure to the films was investigated by atomic force microscopy (AFM). In the AFM the sample is scanned by a sharp tip attached to a cantilever. The forces between the tip and the sample cause the cantilever to bend or deflect and the movement of the cantilever is monitored by means of laser beam and position-sensitive photodetector. As the forces depend on the distance between the tip and the sample, vertical changes in surface profile result in variation of the cantilever deflection. Using a vertical scanner with a feedback control the force on the tip (i.e. cantilever deflection) is kept constant. By measuring and recording the scanner movement a map of the surface morphology is obtained. AFM measurements in this work were carried out in the non-contact regime using a SmartSPM atomic force microscope by AIST-NT. A cantilever with a spring constant of 40-90 N/m and resonant frequency of 360-400 kHz was used. The vibration amplitude ranged from 150 to 200 nm. Besides the height signal, the amplitude and the phase shift of the cantilever vibrations were also recorded. The Image analyzing & processing software by AIST-NT was used for analysis and post-processing of the measured data. For observation of the bacteria after exposure to the films, the following sample preparation procedure was used. Firstly, using a scalpel, a thin surface layer of the Endo agar is extracted from the part of the Petri dish where the diluted bacterial suspension was spread (see section 4.3.8). If no antibacterial effect is observed a bacterial colony is usually formed at this spot. The extracted sample is spread on a silicon wafer (10 mm×10 mm), diluted by a drop of tapwater and left to dry. After drying, single bacteria as well as larger agglomerates of bacteria can be observed by AFM.

4.3.7 Optical properties

Two analytical instruments were used for determination of the films’ optical properties. Spectroscopic ellipsometry was utilized in the case of Al-Cu-O films deposited on Si(100) substrates and UV-Vis spectrometry in the case of Cr-Cu-O films deposited on microscope glass slides.

Spectroscopic ellipsometry

The optical properties of Al-Cu-O films, i.e. the film transmittance T, index of refraction n and the extinction coefficient k, were investigated in the visible (VIS) and near infrared (NIR) regions between 300 and 2000 nm, using a variable angle spectroscopic ellipsometry (VASE) using the J.A. Woollam Co. Inc. instrument. The optical properties were evaluated from reflections at incident angles of 65°, 70° and 75°. The measured data were fitted using the VASE software and the optical model of the system composed of the c-Si substrate and the Al–Cu–O layer described by a Cauchy dispersion formula and a surface roughness layer.

UV-Vis spectrometry

The transmittance spectra of Cr-Cu-O films deposited on the amorphous soda-lime glass substrates were measured using an UV-Vis spectrometer Specord M400 (Carl Zeiss Jena). Photon wavelength range of 200÷900 nm was used. One of the most important optical properties of thin films is its transmittance, defined as

$$T[\%] = \frac{I}{I_0} \cdot 100\% , \tag{4.9}$$

where I and I_0 represent the intensity of the incident light and intensity of the light being transmitted through the sample, respectively. From the obtained spectra the optical transmittance $T_{\lambda=550\mathrm{nm}}$ of the film/substrate system at λ=550 nm was determined.

4.3.8 Antibacterial properties

Antibacterial properties of the films were tested at the Department of Microbiology, Medical Faculty in Plzeň, Charles University in Praha (Czech Republic). In all tests films deposited on polished Si(100) substrate (20 mm×20 mm×0.63 mm) were used. The samples were first washed with a 70 % ethanol to kill any bacteria on the surface and then left to dry. A suspension of the physiological solution (0.85 % w/v of NaCl and water) and *E. coli* bacteria with the initial concentration of 10^6 CFU/ml was prepared (here CFU denotes the colony forming units). A 50 μl dose of this suspension was applied on the surface of the film and the Si substrate for a comparison. The suspension was held in contact with the film by a sterilized glass plate. The samples were then exposed for a selected contact time to ambient indoor daylight at noon (further in the text denoted as “daylight”).The antibacterial activity was tested also in a photography darkroom chamber (in the text denoted as “dark”). In both cases the ambient temperature was 24 °C. After the selected contact time the film and glass plate were washed in 5 ml of a physiological solution and a new diluted suspension was formed. Then, 10 μl of this new diluted suspension were extracted and spread on the surface of a Petri dish covered with an Endo agar. The agar covered with the new diluted suspension was cultivated for 24 h in a biological thermostat at a constant temperature of 37 °C. The grown *E. coli* colonies were clearly visible and counted. The antibacterial efficiency *E* was determined according to

$$E[\%] = \frac{(A - B)}{A} \cdot 100 , \tag{4.10}$$

where *A* is the number of bacterial colonies grown from the suspension which was in contact with the surface of the reference Si substrate and *B* is the number of colonies grown from the suspension which was in contact with the film deposited on a Si substrate.

4.3.9 Phase transformations

The phase transformations in the as deposited Cr–Cu–O films were induced by rapid thermal annealing and the emerging phases were subsequently analyzed by ex-situ XRD analysis. Annealing from room temperature up to temperatures ranging from 400°C to 700°C was carried out in one heating pulse using an Annealsys AS-ONE 100 Rapid Thermal Processor (RTP) at a heating rate of 1°C/s in flowing nitrogen (1 l/h). The cooling, following immediately after reaching the maximum temperature T_a, was spontaneous. The water cooled processing chamber ensured reaching relatively high cooling rates in the initial stage of the cooling, e.g. up to 5°C/s when cooling from 700°C. Schematic illustration of the processing chamber with the main components is illustrated in Fig 4.3.5.

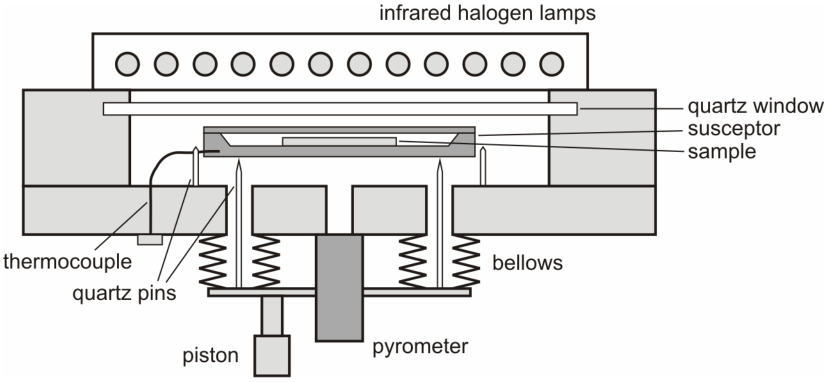

Fig 4.3.5: Schematic illustration of the processing chamber of the ANNEALSYS AS-ONE 100 Rapid Thermal Processor.

The film deposited on a Si(100) substrate (20 mm×20 mm×0.63 mm) is placed into a SiC-coated graphite susceptor positioned on quartz pins. The heating is controlled by the power of 12 infrared halogen lamps and the temperature is continuously monitored at the bottom side of the susceptor by an optical pyrometer. A K-type thermocouple is installed on the side of the susceptor to provide additional information about the sample temperature.

5. Results and discussion

The following chapter is divided into three parts, each of which is dealing with preparation and characterization of thin films of one ternary system containing copper. The first part is focused on enhancing the mechanical properties and resistance to cracking of pure Al_2O_3 films by copper alloying. The second part is aimed at preparation of an antibacterial Cr-Cu-O film able to efficiently kill *E. coli* bacteria without the need of any additional irradiation. The final part is devoted to optimization of the deposition process in order to obtain a multifunctional hard antibacterial Al-Cu-N film with an enhanced resistance to cracking. In all the three subchapters the effect of copper content on the properties of the films is systematically investigated as one of the key parameters. With respect to the particular aims specified in chapter 3 the contingent effect of additional process parameters is also shown and discussed. The materials in the thesis are referred to as Al-Cu-O, Cr-Cu-O and Al-Cu-N which reflects their elemental composition in general. Their specific structure and phase composition is discussed in the corresponding sections. The convention throughout this thesis is, that a slash symbol followed by a substrate material (Si, Mo, glass) indicate the type of substrate the particular film is deposited on (e.g. Al-Cu-O/Si denotes Al-Cu-O film deposited on a Si substrate).

5.1 Hard nanocrystalline Al-Cu-O films resistant to cracking

Aluminum oxide represents one of the most important ceramic materials in the industry. It exists in a wide range in polymorphs that can be prepared by various methods and exhibit different mechanical properties. It has already been shown that composite bulk materials composed of metallic Cu and ceramic Al_2O_3 matrix may exhibit enhanced fracture toughness [273]. However formation of metallic Cu in the process of reactive magnetron sputtering in the presence of O_2 gas remains a difficult task. This is due to relatively high standard enthalpy of formation of CuO (ΔH_f^o(CuO)=-157.3 kJ/mol [196]) combined with its thermal stability exceeding 1000 °C [213], which usually leads to formation of Cu-O bonds rather than metallic Cu. However it has been demonstrated that even in the process of reactive magnetron sputtering addition of Cu may lead to enhancement of mechanical properties compared to pure binary oxide films [59].

The aim of this study is to reactively sputter Al–Cu–O films with different contents of Cu and to investigate the effect of the addition of Cu into an Al_2O_3 film on its structure, mechanical properties and resistance to cracking. The main task of this investigation is to find out if alloying of Al_2O_3 films with Cu can enhance the resistance to cracking.

5.1.1 Deposition conditions

The Al_2O_3 and Al-Cu-O films were deposited using a dual magnetron system illustrated in Fig. 4.1.2. For deposition of pure Al_2O_3 films two identical Al targets were used (see Fig. 4.1.4). For deposition of Al-Cu-O films magnetron 1 was equipped with pure Al target and magnetron 2 with a composed Al/Cu target (Fig. 4.1.5). In this configuration it was possible to control the Cu content in the film by changing the duty cycle (i.e. pulse length) on the individual targets as already described in section 4.1.2.

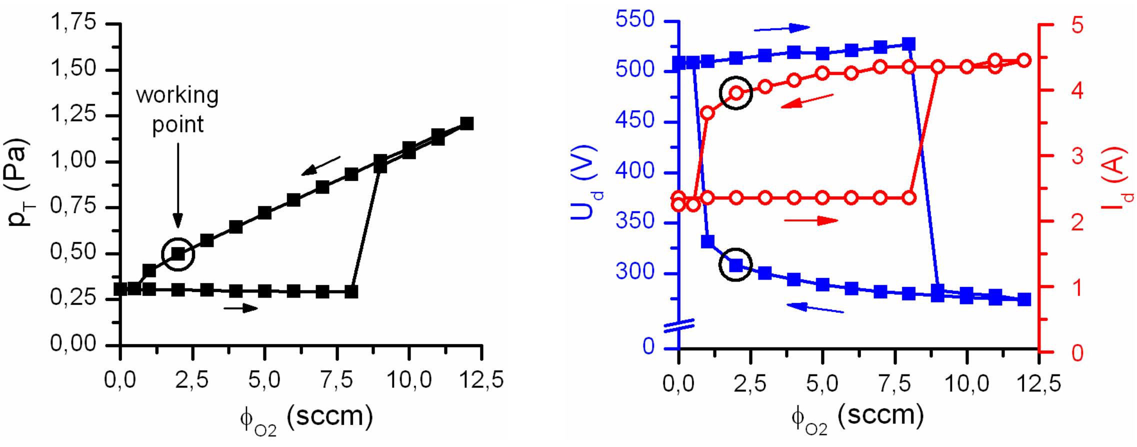

a) **b)**

Fig. 5.1.1: Hysteresis behavior of a) the total pressure p_T and b) the discharge voltage U_d and the discharge current I_d as functions of the oxygen flow rate ϕ_{O2}. The following parameters were fixed: p_{Ar}=0.3 Pa, T_s=500 °C, f_r=25 kHz and P_d= 1.2 kW, $\tau_{Al/Cu}=\tau_{Al}$= 20 µs, Al target on magnetron 1 and composed Al/Cu target on magnetron 2.

All films were deposited in the oxide mode of sputtering and the substrates were held at a floating potential in the distance of 110 mm from the magnetrons (*$d_{s\text{-}t}$=110 mm*). In order to optimize the deposition rate by properly selecting the working point the discharge characteristics (p_T, I_d and U_d) were first measured as a function of oxygen flow rate ϕ_{O2} (see Fig. 5.1.1.a) and 5.1.1. b)). A clear hysteresis behavior can be observed in both figures. To make sure the films are stoichiometric they were prepared in the oxide mode of sputtering at an O_2 partial pressure of *p_{O2}=0.2 Pa*. Higher values of p_{O2} would result in a more pronounced target poisoning and lower deposition rate while lower values of p_{O2} would lead to oscillations of the working point between metallic and oxide mode resulting in formation of inhomogeneous and substoichiometric films. The deposition rate was further increased by operating the discharge at relatively high power P_d=1.2 kW *(≈W_d=60 W/cm^2)* and by keeping the total pressure at its minimum value to minimize the energy losses of ions due to collisions thereby increasing the sputtering yield.

The results and trends related to the Al-Cu-O films are illustrated on series 1 which was prepared at the following deposition conditions:

total pressure	p_T=0.5 Pa
O_2 partial pressure	p_{O2}=0.2 Pa
flow rate of Ar	ϕ_{Ar}=2.7 sccm
substrate temperature	T_s=500 °C
repetition frequency	f_r=25 kHz
average target power in pulse	P_d=1.2 kW

To verify the trends in mechanical properties, another series (series 2) was prepared with some of the deposition parameters modified as follows:

total pressure	$p_T=1.5\ Pa$
O_2 partial pressure	$p_{O2}=0.3\ Pa$
flow rate of Ar	$\phi_{Ar}=11.5\ sccm$
substrate temperature	$T_s=500\ °C$
repetition frequency	$f_r=50\ kHz$
average target power in pulse	$P_d=1.0\ kW$

Unless explicitely stated otherwise the presented results are related to series 1. Within each series of Al-Cu-O films with various Cu contents a pure Al_2O_3 film was also deposited in order to provide a proper comparison. To support the interpretation of some of the results several individual films have also been deposited and their specific deposition conditions are provided in the text.

Fig. 5.1.2 shows the evolution of the deposition rate of Al-Cu-O/Si films with increasing pulse length on the composed Al/Cu target $\tau_{Al/Cu}$. It can be clearly seen, that the deposition rate increases from ≈3.8 nm/min for pure Al_2O_3/Si films and Al-Cu-O/Si film prepared at $\tau_{Al/Cu}=8\ \mu s$ (low Cu content) up to 9.3 nm/min for $\tau_{Al/Cu}=32\ \mu s$ (high Cu content). This increase can probably be related to a higher argon ion sputtering yield of CuO ($\gamma_{CuO}=0.802$) compared to Al_2O_3 ($\gamma_{Al2O3}=0.231$) [274]. Even if the case of a not completely oxidized target surface is considered the sputtering yield of metallic Cu ($\gamma_{Cu}=1.751$) is significantly higher compared to metallic Al ($\gamma_{Al}=0.992$) [275]. The relatively low deposition rate of ≈3.8 nm/min for pure Al_2O_3 deposited in the oxide mode of sputtering agrees well with values reported by Musil et al. [276].

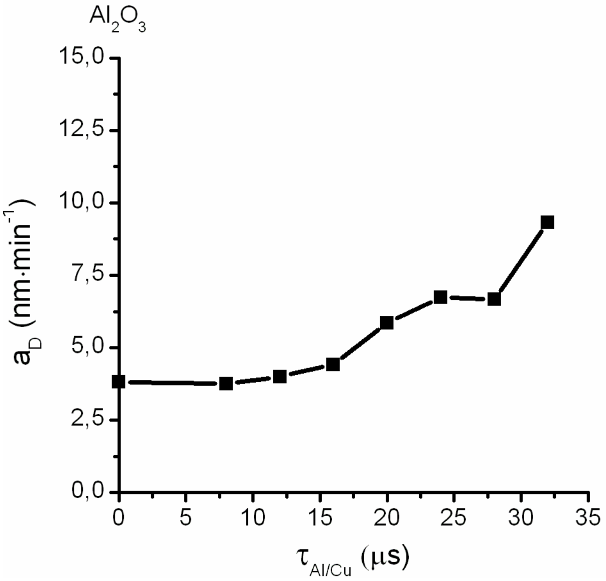

Fig. 5.1.2: Deposition rate of Al-Cu-O/Si films as a function of pulse length $\tau_{Al/Cu}$ on the composed Al/Cu target. The value corresponding to $\tau_{Al/Cu}=0\ \mu s$ represents deposition rate of pure Al_2O_3 film prepared using two Al targets with identical pulse lengths of 20 μs.

5.1.2 Effect of Cu content on structure of Al-Cu-O films

The elemental composition of the films as a function of pulse length $\tau_{Al/Cu}$ on the composed Al/Cu target is shown in Fig. 5.1.3. It can be seen that for the given target geometry it is possible to control the Cu content in the film from 1.7 at.% up to 16 at.% by changing the pulse length from $\tau_{\mathrm{Al/Cu}}$=8 μs (duty cycle=20 %) to $\tau_{\mathrm{Al/Cu}}$=32 μs (duty cycle=80 %). The deviation of the elemental composition of pure Al_2O_3 film from the theoretical composition (indicated by open symbols) lies within the measurement error of the XRF analysis and thus the prepared Al_2O_3 film can be considered very close to the correct stoichiometry.

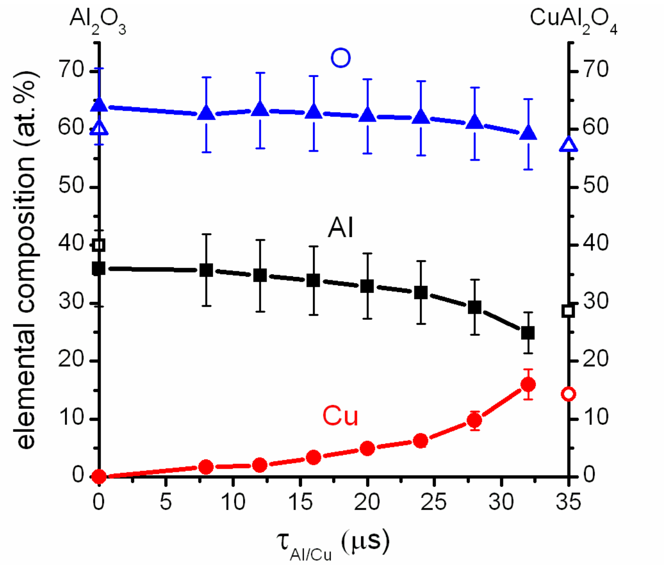

Fig. 5.1.3: Elemental composition of Al–Cu–O/Si films of series 1 as a function of pulse length $\tau_{\mathrm{Al/Cu}}$ on the composed Al/Cu target. Open symbols indicate the theoretical elemental composition of stoichiometric Al_2O_3 and $CuAl_2O_4$ compounds.

The structure of Al-Cu-O/Si films was characterized by glancing incidence X-ray diffraction (GIXRD) technique at the incident angle of 0.75° (Fig. 5.1.4). It can be seen that all films are characterized by relatively broad low-intensity reflections that indicate presence of crystalline nanograins. Moreover a broad amorphous peak is observed around $2\theta \approx 30° \div 40°$ which corresponds to an amorphous phase [276]. The films can thus be described as nanocomposites composed of a mixture of nanograins embedded in an amorphous matrix. In the case of pure Al_2O_3 film this can be denoted as nc-γ-Al_2O_3/a-Al_2O_3 where nc-γ-Al_2O_3 corresponds to the nanocrystalline γ-Al_2O_3 phase (indicated by the presence of the (3 1 1), (4 0 0) and (4 4 0) reflections) and a-Al_2O_3 represents the amorphous Al_2O_3 phase. The addition of Cu in the Al_2O_3 film results in a gradual shift of the (3 1 1), (4 0 0) and (4 4 0) reflections to lower 2θ angles towards the positions corresponding to the $CuAl_2O_4$ phase. As the Cu content in the films increases, the intensities of the reflections change and correspond rather to the $CuAl_2O_4$ standard. Since the macrostress σ in the films does not vary much with an increasing Cu content, these changes indicate that Cu atoms are incorporated into the γ-Al_2O_3 structure and a nanocrystalline solid solution is formed. According to the equilibrium phase diagram for CuO-Al_2O_3 system the $CuAl_2O_4$ phase forms at temperatures above 800°C and below this temperature a mixture of CuO and α-Al_2O_3 is observed [277]. However the phase diagram and mutual insolubility of $CuAl_2O_4$ and Al_2O_3 might change if metastable γ-Al_2O_3 structure is considered instead of α-Al_2O_3 with corundum structure.

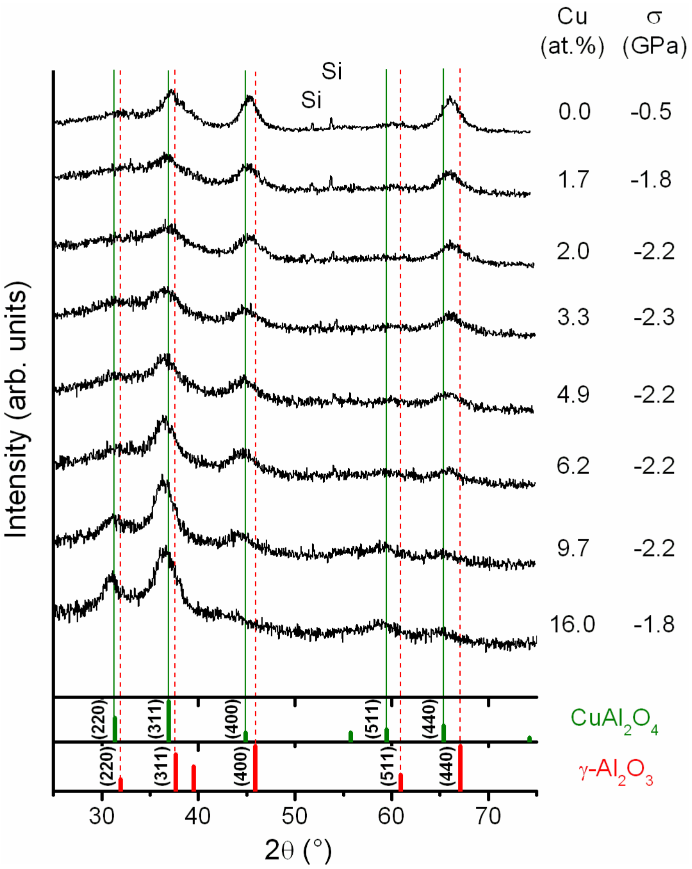

Fig. 5.1.4: GIXRD patterns of the Al_2O_3/Si film and Al–Cu–O/Si films with various Cu contents. "Si" indicates reflections from the silicon substrate.

Assuming that the $CuAl_2O_4$ phase has a spinel structure and γ-Al_2O_3 can be described as defective spinel the solid solution can be expressed as $(Al_{8-2x},Cu_{3x})O_{12}$ giving Al_2O_3 for $x=0$ and $CuAl_2O_4$ for $x=1$. This atypical formula for expressing solid solution is due to the deviation of γ-Al_2O_3 structure from the ideal spinel. The suggested formula $(Al_{8-2x},Cu_{3x})O_{12}$ describes correctly the changes in stoichiometry but it does not indicate which Cu atoms substitute for Al atoms and which fill vacant interstitial sites.

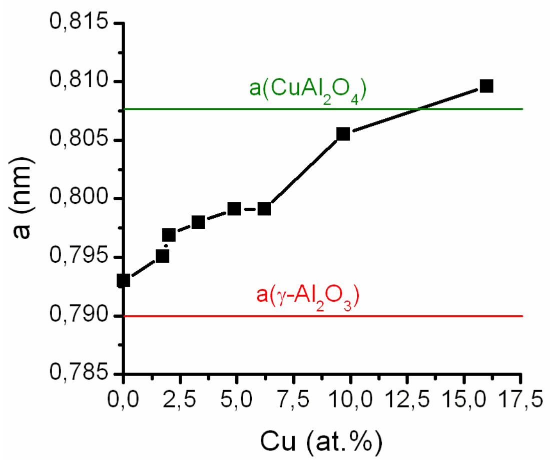

Fig. 5.1.5: Lattice parameter *a* of the Al_2O_3/Si film and Al–Cu–O/Si films with various Cu contents. The values of *a* corresponding to γ-Al_2O_3 and $CuAl_2O_4$ standards are provided as a reference.

Fig. 5.1.5 shows the lattice parameter *a* of the Al–Cu–O/Si films as a function of the Cu content. It can be clearly seen that the lattice parameter gradually increases from 0.793 nm to 0.810 nm which corresponds quite well to values for pure γ-Al_2O_3 (*a*(γ-Al_2O_3)=0.790 nm) and $CuAl_2O_4$ (*a*($CuAl_2O_4$)=0.875 nm), respectively. This gradual change of lattice parameter is typical for solid solutions and is described by the Vegard's law [278]. The deviation of the calculated values from the corresponding standards can be attributed to compressive macrostress that leads to a shift of the reflections towards lower 2θ angles and to a change of the lattice parameter. In order to exclude the effect of the silicon substrate on the position of the XRD peaks (due to mismatch of the thermal expansion coefficients of the film and of the substrate) the Al_2O_3 and Al-Cu-O films were also deposited onto Al foils at deposition conditions corresponding to series 1. Films with three different Cu contents (0.0 at.%, 4.1 at.% and 9.4 at.%) were prepared and the Al substrates were subsequently etched and the remaining film fragments were ground to fine powders (see chapter 4.2). The obtained XRD patterns of the films are presented in Fig. 5.1.6. The shift of the XRD peaks with an increasing Cu content is clearly seen especially in the case of the (440) reflection.

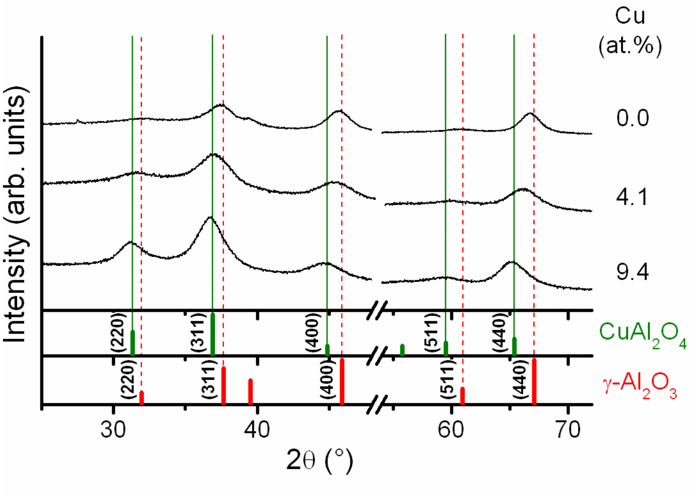

Fig. 5.1.6: XRD patterns of Al_2O_3 and Al-Cu-O powders with various Cu contents obtained after chemical etching of the Al substrate and mechanical grinding of the freestanding fragments of the films.

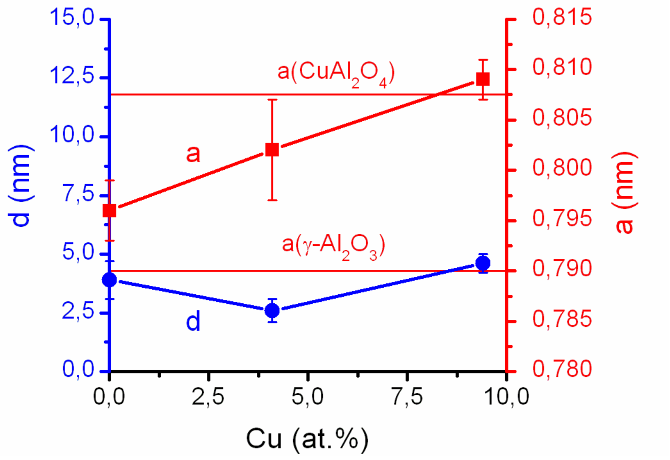

Fig. 5.1.7: Mean crystallite size *d* and lattice parameter *a* of Al_2O_3 powder and Al-Cu-O powders with various Cu contents calculated from the XRD patterns presented in Fig. 5.1.6.

Fig. 5.1.7 shows the plot of the lattice parameter and mean crystallite size as functions of Cu content in the film. While the mean crystallite size does not show significant variations with an increasing Cu content, the lattice parameter clearly increases in the same manner as observed for Al-Cu-O films deposited on the Si substrate (see Fig. 5.1.5). The shift of the lattice parameter is observed even for powdered samples which suggests, that the compressive stress in the film was not eliminated by etching the Al substrate and originates from the intrinsic stress rather than from thermal expansion mismatch of the film and the substrate.

5.1.3 Effect of Cu content on mechanical properties

The evolution of mechanical properties of Al-Cu-O/Si films with an increasing Cu content is shown in Fig. 5.1.18 a) and b). The exact values of mechanical properties and other characteristics are provided in Tab. 5.1. From Fig. 5.1.18 a) it is seen that the incorporation of Cu into Al_2O_3 leads to a significant improvement of hardness from 7.1 GPa up to 20.1 GPa as the Cu content increases from 0.0 at.% to 16.1 at.%. Since the macrostress in the Al-Cu-O/Si films is approximately constant ($\sigma \approx$ -2 GPa), the changes in hardness cannot be attributed to compressive macrostress alone and are rather related to changes in the structure of the films. As can be seen from Tab. 5.1 the gradient of H with respect to Cu content is much higher compared to the gradient of E^*. This results in a significant improvement of the H/E^* ratio of the films exceeding the value of 0.1 for Cu contents >2 at.% as shown in Fig. 5.1.18 b). As can bee seen from Fig. 5.1.18 b) the elastic recovery follows the same trend as H/E^* ratio and reaches up to 77 % for 16 at.% of Cu indicating that the deformation work during indentation is predominantly elastic. This clearly shows that the Cu content can be effectively used to tune not only the hardness of the Al-Cu-O films but also their elastic recovery and H/E^* ratio, which plays a significant role for the films' resistance to cracking.

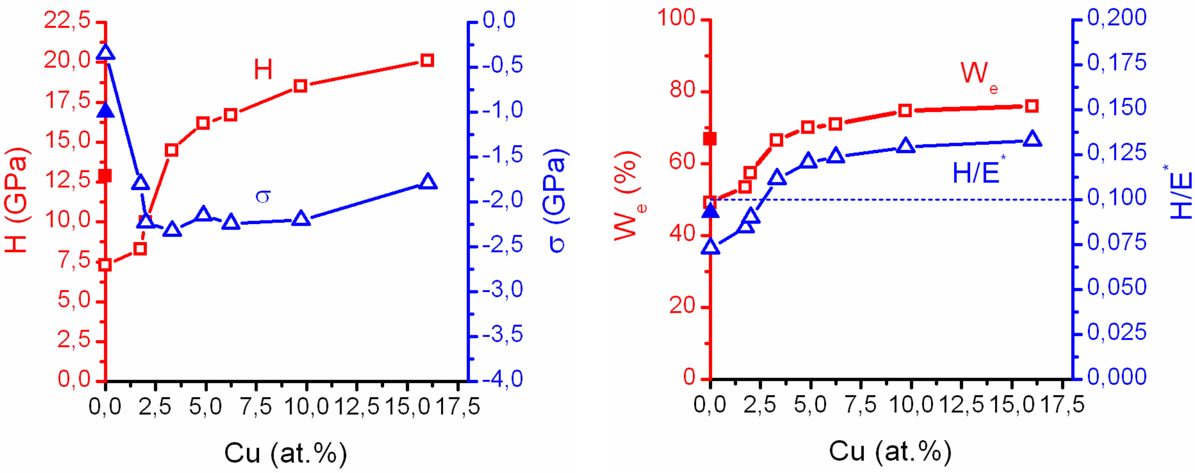

a) **b)**

Fig. 5.1.8: a) Hardness H and macrostress σ and b) elastic recovery W_e and H/E^* ratio of Al_2O_3/Si films and Al–Cu–O/Si films with various Cu contents. Full symbols represent Al_2O_3/Si film deposited at identical deposition conditions with higher flow rates of Ar and O_2 gases (ϕ_{Ar}=15 sccm, $\phi_{O2} \approx 14.9$ sccm) compared to the rest of the films (ϕ_{Ar}=2.7 sccm, $\phi_{O2} \approx 2.4$ sccm).

The hardness of 7.3 GPa corresponding to a pure nanocrystalline Al_2O_3/Si film presented in Tab. 5.1 (film 2) is relatively low. The hardness of nanocrystalline γ-Al_2O_3 films presented by other authors typically ranges from 10 GPa to 20 GPa [175, 179]. This may be attributed to relatively low flow rates of O_2 and Ar gases used for deposition of series 1 and possible contamination of the gas mixture by residual gases. For that reason another Al_2O_3/Si film was prepared at identical deposition condition but at higher flow rates with the gate valve open wider. The mechanical properties of this film (film 1) are provided in Tab. 5.1 and illustrated in Fig. 5.1.18 by full symbols. A clear improvement of all mechanical properties is observed compared to the pure Al_2O_3/Si film prepared at low flow rates. However even this optimized Al_2O_3 film exhibits a significantly lower hardness and H/E^* ratio when compared to the Al-Cu-O/Si films with Cu content ≥5 at.%.

Tab. 5.1: Characteristics of Al_2O_3/Si films and Al–Cu–O/Si films with various Cu contents prepared at p_T=0.5 Pa, p_{O2}=0.2 Pa, W_d=61 W/cm^2, f_r=25 kHz, T_s=500 °C, $d_{s\text{-}t}$=110 mm. Film 1 was prepared at high flow rates (ϕ_{Ar}=15 sccm, ϕ_{O2}≈14.8 sccm) while films 2-9 were prepared at low flow rates (ϕ_{Ar}=2.7 sccm, ϕ_{O2}≈2.5 sccm).

film no.	Cu (at.%)	a_D (nm/min)	h (nm)	σ (GPa)	H (GPa)	E* (GPa)	W_e (%)	H/E*	H^3/E^{*2} (GPa)
1	0.0	3.52	1480	-1.0	12.9	138	67	0.093	0.113
2	0.0	3.82	2550	-0.4	7.3	100	49	0.073	0.039
3	1.7	3.75	2080	-1.8	8.3	98	54	0.085	0.060
4	2.0	4.00	1930	-2.2	10.0	111	58	0.090	0.081
5	3.3	4.42	1900	-2.3	14.5	130	67	0.112	0.180
6	4.9	5.85	1990	-2.2	16.2	134	70	0.121	0.237
7	6.2	6.73	2020	-2.2	16.7	135	71	0.124	0.256
8	9.7	6.66	2070	-2.2	18.5	143	75	0.129	0.310
9	16.0	9.33	3080	-1.8	20.1	151	76	0.133	0.356

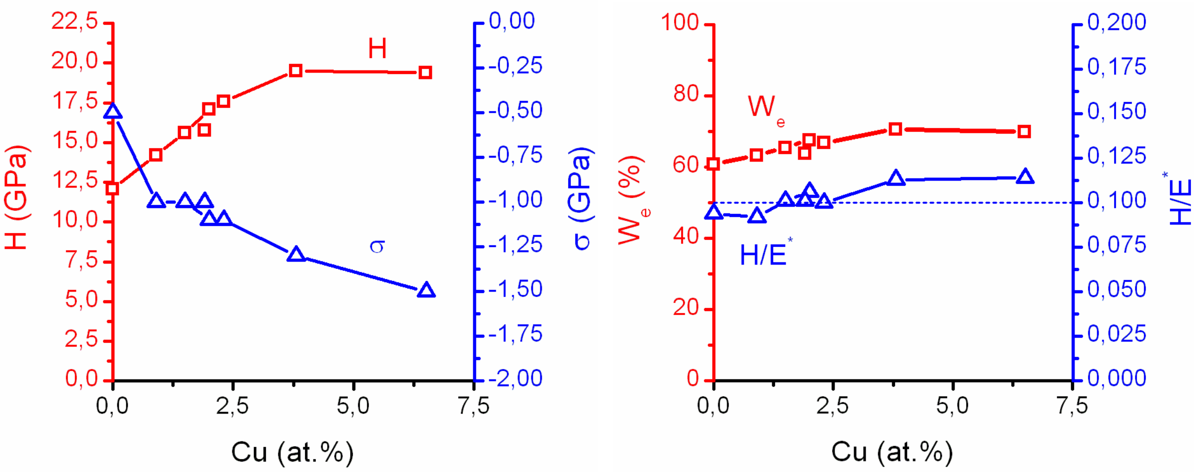

a) **b)**

Fig. 5.1.9: a) Hardness H and macrostress σ and b) elastic recovery W_e and H/E^* ratio of Al_2O_3/Si films and Al–Cu–O/Si films with various Cu corresponding to series 2. Deposition conditions: p_T=1.5 Pa, p_{O2}=0.3 Pa, ϕ_{Ar}=11.5 sccm, T_s=500 °C, f_r=50 kHz, P_d=1.0 kW.

Based on the observations above another series of Al_2O_3/Si and Al-Cu-O/Si films (denoted as series 2) was prepared with higher flow rates of Ar and O_2 gases. Due to gradual coverage of the target surface by a non-conductive compound resulting in slight microarc events on the target. For that reason the average target power in pulse was reduced to 1.0 kW and the repetition frequency and total pressure were increased to 50 kHz and 1.5 Pa, respectively. The mechanical properties of Al_2O_3/Si films and Al–Cu–O/Si films with various Cu contents corresponding to series 2 are shown in Figs. 5.1.9 a) and b). Due to a procceeding erosion of the Cu part of the composed Al/Cu target it was not possible to to achieve Cu contents as high (≈16 at.%) as presented in series 1. The higher flow rates resulted in improvement of hardness of pure Al_2O_3/Si film to *H≈12.4 GPa*. As the Cu content in the Al–Cu–O/Si films increases, the *H*, W_e and *H/E** values increase up to 19.5 GPa, 71 % and 0.113, respectively. These results show that even for modified deposition conditions the alloying of pure Al_2O_3 films with Cu leads to a significant improvement of mechanical properties of the films.

5.1.4 Resistance of Al-Cu-O films to cracking

It is generally known that pure Al_2O_3 films can be prepared in the form of various polymorphs with different mechanical properties. As a result these polymorphs can be expected to exhibit also different resistance to cracking. The mechanical properties of amorphous (a-Al_2O_3) and nanocrystalline (nc-γ-Al_2O_3) alumina films are illustrated in Tab. 5.2. Here the structure of the Al_2O_3 films was controlled by the energy delivered to the growing film, which can be supplied e.g. in the form of substrate heating (T_s) or target power density (W_d). Whereas for low target power density (30.6 $W.cm^{-2}$) and unheated substrates an amorphous a-Al_2O_3 film is formed, increasing the substrate temperature and target power density to 500°C and 50.9 $W.cm^{-2}$ results in formation of a nanocrystalline nc-γ-Al_2O_3 structure. The difference in the structure of the resulting films is illustrated in Fig. 5.1.10. Since possible admixture of amorphous phase can not be excluded, the nanocrystalline film is denoted as nc-γ-Al_2O_3/a-Al_2O_3. From Tab. 5.2 it is apparent that the nanocrystalline alumina film exhibits a significantly higher hardness (*H*=12.1 GPa) compared to the amorphous film (*H*=7.6 GPa).

Tab. 5.2: Deposition parameters and characteristics of Al_2O_3/Si films with amorphous (a-) and nanocrystalline (nc-γ) structure. Except for the W_d and T_s values presented in the table the other deposition parameters were the same for both films: p_T=1.5 Pa, p_{O2}=0.3 Pa, f_r=50 kHz, U_s=U_{fl}, ϕ_{Ar}=11.5 sccm, ϕ_{O2}≈3.7 sccm. ”RT” indicates room temperature.

film structure	W_d (W/cm^2)	T_s (℃)	h (nm)	σ (GPa)	H (GPa)	E* (GPa)	W_e (%)	H/E*	H^3/E^{*2} (GPa)
amorph.	30.6	RT	2190	0	7.6	119	41.5	0.064	0.064
nc-γ /amorph.	50.9	500	2030	-0.5	12.1	129	60.9	0.094	0.094

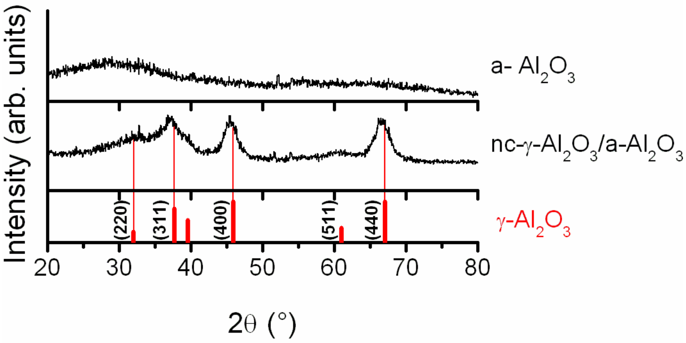

Fig. 5.1.10: GIXRD patterns of amorphous a-Al_2O_3 and nanocrystalline nc-γ-Al_2O_3/a-Al_2O_3 films.

The effect of different structure of Al_2O_3 films on their resistance to cracking is illustrated in Fig. 5.1.11, which shows SEM images of diamond indenter imprints into the nanocrystalline and amorphous alumina films shown in Fig. 5.1.10. In order to provide a more detailed comparison of the performance of these films in the indentation test, three different indenter loads were applied. As can be seen from Fig. 5.1.11 the nanocrystalline Al_2O_3 film does not exhibit any cracks when low indenter load of 0.4 N is used. On the other hand the amorphous Al_2O_3 film clearly shows presence of radial cracks. Increasing the indenter load leads to formation of cracks even in the nanocrystalline nc-γ-Al_2O_3/a-Al_2O_3 film. However their size is generally smaller compared to the amorphous film. Thus it can be concluded that nanocrystalline Al_2O_3 films are harder (H=12.1 GPa) and exhibit a higher resistance to cracking compared to amorphous Al_2O_3 films with low hardness (H=7.6 GPa).

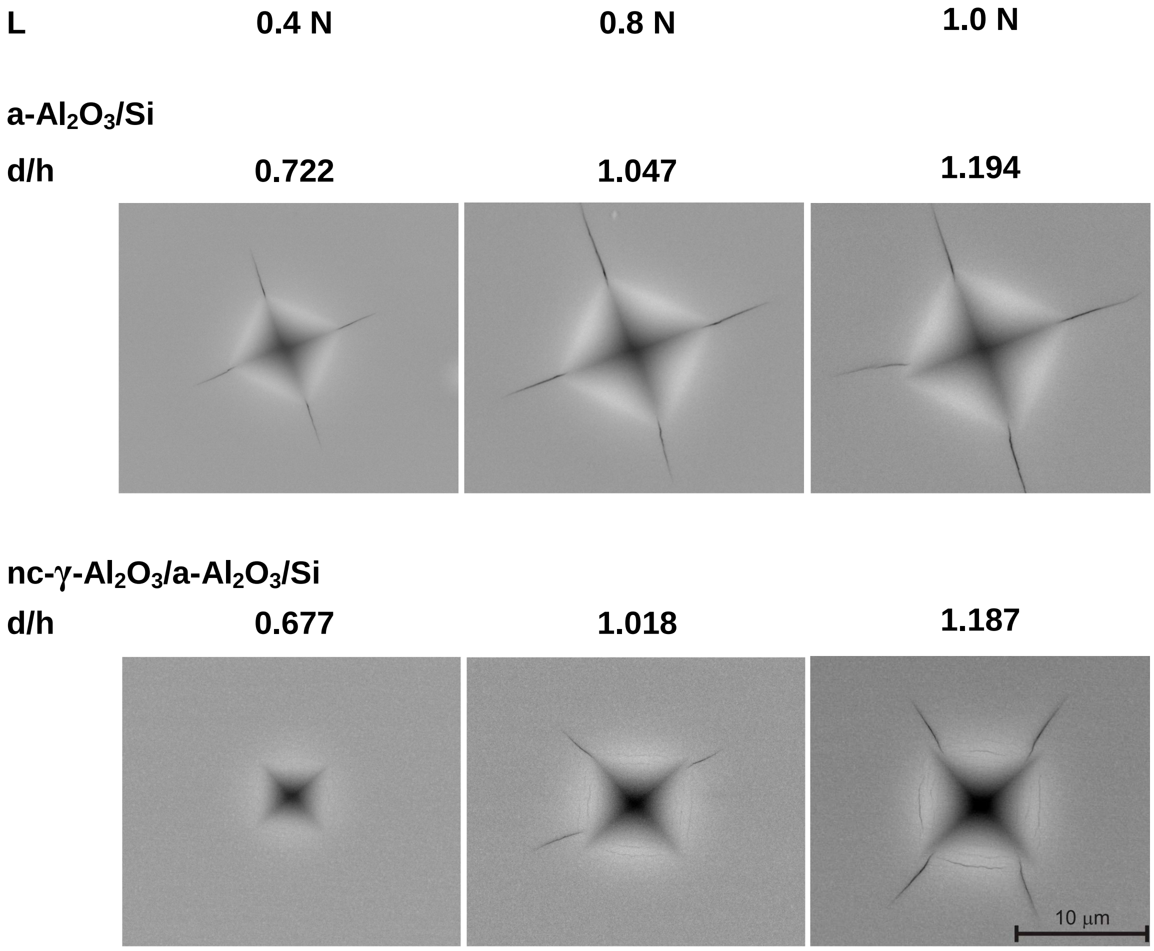

Fig. 5.1.11: SEM images of diamond indenter imprints in amorphous (a-) and nanocrystalline (nc-) Al_2O_3 films formed in the indentation test using various indenter loads L. The indentation depth to film thickness ratio (d/h) is shown for comparison.

In section 5.1.3 it was found that addition of Cu significantly improves the H/E^* ratio and the elastic recovery of pure Al_2O_3 films. Since both H/E^* and H^3/E^{*2} ratios were reported to affect the resistance of thin films to cracking (see section 2.2.3.1) the indentation test was performed on the Al_2O_3/Si film and Al–Cu–O/Si films with various Cu contents (series 1). Fig. 5.1.12 illustrates the effect of the Cu content on resistance of the films to cracking. It is seen that only the pure Al_2O_3/Si film and the Al–Cu–O/Si film with 2 at.% Cu exhibit presence of radial cracks. No cracks are formed in the films with Cu content >2 at.%. It indicates that the incorporation of Cu in Al_2O_3 enhances the films' resistance to cracking. However, the amount of Cu incorporated in the film needs to reach a certain critical value which ensures that the film is highly elastic (high $W_e \geq 60\%$), resistant to plastic deformation (H^3/E^{*2}>0.1 GPa) and that the applied load is sufficiently distributed in the film to prevent formation of cracks (H/E^*>0.1). As seen from Tab. 5.1 these requirements are met for the Al–Cu–O/Si nanocomposite films with nc-$(Al_{8-2x},Cu_{3x})O_{12}$/a-(Al–Cu–O) structure and Cu content >2 at.%.

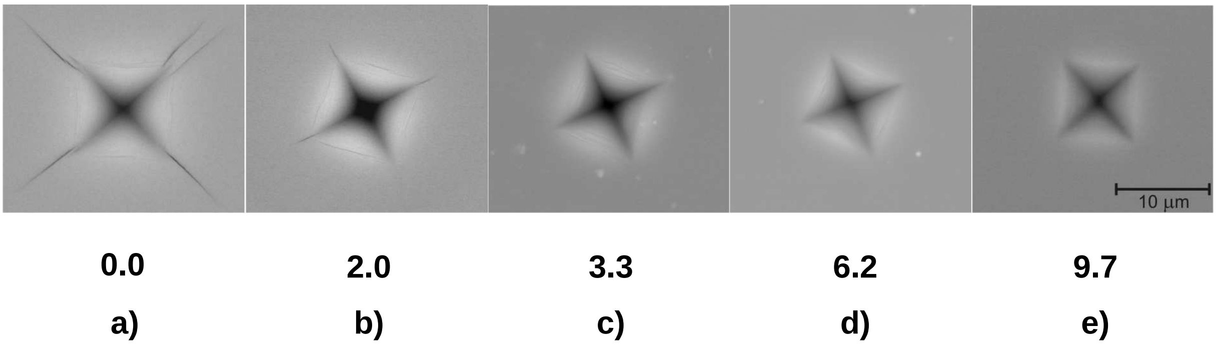

Fig. 5.1.12: SEM images of diamond indenter imprints in (a) Al_2O_3/Si film and (b)–(e) Al–Cu–O films with various Cu contents formed in the indentation test using indenter load of L = 1 N. The Cu content in at.% is indicated below each image.

As shown in Fig. 5.1.12 a) the Al_2O_3/Si film exhibits very low resistance to cracking compared to Al-Cu-O/Si films with >2 at.%. This low resistance to cracking can however be partially attributed to relatively low hardness of the Al_2O_3/Si film prepared at given deposition conditions. The value of H=7.3 GPa is closer to typical hardness of amorphous Al_2O_3 films (see Tab. 5.2). For that reason the indentation test was also performed with a nanocrystalline Al_2O_3/Si film prepared at the same deposition conditions but with higher flow rates of Ar and O_2. As mentioned before the increase of flow rates leads to improvement of the hardness of the nanocrystalline Al_2O_3/Si film to H=12.9 GPa. Comparison of the results of the indentation test on nanocrystalline Al_2O_3/Si film with low hardness, nanocrystalline Al_2O_3/Si film with high hardness and nanocrystalline Al-Cu-O film with 9.7 at.% of Cu is provided in Fig. 5.1.13. In order to make a proper comparison to the Al-Cu-O/Si film and to eliminate the effect of different thickness, the indentation of nanocrystalline Al_2O_3/Si film with high hardness was conducted in three indentation regimes: (1) constant load of 1 N, (2) constant ratio of indentation depth to film thickness ($d/h \approx$const.), (3) constant distance from the film-substrate interface (h-$d \approx$const.). From Fig. 5.1.13 a) it is clear that the nanocrystalline Al_2O_3/Si film with low hardness exhibits the lowest resistance to cracking. The resistance to cracking is improved for nanocrystalline Al_2O_3/Si film with high hardness. However the radial cracks can still be seen in all three indentation regimes (Fig. 5.1.13 b)-d)). In the case of the nanocrystalline Al-Cu-O/Si film with 9.7 at.% of Cu, H=18.5 GPa, W_e=75 %, H/E^*=0.129 and σ=-2.2.GPa no cracks are observed indicating a high resistance to cracking.

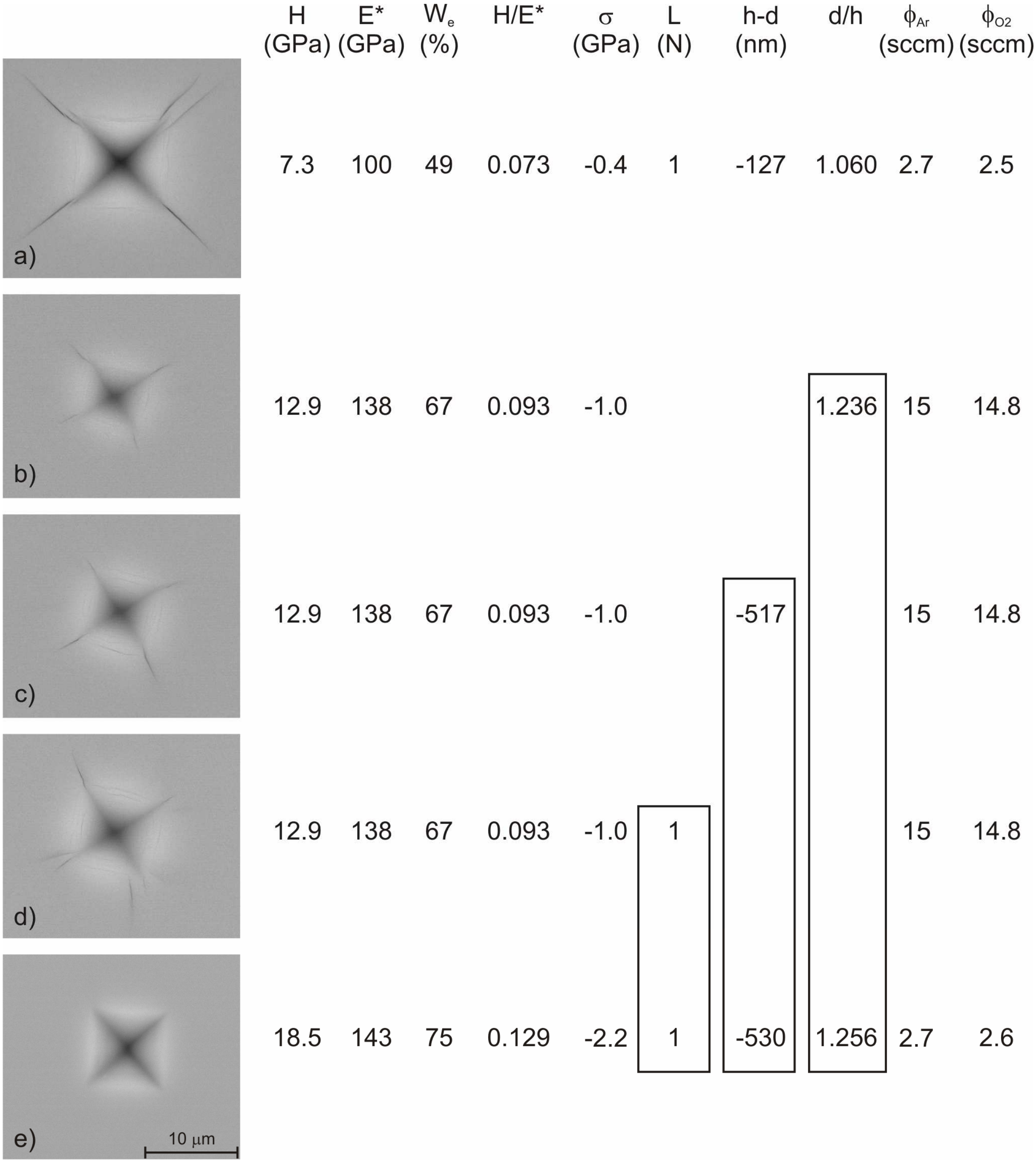

Fig. 5.1.13: Comparison of SEM images of diamond indenter imprints in a) nc-γ-Al_2O_3/ a-Al_2O_3 deposited at low flow rates, b)-d) nc-γ-Al_2O_3/a-Al_2O_3 deposited at high flow rates and e) nc-(Al-Cu-O)/a-(Al-Cu-O) film with 9.7 at.% of Cu. Deposition conditions: p_T=0.5 Pa, p_{O2}=0.2 Pa, T_s=500 °C, f_r=25 kHz, W_d=60 W.cm^{-2}.

It has already been shown that one of the key parameters affecting the formation of cracks is the macrostress σ generated in the film during its growth [77]. Fig. 5.1.14 illustrates this effect for two Al-Cu-O/Si films with a similar Cu content but a different value of compressive macrostress. The macrostress was controlled by the total pressure p_T of the sputtering gas mixture. As expected, the film sputtered at a lower value of p_T exhibits a higher value of σ. It can be seen from Fig. 5.1.14 that the Al-Cu-O/Si nanocomposite film with a higher compressive stress (σ=-2.2 GPa) exhibits no cracks. On the contrary, the nanocomposite

Al-Cu-O/Si film with almost the same content of Cu and a lower macrostress (σ=-1.5 GPa) exhibit clear radial cracks. This observation confirms that a higher compressive macrostress increases the film‘s resistance to cracking. There are at least two mechanisms that contribute to an enhanced resistance to cracking in the case of compressively stressed films. Firstly when a film exhibiting compressive stress is put under tension a certain elongation is first necessary to compensate for the compressive stress to achieve a stress-free state [69]. Secondly once the crack is formed in the film the compressive stress helps to close the crack after unloading the diamond indenter. Tab. 5.3 summarizes the mechanical properties of the two Al-Cu-O/Si films with different values of macrostress. It can be seen that both films exhibit almost the same values of W_e and H^3/E^{*2} (resistance to plastic deformation) but very different values of E^* and H/E^*. Also note that the hardness of the film prone to formation of cracks is significantly higher (19.4 GPa). Comparison of these data indicates that high hardness alone is not a sufficient condition to ensure high resistance to cracking. Similarly not even identical values of W_e and H^3/E^{*2} ensure similar resistance to cracking. Instead a high value of H/E^* ratio and a low effective Young’s modulus could be the key parameters deciding about the film’s resistance to cracking.

Tab.5.3: Characteristics of two Al–Cu–O/Si films with similar Cu content but different compressive macrostress. Films 7 and 10 in Tab. 5.3 correspond to imprints a) and b) in Fig. 5.1.14.

film no.	p_T (Pa)	Cu (at.%)	a_D (nm/min)	h (nm)	σ (GPa)	H (GPa)	E* (GPa)	W_e (%)	H/E*	H^3/E^{*2} (GPa)
7	0.5	6.2	6.73	2020	-2.2	16.7	135	71	0.124	0.256
10	1.5	6.5	6.61	1850	-1.5	19.4	170	70	0.114	0.253

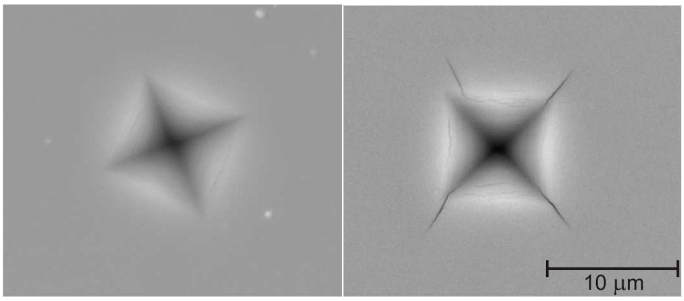

σ=-2.2 GPa **σ=-1.5 GPa**

a) **b)**

Fig. 5.1.14: SEM images of diamond indenter imprints in Al–Cu–O/Si films with similar Cu contents but different magnitude of compressive macrostress. (a) σ=−2.2 GPa, *Cu*=6.2 at.% GPa (b) σ=−1.5 GPa, *Cu*=6.5 at.%. The indenter load of *L*= 1 N was used to generate the imprints.

In summary, the resistance to cracking of Al-Cu-O/Si films with various Cu contents was compared to Al_2O_3/Si films with various structures and mechanical properties. It was found, that the addition of Cu into nanocomposite nc-γ-Al_2O_3/a-Al_2O_3 films results in a significant improvement of their resistance to cracking in the indentation test. The Al-Cu-O films with an enhanced resistance to cracking are characterized by Cu content >2 at.%, W_e>60 %, H/E^*>0.1 and compressive stress $\sigma \approx$-2 GPa.

5.1.5 Optical properties of Al-Cu-O films

The transmittance *T*, index of refraction *n* and extinction coefficient *k* of the Al–Cu–O films with various Cu contents deposited on a Si substrate were measured using spectroscopic ellipsometry. The transmittance spectra of the films are displayed in Fig. 5.1.15. As can be seen the pure Al_2O_3 film and Al-Cu-O films with low Cu contents (<2 at.%) exhibit high transparency in the visible spectrum, which is consistent with high value of the optical band gap (E_g>6 eV) of Al_2O_3 [279]. The transmittance of the Al–Cu–O films gradually decreases with an increasing Cu content and the film with 16 at.% of Cu is completely non-transparent in the visible spectrum.

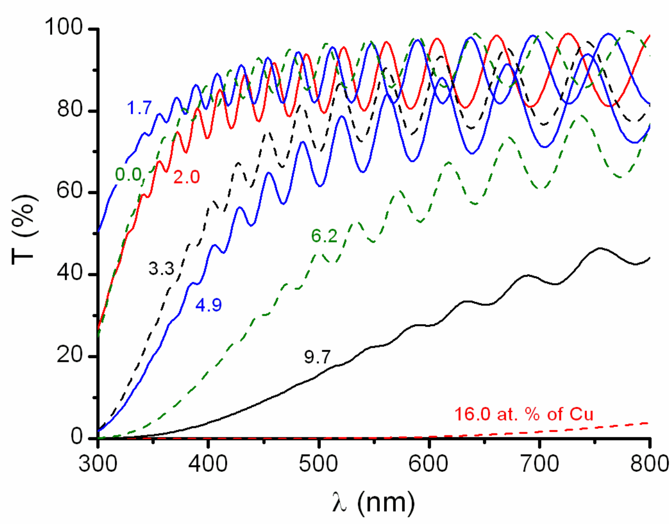

Fig. 5.1.15: Transmittance *T* of Al_2O_3/Si film and Al–Cu–O/Si films with various Cu contents as a function of the photon wavelength λ.

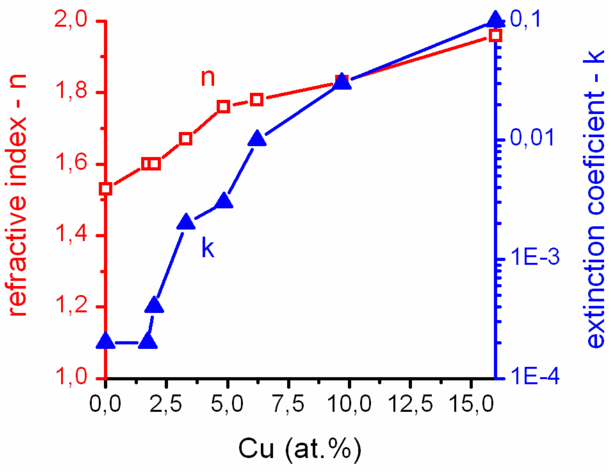

Fig. 5.1.16: Index of refraction *n* and extinction coefficient *k* of Al–Cu–O films as a function of the Cu content. The presented values correspond to a photon wavelength of λ=550 nm.

The evolution of the index of refraction and the extinction coefficient with increasing Cu content is displayed in Fig. 5.1.16. Both quantities clearly increase with increasing Cu content. The index of refraction of n=1.53 observed for Al_2O_3 film corresponds well to the value of n=1.525 reported by Vitanov [279]. The value of n=1.96 measured for the film with

16 at.% of Cu is somewhat higher compared to n≈1.70 corresponding to $CuAl_2O_4$ film as determined by Leu et Al. [215]. This can probably be attributed to the difference in the film crystallinity since Leu et al. reported on the optical properties of highly crystalline epitaxially grown $CuAl_2O_4$ phase whereas films presented in this study are nanocrystalline with a possible admixture of an amorphous phase.

5.2 Antibacterial Cr-Cu-O films

Antibacterial films represent one of the most intensely studied fields in surface engineering. Such films are intended to reduce the spread of infections and drug-resistant bacteria in hospital environments as well as in public settings. Moreover, these films can be used for modification of the surface of biomedical implants in order to reduce the risk of inflammatory processes. Recently Chiu et al. prepared an antibacterial delafossite $CuCrO_2$ film by means of RF magnetron sputtering followed by two-step post-deposition annealing [138]. For achieving the antibacterial effect no artificial UV irradiation was necessary. This represents a significant advantage compared e.g. to the UV radiation-induced antibacterial action of TiO_2–based films [126, 135, 280]. The two-step annealing procedure proposed by Chiu et al. for obtaining the crystalline $CuCrO_2$ phase however represents additional costs in the potential production of the antibacterial film. Moreover the high annealing temperature (≈700 °C) limits application of such antibacterial film to some heat sensitive substrates.

The main aim of the following study is to investigate whether also the as-deposited Cr–Cu–O films can exhibit antibacterial activity against *E. coli* bacteria. Special attention is paid to determining the minimum Cu content in the film and the minimum contact time which ensure 100% killing of the *E. coli* bacteria. The antibacterial efficiency of the as-deposited films is compared to the antibacterial efficiency of crystalline Cr–Cu–O films with various phase compositions obtained by rapid thermal annealing process. Mechanical properties of the as-deposited and annealed Cr–Cu–O films are also investigated.

5.2.1 Deposition conditions

Contrary to the Al-Cu-O films with various Cu contents depositions of the Cr-Cu-O films were performed with identical composed Cr/Cu targets mounted on both magnetrons (see Fig. 4.1.6). In order to produce stoichiometric films, the working point needs to be properly selected to supply a sufficient amount of oxygen into the growing film. For that reason the discharge characteristics were studied as a function of oxygen partial pressure p_{O2} with other deposition parameters fixed (p_T=1.50 Pa, p_{Ar}=1.50-p_{O2}, P_d=0.6 kW, f_r=20 kHz, τ/T=0.5). The measured current waveforms of both magnetrons are displayed in Fig. 5.2.1. For p_{O2}<0.08 Pa the discharge in front of both magnetrons exhibited metallic color (bright torquoise in this case) and the ion and electron currents on a single magnetron were approximately the same (see p_{O2}=0.08 Pa in Fig. 5.2.1). For $p_{O2}\geq$0.16 Pa the discharge in front of one magnetron changed color to light pink indicating target poisoning, while the discharge in front of the opposite magnetron retained the original metallic bright turquoise appearance. The change of discharge color to light pink is accompanied by a significant decrease of ion current on the corresponding magnetron. With increasing p_{O2} the color of the opposite “metallic discharge” gradually turns to light pink as well and the asymmetry of the ion and electron currents becomes smaller. The author of this thesis suggests the following explanation of this phenomenon. Let’s assume that the coefficient of secondary electron emission of oxidized Cr target is smaller compared to metallic Cr target (will be confirmed later). As one of the targets becomes slightly more oxidized the electron emission decreases resulting in a reduced concentration of ions in front of this target. Due to lower ion bombardment this target is less intensely cleaned from the surface oxide layer and the oxidization is further enhanced. Forced to keep the average discharge power constant the power supply increases the voltage, which however leads to enhanced cleaning of the metallic target but is not sufficient to clean the already oxidized target. This way the individual targets of the dual magnetron are unevenly poisoned resulting in a strongly asymmetric distribution particles in the plasma.

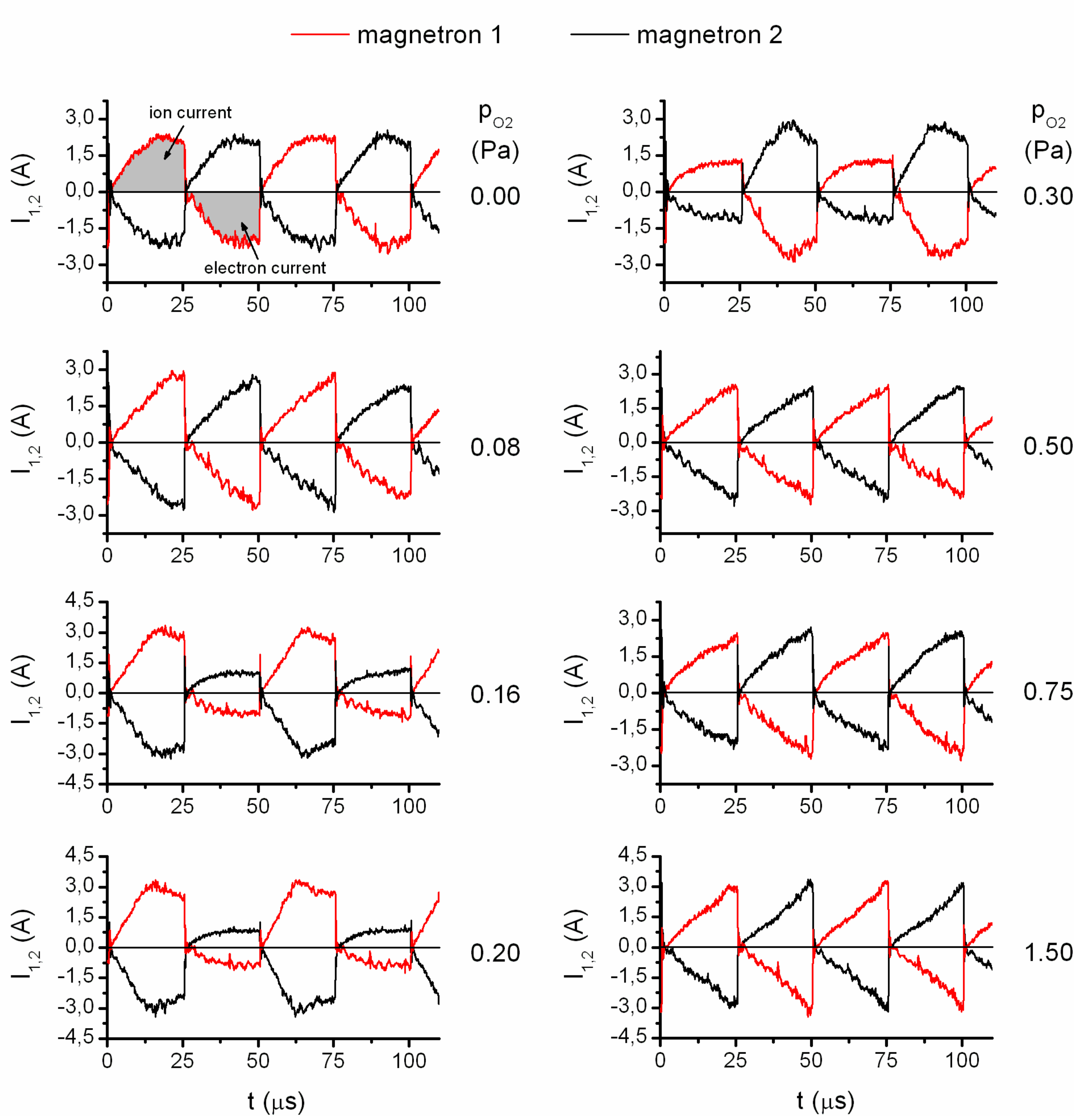

Fig. 5.2.1: Current waveforms on magnetron 1(red) and magnetron 2 (black) for various oxygen partial pressures p_{O2}. Deposition conditions: p_T=1.50 Pa, p_{Ar}=1.50-p_{O2}, P_d=0.6 kW average target power in negative pulse, f_r=20 kHz, τ/T=0.5.

As the value of p_{O2} increases further, even the surface of the target with metallic surface gradually oxidizes. For $p_{O2} \geq 0.5$ Pa both targets are oxidized and the ion and electron currents on each magnetron become symmetric again. The assumption of lower coefficient of secondary electron emission of oxidized Cr target is supported in Fig. 5.2.2, which shows a hysteresis behavior of the total pressure and discharge current for sputtering of pure Cr targets at constant discharge voltage.

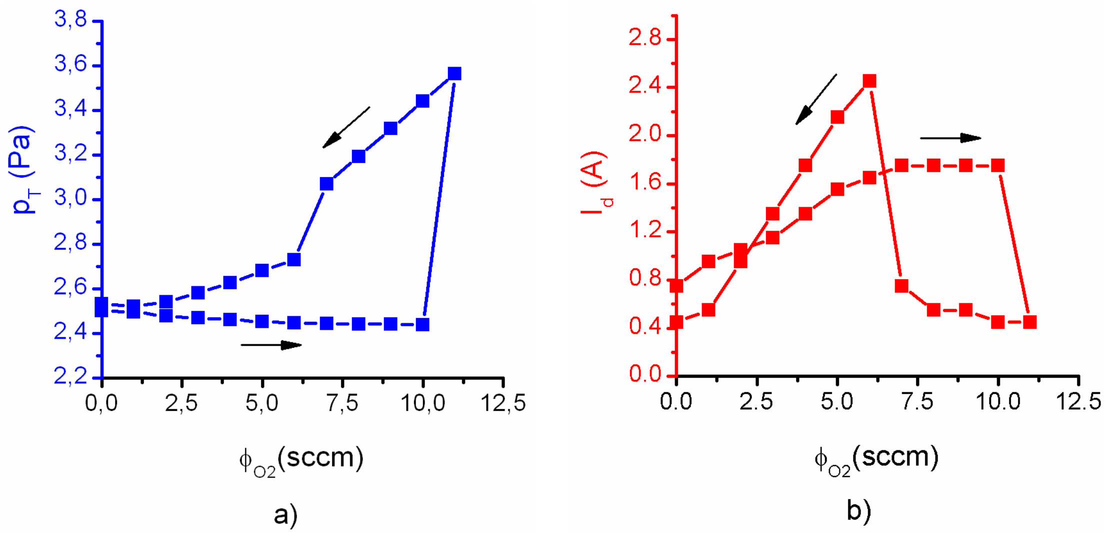

Fig. 5.2.2: a) total pressure p_T and b) discharge current I_d as a function of O_2 flow ϕ_{O2} for a dual magnetron with 2 identical Cr targets at p_{Ar}=2.5 Pa and U_d=const.=430 V. The arrows indicate increase and decrease of oxygen flow. Here the ϕ_{O2} value was set manually and no PID feedback control was employed.

As can be seen from Fig 5.2.2 a) the total pressure rapidly increases for ϕ_{O2}>10 sccm which indicates target poisoning. At this point a clear decrease of discharge current can be seen from Fig. 5.2.2 b). This observation supports the assumption that the coefficient of secondary electron emission of the poisoned Cr target is lower compared to the coefficient of secondary electron emission of the metallic Cr target and is responsible for the uneven poisoning of the individual targets. This hypothesis is also supported by the fact that no such uneven poisoning was observed during depositions of Al_2O_3 films using aluminum targets where the discharge current increases after target poisoning i.e. secondary electron emission of oxidized target is higher compared to metallic target (contrary to chromium). Similar behavior of a dual magnetron system in reactive sputtering has been reported by Kadlec et al. [281].

In the following study two series of Cr-Cu-O films were prepared. In order to ensure deposition of stoichiometric Cr-Cu-O films in the oxide mode of sputtering the O_2 partial pressure was set to a relatively high value of 0.5 Pa. All films were deposited with the substrates held on a floating potential in the distance of 110 mm from the magnetrons ($d_{s\text{-}t}$=110 mm). In the case of series 1 the effect of Cu content on the properties of as-deposited films was investigated and the following deposition conditions were used:

total pressure	p_T=1.5 Pa
O_2 partial pressure	p_{O2}=0.5 Pa
flow rate of Ar	ϕ_{Ar}=9.7 sccm
substrate temperature	T_s=500 °C
repetition frequency	f_r=20 kHz
duty cycle	δ=0.5=50% (*identical on both magnetrons*)
average target power in pulse	P_d=0.6 kW
inner diameter of the Cu ring	$\varnothing_{in}$=28÷34 mm (*variable parameter*)

In order to investigate the effect of phase composition of the Cr-Cu-O/Si films on their antibacterial and mechanical properties several films were prepared at identical deposition conditions. These films were subsequently annealed to various annealing temperatures using the rapid thermal processor described in section 4.3.9. In the following text these films are denoted as series 2 or "annealed to various temperatures".

total pressure	p_T=2.0 Pa
O_2 partial pressure	p_{O2}=0.5 Pa
flow rate of Ar	ϕ_{Ar}=14.8 sccm
inner diameter of the Cu ring	$Ø_{in}$=31 mm

The content of both Cr and Cu in the annealed films was approximately ≈20 at.% yielding the Cr/Cu ratio ≈1. This ratio was intentionally selected to obtain stoichiometric delafossite $CuCrO_2$ structure in order to make the comparison to the results of Chiu et al. possible [138]. Based on our previous experiments this ratio is obtained if the inner diameter of the Cu rings is set to $Ø_{in}$=31 mm and the total pressure is increased to p_T=2.0 Pa i.e. p_{Ar}=1.5 Pa.

5.2.2 Elemental composition

The elemental composition of the Cr-Cu-O films was controlled by the inner diameter $Ø_{in}$ of the Cu rings used for fixing the Cr targets (see Fig. 5.2.3). As can be seen the Cu content in the Cr-Cu-O films gradually decreases from 28.5 at.% down to 10.0 at.% with an increasing $Ø_{in}$ from 28 mm to 34 mm, respectively. This can be simply explained by the fact that for a higher $Ø_{in}$, a smaller portion of the Cu fixing ring reaches the erosion area and less Cu is sputtered.

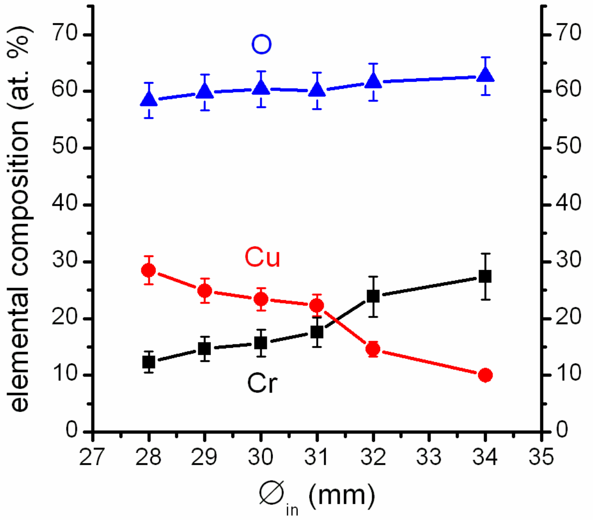

Fig. 5.2.3: Elemental composition of Cr-Cu-O/Si films as a function of the inner diameter $Ø_{in}$ of the Cu rings.

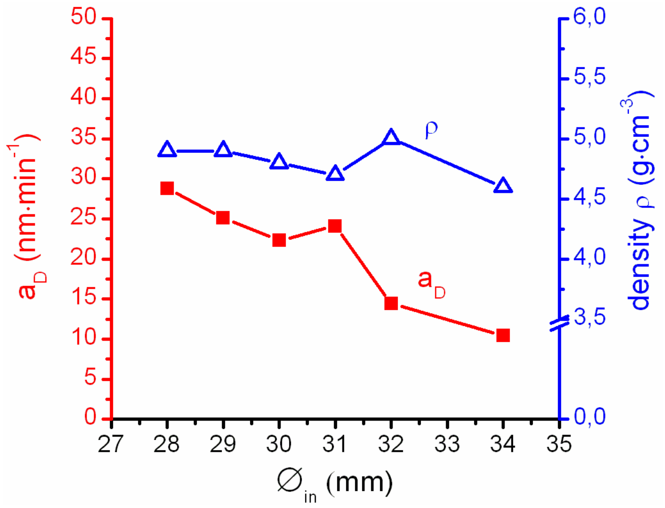

Fig. 5.2.4: Deposition rate a_D and density ρ of Cr-Cu-O/Si films as functions of the inner diameter $Ø_{in}$ of the Cu rings.

The evolution of the film density and deposition rate as functions of $Ø_{in}$ is displayed in Fig. 5.2.4. While there is no significant difference in the film density, with increasing $Ø_{in}$ the deposition rate of the films clearly decreases from 28.8 nm/min down to 10.4 nm/min. Similarly to the case of Al-Cu-O films this can be related to a higher Ar ion sputtering yield of CuO (γ_{CuO}=0.802) compared to Cr_2O_3 (γ_{Cr2O3}=0.675) [274]. The sputtering yield of metallic Cu (γ_{Cu}=1.751) is also higher compared to metallic Cr (γ_{Cr}=1.131) [275].

5.2.3 Structure and phase composition

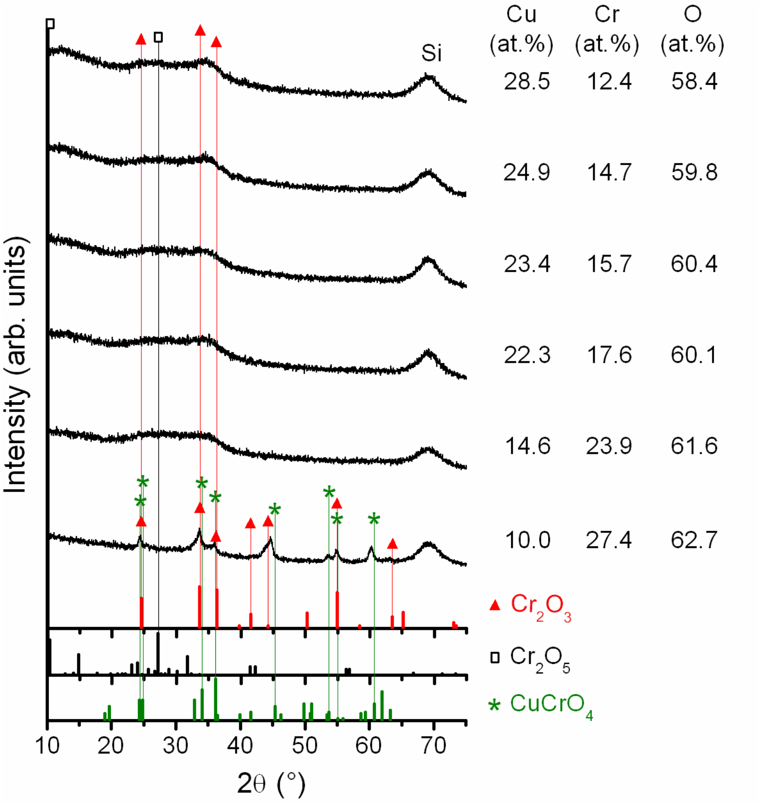

Fig. 5.2.5: XRD patterns and elemental composition of Cr-Cu-O/Si films with various Cu contents (series 1). “Si“ indicates reflection from the silicon substrate.

The effect of Cu content on the structure of the Cr-Cu-O films was investigated by XRD analysis (see Fig. 5.2.5). From this figure it is seen that the Cr–Cu–O films with ≥15 at.% Cu are characterized by a very broad diffraction peak between $2\theta \approx 20° \div 40°$ indicating that the films are X-ray amorphous. The formation of amorphous Cr-Cu-O films at the substrate temperature of 500 °C is consistent with the observation of Yu et. al [282]. They found that amorphous Cr-Cu-O films with Cr/Cu ratio ≈1 prepared by reactive magnetron sputtering require annealing to 550 °C to exhibit presence of crystalline CuO and $CuCr_2O_4$ phases. For Cu content of 10.0 at.% reflections of Cr_2O_3 and $CuCrO_4$ are observed in the XRD pattern indicating that the film is composed of a mixture of Cr_2O_3 and $CuCrO_4$ oxide phases. This correlates well with reports of Luo et al. and Contoux et al. who showed that crystalline Cr_2O_3 films can be prepared by reactive magnetron sputtering at substrate temperatures as low as 200 °C [283, 284].

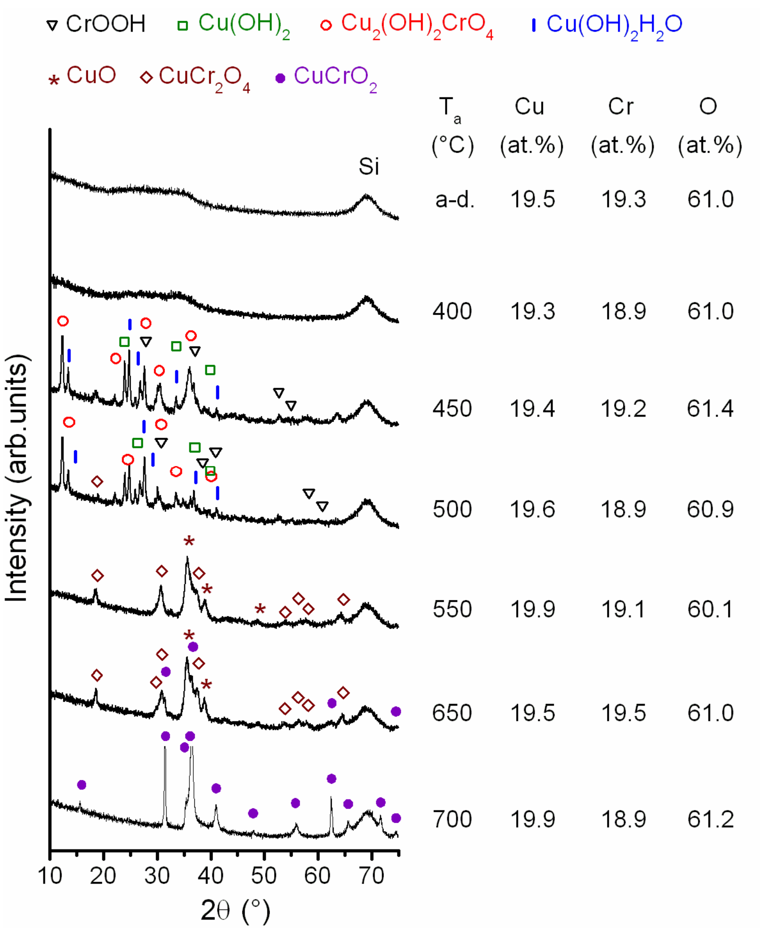

T_a (°C)	Cu (at.%)	Cr (at.%)	O (at.%)
a-d.	19.5	19.3	61.0
400	19.3	18.9	61.0
450	19.4	19.2	61.4
500	19.6	18.9	60.9
550	19.9	19.1	60.1
650	19.5	19.5	61.0
700	19.9	18.9	61.2

Fig. 5.2.6: XRD patterns and elemental composition of Cr-Cu-O/Si films with ≈20 at. % of Cu and Cr/Cu ratio ≈1 annealed to various maximum temperatures T_a (series 2). “Si“ indicates reflection from the silicon substrate.“a.-d.“ indicates as-deposited film. The presented elemental compositions were measured before the annealing procedure.

Fig. 5.2.6 shows the elemental composition and XRD patterns of Cr-Cu-O/Si films annealed up to 700 °C. Note that the reproducibility of the elemental composition of all films (measured before annealing) is very good giving ≈20 at.% of Cu and Cr/Cu ratio ≈1. It can be seen that the rapid thermal annealing up to T_a= 400 °C does not change the film structure and the film remains X-ray amorphous. This can be explained by a relatively high substrate temperature used for deposition of the films (T_s=500 °C). The X-ray amorphous film is converted to a well crystalline one for $T_a \geq 450$ °C. The crystalline structure of the films annealed to 450 °C and 500 °C was identified as a mixture of $Cu(OH)_2$, CrOOH, $Cu_2(OH)_2CrO_4$ and $Cu(OH)_2H_2O$ phases. Formation of these hydrogen-containing compounds can be explained by reaction of residual hydrogen or water vapor with Cr, Cu and O. As shown by Šícha et al. the presence of oxygen in the deposition chamber during reactive sputtering process leads to an increase in concentration of impurities in the total ion flux on the substrate, particularly H_2O^+ [28]. The films annealed to T_a ranging from 550 °C to 650 °C are multi-phase films composed of a mixture of CuO and tetragonal t-$CuCr_2O_4$ crystalline oxide phases with a small admixture of the delafossite $CuCrO_2$ phase at T_a=*650°C*. The reflections of CuO and t-$CuCr_2O_4$ phases completely disappear at T_a=*700 °C* when a single-phase Cr–Cu–O film with the delafossite $CuCrO_2$ structure is formed. The formation of a pure delafossite $CuCrO_2$ phase without any trace amount of other phases is consistent with the almost stoichiometric ratio of Cr/Cu≈1.

5.2.4 Antibacterial properties of Cr-Cu-O films

The antibacterial efficiency *E* was determined for both the as-deposited (series 1) as well as for the annealed (series 2) Cr–Cu–O/Si films. The antibacterial tests were performed with four different contact times in the daylight (*t*=0.5 h, 1 h, 3 h and 5 h). In order to find out if the irradiation by daylight has any effect on the antibacterial activity of the films, the antibacterial test was also performed in the dark with *t*=5 h.

Effect of Cu concentration

The antibacterial efficiency *E* of Cr-Cu-O films with various Cu contents as a function of contact time *t* in the daylight and for *t*=5 h in the dark is displayed in Fig. 5.2.7. As can be seen the antibacterial efficiency increases with increasing *t*. This is a general trend commonly observed for antibacterial films [132, 138].

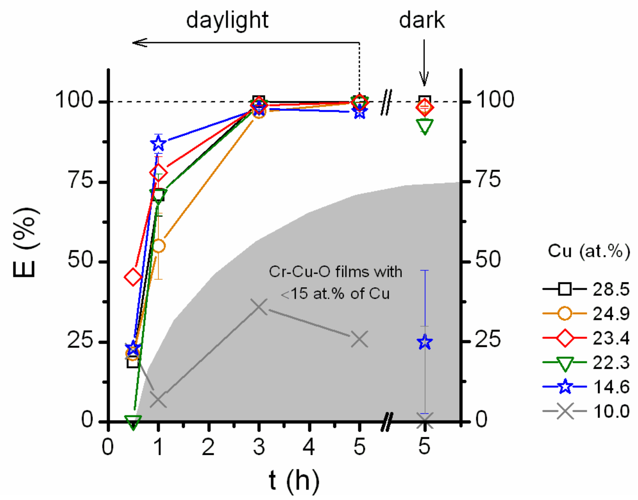

Fig. 5.2.7: Antibacterial efficiency *E* of Cr-Cu-O films with various Cu contents as a function of contact time *t*. For a better lucidity of the figure the large error bars (typically 10÷30 %) for *E*< 50 % were omitted from the graph.

Moreover the antibacterial efficiency is strongly dependent on the Cu content in the film. While the Cr–Cu–O/Si films with <15 at.% Cu exhibit low antibacterial efficiency, films with ≥15 at.% of Cu efficiently kill bacteria both in the daylight and in the dark. Since the antibacterial effect is observed in the dark, we can conclude that the killing of *E. coli* bacteria on the surface of the Cr–Cu–O/Si films is due to the antibacterial action of copper. Comparison of the results for *t*=5 h in the daylight and in the dark shows that there is a certain decrease of *E* if no daylight is present. This might indicate some contribution of photocatalytical effect on the antibacterial efficiency of the films. A more detailed study would however be useful to confirm this hypothesis. Photos of Petri dishes illustrating the results of the antibacterial test performed in the dark are shown in Fig. 5.2.8. There is a clear increase in the antibacterial efficiency with an increasing Cu content in the film. This behavior is consistent with studies by other authors reporting on antibacterial properties of Cu-containing films [147, 150].

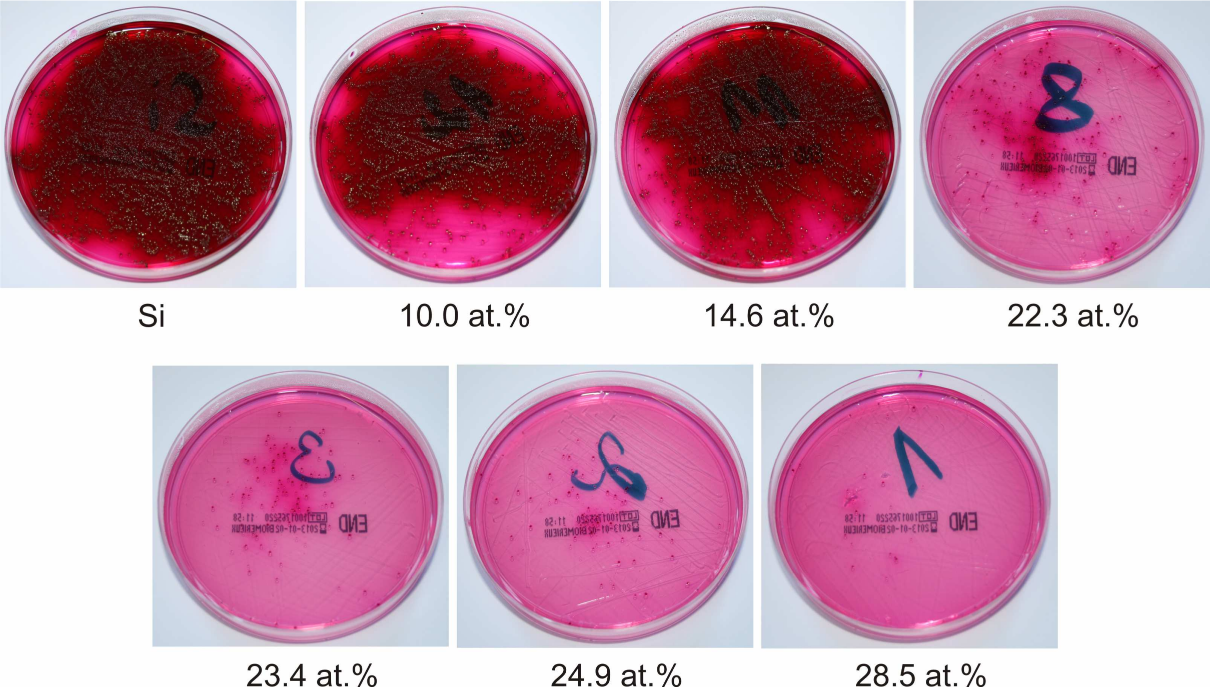

Fig. 5.2.8: Photos of Petri dishes with Endo agar and bacteria cultivated from bacterial suspension which was in contact with Cr–Cu–O/Si film with various Cu contents and Si substrate in the dark for *t*=5 h.

Effect of phase composition

In order to investigate the effect of phase composition of the Cr-Cu-O/Si films on their antibacterial properties, films annealed to various temperatures (see Fig. 5.2.6) were also subjected to the antibacterial test. The antibacterial efficiency of Cr-Cu-O/Si films with various phase compositions as a function of contact time is shown in Fig. 5.2.9. As can be seen from this figure the antibacterial efficiency of the Cr-Cu-O/Si films depends on their phase composition. Clearly the as-deposited amorphous film and the crystalline film with delafossite $CuCrO_2$ structure exhibit the highest *E*. These films are able to eliminate 100 % of the bacteria within 3 h in the daylight and the same efficiency is observed for 5 h in the dark. On the other hand the lowest antibacterial efficiency was found for the crystalline films annealed to 550 °C and 650 °C which predominantly consist of CuO and t-$CuCr_2O_4$ phases. An intermediate antibacterial efficiency was observed for amorphous films annealed to 400 °C or for the films annealed to 500°C consisting of a mixture of different hydroxides of Cu and Cr. The statements above are supported by Fig. 5.2.10 showing the Petri dishes after performing the antibacterial test with a contact time of 5 h in the dark.

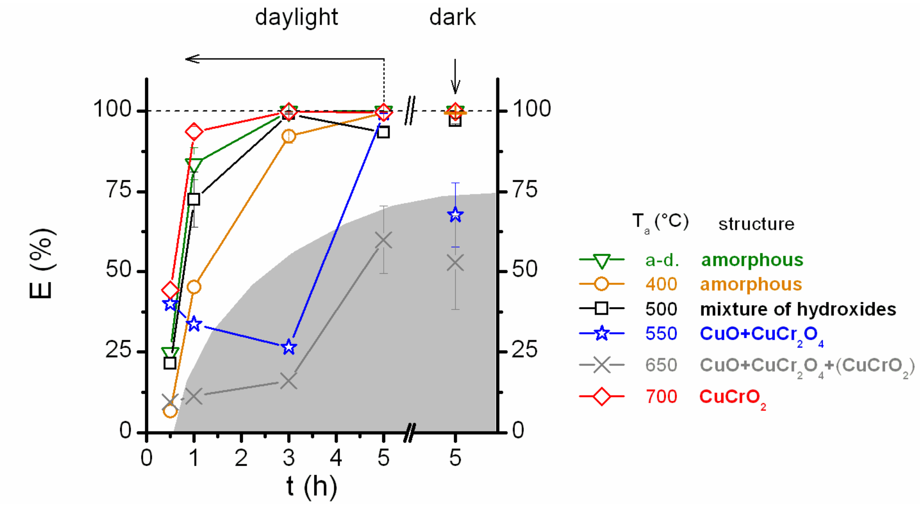

Fig. 5.2.9: Antibacterial efficiency *E* of Cr-Cu-O film with ≈20 at. % of Cu annealed to various temperatures T_a as a function of contact time of the bacterial suspension with the film. For a better lucidity of the figure the large error bars (typically 10÷30 %) for $E < 50$ % were omitted from the graph.

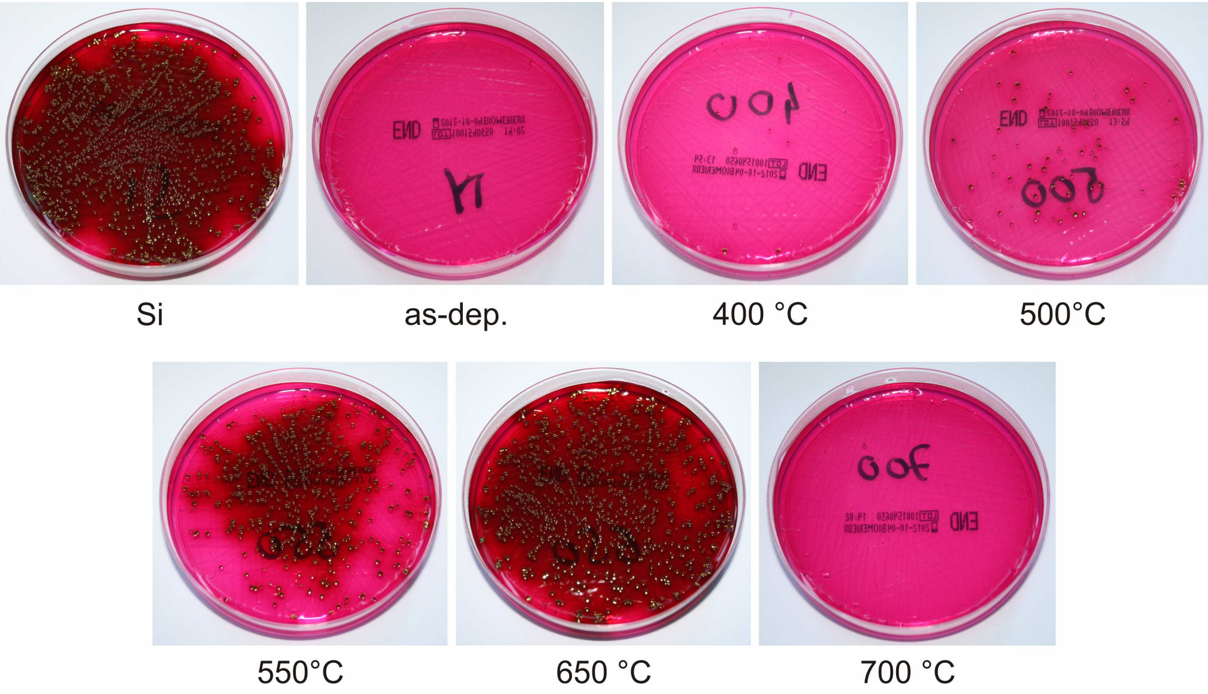
Si
as-dep.
400 °C
500°C
550°C
650 °C
700 °C

Fig. 5.2.10: Photos of Petri dishes corresponding to Cr-Cu-O films with Cr/Cu ratio ≈1 annealed to various temperatures after performing an antibacterial test in the dark for a contact time of 5 hours. The annealing temperature of the Cr-Cu-O film is indicated below the photo. „Si“ and „as-dep.“ indicate results corresponding to Si substrate and as-deposited Cr-Cu-O film, respectively.

The reason for this specific dependency of antibacterial efficiency on the phase composition of the films is not clear. However the highest *E* was observed for $CuCrO_2$ having Cu^+ oxidation state while the lowest *E* was observed for CuO and t-$CuCr_2O_4$ phases with Cu^{2+} oxidation state. This might indicate that the antibacterial action is predominantly caused by generation of free radicals produced in reaction of Cu^+ with H_2O_2 as indicated by Eq. 2.25.

In summary it can be concluded that the antibacterial efficiency of the killing of the *E. coli* bacteria strongly depends not only on the content of Cu in the Cr–Cu–O film but also on its structure and phase composition.

Morphology of bacterial cells after exposure to Cr-Cu-O film

The morphology of the *E. coli* bacteria after performing the antibacterial test was studied by atomic force microscope (AFM). Fig. 5.2.10 a) shows *E. coli* bacteria extracted from a Petri dish corresponding to the reference Si substrate. It can be seen that the surface of the bacterial cell is compact and smooth showing no signs of damage or disintegration. On the other hand the bacteria exposed to the Cr-Cu-O/Si film with 28.5 at.% of Cu exhibit a severely disintegrated cell wall which inevitable leads to bacterial death (Fig. 5.2.11 b)). However as shown in Fig. 5.2.11 c) not all bacteria extracted from the Petri dish corresponding to the highly antibacterial Cr-Cu-O/Si film showed clearly disintegrated cell wall. This suggests that the mechanism of toxicity of the Cr-Cu-O/Si films to *E. coli* bacteria is probably a combination of cell wall damage combined with alterations in physical and functional properties of the cell membrane causing decrease of cell viability.

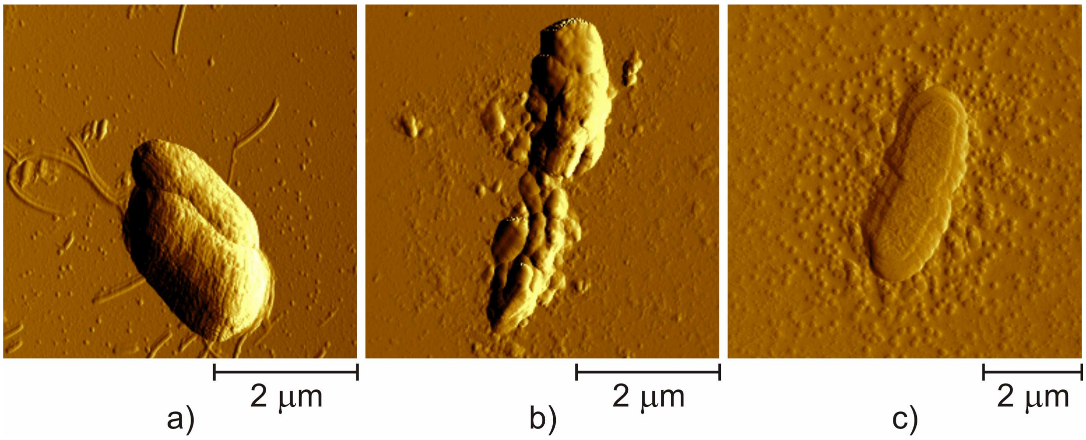

Fig. 5.2.11: AFM images of *E. coli* bacteria after performing the antibacterial test. a) Viable *E. coli* bacteria extracted from a Petri dish corresponding to reference Si substrate. b) and c) *E. coli* bacteria extracted from a Petri dish corresponding to as-deposited Cr-Cu-O/Si film containing 28.5 at.% of Cu. The contact time of the bacteria with the Si substrate and the film was 5 hours in the dark.

5.2.5 Mechanical properties of Cr-Cu-O films

Mechanical properties of both series of Cr-Cu-O/Si films (as-deposited and annealed) were measured by instrumented indentation using a Vickers diamond indenter. Prior to measuring the mechanical properties of the individual films the hardness of Cr-Cu-O/Si film with ≈23.4 at.% of Cu was investigated as a function of the indenter load L. According to Fig. 5.2.12, the indentation depth to film thickness ratio is <0.1 for $L \leq 5$ mN and the corresponding hardness is $H(L=5$ mN$)=$ 3.4 GPa. For such loads the standard deviation of the measurement is however relatively high due to surface roughness of the film. For $L=10\div20$ mN the standard deviation is significantly reduced while the measured hardness does not significantly differ although d/h exceeds 0.1 ($H(L=20$ mN$)=$ 3.9 GPa, $d/h=0.16$). In order to reduce the standard deviation and maintain the indenter load the same as in the case of Al-Cu-O/Si and Al-Cu-N/Si films the mechanical properties of Cr-Cu-O/Si films were measured using an indenter load of $L=20$ mN.

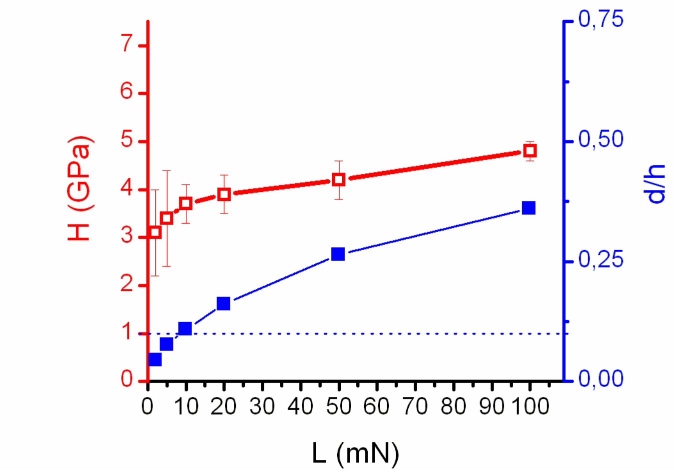

Fig. 5.2.12: Hardness *H* and indentation depth to film thickness ratio *d/h* of Cr-Cu-O/Si film with 23.4 at. % of Cu as a function of the indenter load *L*.

The hardness and effective Young’s modulus of the as-deposited Cr–Cu–O/Si films with various Cu contents are displayed in Fig. 5.2.13. A detailed summary of mechanical properties and other characteristics of the films is provided in Tab. 5.4. From Fig. 5.2.13 it can be seen that sputtered Cr–Cu–O/Si films exhibit a relatively low hardness decreasing from ≈8 GPa to ≈4 GPa with an increasing Cu content. This decrease is however most apparent for Cu content ranging from 10.0 to 22 at.% of Cu. For higher Cu contents the mechanical properties remain roughly constant. A similar trend is also observed for the effective Young’s modulus and the elastic recovery of the films. Compared to the hard Al-Cu-O/Si films the H/E^* and H^3/E^{*2} ratios are very small - less than ≈0.07 and ≈0.03 GPa, respectively - and generally decrease with an increasing Cu content. This evolution of mechanical properties can be correlated with the structure of the films, which is amorphous for high Cu contents ($Cu \geq 15$ at.%) but exhibits presence of crystalline Cr_2O_3 and $CuCrO_4$ phases for the lowest Cu content (Cu=10.0 at.%). The pure Cr_2O_3 films prepared by pulsed reactive sputtering were reported to exhibit hardness of up to 22 GPa [285]. Although the antibacterial amorphous Cr-Cu-O/Si film in the as-deposited state do not exhibit such high hardness, the value of $H \approx 4$ GPa being still higher than common stainless steel can be sufficient for some antibacterial protective surfaces [286].

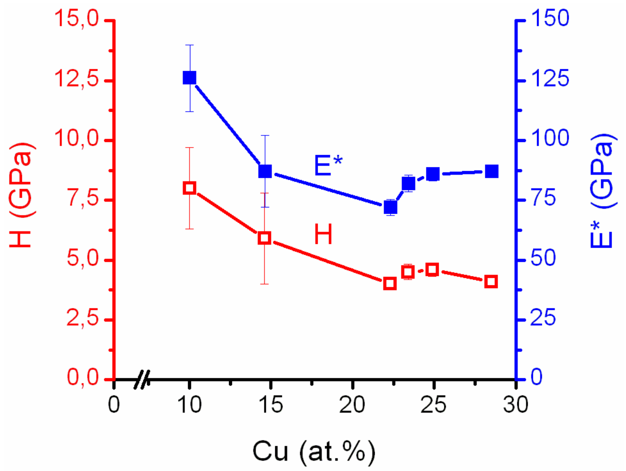

Fig. 5.2.13: Hardness *H* and effective Young´s modulus E^* of Cr-Cu-O/Si films as a function of the Cu content.

Tab. 5.4: Characteristics of as-deposited Cr-Cu-O/Si films with various Cu contents.

Cu (at.%)	a_D (nm/min)	h (nm)	σ (GPa)	H (GPa)	E* (GPa)	W_e (%)	H/E*	H^3/E^{*2} (GPa)
28.5	28.8	2450	0.2	4.1	87	35.5	0.047	0.009
24.9	25.1	2310	0.2	4.6	86	36.2	0.053	0.013
23.4	22.3	2390	0.1	4.5	82	37.2	0.055	0.014
22.3	24.2	2900	0.0	4.0	72	37.0	0.055	0.012
14.6	14.4	3050	0.1	5.9	87	44.7	0.068	0.027
10.0	10.4	2080	0.1	8.0	126	47.9	0.063	0.032

The evolution of hardness and effective Young´s modulus of the Cr-Cu-O/Si films with ≈20 at. % annealed to various temperatures is shown in Fig. 5.2.14. The particular values together with other characteristics of the films are summarized in Tab. 5.5. It was found that the hardness remains approximately constant H=2.5–2.6 GPa up to T_a=500 °C. A further increase of T_a results in a gradual decrease of hardness down to 1.2 GPa for T_a=700 °C. The other mechanical parameters such as the effective Young´s modulus, the elastic recovery and the H/E^* ratio follow basically the same trend as hardness i.e. they do not change significantly up to 500 °C, start to decrease at higher temperatures and reach the minimum value at T_a=700 °C. These observations indicate that the Cr–Cu–O/Si films could operate well up to 500 °C. By comparing the data shown in tables 5.4 and 5.5 it is clear that the hardness of the as-deposited Cr–Cu–O/Si film with ≈20 at.% of Cu prepared at total pressure of p_T=1.5 Pa (H≈4 GPa) is higher than hardness of the film prepared at p_T=2.0 Pa (H≈2.5 GPa). This difference can be attributed to a higher densification of the Cr–Cu–O/Si film prepared at a lower total pressure. This has been experimentally confirmed by measuring the density of the films using the XRF method. The density of the "softer" (H≈2.5 GPa) as-deposited film with 19.5 at.% of Cu prepared at $p_T=2.0$ *Pa* was 4.05 g/cm^3 only. On the other hand the density of the "harder" (H≈4.0 GPa) as-deposited films with 14.6 at.% and 22.5 at.% of Cu prepared at p_T=1.5 Pa was 5.0 and 4.7 g/cm^3, respectively.

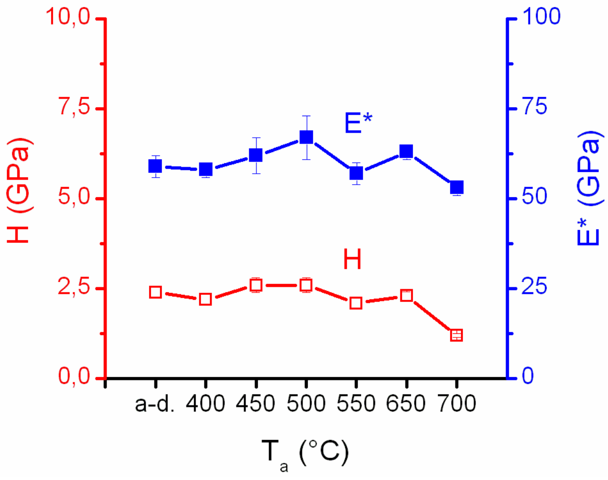

Fig. 5.2.14: Hardness H and effective Young´s modulus E^* of Cr-Cu-O/Si films with ≈20 at. % annealed to various temperatures T_a.

Tab. 5.5: Characteristics of Cr-Cu-O/Si films with ≈20 at. % of Cu annealed to various temperatures T_a and their mechanical properties after annealing.

T_a (℃)	Cu (at.%)	a_D (nm/min)	h (nm)	H (GPa)	E* (GPa)	W_e (%)	H/E*	H^3/E^{*2} (GPa)
as-dep.	19.5	16.0	2110	2.5	62	35.2	0.040	0.004
400	19.3	16.5	2180	2.2	58	35.7	0.038	0.003
450	19.4	16.2	2110	2.6	62	37.2	0.042	0.005
500	19.6	16.1	2120	2.6	61	36.4	0.043	0.005
550	19.9	16.2	2110	2.1	57	30.0	0.037	0.003
650	19.5	17.5	2280	2.3	63	28.9	0.037	0.003
700	19.2	15.1	1840	1.2	53	21.0	0.023	0.001

5.2.6 Transmittance of antibacterial Cr-Cu-O films

For some applications such as touchscreens in various digital appliances (ATMs, smartphones, tablets etc.) the antibacterial film not only needs to exhibit suitable mechanical properties but also needs to be transparent or at least semitransparent. Accordng to the Beer–Lambert law the transparency of thin films can be increased by decreasing the distance the light travels through the material i.e. by decreasing the film thickness. For that reason the effect of film thickness on its optical transparency was investigated for the antibacterial Cr-Cu-O film with ≈20 at. % of Cu deposited on glass substrates. The deposition conditions corresponded to series 1 (see section 5.2.1) and the deposition time was varied from 3 to 32 minutes in order to obtain films with various thicknesses ranging from 70 nm to 1140 nm. The Cu content measured for the 1140 nm and 620 nm thick films was 20.9 at.% and 22.3 at.%, respectively. For lower film thicknesses the Cu content could not be determined by the XRF method. The transmittance spectra of the films are presented in Fig. 5.2.15. It can be seen that the thickest film with *h*=1140 nm is completely opaque in the visible spectrum. As the film thickness decreases the transmittance gradually increases and reaches the maximum value of $T_{\lambda=550nm}$=42.5 % for the thinnest film with *h*=70 nm.

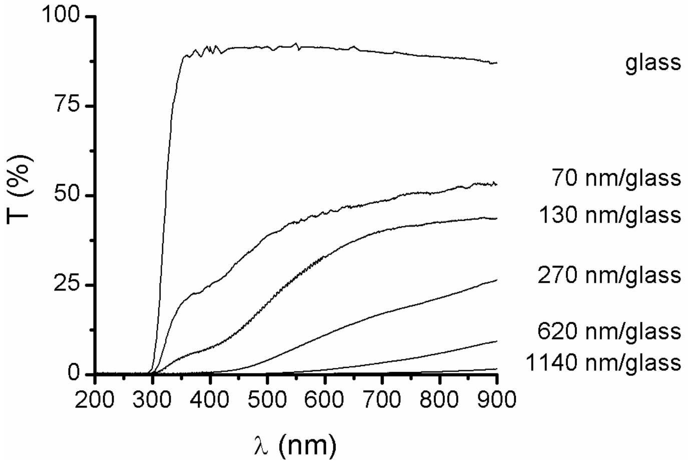

Fig. 5.2.15: Transmittance spectra of Cu-Cr-O films with ≈20 at.% of Cu and various thicknesses deposited on a glass substrate. Transmittance spectrum of uncoated glass substrate is also shown for reference.

The 70 nm thin Cr-Cu-O film on a glass substrate and the glass substrate alone are shown in Figs. 5.2.16 c) and d). In order to verify that even the 70 nm thin semitransparent film exhibits antibacterial properties, an antibacterial test was performed with a contact time of 5 h in the dark (Fig. 5.2.16 a)). As can be seen the bacterial growth is strongly suppressed compared to the reference Si substrate shown in Fig. 5.2.16 b). These results are in a good qualitative agreement with results presented in Fig. 5.2.8.

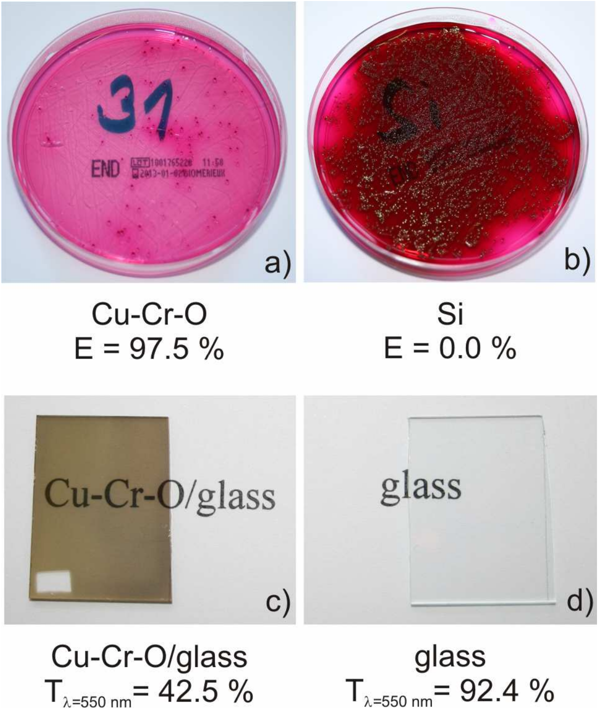

Fig. 5.2.16: Photos of Petri dishes corresponding to a) a 70 nm thick Cr-Cu-O/Si film with ≈20 at.% of Cu and b) a Si substrate after performing the antibacterial test in the dark for a contact time of 5 hours. Photos of c) the 70 nm thick Cr-Cu-O film with ≈20 at. % of Cu deposited on a glass substrate and d) the glass substrate alone. The values of the antibacterial efficiency E and the transmittance $T_{\lambda=550\mathrm{nm}}$ for λ=550 nm are given below the figures. In case of the Cr-Cu-O film on a glasss substrate transmitance of the whole film+glass substrate system is given.

It can be concluded that the antibacterial as-deposited amorphous Cr-Cu-O films with ≈20 at. % of Cu are semitransparent if the thickness of the film is reduced below 270 nm. The transmittance of $T_{\lambda=550\mathrm{nm}}$=42.5 % was achieved for a 70 nm thin film deposited on a glass substrate.

5.3 Hard antibacterial Al-Cu-N films resistant to cracking

Copper-containing nitride films such as TiN-Cu or TaN-Cu represent an interesting group of multifunctional materials. This is because copper alloying leads to formation of a nanocomposite structure with enhanced mechanical properties [107] and simultaneously these films become antibacterial [150, 152, 287]. It has been demonstrated that alloying of AlN with Cu results in formation of a nanocomposite structure with an enhanced hardness and high ratios H/E^* and H^3/E^{*2} [260]. While the latter two might indicate a high resistance to cracking, the presence of Cu in the film could provide the antibacterial effect similarly as in the case of TiN-Cu or TaN-Cu films. However no investigation of antibacterial properties or resistance to cracking of Al-Cu-N films has been conducted so far.

The main aim of this study is to prepare a multifunctional hard antibacterial Al-Cu-N film with an enhanced resistance to cracking. For the design of a multifunctional film exhibiting (1) a high hardness, (2) an enhanced resistance to cracking and (3) antibacterial properties, the following procedure was used. In the first step the effect of the main deposition parameters on the mechanical properties and resistance to cracking of Al-Cu-N films was investigated. The deposition parameters tested were: the nitrogen partial pressure p_{N2}, the target composition, the discharge current I_d, the substrate bias U_s and the total pressure of the gas mixture p_T. In the next step Al-Cu-N films with different structures and Cu contents were selected and their antibacterial properties were tested. Based on the obtained results, an optimized Al-Cu-N film was prepared and its multifunctional nature was verified.

With regard to the relatively high number of process parameters that were investigated in this study the particular deposition conditions are provided in individual sections. For the same reason the number of graphs and tables is kept to minimum and the elemental composition and other characteristics are usually shown together with the XRD patterns of the films. Some of the deposition conditions were however fixed in all the experiments presented. These were: the substrate-to-target distance d_{s-t}=80 mm, the substrate temperature T_s=400 °C and the repetition frequency of the plasma power supply f_r=5 kHz. The pulsed power supply used for biasing the substrates was set to the following values: repetition frequency f_s=20 kHz, duty cycle of the negative pulse δ_{s-}=50 %, duty cycle of the positive pulse δ_{s+}=45 % and bias voltage in the positive pulse U_{s+}=+10 V. The value of the substrate bias $U_s \equiv U_{s-}$ provided in the text below corresponds to the bias voltage in the negative pulse. The Cu content in the film was varied by changing the inner diameter $Ø_{in}$ of the Cu ring. In order to provide a proper comparison to a known reference material a pure AlN film was also prepared using two compact Al targets illustrated in Fig. 4.1.4.

5.3.1 Effect of nitrogen partial pressure

One of the main deposition parameters affecting the structure and properties of thin films in reactive magnetron sputtering is the partial pressure of the reactive gas. The evolution of the deposition rate a_D of the Al-Cu-N/Si films and the discharge voltage U_d with an increasing nitrogen partial pressure p_{N2} is shown in Fig. 5.3.1. Both these quantities sharply decrease from 121.7 nm/min and 361 V down to 44 nm/min and 256 V as p_{N2} increases from 0.06 Pa to 0.25 Pa. These phenomena can be explained by reaction of nitrogen with the target surface (i.e. “target poisoning“) resulting in a decrease of the sputtering yield and increase of secondary electron emission. A further increase of p_{N2} from 0.25 Pa to 0.5 Pa does not lead to a significant change in the discharge voltage and the deposition rate. This indicates that for p_{N2}=0.25 Pa the targets is almost fully poisoned.

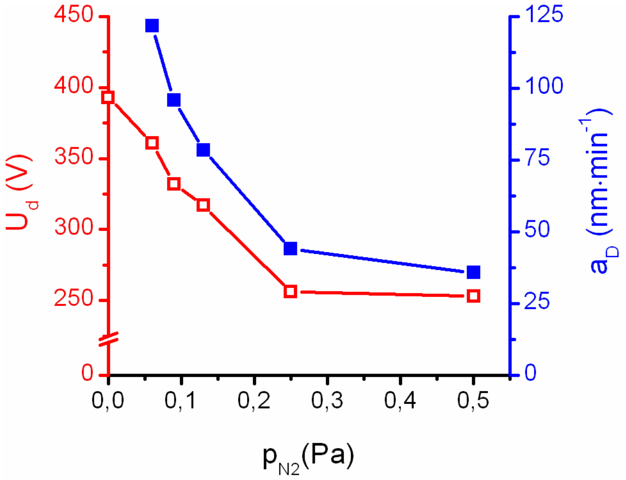

Fig. 5.3.1: Discharge voltage U_d and deposition rate a_d of Al-Cu-N/Si films as a function of nitrogen partial pressure p_{N2}. Deposition conditions I_d=1.00 A, p_T=2.00 Pa, T_s=400 °C, $Ø_{in}$=30 mm.

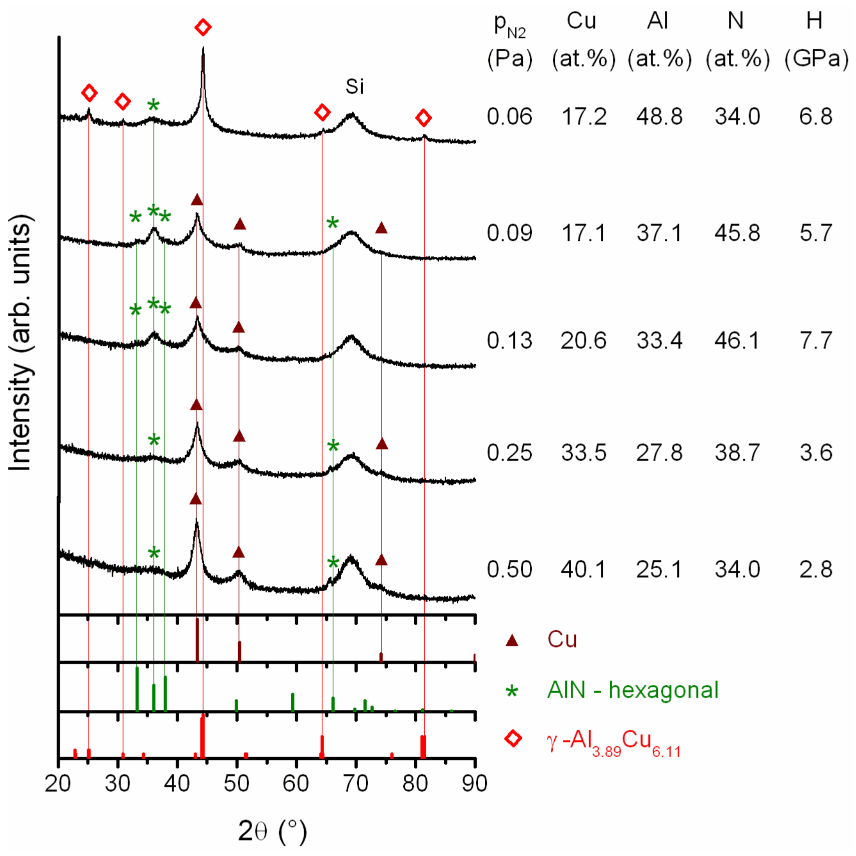

p_{N2} (Pa)	Cu (at.%)	Al (at.%)	N (at.%)	H (GPa)
0.06	17.2	48.8	34.0	6.8
0.09	17.1	37.1	45.8	5.7
0.13	20.6	33.4	46.1	7.7
0.25	33.5	27.8	38.7	3.6
0.50	40.1	25.1	34.0	2.8

Fig. 5.3.2: XRD patterns, elemental composition and hardness of Al-Cu-N/Si films deposited at various p_{N2}. Deposition conditions: p_T=2.00 Pa, $Ø_{in}$=30 mm, T_s=400 °C and I_d=1.00 A. “Si” indicates reflection of the Si(100) substrate.

XRD patterns, elemental composition and hardness of Al-Cu-N/Si films prepared at various p_{N2} are summarized in Fig. 5.3.2. It can be seen that for p_{N2}=0.06 Pa the film is characterized by a broad low intensity reflection of the hexagonal wurzite AlN and relatively sharp peaks corresponding to the γ-$Al_{3.89}Cu_{6.11}$ phase. The presence of the latter indicates that p_{N2}=0.06 Pa is not sufficient for the reaction of all the aluminum atoms in the film with nitrogen. Higher values of nitrogen partial pressure (p_{N2}≥0.09 Pa) result in a formation of films characterized by relatively broad reflections of h-AlN and metallic Cu phases. The films prepared at p_{N2}≥0.09 *Pa* can thus be described as nanocomposite films composed of nanocrystalline h-AlN and metallic Cu phases (nc-h-AlN/Cu). As p_{N2} increases the intensities of the Cu reflections gradually increase while the reflections of h-AlN are suppressed. This can be attributed to an increase of the Cu content in the film with increasing p_{N2}. Such behavior is explained by a gradual extension of the poisoned surface from the outer parts of the target further into the erosion zone of the target. While for low p_{N2} the outer parts of the target (i.e. the Cu ring) are already poisoned and the deposition rate of Cu is reduced the erosion zone (i.e. the Al target) remains metallic and high amount of Al is sputtered. As the value of p_{N2} increases the poisoned surface extends into the erosion zone of the target and the sputtering rate of Al is also reduced. As a result the Cu content in the film increases with an increasing p_{N2}. This partial poisoning of the magnetron target is called differential poisoning and has already been described in [2]. The existence of metallic Cu in the films even at high p_{N2} can be explained by a relatively low thermal stability of CuN, which is probably decomposed as a result of a combined action of substrate heating, bombardment of the growing film by energetic particles and the heat released during the formation of AlN [264]. A significantly lower hardness of the Al-Cu-N compared to ref. [260] is attributed to a high Cu content in the film. Since the maximum hardness was observed for p_{N2}=0.13 Pa and concurrently this value is high enough to ensure that all aluminum in the film forms h-AlN phase, the nitrogen partial pressure in the following experiments was set to 0.13 Pa.

5.3.2 Effect of Cu content at low energy delivered to the growing film

As reported by Musil et al. the Cu concentration represents one of the most important factors affecting the structure and mechanical properties of the Al-Cu-N films [260]. In order to find the optimum Cu content to achieve a high hardness, the inner diameter of the Cu-ring was varied from 28 mm to 36 mm while the other deposition parameters were fixed at the following values: p_T=2.00 Pa, p_{N2}=0.13 Pa, T_s=400 °C, I_d=1.00 A and U_s=U_{fl}. As will be shown later these deposition conditions represent a relatively low energy delivered to the growing film, which is indicated in the title of this section. The structure, elemental composition and hardness of the films are presented in Fig. 5.3.3. Clearly the Cu content significantly affects the structure of the Al-Cu-N films. For the smallest inner diameter of the Cu ring ($Ø_{in}$=28 mm) the films contain 24.3 at.% of Cu and are characterized by a pronounced reflection of metallic Cu and a low broad reflection corresponding to a nanocrystalline h-AlN phase. For $Ø_{in}$=28 mm the film is characterized by broad low-intensity reflections of both h-AlN and Cu phases indicating a nanocomposite structure consisting of a mixture of nanocrystalline nc-h-AlN and nanocrystalline nc-Cu. With an increasing $Ø_{in}$ the intensities of Cu reflections gradually decrease while the intensities of h-AlN reflections increase. For $Ø_{in}$≥34 mm i.e. *Cu*≤3.9 at.% only reflections of crystalline h-AlN are observed. The absence of Cu reflections at $Ø_{in}$=34 mm and *Cu*=3.9 at.% can be explained by segregation of Cu atoms to the h-AlN grain boundaries forming a very thin tissue phase that cannot be detected by XRD. As can be seen, none of these films with Cu contents ranging from 0.0 at.% to 24.3 at.% exhibits a significantly high hardness. A possible explanation could be the relatively low energy delivered to the growing film, which was reported to have a strong influence on the film hardness [288, 289]. Since the substrate bias U_s, the discharge current I_d and the total pressure p_T are among the most important parameters determining the energy delivered to the growing film [57], the inner diameter of the Cu ring was fixed at $Ø_{in}$=34 mm and the effect of these quantities on the structure and mechanical properties of Al-Cu-N/Si films was investigated in the following sections.

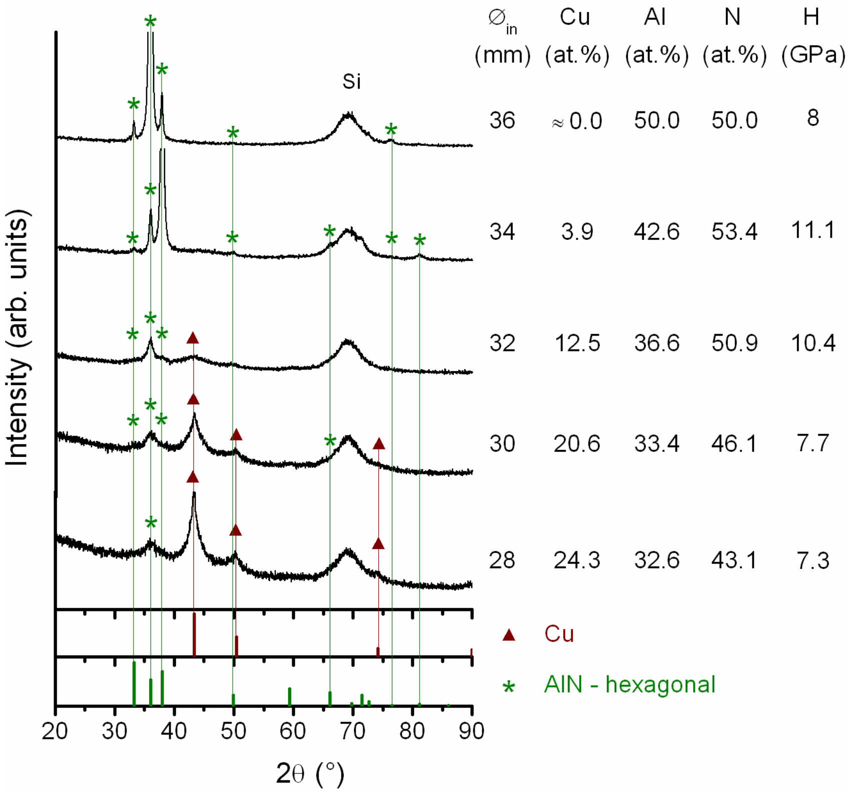

$Ø_{in}$ (mm)	Cu (at.%)	Al (at.%)	N (at.%)	H (GPa)
36	≈ 0.0	50.0	50.0	8
34	3.9	42.6	53.4	11.1
32	12.5	36.6	50.9	10.4
30	20.6	33.4	46.1	7.7
28	24.3	32.6	43.1	7.3

Fig. 5.3.3: XRD patterns, elemental composition and hardness of Al-Cu-N/Si films deposited using a Cu ring with various inner diameters $Ø_{in}$. Deposition conditions: p_T=2.00 Pa, p_{N2}=0.13 Pa, T_s=400 °C, I_d=1.00 A and U_s=U_{fl}. “Si” indicates reflection of the Si(100) substrate.

5.3.3 Effect of substrate bias

Fig. 5.3.4 illustrates the effect of the substrate bias on the structure and properties of Al-Cu-N/Si films prepared at p_T=2.00 Pa, p_{N2}=0.13 Pa, $Ø_{in}$=34 mm, T_s=400 °C and I_d=1 A. The substrate bias U_s was varied from a floating potential U_{fl} down to -150 V. As can be seen all the films are characterized by multiple reflections of h-AlN phase. However the film texture clearly changes by applying a substrate bias. While the Al-Cu-N/Si film prepared with substrates held at a floating potential exhibits a (101) preferred orientation, the films deposited with a substrate bias are characterized by a (002) preferred orientation (except for U_s=-75 V). The most significant change in the structure is observed for the Al-Cu-N/Si film prepared at U_s=-100 V. This film exhibits a relatively broad low intensity reflection of the (002) plane indicating presence of fine nanocrystals of the (002) h-AlN phase. This film exhibits the highest hardness (H=20.9 GPa) and elastic recovery (W_e=74 %) and H/E^* ratio exceeding 0.1. According to XRF measurements the Cu content in the films decreases with an increasing substrate bias. This phenomenon has already been reported by Musil et al. and can be explained by a preferential resputtering of Cu from the growing film due to its high sputtering yield [260].

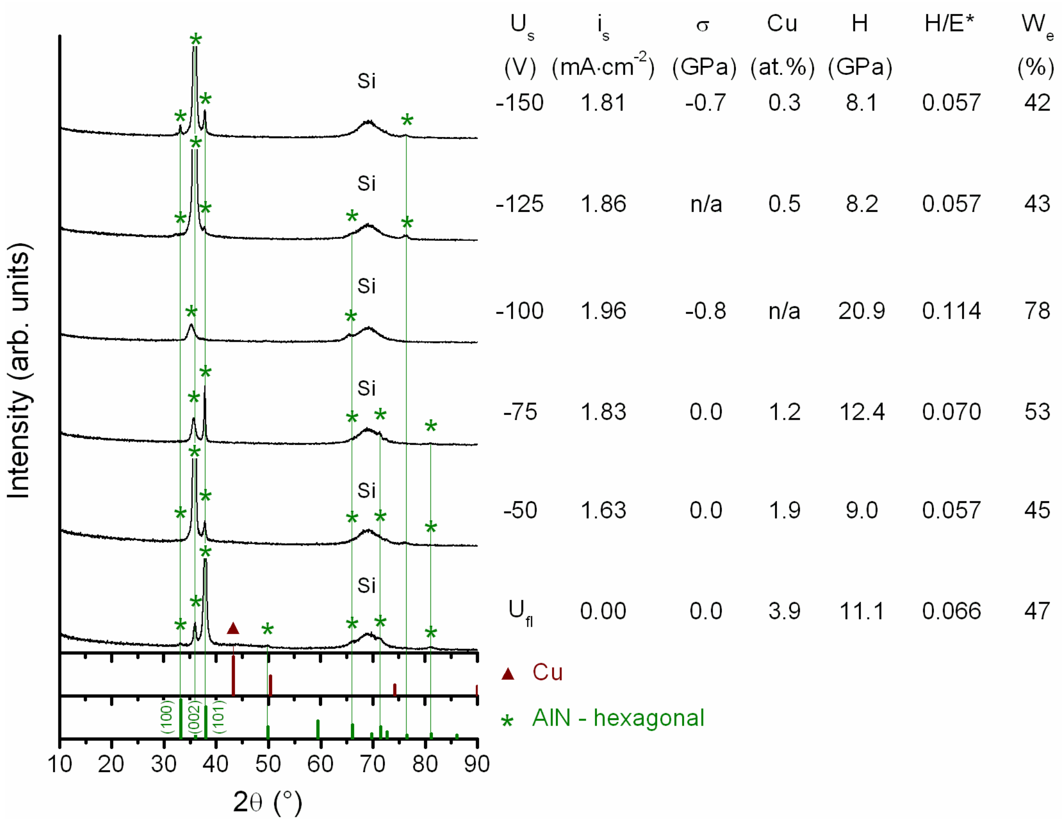

Fig. 5.3.4: XRD patterns and characteristics of Al-Cu-N/Si films deposited at various values of the substrate bias U_s. Deposition conditions: p_T=2.00 Pa, p_{N2}=0.13 Pa, $Ø_{in}$=34 mm, T_s=400 °C and I_d=1 A. “Si” indicates reflection of the Si(100) substrate. “n/a” indicates that the characteristic could not be determined due to a partial delamination of the film.

5.3.4 Effect of discharge current

Another process parameter determining the energy delivered to the growing film is the discharge power [57]. Here the discharge power was varied by changing the discharge current I_d. Since it was found that the mechanical properties of the Al-Cu-N films are enhanced for U_s=-100 V, this substrate bias was applied in all the following experiments. The discharge current was varied from 1.0 A up to 2.0 A. According to the XRD patterns in Fig. 5.3:5 the structure of all films can be described as a nanocomposite composed of nanocrystalline h-AlN and Cu phases i.e. nc-h-AlN/nc-Cu. The film prepared at a low I_d=*1.0 A* is polycrystalline with dominant reflections of the (100), (002) and (101) planes. For $I_d \geq 1.5$ A the films exhibit a clear (002) texture. These structure changes can be related to the substrate current density i_s, which increases with an increasing I_d, and to corresponding changes in the stress state of the films. For a low I_d=1.0 A the ion bombardment of the growing film is low and the competitive growth results in a formation of randomly oriented nanocrystals. For $I_d \geq 1.5$ A, the high substrate current density results in generation of compressive stress in the film and the strain-induced recrystallization mechanism leads to the formation of a textured structure. A moderate increase of Cu content in the films can be seen with an increasing I_d. This can be explained by gradual extension of the target erosion area to the outer parts of the target (i.e. towards the Cu ring) with an increasing I_d, which leads to an increased amount of Cu atoms sputtered from the Cu rings. Surprisingly, the highest hardness is not observed for the film sputtered at the highest I_d and i_s but for an intermediate I_d=1.5 A. Later on in section 5.3.6 it will be shown that increasing the Cu content in the film above ≈11 at.% leads to a sharp decrease of hardness and compressive stress. This explains the decrease of *H* and $|\sigma|$ in the case of Al-Cu-N/Si film prepared at a “high“ discharge current of I_d=2.0 A in spite of the fact that this film was deposited at higher energy delivered to the growing film compared to I_d=1.5 A.

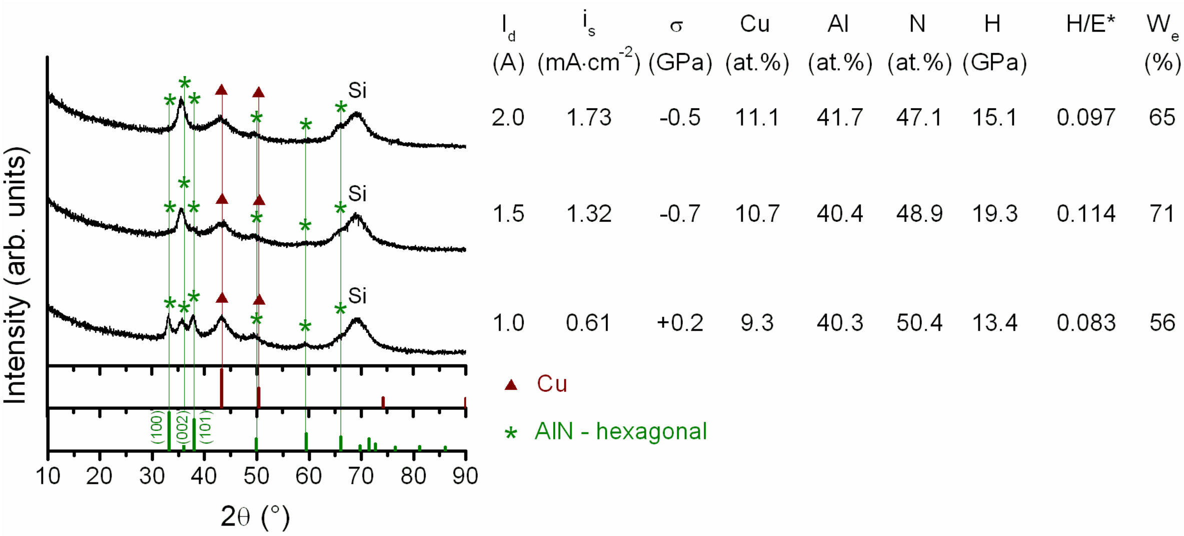

I_d (A)	i_s (mA·cm^{-2})	σ (GPa)	Cu (at.%)	Al (at.%)	N (at.%)	H (GPa)	H/E*	W_e (%)
2.0	1.73	-0.5	11.1	41.7	47.1	15.1	0.097	65
1.5	1.32	-0.7	10.7	40.4	48.9	19.3	0.114	71
1.0	0.61	+0.2	9.3	40.3	50.4	13.4	0.083	56

Fig. 5.3.5: XRD patterns and characteristics of Al-Cu-N/Si films deposited at various values of the discharge current I_d. Deposition conditions: p_T=2.00 Pa, p_{N2}=0.13 *Pa*, $Ø_{in}$=34 mm, T_s=400 °C and U_s=-100 V. “Si” indicates reflection of the Si(100) substrate.

5.3.5 Effect of total pressure

The effect of the total pressure of the gas mixture on the structure and properties of the films was investigated by keeping the nitrogen partial pressure fixed at p_{N2}=0.13 Pa and by varying the argon partial pressure from 0.87 Pa up to 2.12 Pa. This way the total pressure p_T was varied from 1.00 Pa to 2.25 Pa. During all depositions, the substrate current density i_s was recorded using an oscilloscope. The evolution of i_s and film macrostress σ with an increasing total pressure is shown in Fig. 5.3.6. The total pressure significantly influences the substrate current density, which decreases from 2.11 mA/cm^2 down to 1.12 mA/cm^2 as the total pressure increases from 1.00 Pa to 2.25 Pa. These changes of the ion bombardment of the growing film result in pronounced changes in the film macrostress. For p_T=2.25 Pa the film macrostress has an intermediate value of σ=-1.6 GPa. As the substrate current density increases, the magnitude of the compressive stress increases up to σ=-5.2 GPa for p_T=1.5 Pa and i_s=1.55 mA/cm^2. A further increase of substrate current density results in generation of high compressive stresses and subsequent delamination of the film. The evolution of structure, elemental composition and mechanical properties of the films deposited at various total pressures is summarized in Fig. 5.3.7. The structure of the films prepared at p_T ranging from 1.5 Pa to 2.25 Pa corresponds to a nc-h-AlN/nc-Cu nanocomposite already described in section 5.3.4. An intensive ion bombardment at p_T=1.0 Pa results in an increased preferential resputtering of Cu, a significant decrease of the Cu content in the film and consequently to the formation of a textured structure characterized by (002) and (103) reflections of h-AlN. Except for the film prepared at p_T=2.25 Pa with a relatively low substrate current density all Al-Cu-N/Si films exhibit a high hardness ($H \geq 18$ GPa), high elastic recovery ($W_e \geq 69$ %) and $H/E^*>0.1$.

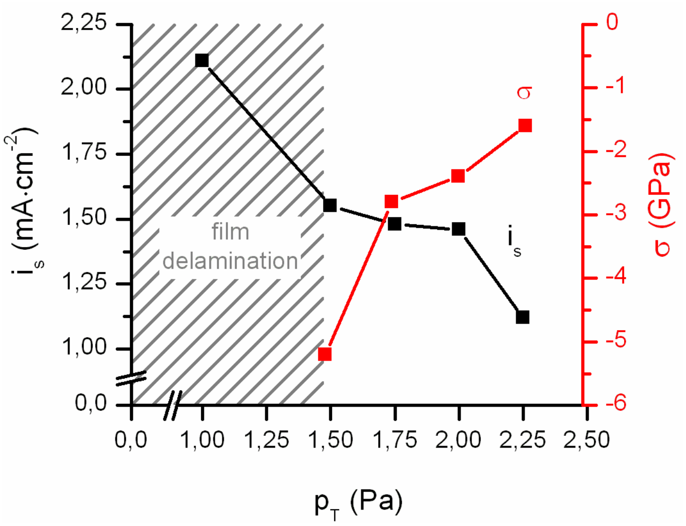

Fig 5.3.6: Average substrate ion current density in pulse i_s and film macrostress σ as functions of the total pressure. Deposition conditions: I_d=1.5 A, p_{N2}=0.13 Pa, $Ø_{in}$=34 mm, T_s=400 °C and U_s=-100 V.

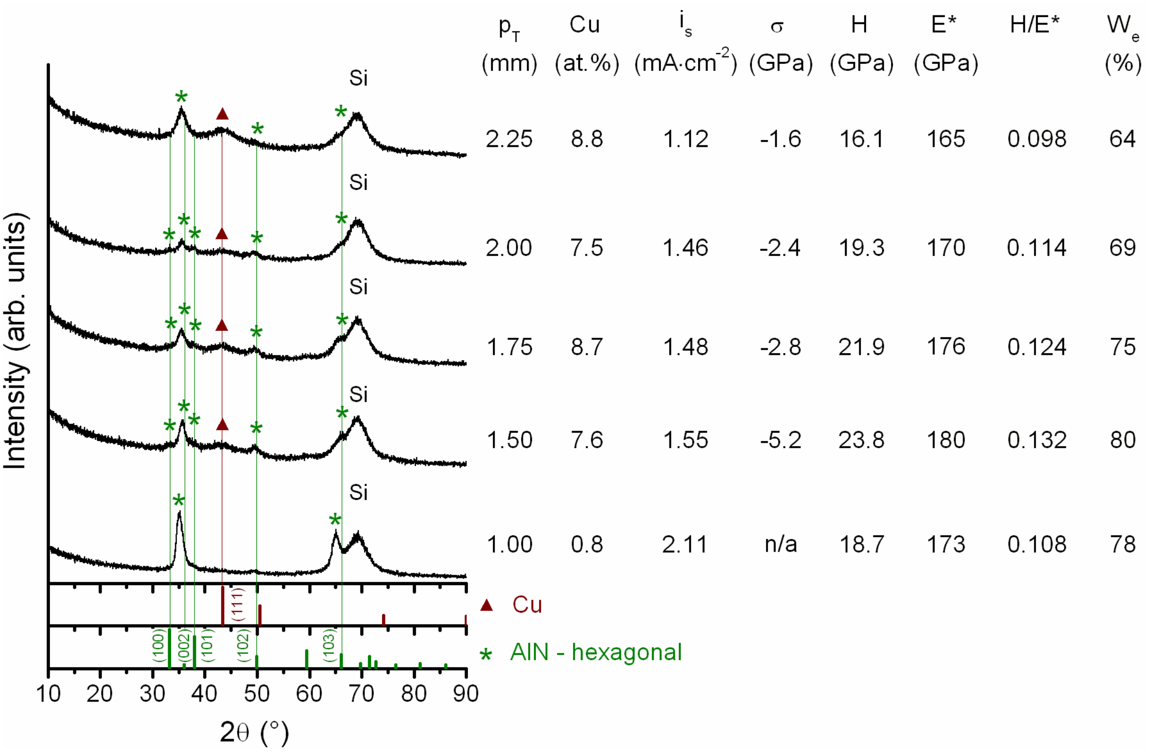

p_T (mm)	Cu (at.%)	i_s (mA·cm^{-2})	σ (GPa)	H (GPa)	E* (GPa)	H/E*	W_e (%)
2.25	8.8	1.12	-1.6	16.1	165	0.098	64
2.00	7.5	1.46	-2.4	19.3	170	0.114	69
1.75	8.7	1.48	-2.8	21.9	176	0.124	75
1.50	7.6	1.55	-5.2	23.8	180	0.132	80
1.00	0.8	2.11	n/a	18.7	173	0.108	78

Fig. 5.3.7: XRD patterns and characteristics of Al-Cu-N/Si films deposited at various values of the total pressure p_T. Deposition conditions: I_d=2.0 A, p_{N2}=0.13 Pa, $Ø_{in}$=34 mm, T_s=400 °C and U_s=- 100 V. “Si” indicates reflection of the Si(100) substrate. “n/a” indicates that the film macrostress could not be determined due to film delamination.

In summary, it has been demonstrated that the magnitude of compressive macrostress in hard Al-Cu-N films can be effectively controlled by changing the total pressure of the gas mixture. This is an important finding since the type and magnitude of macrostress largely influences toughness of thin films [59].

5.3.6 Effect of Cu content at high energy delivered to the growing film

Based on the results presented in sections 5.3.3 and 5.3.4 another series of Al-Cu-N films was prepared at I_d=1.5 A and U_s=-100 V with the aim to increase the energy delivered to the growing film. In this series the inner diameter of the Cu rings was varied in fine steps in order to investigate the effect of Cu content on structure and properties of the films. The evolution of structure, macrostress and mechanical properties of the films is summarized in Fig. 5.3.8. As the Cu content in the film decreases the structure changes from a nanocomposite composed of nanocrystalline h-AlN and crystalline Cu (nc-h-AlN/Cu) via a nanocomposite composed of a mixture of very fine nanocrystals of both h-AlN and Cu phases (nc-h-AlN/nc-Cu) to crystalline films exhibiting presence of h-AlN phase only. As can be seen the highest hardness (H=23.8 GPa), elastic recovery (W_e=81 %), H/E^* ratio (=0.131) and compressive macrostress (σ=-2.3 GPa) were measured for Al-Cu-N/Si film with 4.4 at.%, which is characterized by the lowest reflections of h-AlN phase indicating the presence of very fine nanocrystals.

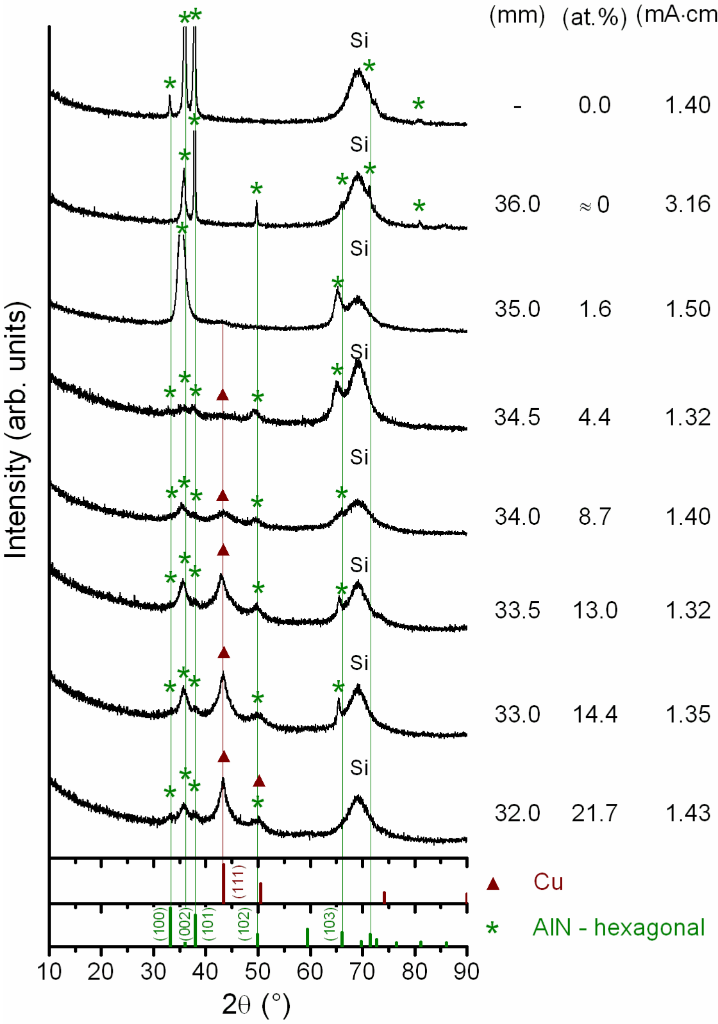

$\varnothing_{in}$ (mm)	Cu (at.%)	i_s (mA·cm^{-2})	σ (GPa)	H (GPa)	E* (GPa)	H/E*	W_e (%)
-	0.0	1.40	-0.1	11	155	0.071	49
36.0	≈ 0	3.16	n/a	15.5	188	0.082	60
35.0	1.6	1.50	-1.6	17.4	188	0.093	68
34.5	4.4	1.32	-2.3	23.8	181	0.131	81
34.0	8.7	1.40	-1.1	19.9	168	0.118	74
33.5	13.0	1.32	-0.1	11.2	151	0.074	53
33.0	14.4	1.35	0.2	11.9	149	0.080	58
32.0	21.7	1.43	0.2	7.7	130	0.059	43

Fig. 5.3.8: XRD patterns and characteristics of Al-Cu-N/Si films deposited using various inner diameter of the Cu ring $\varnothing_{in}$ at high energy delivered to the growing film. Deposition conditions: p_T=2.00 Pa, p_{N2}=0.13 Pa, I_d=1.5 A, T_s=400 °C and U_s=-100 V. “Si” indicates reflection of the Si(100) substrate. $\varnothing_{in}$ denoted as “-” represents pure AlN film deposited using two Al targets without Cu rings. “n/a” indicates that the characteristic could not be determined due to partial delamination of the film.

This observation is consistent with previous results of Musil et al. who found that the hardest Al-Cu-N films are composed of AlN nanocrystals with a typical size below 10 nm [260]. For comparison the structure and properties of pure AlN/Si film are also provided. In order to suppress arcing during deposition and reduce the substrate current density to produce a film with smooth surface and good adhesion the pure AlN film was prepared at p_T=3.00 Pa and U_s=-30 V . It can be clearly seen that the pure aluminum nitride film exhibits significantly lower H, W_e and H/E^* ratio compared to the nanocrystalline nc-h-AlN/nc-Cu films.

The hardness and effective Young's modulus of Al-Cu-N/Si films as functions of Cu content prepared at identical deposition conditions but with different Cu rings are shown in Figs. 5.3.9 a) and b), respectively. The experimental data are fitted by a 4th (H) and 3rd (E^*) order polynomials. A clear difference between the trends of hardness and effective Young's modulus is observed. The hardness of Al-Cu-N/Si films reaches a maximum value of H=23.8 GPa for Cu=4.4 at.%, which is significantly higher compared to pure AlN/Si films (H=9.7÷15.5 GPa) or Al-Cu-N/Si films with high Cu content (H>10 GPa). On the other hand, the effective Young's modulus decreases almost monotonically as the Cu content in the film increases, and for Cu=0.0 at.% it is comparable to the effective Young's modulus of the Al-Cu-N/Si film with the highest hardness (see Fig. 5.3.9. b)).

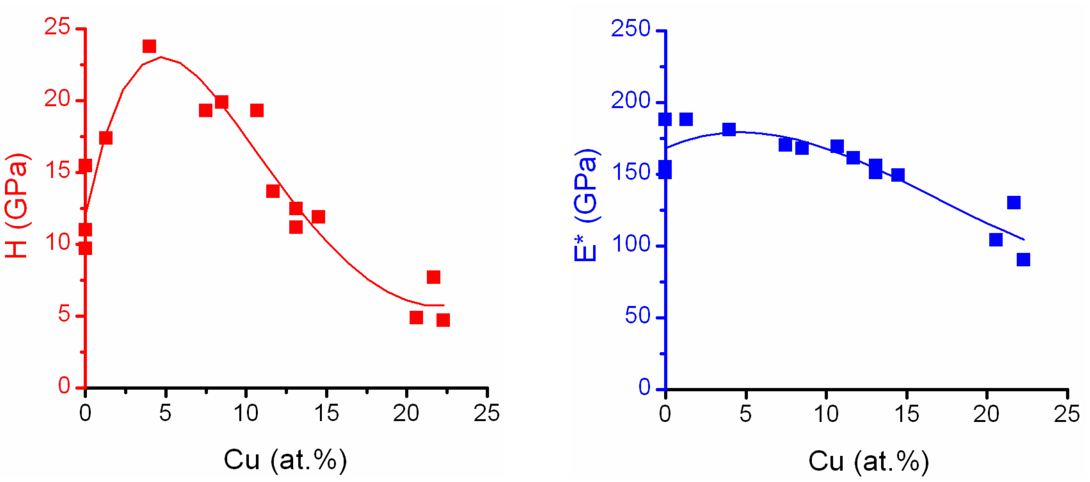

a) **b)**

Fig. 5.3.9: a) hardness H and b) effective Young's modulus E^* of Al-Cu-N/Si films as functions of the Cu content deposited at high energy delivered to the growing film. Deposition conditions: p_T=2.00 Pa, p_{N2}=0.13 Pa, I_d=1.5 A, T_s=400 °C and U_s=-100 V.

The different trends in hardness and effective Young's modulus of Al-Cu-N/Si films presented in Fig. 5.3.9 leads to H/E^*>0.1 in a certain concentration range. Fig 5.3.10 shows the fitting curves of H and E^* in a single graph. The shaded area indicates the range of Cu contents where H/E^*>0.1. It can be seen that films with H/E^*>0.1 are produced for Cu contents ranging approximately from 2 at.% to 11 at.%.

The evolution of macrostress with an increasing Cu content in the film is shown in Fig. 5.3.11. A similar trend as in the case of film hardness is observed. The well crystalline pure AlN/Si films are characterized by relatively low compressive stress (≈-0.2 GPa). The addition of a low amount of Cu (<8 at.%) results in formation of a nanocrystalline structure and a gradual increase of film macrostress up to its maximum value of $\sigma\approx$-2.5 GPa. Higher contents of Cu (>8 at.%) however lead to a reduction of the macrostress. For Cu contents ≥15 at.%, the macrostress becomes tensile. The decrease of σ for Cu>8 at.% can be explained by the formation of a ductile metallic Cu phase, which is able to efficiently relax the film macrostress due to its plastic deformation. The decrease of the film stress with an increasing Cu content in the film has already been reported by Jirout for ZrC/Cu films [42]. Comparing Figs. 5.3.9 a) and 5.3.11 it can be seen that even a very slight increase of Cu content in the range from ≈8 at.% to ≈11 at.% leads to a pronounced decrease of film stress from σ=-2.5 at.% down to σ=-0.8 GPa while its hardness is maintained approximately constant H≈19.5 GPa. This indicates that slight changes in the Cu content can be used to control the magnitude of compressive macrostress in hard nanocomposite Al-Cu-N films.

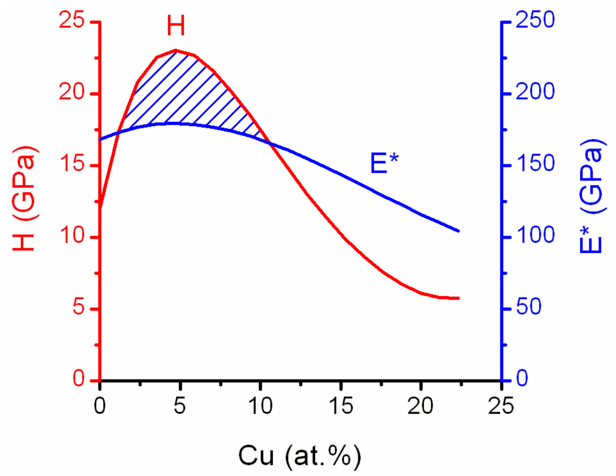

Fig. 5.3.10: Fitting curves of hardness and H and effective Young's modulus E^* of Al-Cu-N/Si films with various Cu contents. Deposition conditions: p_T=2.00 Pa, p_{N2}=0.13 Pa, I_d=1.5 A, T_s=400 °C and U_s= -100 V. The shaded area indicates the range of the Cu content where H/E^*>0.1 is achieved.

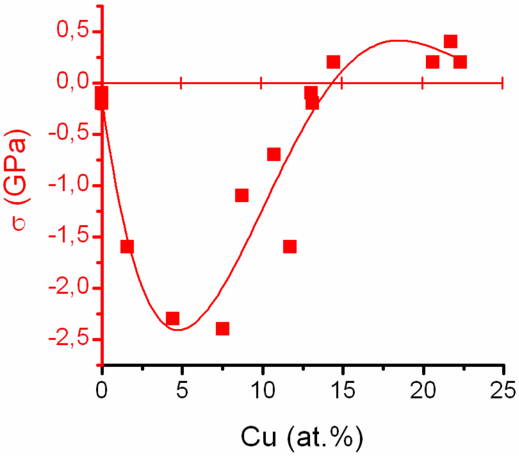

Fig. 5.3.11: Macrostress of Al-Cu-N/Si films as a function of the Cu content deposited at a high energy delivered to the growing film. Deposition conditions: p_T=2.00 Pa, p_{N2}=0.13 Pa, I_d=1.5 A, T_s=400 °C and U_s= -100 V.

5.3.7 Resistance of Al-Cu-N films to cracking

The resistance of the Al-Cu-N films to cracking was investigated using two different methods. In the indentation test the film is subjected to a constant load which, depending on the particular mechanical properties of the film, may result in different indentation depths i.e. different film strains. The bending test represents a procedure, in which the film is bent over a cylinder of a given diameter. Therefore, irrespective of the mechanical properties, the films are subjected to a constant strain. Since both these tests enable a qualitative comparison only, several Al-Cu-N or AlN films are selected in each section and the presence of cracks at various loads or strains is monitored.

5.3.7.1 Indentation test

The indentation test was performed using four different indenter loads (*L*=1.00 N, 0.75 N, 0.50 N and 0.25 N). It has already been demonstrated that the resistance of thin films to cracking in an indentation test can be improved by increasing the compressive macrostress [59]. For that reason the effect of film macrostress is not investigated in this section and the main attention is focused on the effect of the Cu content and the film thickness on its resistance to cracking.

Effect of Cu - content

Three different films were selected to illustrate the effect of the Cu content on the resistance to cracking in the indentation test. These films can be described as a pure crystalline h-AlN film with 0.0 at.% of Cu, a nanocomposite nc-AlN/nc-Cu film with a ”low“ Cu content (≈8.7 at.%) and a nanocomposite nc-AlN/nc-Cu film with a “high“ Cu content (≈13.0 at.%), respectively. The structure of these films is shown in Fig. 5.3.12. and selected process parameters and characteristics of the films are summarized in Tab. 5.6. As can be seen the values of mechanical properties in Tab. 5.6 are consistent with the results presented in section 5.3.6. The nanocomposite Al-Cu-N/Si film with a ”low“ Cu content exhibits high values of hardness, (H=19.9 GPa), elastic recovery (W_e=74 %), H/E^* ratio (H/E^*=0.118) and compressive macrostress (σ=-2.3 GPa). For the pure AlN film or the Al-Cu-N film with high Cu content all these quantities are significantly lower.

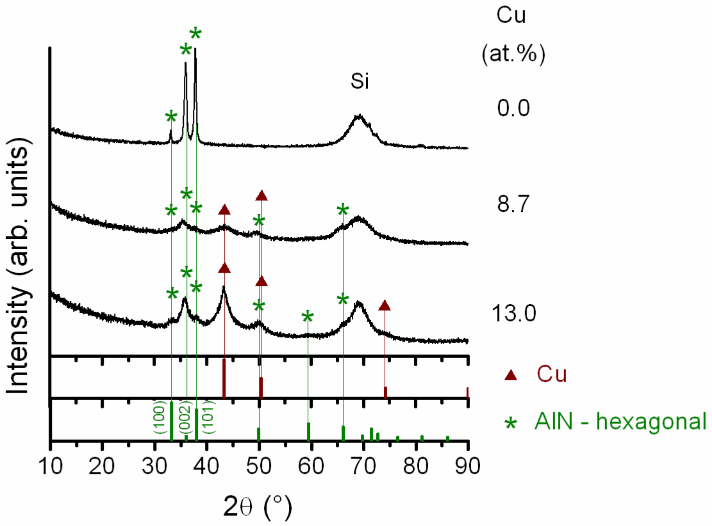

Fig. 5.3.12: XRD patterns of AlN/Si film and Al-Cu-N/Si films with two different Cu contents subjected to indentation test.

Tab. 5.6: Process parameters and characteristics of AlN/Si film and Al-Cu-N/Si films with two different Cu contents subjected to indentation test. Deposition conditions: p_{N2}=0.13 Pa, I_d=1.5 A, T_s=400 °C.

Cu (at.%)	f_r (kHz)	p_T (Pa)	U_s (V)	a_D (nm/min)	h (nm)	σ (GPa)	H (GPa)	E* (GPa)	W_e (%)	H/E*	H^3/E^{*2} (GPa)
0.0	30	3.0	-30	55.0	2200	-0.1	8.2	140	41	0.059	0.028
8.7	5	2.0	-100	70.0	2170	-1.1	19.9	168	74	0.118	0.279
13.0	5	2.0	-100	92.3	2400	-0.1	11.2	151	53	0.074	0.062

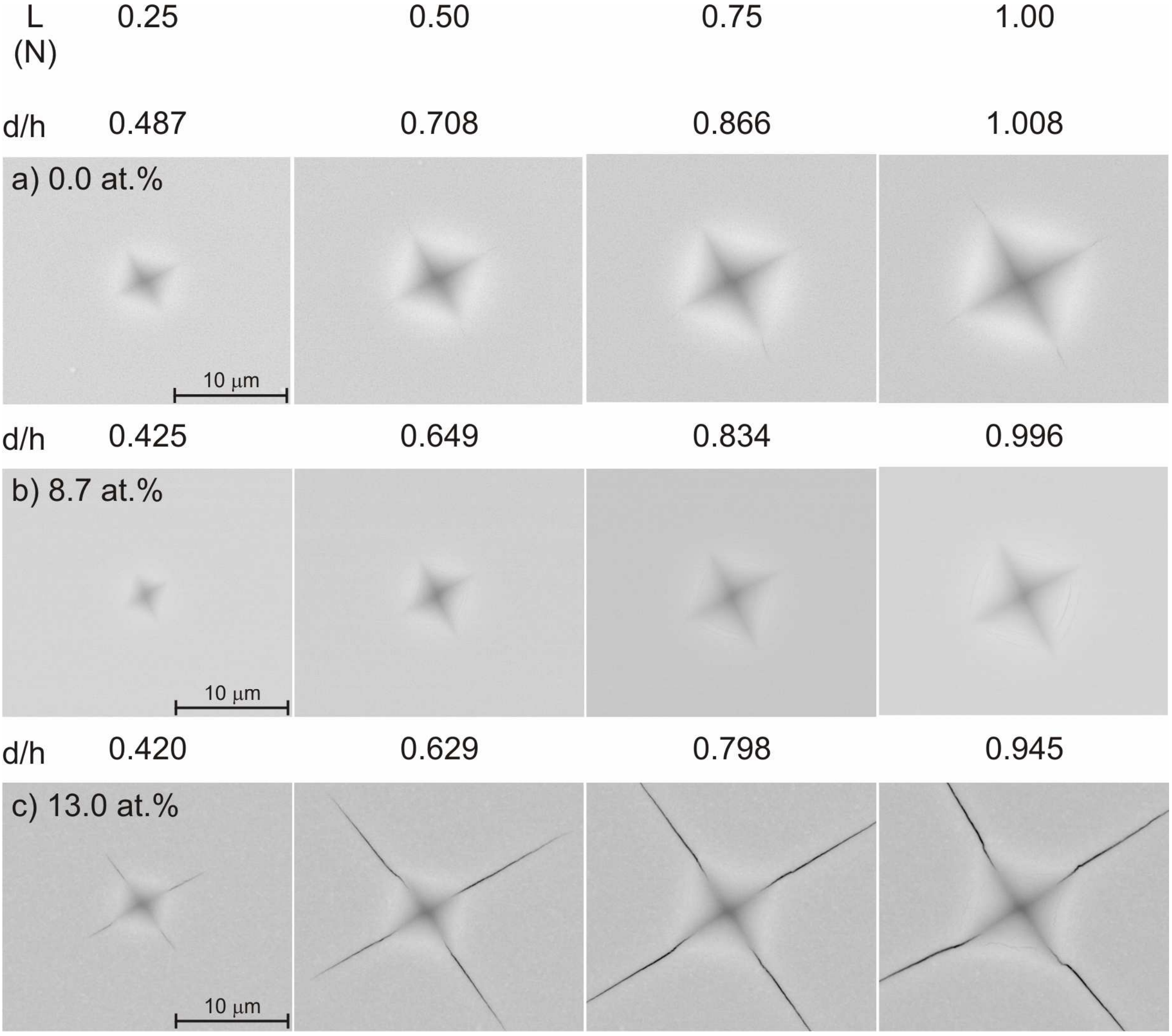

Fig. 5.3.13: SEM images of Vickers diamond indenter imprints in a) pure AlN/Si b) Al-Cu-N/Si film with 8.7 at.% of Cu and c) Al-Cu-N/Si film with 13.0 at.% of Cu. The corresponding indentation depth to film thickness ratio *d/h* is shown above each image. The indenter load *L* is shown at the very top of the figure.

The results of the indentation test are shown in Fig. 5.3.13. Clearly the lowest resistance to cracking is observed for the nanocomposite Al-Cu-N/Si film with 13.0 at.% of Cu, where clear radial cracks are formed even at the lowest indenter load of 0.25 N corresponding to a low *d/h* ratio. The resistance to cracking is higher in the case of the pure AlN film where first cracks are observed at *L*=0.75 N and *d/h*=0.866. For the nanocomposite Al-Cu-N/Si film with 8.7 at.% of Cu no radial cracks are observed even for the highest load of 1.00 N. With respect to mechanisms described in section 2.2.2 this enhancement of resistance to cracking in the case of Al-Cu-N/Si film with 8.7 at.% of Cu can be attributed to several factors such as formation of a nanocomposite structure, increased compressive macrostress or incorporation of a ductile phase. In terms of mechanical properties this film is characterized by a high elastic recovery, high hardness and a relatively low effective Young's modulus i.e. high H/E^* ratio resulting in a low deformation of the film and a high ability to distribute the applied load to a larger volume.

Effect of film thickness

In order to illustrate the effect of the film thickness on its resistance to cracking, three Al-Cu-N films were deposited on silicon substrates at identical deposition conditions with different deposition time *t*. The characteristics of the films and the particular deposition conditions are presented in Tab. 5.7.

Tab. 5.7: Characteristics of Al-Cu-N/Si films prepared at identical deposition conditions (p_T=1.0 Pa, p_{N2}=0.13 Pa, I_d=1.5 A, T_s=400 °C, U_s= -100 V, $Ø_{in}$=33 mm, f_r=5 kHz) but with different deposition times *t*.

t (min)	a_D (nm/min)	h (nm)	σ (GPa)	H (GPa)	E* (GPa)	W_e (%)	H/E*	H^3/E^{*2} (GPa)
42	32.4	1360	-0.9	16.8	158	67	0.106	0.190
73	31.4	2290	-1.1	17.0	160	67	0.106	0.192
120	25.5	3060	-1.0	16.8	157	67	0.107	0.192

As can be seen all Al-Cu-N/Si films exhibit almost identical mechanical properties (H≈16.9 GPa, E^* ≈158 GPa, W_e≈67 %, H/E^*≈0.106) and compressive macrostress (σ=-1.0 GPa) while the thickness varies from 1360 nm to 3060 nm.. This makes it possible to investigate purely the effect of film thickness on its resistance to cracking. Optical microscope images of the indenter imprints for different loads are shown in Fig. 5.3.14. In the case of a 3060 nm thick Al-Cu-N/Si film no cracks are observed even for the maximum load of 1.00 N. As the film thickness decreases to 2290 nm some minor cracks are formed at 1.00 N and their length and number further increases for the 1360 nm thick film. Similarly if a film of a given thickness is considered and the indenter load is increased, more pronounced crack patterns are observed. This can be illustrated in the case of the 1360 nm thick film.

A similar but more detailed illustration of this effect is provided in Fig. 5.3.15, which shows SEM images of two Al-Cu-N/Si films with optimized mechanical properties (high hardness, high elastic recovery, H/E^*>0.1 and compressive stress) that differ in their thickness. Both radial and lateral cracks form in the thinner film (h=1660 nm, d/h=1.303), while no cracks are observed in the thicker film (h=2170 nm, d/h=0.996). It is worthwhile to note that the cracks are formed in the thinner film even though it exhibits a significantly higher value of compressive macrostress.

The formation of cracks in thinner films can be explained as follows. Let us assume that identical deposition conditions and mechanical properties imply that all the films with various thicknesses exhibit identical toughness (i.e. the ability to absorb deformation work before fracture). Since no cracks are observed in the 3060 nm thick film the formation of cracks in the thinner film must be related to the underlying substrate. Similarly as reported by Galvan et al. it is suggested that the cracks are initiated in the silicon substrate due to a high *d/h* ratio [95]. As the crack propagates from the substrate through the film, its growth is gradually hindered by the tough film. Since for a lower thickness the total deformation work that can be absorbed by the film is smaller, the propagating cracks can not be fully stopped and consequently reach the surface of the thin film.

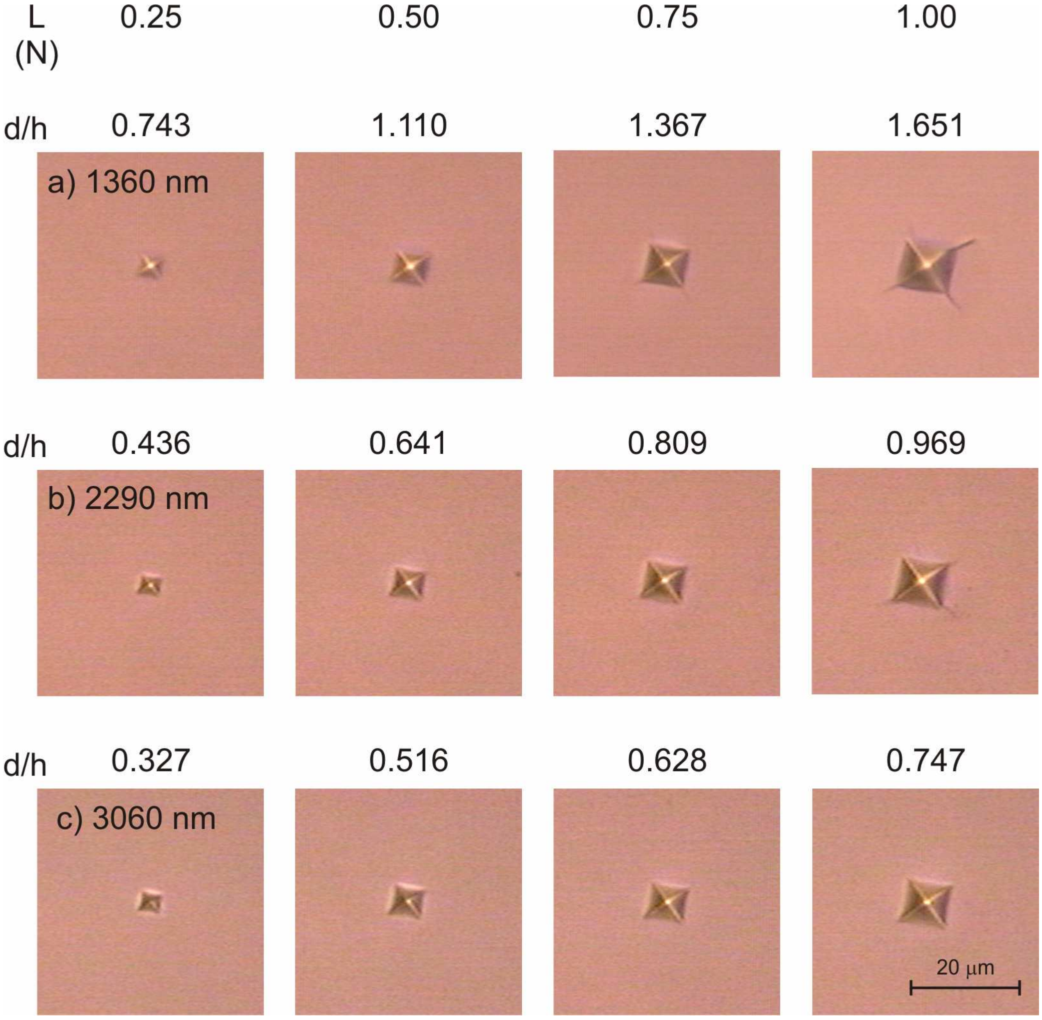

Fig. 5.3.14: Optical microscope images of Vickers diamond indenter imprints Al-Cu-N/Si films with the same mechanical properties (shown in Tab. 5.7) but different thickness. The corresponding indentation depth to film thickness ratio *d/h* is shown above each image. The indenter load *L* is show at the very top of the figure. Mechanical properties of the films are summarized in Tab. 5.7.

It can be concluded that the hard nanocomposite Al-Cu-N films with ≈8.7 at.% of Cu exhibit an enhanced resistance to cracking in the indentation test compared to pure AlN films and Al-Cu-N films with a high Cu content (≈13.0 at.%). The films with an enhanced resistance to cracking are characterized by high values of hardness ($H \geq 17$ GPa), elastic recovery ($W_e \geq 67$ GPa), compressive macrostress ($\sigma \leq -1.0$ GPa) and H/E^* ratio ($H/E^* > 0.1$). The structure of these films can be described as nanocomposite composed of very fine nanocrystals of h-AlN and Cu phases. It has also been demonstrated that the film thickness represents a very important factor affecting the formation of cracks if high indenter loads are applied. In order to prevent the formation of cracks in the film, its thickness needs to be high enough to (1) avoid the initiation of cracks in the substrate and (2) stop propagation of the existing cracks by absorbing the deformation energy.

5.3.7.2 Bending test

It can be expected that an enhanced resistance to cracking of harder films observed in the indentation test can partially be attributed to a lower indentation depth i.e. a lower film strain. For that reason the resistance of Al-Cu-N films to cracking was also investigated using the bending test, which produces deformation with a constant strain.

Effect of Cu - content

The effect of Cu content on the resistance of Al-Cu-N/Mo films to cracking in bending is illustrated for a pure AlN, a nanocomposite Al-Cu-N film a ”low“ Cu content (≈8.7 at.%) and a nanocomposite Al-Cu-N film with a “high“ Cu content (≈13.0 at.%). Structure and mechanical properties of these films have already been described in Fig. 5.3.12 and Tab. 5.6, respectively. Optical microscope (OM) images of the surface of the films after bending over various cylinders are shown in Fig. 5.3.16. The presence or absence of cracks at selected strains was verified using a scanning electron microscope. Similarly to the case of the indentation test the lowest resistance to cracking was found for the Al-Cu-N film with a “high“ Cu content (≈13.0 at.%) and cracks perpendicular to the direction of bending were observed already for the lowest strain of ε=0.61 %. The pure crystalline AlN film exhibits a slightly higher resistance to cracking with the first cracks observed at ε=0.76 %. As can be seen from the SEM images no cracks were found on the surface of the nanocomposite Al-Cu-N film with a ”low“ Cu content (≈8.7 at.%) even for the highest strain ε=1.01 %. This indicates that the nanocomposite Al-Cu-N film with a ”low“ Cu content exhibits an enhanced resistance to cracking in both the indentation and the bending tests. The origin of the enhanced resistance to cracking in bending is not perfectly clear. However it will be shown later, that the film macrostress has a large influence on the resistance to cracking in bending. From Tab. 5.6 it is clear that the nanocomposite Al-Cu-N film with a ”low“ Cu content exhibits a relatively high compressive macrostress (σ=-1.1 GPa) while both the pure AlN film and the Al-Cu-N film with a “high“ Cu content are characterized by a very low compressive macrostress (σ=-0.1 GPa).

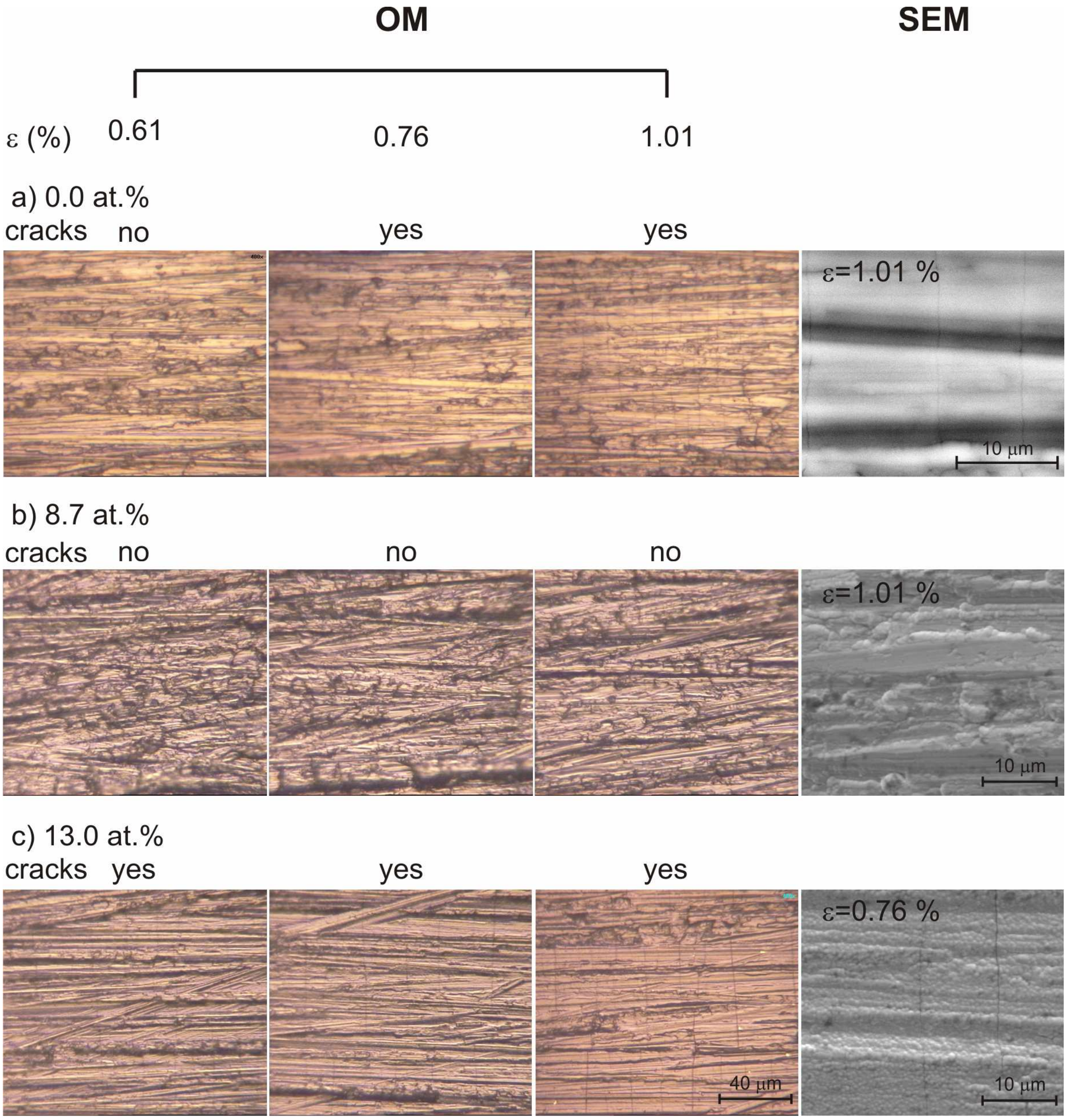

Fig. 5.3.16: Optical microscope (OM) and scanning electron microscope (SEM) images of the surface of a) pure AlN/Mo film b) Al-Cu-N/Mo film with 8.7 at.% of Cu and c) Al-Cu-N/Mo film with 13.0 at.% of Cu after bending over cylinders of various diameters. The corresponding film strain ε is show at the very top of the figure.

Effect of film thickness

The effect of the film thickness on its resistance to cracking in bending has also been investigated (see Fig. 5.3.17). Due to high surface roughness of the molybdenum substrate the mechanical properties could not be properly measured. Instead the values corresponding to the Si substrate (shown in Tab. 5.7) are used as a reference. The film thickness measured on a Mo substrate (used in bending test) however differs slightly from the values presented in Tab. 5.7. This is due to different positions of the Si and Mo substrates on the substrate holder.

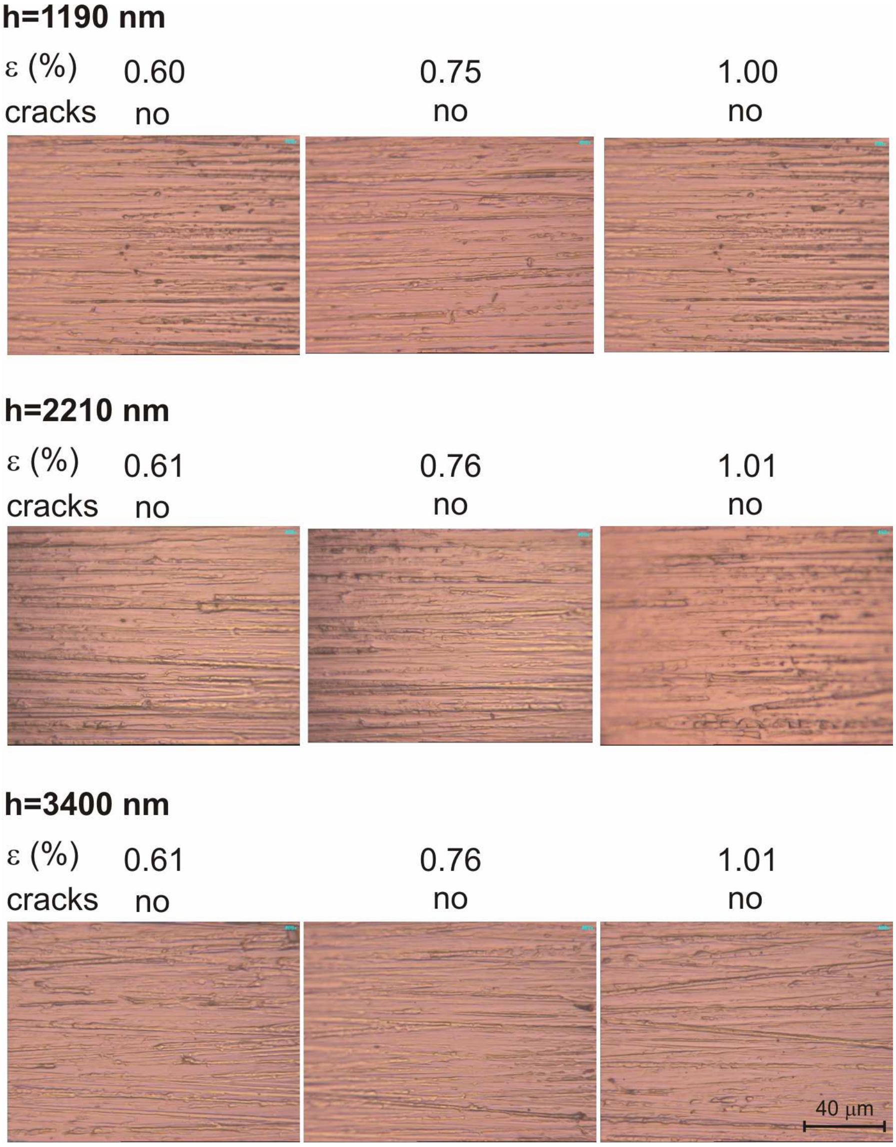

Fig. 5.3.17: Optical microscope (OM) images of the surface of Al-Cu-N/Mo films with various thicknesses after bending over cylinders of various diameters. The corresponding film strain ε is shown above each image. Mechanical properties of the films are summarized in Tab. 5.7.

As can be seen from Fig. 5.3.17 neither of the Al-Cu-N/Mo films with various thicknesses shows cracks after performing the bending test. These results indicate that the resistance to cracking in bending does not depend on the film thickness. This is consistent with Eq. 4.8 (section 4.3.3) used for calculation of film strain in bending. For example let us consider the fixed cylinder with a diameter of 25 mm and the thickness of the molybdenum substrate of h_s=150 µm. For the thinnest h=1190 nm and the thickest h=3400 nm films almost identical strains of $\varepsilon_{1190\ \mathrm{nm}}$=0.60 % and $\varepsilon_{3400\ \mathrm{nm}}$=0.61 % are obtained, respectively. Similarly only very slight differences are found for cylinders with smaller bending diameters (see Fig. 5.3.17). If we assume that identical deposition conditions and mechanical properties of these three films imply identical toughness than the same strains should also yield the same resistance to cracking in bending. These results show that, for typical cylinder diameters ($\O_f$=25÷15 mm) and typical substrate (h_s=150 µm) and films thicknesses (h_f=1200 ÷3400 nm) presented in this study, the dependency of the resistance to cracking in bending on the film thickness is very weak.

Effect of film macrostress

The results presented above, i.e. the fact that the film thickness does not significantly affect the resistance to cracking in bending, enable to investigate the effect of the magnitude of the compressive macrostress. Fig. 5.3.18 shows XRD patterns and characteristics of three hard Al-Cu-N films with a nanocrystalline nc-AlN/nc-Cu structure, very similar mechanical properties but different stress state. As reported in section 5.3.6 the magnitude of compressive macrostress can be controlled by slightly changing the Cu content in the film while keeping it in the range necessary to obtain high hardness (i.e. *Cu*≈8÷11 at.%).

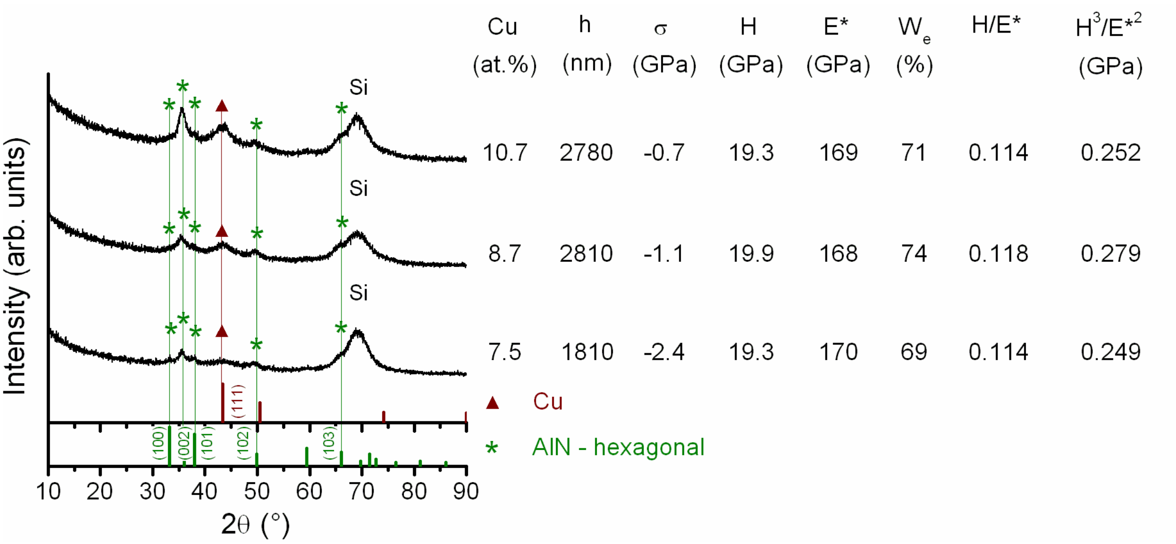

Cu (at.%)	h (nm)	σ (GPa)	H (GPa)	E* (GPa)	W_e (%)	H/E*	H^3/E^{*2} (GPa)
10.7	2780	-0.7	19.3	169	71	0.114	0.252
8.7	2810	-1.1	19.9	168	74	0.118	0.279
7.5	1810	-2.4	19.3	170	69	0.114	0.249

Fig. 5.3.18: XRD patterns and characteristics of hard Al-Cu-N/Si films with similar mechanical properties but different value of compressive macrostress. Deposition conditions p_T=2.0 Pa, p_{N2}=0.13 Pa, I_d=1.5 A, T_s=400 °C, U_s= -100 V, $Ø_{in}$=34 mm, f_r=5 kHz).

Results of the bending test are summarized in Fig. 5.3.19. In the case of Al-Cu-N/Mo film with 10.7 at.% of Cu and the lowest macrostress of σ=-0.7 GPa first cracks are observed for ε=0.76 % and their density increases with an increasing strain. The film with 8.7 at.%, which exhibits a higher compressive stress of σ=-1.1 GPa, is already crack-free in the whole range of strains tested. Due to a higher surface roughness of the substrate the absence of cracks was confirmed by SEM. A further slight decrease of Cu content in the film leads to an increase of macrostress up to σ=-2.4 GPa and again no cracks are observed in the film even for the highest strain. Based on the relation between macrostress and cracking resistance of thin films presented by Wiklund et al. the results above can be explained as follows [69]. If a thin film exhibiting compressive macrostress is subjected to bending, a certain elongation is first necessary to compensate for the compressive macrostress and to reach a “stress-free“ state at the outer fiber (i.e. on the surface of the film). A further increase of the film strain leads to generation of tensile stresses, which-after reaching a certain critical value-result in the formation of cracks. Since a higher residual compressive macrostress requires a higher bending strain to reach the “stress-free“ state, the formation of cracks is also shifted to higher strains (i.e. to lower diameters of the fixed bending cylinder).

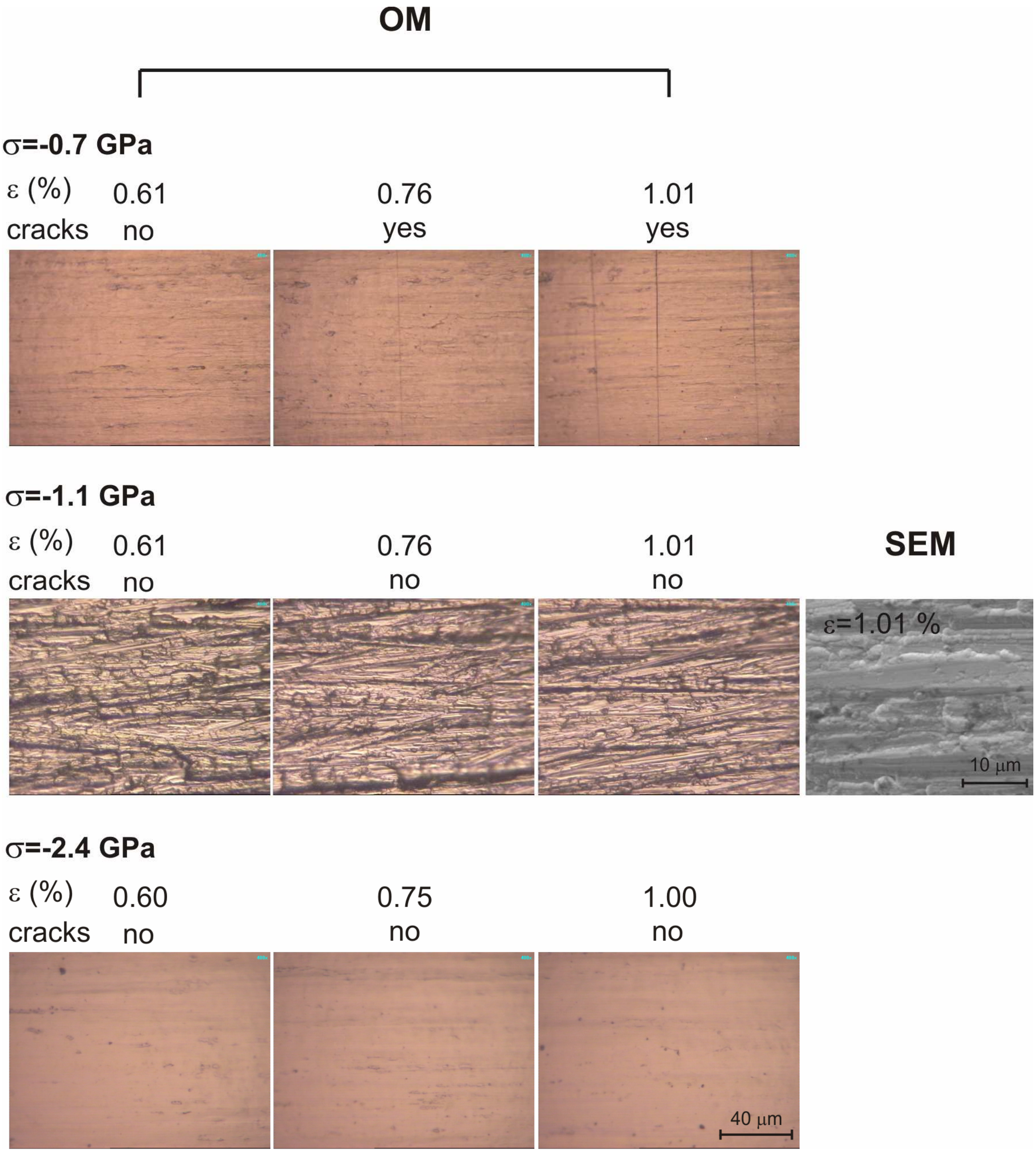

Fig. 5.3.19: Optical microscope (OM) images of the surface of hard Al-Cu-N/Si films with similar mechanical properties but different values of the compressive macrostress after bending over cylinders of various diameters. The corresponding film strain ε is shown above each image. A scanning electron microscope (SEM) image of the surface of Al-Cu-N/Si film with macrostress of σ=-1.1 GPa corresponding to a strain of ε=1.01 % is also shown to confirm absence of cracks in the film.

5.3.8 Antibacterial efficiency of Al-Cu-N films

Similarly to the case of Cr-Cu-O films the antibacterial efficiency of Al-Cu-N films was investigated as a function of contact time (t=0.5 h, 1 h, 3 h and 5 h) in the daylight. The antibacterial efficiency for t=5 h in the dark was also determined to find out if the antibacterial effect is conditioned by the irradiation by daylight. It has already been demonstrated in section 5.2.4 that the Cu content represents one of the most important factors affecting the antibacterial efficiency. Several Al-Cu-N films with various Cu contents ranging from 0.0 at.% up to 17 at.% were prepared at different deposition conditions and the antibacterial tests were performed. The structure and characteristics of these films as well as the corresponding deposition conditions are shown in Fig 5.3.20. As can be seen the structure of the selected films ranges from pure well-crystalline h-AlN via a very fine-grained nc-h-AlN/nc-Cu nanocomposite towards a nanocomposite film composed of a mixture of nanocrystalline h-AlN phase with a relatively high content of a crystalline Cu phase.

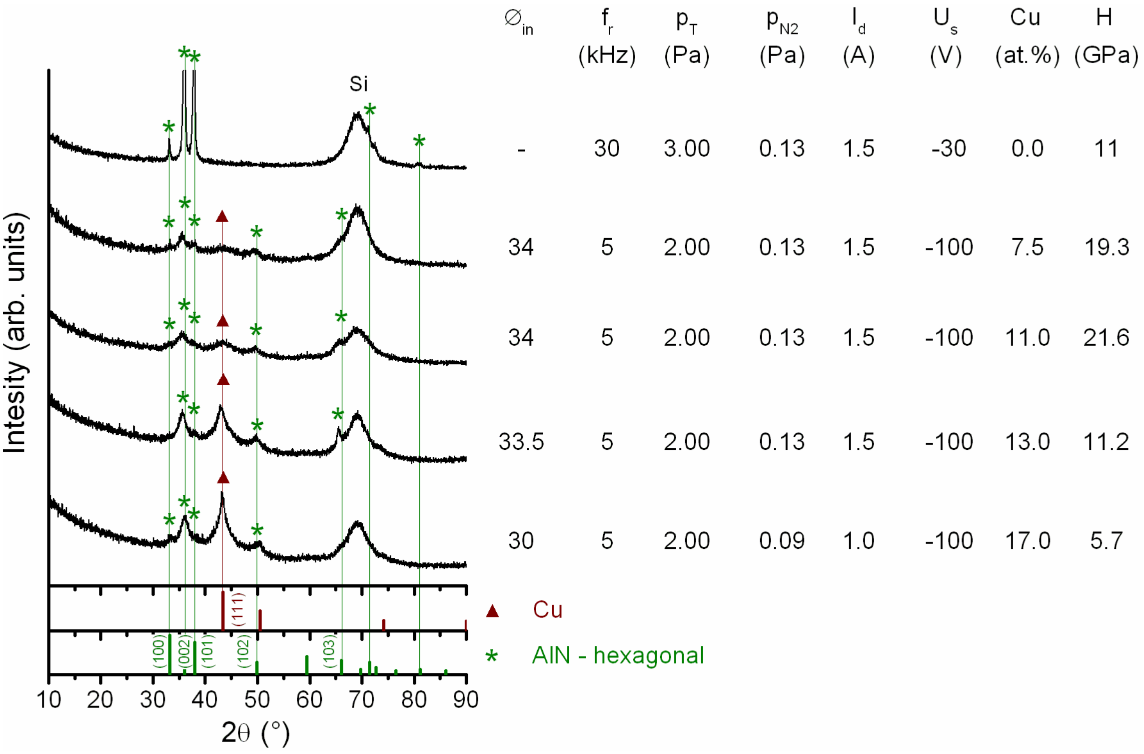

Ø_{in}	f_r (kHz)	p_T (Pa)	p_{N2} (Pa)	I_d (A)	U_s (V)	Cu (at.%)	H (GPa)
-	30	3.00	0.13	1.5	-30	0.0	11
34	5	2.00	0.13	1.5	-100	7.5	19.3
34	5	2.00	0.13	1.5	-100	11.0	21.6
33.5	5	2.00	0.13	1.5	-100	13.0	11.2
30	5	2.00	0.09	1.0	-100	17.0	5.7

Fig. 5.3.20: XRD patterns, selected deposition parameters and characteristics of AlN/Si film and Al-Cu-N/Si films with various Cu contents tested for antibacterial efficiency. Deposition conditions: p_{N2}=0.13 Pa, I_d=1.5 A, T_s=400 °C and $d_{s\text{-}t}$= 80 mm. “Si” indicates reflection of the Si(100) substrate. $Ø_{in}$ denoted as “-” represents pure AlN film deposited using two Al targets without Cu rings.

The antibacterial efficiency as a function of the contact time in the daylight and for t=5 h in the dark is shown in Fig. 5.3.21. The antibacterial efficiency of all Al-Cu-N films increases with an increasing t. The fastest antibacterial effect is observed for the Al-Cu-N film with the highest Cu content (≈17 at.%). In this case 100 % of all *E. coli* bacteria is inactivated within 1 hour (see Fig. 5.3.22). The Al-Cu-N films with the Cu content <17 at.% exhibit a lower antibacterial efficiency for t=1 h. However all these films achieve E=100 % when the contact time is increased to 3 h. The antibacterial efficiency of E=100 % is also observed in the dark. This suggests that the antibacterial effect of Al-Cu-N films is caused by presence of Cu ions rather than by photocatalytic reaction. The antibacterial efficiency of a pure AlN film was also determined. However no significant antibacterial effect was observed in any of the tests.

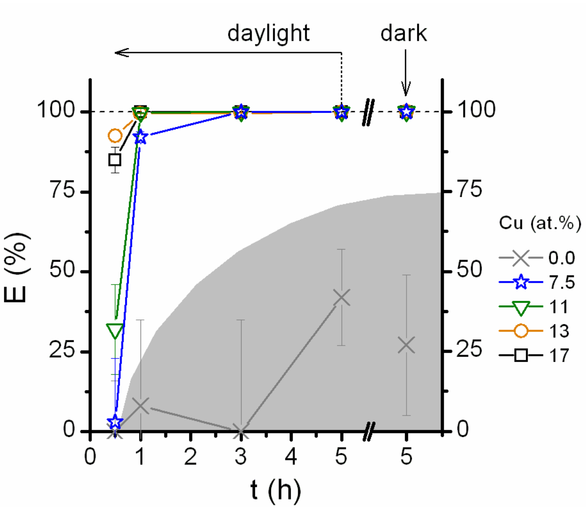

Fig. 5.3.21: Antibacterial efficiency *E* of Al-Cu-N/Si films with various Cu contents as a function of contact time *t*.

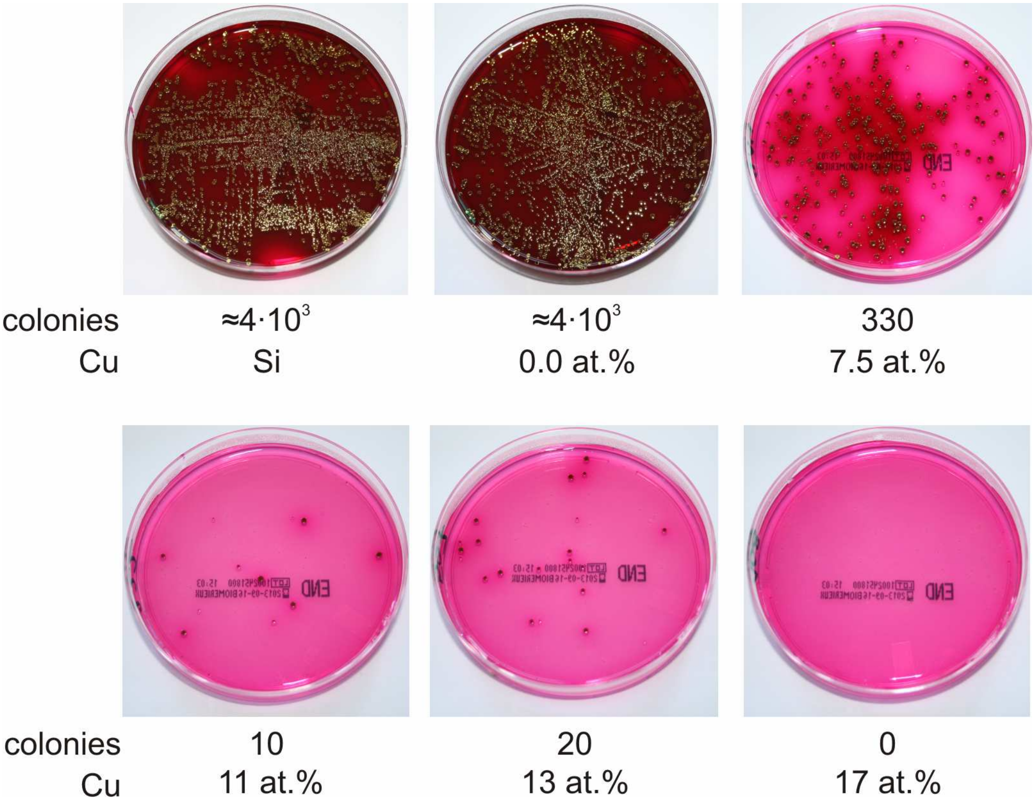

Fig. 5.3.22: Photos of Petri dishes with Endo agar and bacterial colonies cultivated from a bacterial suspension which was in contact with the Si substrate and the Al-Cu-N/Si films with various Cu contents in the daylight for 1 h.

Photos of Petri dishes after performing the antibacterial test with *t*=1 h in the daylight are shown in Fig. 5.3.22. Together with the data provided in Fig. 5.3.21 these photos illustrate the effect of the Cu content in the film on its antibacterial efficiency. Clearly the reference AlN film exhibits a comparable concentration of bacterial colonies with the reference Si substrate. As the Cu content in the film increases, the number of colonies generally decreases and for the film with the highest Cu content of 17 at.% no bacterial colonies are observed on the Petri dish. Although the Al-Cu-N film with 7.5 at.% of Cu exhibits antibacterial efficiency of 92.1 % after 1h in the daylight, *E*=100 % is achieved after *t*=3 h. This shows, that a Cu content as low as 7.5 at.% is sufficient to effectively eliminate *E. coli* bacteria on its surface.

Aging of antibacterial Al-Cu-N films

The effect of the number of antibacterial tests performed with a single Al-Cu-N film on its antibacterial efficiency was also investigated. For that purpose two Al-Cu-N/Si films with Cu contents of 7.5 at.% and 17 at.% were selected. As described above these films are able to eliminate 100 % of the *E. coli* bacteria in the daylight within 3 h and 1 h, respectively. Fig. 5.3.23 shows the antibacterial efficiency of these two films in four consecutive antibacterial tests performed with a contact time of 5 hours in the dark. The antibacterial efficiency of both films in the first two tests is 100 %. However in the third test the antibacterial efficiency of the Al-Cu-N film with 17 at.% is reduced to ≈95 % and similar value is observed in the following fourth test as well. In the case of Al-Cu-N film with 7.5 at.% a reduction of *E* from 100 % down to ≈88 at.% occurred between the third and the fourth test. This might be explained by a gradual leaching of copper from the Al-Cu-N film resulting in a decreased concentration of Cu ions available in the consecutive test. Using the XRF method no measurable difference of the Cu content in the Al-Cu-N films was observed (not shown). However the antibacterial action might be related to a very thin surface layer of the Al-Cu-N film. Thus another analytical method would be more suitable to check a possible decrease of the Cu content in the surface layer. Although more experimental data would be appropriate to confirm the trend observed in Fig. 5.3.23, the results already at hand might indicate a possible weak point of the antibacterial films based on presence of copper or silver i.e. gradual decrease of the antibacterial effect.

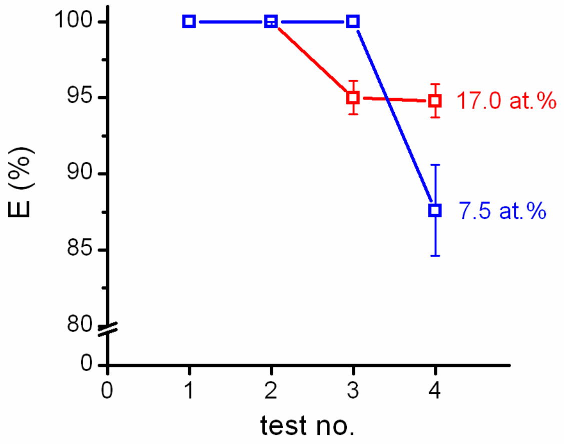

Fig. 5.3.23: Antibacterial efficiency *E* of two Al-Cu-N/Si films with various Cu contents as a function of number of antibacterial tests performed. In all tests the bacteria were in contact with the Al-Cu-N/Si films for 5 h in the dark.

From the point of view of fabrication of a multifunctional Al-Cu-N film the most important finding of this section is that already 7.5 at.% of Cu represents a sufficient Cu content providing a strong antibacterial effect. Moreover this antibacterial effect is independent of the presence of visible light and the film can effectively kill *E. coli* bacteria in the daylight as well as in the dark.

5.3.9 Designing a multifunctional Al-Cu-N film

The main goal of this study was to develop an antibacterial Al-Cu-N film with an enhanced hardness and an enhanced resistance to cracking. Based on the results presented in sections 5.3.1.-5.3.8. the following conditions need to be fulfilled to achieve the individual properties:

Hardness
It has been demonstrated that Al-Cu-N films exhibit a high hardness ($H \geq 19$ GPa) if (1) the Cu content in the film ranges from ≈4.4 at.% to ≈11 at.% and (2) a sufficient energy is delivered to the growing film. The latter can be increased e.g. by increasing the discharge current ($I_d \geq 1.5$ A), applying substrate bias ($U_s = -100$ V) or by decreasing the total pressure.

Antibacterial effect
The antibacterial efficiency of Al-Cu-N films generally increases with an increasing Cu content. However a Cu content as low as 7.5 at.% is sufficient to achieve 100 % killing of *E. coli* bacteria within 3 hours in the daylight or 5 hours in the dark.

Resistance to cracking in indentation test
The nanocomposite Al-Cu-N films with an enhanced resistance to cracking in the indentation test are characterized by (1) a very fine-grained nanocomposite structure composed of a mixture of nanocrystalline nc-h-AlN and nc-Cu phases i.e. nc-h-AlN/nc-Cu, (2) a Cu content of ≈9 at.% and (3) $H \geq 16.9$ GPa, $W_e \geq 67$ %, $H/E^* \geq 0.106$ and $\sigma \leq -1.0$ GPa. The indentation depth to film thickness ratio d/h however needs to be lower than ≈0.8 to avoid a strong interaction with the brittle Si substrate.

Resistance to cracking in bending test
The fine-grained nanocomposite nc-h-AlN/nc-Cu films exhibit enhanced resistance to cracking in bending characterized by absence of cracks for film strains up to $\varepsilon = 1.00$ % if the magnitude of compressive macrostress is ≥1.0 GPa (i.e. $\sigma \leq -1.0$ GPa). The compressive macrostress in the film can be increased e.g. by decreasing the total pressure of the gas mixture.

The conditions presented above such as the Cu content or mechanical properties represent values or ranges for which the required properties were experimentally confirmed. However it is very likely that the given intervals are wider and their further extension is possible. To verify the validity of the statements presented above a single Al-Cu-N film was prepared at optimized deposition conditions (see Tab. 5.8) and its mechanical properties, antibacterial properties and resistance to cracking were measured.

Tab. 5.8: Optimized process parameters used for deposition of a hard antibacterial Al-Cu-N/Si film with enhanced resistance to cracking.

d_{s-t} (mm)	$Ø_{in}$ (mm)	f_r (kHz)	p_T (Pa)	p_{N2} (Pa)	I_d (A)	U_s (V)	i_s (mA/cm^2)	T_s (°C)
80	34	5	1.75	0.13	1.5	-100	138	400

The deposition conditions listed in Tab.5.8 resulted in the formation of an Al-Cu-N film, whose structure and other characteristics are shown in Fig. 5.3.24. The film is characterized by a Cu content of 9.6 at.% and relatively broad low intensity reflections of both h-AlN and Cu phases indicating a nanocomposite nc-h-AlN/nc-Cu structure. A high hardness of H=21.9 GPa was achieved and values of the other characteristics (h=2730 nm, W_e=74 %, H/E^*>0.122, σ=-1.7 GPa) comply with the requirements for an enhanced resistance to cracking. As can be seen from Fig. 5.3.25 no cracks were observed in the film after performing the indentation as well as bending tests even for the highest indenter load (L=1.00 N) or film strain (ε=1.01 %), respectively. It is important to point out that the deposition rate of the Al-Cu-N film was ≈63.5 nm/min which is significantly higher compared to the hard Al-Cu-O film that also exhibited enhanced resistance to cracking.

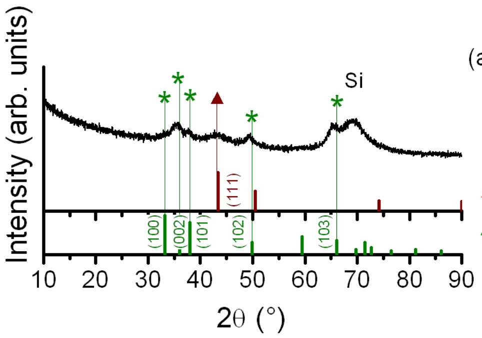

Cu (at.%)	h (nm)	σ (GPa)	H (GPa)	E* (GPa)	W_e (%)	H/E*	H^3/E^{*2} (GPa)
9.6	2730	-1.7	21.9	180	74	0.122	0.324

Fig. 5.3.24: XRD patterns and characteristics of an optimized Al-Cu-N/Si film. “Si” indicates reflection of the Si(100) substrate. Deposition conditions are summarized in Tab. 5.8.

Indentation test

L (N)	0.25	0.50	0.75	1.00
d/h	0.318	0.484	0.622	0.744
cracks	no	no	no	no

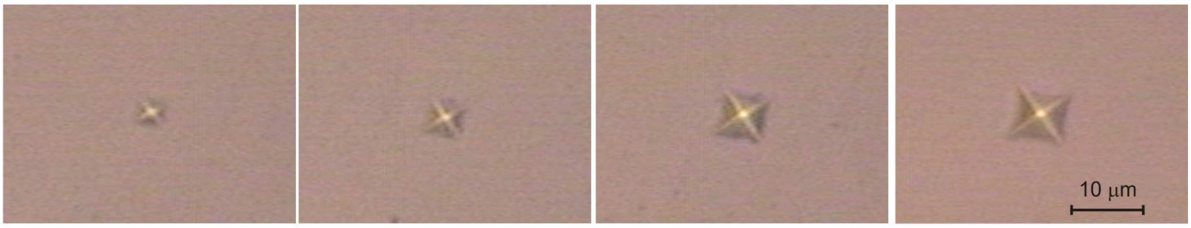

Bending test

ε (%)	0.61	0.76	1.01
cracks	no	no	no

Fig. 5.3.25: Performance of the optimized Al-Cu-N/Si film in the indentation test using different loads L and in the bending test at different film strains ε.

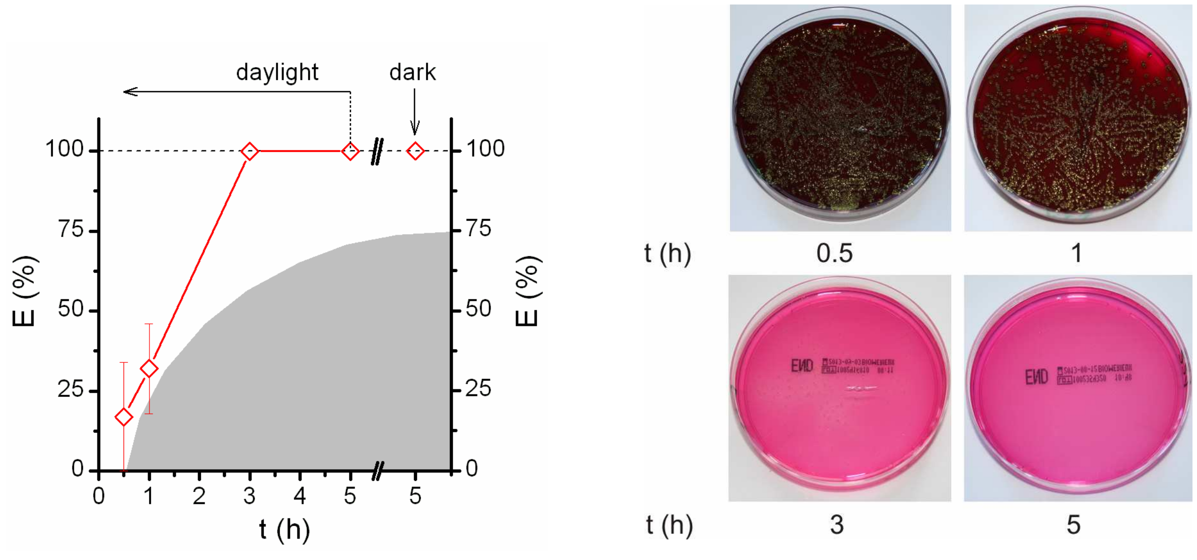

a) **b)**

Fig. 5.3.26: a) Antibacterial efficiency *E* of an optimized hard and tough Al-Cu-N/Si film resistant to cracking as a function of contact time *t*. b) Petri dishes showing results of the tests performed in the daylight.

The antibacterial efficiency of the optimized nanocomposite Al-Cu-N film as a function of the contact time *t* is shown in Fig. 5.3.26 a). The photos of Petri dishes corresponding to tests with different *t* in the daylight are displayed in Fig. 5.3.26 b). As expected the Cu content of 9.6 at.% is high enough to completely restrict the growth of bacterial colonies within a contact time of 3 h in the daylight and the same antibacterial efficiency (*E*=100 %) has also been achieved for *t*=5 h in the dark. As can be seen from Fig. 5.3.26 a) the antibacterial efficiency observed for *t*=1 h in the daylight is relatively low (*E*(1 h)=32 %) compared, for example, to *E*(1 h)=92.1 % observed for the Al-Cu-N film with 7.5 at.% of Cu presented in Fig. 5.3.21. This difference might be attributed to a lower surface roughness of the Al-Cu-N film with 9.6 at.% of Cu (R_a=3.0 nm) compared to the film with 7.5 at.% of Cu (R_a=4.5 nm). Based on their experiments, Bagheriche et al. suggested that the most effective inactivation of *E. coli* bacteria on the surface of Ag-ZrN films is achieved if the overall content of Ag and the size of Ag particles are optimized to obtain the highest amount of active Ag sites i.e. the highest surface area of Ag particles [157]. Similarly a lower surface area, i.e. a lower roughness, of the Al-Cu-N film with 9.6 at.% of Cu might result in a reduced antibacterial efficiency of this film. A further optimization of the antibacterial effect is however possible. This can be achieved e.g. by slightly increasing the Cu content yet keeping it below 11 at.% to sustain the high hardness and high resistance to cracking or by increasing the surface roughness.

In conclusion, deposition conditions have been identified that are required for fabrication of a hard antibacterial Al-Cu-N film with enhanced resistance to cracking. A single Al-Cu-N film has been prepared at a relatively high deposition rate and its multifunctional nature was verified.

6. Conclusions

The subject of this Ph.D. thesis was to develop three kinds of new nanostructured films containing copper - (1) Al-Cu-O, (2) Cr-Cu-O and (3) Al-Cu-N – and to investigate their physical, mechanical and antibacterial properties. These films were prepared by pulsed reactive magnetron sputtering using a dual magnetron system. The results of the study can be summarized as follows:

6.1 Hard nanocrystalline Al-Cu-O films resistant to cracking

Al-Cu-O films with Cu content of up to 16 at.% were prepared and the effect of Cu addition on their structure, mechanical properties and resistance to cracking was studied in detail. It was found that alloying of nanocrystalline Al_2O_3 films with up to 16 at.% of Cu results in a formation of nanocomposite films composed of crystalline nanograins embedded in amorphous a-(Al–Cu–O) matrix. The structure of the nanograins continuously varies from γ-Al_2O_3 through $(Al_{8-2x},Cu_{3x})O_{12}$ solid solution to $CuAl_2O_4$. The hardness, the effective Young’s modulus and the elastic recovery significantly increase with increasing Cu content. For ≈16 at.% of Cu the nanocomposite films exhibit a high hardness H≈20 GPa, a low effective Young’s modulus E^*≈150 GPa and a very high elastic recovery W_e≈77 %. For Cu content ≥3.5 at.% the increase of the effective Young’s modulus is slowed down compared to the increase of hardness resulting in a high ratio $H/E^*>0.1$. The indentation test showed that the nanocomposite Al-Cu-O films with >2 at.% exhibit an enhanced resistance to cracking compared to pure Al_2O_3 film. The films with enhanced resistance to cracking are characterized by high ratio $H/E^*>0.1$, low effective Young’s modulus and compressive residual stress of $\sigma \approx -2$ GPa. It has also been demonstrated in this study that changing the pulse length on the individual magnetrons of the dual magnetron system represents an efficient tool for controlling the concentration of the alloying element in the growing film.

6.2 Antibacterial Cr-Cu-O films

The effects of Cu content and annealing temperature on the structure, antibacterial and mechanical properties of Cr-Cu-O films were investigated. It was observed that the as-deposited Cr–Cu–O films with ≈10 at.% of Cu are composed of a mixture of Cr_2O_3 and $CuCrO_4$ phases. For a Cu content ≥15 at.% the films exhibit amorphous structure. Rapid thermal annealing of Cr–Cu–O films with ≈20 at.% of Cu up to 700 °C resulted in a change of the film structure from amorphous via a mixture of crystalline CuO and tetragonal $CuCr_2O_4$ phases to a delafossite $CuCrO_2$ phase. The antibacterial efficiency of the as-deposited Cr–Cu–O films increases with an increasing Cu content. For a Cu content >15 at.% the films efficiently kill the *E. coli* bacteria and are able to eliminate 100% of the bacteria within the contact time of 3 hours. It was demonstrated that the antibacterial efficiency depends on the phase composition of the Cr-Cu-O film. The highest antibacterial efficiency was observed for amorphous as-deposited film and for crystalline film with a delafossite $CuCrO_2$ structure. The killing of *E. coli* bacteria by the Cr-Cu-O film requires no excitation by UV or visible light and operates both in the daylight as well as in the dark. The antibacterial Cr-Cu-O films exhibit a hardness of ≈4 GPa and their mechanical properties are stable up to 500 °C. It was shown that transparent antibacterial Cr-Cu-O films can be prepared if their thickness is reduced. This way a transmittance of 42.5 % was achieved for a 70 nm thin antibacterial film.

6.3 Hard antibacterial Al-Cu-N films resistant to cracking

The effect of different deposition parameters on the properties of Al-Cu-N films was investigated in detail. It was found that Al-Cu-N films with a high hardness reaching up to ≈23 GPa can be prepared if the Cu content in the film is reduced below ≈11 at.% and a sufficient energy is delivered to the growing film. The energy delivered to the growing film can be increased by increasing the substrate bias or the discharge current or by decreasing the total pressure. The hard Al-Cu-N films are characterized by a very fine-grained nanocomposite structure composed of a mixture of nanocrystalline h-AlN and nanocrystalline Cu phases. The hard nanocomposite Al-Cu-N films exhibit enhanced resistance to cracking in the indentation test. The observation of cracks in the indentation test however strongly depends on the indentation depth to film thickness ratio d/h. The resistance of Al-Cu-N films to cracking in bending is independent of the film thickness and increases with an increasing magnitude of the compressive macrostress, which can be effectively controlled by the total pressure of the gas mixture. Antibacterial tests showed that the Al-Cu-N films are able to inactivate *E. coli* bacteria in the daylight as well as in the dark. The antibacterial efficiency generally increases with an increasing Cu content but already 7.5 at.% of Cu is sufficient to inactivate 100 % of the bacteria within 3 hours in the daylight.

Based on the experimental results, an optimized multifunctional Al-Cu-N film was prepared at a high deposition rate ($a_D \approx 63.5$ nm/min). This film is characterized by a Cu content of 9.6 at.% and a nanocomposite structure composed of a mixture of very fine nanocrystals of h-AlN and Cu phases. It exhibits a high hardness ($H \approx 22$ GPa) and high elastic recovery ($W_e \approx 74$), H/E^* ratio >0.1 and compressive macrostress of $\sigma = -1.7$ GPa. Such film is resistant to cracking in the indentation as well as in the bending tests and it is able to efficiently kill *E. coli* bacteria on its surface in the daylight as well as in the dark.

All results presented in this thesis are original and have been published in the scientific journal Applied Surface Science and presented at three international scientific conferences. The obtained results contribute to expansion of the current knowledge in the field of thin films.

References

[1] J. Musil, J. Vlček, P. Baroch, Magnetron Discharges for Thin Films Plasma Processing, in: Y. Pauleau, Materials surface processing by derected energy techniques, Elsevier Ltd., London, (2006) 67–110.

[2] I. Safi, Recent aspects concerning DC reactive magnetron sputtering of thin films: a review, Surface and Coatings Technology 127 (2000) 203-218.

[3] J. Musil, P. Baroch, J. Vlček, K.H. Nam, J.G. Han, Reactive magnetron sputtering of thin films: present status and trends, Thin Solid Films 475 (2005) 208– 218.

[4] J. Vlček, A.D. Pajdarová, J. Musil, Pulsed dc Magnetron Discharges and their Utilization in Plasma Surface Engineering, Contributions to Plasma Physics 44 (2004) 426 – 436.

[5] J.S.Chapin: Sputtering process and apparatus, US Patent 4166018, Airco, NJ, U.S.A. (1979).

[6] P.Eh. Hovsepian, Q. Luo, G. Robinson, M. Pittman, M. Howarth, D. Doerwald, R. Tietema, W.M. Sim, A. Deeming, T. Zeus, TiAlN/VN superlattice structured PVD coatings: A new alternative in machining of aluminium alloys for aerospace and automotive components, Surface and Coatings Technology 201 (2006) 265–272.

[7] V. Fox, J. Hampshire, D. Teer, MoS_2/metal composite coatings deposited by closed-field unbalanced magnetron sputtering: tribological properties and industrial uses, Surface and Coatings Technology 112 (1999) 118–122.

[8] S. Zhao, E. Avendaño, K. Gelin, J. Lu, E. Wäckelgård, Optimization of an industrial DC magnetron sputtering process for graded composition solar thermal absorbing layer, Solar Energy Materials and Solar Cells 90 (2006) 308–328.

[9] Y. Song, T. Sakurai, High-rate, low-temperature radical-assisted sputtering coater and its applications for depositing high-performance optical filters, Vacuum 74 (2004) 409–415.

[10] T. Hurkmans, F. Hauzer, B. Bud, K. Engel, R. Tietema, A new large volume PVD coating system using advanced controlled arc and combined arc/unbalanced magnetron (ABS^{TM}) deposition techniques, Surface and Coatings Technology 92 (1997) 62-68.

[11] Y.S. Ocak, M.F. Genisel, T. Kılıçoğlu, Ta/Si Schottky diodes fabricated by magnetron sputtering technique, Microelectronic Engineering 87 (2010) 2338–2342.

[12] P.J. Kelly, G. West, Y.N. Kok, J.W. Bradley, I. Swindells, G.C.B. Clarke, A comparison of the characteristics of planar and cylindrical magnetrons operating in pulsed DC and AC modes, Surface and Coatings Technology 202 (2007) 952–956.

[13] J. T. Gudmundsson, N. Brenning, D. Lundin and U. Helmersson, High power impulse magnetron sputtering discharge, Journal of Vacuum Science and Technology A 30 (2012) 030801.

[14] J. Lin, W. D. Sproul, J. J. Moore, Z. Wu, S. Lee, R. Chistyakov, B. Abraham, Recent advances in Modulated Pulsed Power Magnetron sputtering for surface engineering, JOM 63 (2011) 48-58.

[15] K. Hori, T. Namazu, S. Inoue, Effect of Cu content on the shape memory behavior of Ti–Ni–Cu alloy thin films prepared by triple-source dc magnetron sputtering, Thin Solid Films 518 (2010) S26-S28.

[16] J.F. Chang, H.Y. Ueng, T.F. Young, Y.C. Wang, W.C. Hwang, Combined magnetron sputtering and ECR-CVD deposition of diamond-like carbon films, Surface and Coatings Technology 157 (2002) 179-184.

[17] K. Yamamoto, S. Kujime, K. Takahara, Properties of nano-multilayered hard coatings deposited by a new hybrid coating process: Combined cathodic arc and unbalanced magnetron sputtering, Surface and Coatings Technology 200 (2005) 435-439.

[18] J.G. Jones, C. Muratore, A.R. Waite, A.A. Voevodin, Plasma diagnostics of hybrid magnetron sputtering and pulsed laser deposition, Surface and Coatings Technology 201 (2006) 4040-4045.

[19] D. Bharathi Mohan, A. Cavaleiro, Experimental development and deposition of nanocomposite films by a hybrid dc magnetron sputtering and cluster gun technique, Vacuum 83 (2009) 1257-1261.

[20] J. C. Sellers, The disappearing anode myth: strategies and solutions for reactive PVD from single magnetrons, Surface and Coatings Technology 91-95 (1997) 184- 188.

[21] K. Koski, J. Hölsä, P. Juliet, Surface defects and arc generation in reactive magnetron sputtering of aluminium oxide thin films, Surface and Coatings Technology 115 (1999) 163–171.

[22] S. Schiller, K. Goedicke, J. Reschke, V. Kirchhoff, S. Schneider, F. Milde, Pulsed magnetron sputter technology, Surface and Coatings Technology 61 (1993) 331-337.

[23] A. Anders, Physics of arcing, and implications to sputter deposition, Thin Solid Films 502 (2006) 22 – 28.

[24] P.J. Kelly, R.D. Arnell, Magnetron sputtering: a review of recent developments and applications, Vacuum 56 (2000) 159-172.

[25] M. Meissner, T. Tölg, P. Baroch, J. Musil, Elimination of Arcing in Reactive Sputtering of Al_2O_3 Thin Films Prepared by DC Pulse Single Magnetron, Plasma Processes and Polymers 8 (2011) 500-504.

[26] A. Belkind, A. Freilich, R. Scholl, Pulse duration effects in pulse-power reactive sputtering of Al_2O_3, Surface and Coatings Technology 108–109 (1998) 558–563.

[27] M. Åstrand, T.I. Selinder, M.E. Sjöstrand, Deposition of $Ti_{1-x}Al_xN$ using bipolar pulsed dual magnetron sputtering, Surface and Coatings Technology 200 (2005) 625-629.

[28] J. Šícha, O. Novák, J. Vlček, P. Kudláček, Ion Flux Characteristics in Pulsed Dual Magnetron Discharges Used for Deposition of Photoactive TiO_2 Films, Plasma Processes and Polymers 8 (2011) 191–199.

[29] O. Zywitzki, G. Hoetzsch, F. Fietzke, K. Goedicke , Effect of the substrate temperature on the structure and properties of Al_2O_3 layers reactively deposited by pulsed magnetron sputtering, Surface and Coatings Technology 82 (1996) 169-175.

[30] P. Baroch, J. Musil, Plasma Drift in Dual Magnetron Discharge, IEEE Transactions on plasma science 36 (2008) 1412-1413.

[31] J. Musil, P. Baroch, High-rate pulsed reactive magnetron sputtering of oxide nanocomposite coatings, Vacuum 87 (2013) 96-102.

[32] A. Belkind, S. Song, G. McDonough, R. Scholl, Biased Dual Magnetron Sputter Deposition of Alumina, Proceedings of the 45th Annual Technical Conference, Society of Vacuum Coaters 2002 (2002) 184-189.

[33] J. O'Brien, P. J. Kelly, J. W. Bradley, R. Hall, R. D. Arnell, Substrate Response During Dual Bipolar Pulsed Magnetron Sputtering, Proceedings of the 45th Annual Technical Conference, Society of Vacuum Coaters 2002 (2002) 184-189.

[34] E. Kusano, A. Sato, N. Kikuchi, H. Nanto, A. Kinbara, Preparation of TiC films by alternate deposition of Ti and C layers using a dual magnetron sputtering source, Surface and Coatings Technology 120–121 (1999) 378-382.

[35] P. Baroch, J. Musil, J. Vlcek, K.H. Nam, J.G. Han, Reactive magnetron sputtering of TiO_x films, Surface and Coatings Technology 193 (2005) 107-111.

[36] A. Aijaz, D. Lundin, P. Larsson, U. Helmersson, Dual-magnetron open field sputtering system for sideways deposition of thin films, Surface and Coatings Technology, 204 (2010) 2165-2169.

[37] R.J.D. Tilley, Understanding solids, John Wiley & Sons Ltd., Chichester, (2004).

[38] R.W. Hertzberg, Deformation and Fracture Mechanics of Engineering Materials, 4th edition, John Wiley & Sons Ltd., (1996).

[39] A. H. De Aza, J. Chevalier, G. Fantozzi, M. Schehl, R. Torrecillas, Crack growth resistance of alumina, zirconia and zirconia toughened alumina ceramics for joint prostheses, Biomaterials 23 (2002) 937-945.

[40] Zhihui Li, Baiqing Xiong, Yongan Zhang, Baohong Zhu, Feng Wang, Hongwei Liu, Investigation on strength, toughness and microstructure of an Al–Zn–Mg–Cu alloy pre-stretched thick plates in various ageing tempers, Journal of Materials Processing Technology 209 (2009) 2021-2027.

[41] N. Vardar, A. Ekerim, Failure analysis of gas turbine blades in a thermal power plant, Engineering Failure Analysis 14 (2007) 743-749.

[42] M. Jirout, Houževnatost tvrdých vrstev připravených magnetronovým naprašováním, Ph.D. thesis, University of West Bohemia in Pilsen, (2007).

[43] F. Kustas, B. Mishra, J. Zhou, Metal/carbide co-sputtered wear coatings, Surface and Coatings Technology 120–121 (1999) 489-494.

[44] J. Soldán, J. Musil, Structure and mechanical properties of DC magnetron sputtered TiC/Cu films, Vacuum 81 (2006) 531-538.

[45] B. Lotfi, P.H. Shipway, D.G. McCartney, H. Edris , Abrasive wear behaviour of Ni(Cr)–TiB_2 coatings deposited by HVOF spraying of SHS-derived cermet powders, Wear 254 (2003) 340-349.

[46] R.S. Mishra, A.K. Mukherjee, Processing of high hardness-high toughness alumina matrix nanocomposites, Materials Science and Engineering 301 (2001) 97-101.

[47] M. Kašiarová, J. Winzer, L. Weiler, J. Dusza, Fracture characterization of Al_2O_3/Cu with different amount of copper, Powder Metallurgy Progress 8 (2008) 315-319.

[48] A.A. Voevodin, S. V. Prasad, J. S. Zabinski, Nanocrystalline carbide/amorphous carbon composites, Journal of Applied Physics 82 (1997) 855-858.

[49] A.A Voevodin, J.J Hu, J.G Jones, T.A Fitz, J.S Zabinski, Growth and structural characterization of yttria-stabilized zirconia–gold nanocomposite films with improved toughness, Thin Solid Films, 401 (2001) 187-195.

[50] U. Wiklund, P. Hedenqvist, S. Hogmark, Multilayer cracking resistance in bending, Surface and Coatings Technology 97 (1997) 773-778.

[51] J.Y. Zhang, G. Liu, X. Zhang, G.J. Zhang, J. Sun, E. Ma, A maximum in ductility and fracture toughness in nanostructured Cu/Cr multilayer films Scripta Materialia 62 (2010) 333-336.

[52] A. Leyland, A. Matthews, On the significance of the H/E ratio in wear control: a nanocomposite coating approach to optimised tribological behaviour, Wear 246 (2000) 1-11.

[53] P. Wu, H.M. Du, X.L. Chen, Z.Q. Li, H.L. Bai, E.Y. Jiang, Influence of WC particle behavior on the wear resistance properties of Ni–WC composite coatings, Wear 257 (2004) 142-147.

[54] Z. Xia, L. Riester, W.A. Curtin, H. Li, B.W. Sheldon, J. Liang, B. Chang, J.M. Xu, Direct observation of toughening mechanisms in carbon nanotube ceramic matrix composites, Acta Materialia 52 (2004) 931-944.

[55] J.-H. Shin, S.-H. Hong, Microstructure and Properties of Single Wall Carbon Nanotube Reinforced Yttria Stabilized Zirconia Ceramics, 221st ECS Meeting abstracts, The Electrochemical Society (2012) 1205-1205.

[56] D. Casellas, F.L. Cumbrera, F. Sánchez-Bajo, W. Forsling, L. Llanes, M. Anglada, On the transformation toughening of Y–ZrO_2 ceramics with mixed Y–TZP/PSZ microstructures,
Journal of the European Ceramic Society 21 (2001) 765-777.

[57] J. Musil, Hard nanocomposite coatings: Thermal stability, oxidation resistance and toughness, Surface and Coatings Technology 207 (2012) 50-65.

[58] X.C. Zhang, C.J. Liu, F.Z. Xuan, Z.D. Wang, S.T. Tu, Effect of residual stresses on the strength and fracture energy of the brittle film: Multiple cracking analysis, Computational Materials Science 50 (2010) 246–252.

[59] M. Jirout, J. Musil, Effect of addition of Cu into ZrO_x film on its properties, Surface and Coatings Technology 200 (2006) 6792-6800.

[60] J. Soldán, Preparation and characterization of new nanocomposite films, Ph.D. thesis, University of West Bohemia in Pilsen, (2008).

[61] K. Zhang, M. Wen, Q.N. Meng, C.Q. Hu, X. Li, C. Liu, W.T. Zheng, Effects of substrate bias voltage on the microstructure, mechanical properties and tribological behavior of reactive sputtered niobium carbide films, Surface and Coatings Technology 212 (2012) 185-191.

[62] K. Chu, P.W. Shum, Y.G. Shen, Substrate bias effects on mechanical and tribological properties of substitutional solid solution (Ti, Al)N films prepared by reactive magnetron sputtering, Materials Science and Engineering: B 131 (2006) 62-71.

[63] S. Zhang, X. Zhang, Toughness evaluation of hard coatings and thin films, Thin Solid Films 520 (2012) 2375-2389.

[64] J.O. Carneiro, J.P. Alpuim, V. Teixeira, Experimental bending tests and numerical approach to determine the fracture mechanical properties of thin ceramic coatings deposited by magnetron sputtering, Surface and Coatings Technology 200 (2006) 2744-2752.

[65] K.W. McElhaney, Q. Ma, Investigation of moisture-assisted fracture in SiO_2 films using a channel cracking technique, Acta Materialia 52 (2004) 3621-3629.

[66] J. Musil, J. Sklenka, R. Cerstvy, Transparent Zr–Al–O oxide coatings with enhanced resistance to cracking, Surface and Coatings Technology 206 (2012) 2105-2109.

[67] J. Musil, R. Jílek, M. Meissner, T. Tölg, R. Čerstvý, Two-phase single layer Al-O-N nanocomposite films with enhanced resistance to cracking, Surface and Coatings Technology 206 (2012) 4230-4234.

[68] H. Ollendorf, D. Schneider, Th. Schwarz, G. Kirchhoff, A. Mucha, A comparative study of the mechanical properties of TiN coatings using the non-destructive surface acoustic wave method, scratch test and four-point bending test, Surface and Coatings Technology 84 (1996) 458-464.

[69] U. Wiklund, M. Bromark, M. Larsson, P. Hedenqvist, S. Hogmark, Cracking resistance of thin hard coatings estimated by four-point bending, Surface and Coatings Technology (1997) 57-63.

[70] Z. Chen, Z. Gan, Fracture toughness measurement of thin films on compliant substrate using controlled buckling test, Thin Solid Films 515 (2007) 3305-3309.

[71] Z. Chen, B. Cotterell, W. Wang, The fracture of brittle thin films on compliant substrates in flexible displays, Engineering Fracture Mechanics 69 (2002) 597-603.

[72] P. Jedrzejowski, J.E. Klemberg-Sapieha, L. Martinu, Relationship between the mechanical properties and the microstructure of nanocomposite TiN/SiN$_{1.3}$ coatings prepared by low temperature plasma enhanced chemical vapor deposition, Thin Solid Films 426 (2003) 150-159.

[73] Linhai Tian, Yang Zhang, Yong Ma, Xiaodong Zhu, Bin Tang, Effect of Cu content and ion beam bombardment on microstructure and mechanical properties of Cr–Cu–N films, Surface and Coatings Technology 228 (2013) S495-S498.

[74] P. Kodali, K.C. Walter, M. Nastasi, Investigation of mechanical and tribological properties of amorphous diamond-like carbon coatings, Tribology International 30 (1997) 591-598.

[75] Xiaodong Li, Bharat Bhushan, Evaluation of fracture toughness of ultra-thin amorphous carbon coatings deposited by different deposition techniques, Thin Solid Films 355–356 (1999) 330-336.

[76] Xiaodong Li, Bharat Bhushan, Micro/nanomechanical characterization of ceramic films for microdevices, Thin Solid Films 340 (1999) 210-217.

[77] J. Musil, M. Jirout, Toughness of hard nanostructured ceramic thin films, Surface and Coatings Technology 201 (2007) 5148-5152.

[78] H. Hosokawa, A.V. Desai, M.A. Haque, Plane stress fracture toughness of freestanding nanoscale thin films, Thin Solid Films 516 (2008) 6444-6447.

[79] B. D. Beake, M. J. I. García, J. F. Smith, Micro-impact testing: a new technique for investigating fracture toughness Thin Solid Films 398–399 (2001) 438-443.

[80] S. Zhang, D. Sun, Y. Fu, H. Du, Toughness measurement of thin films: a critical review, Surface and Coatings Technology 198 (2005) 74-84.

[81] S. Zhang, X. L. Bui, Y. Fu, D. L. Butler, H. Du, Bias-graded deposition of diamond-like carbon for tribological applications, Diamond and Related Materials 13 (2004) 867-871.

[82] G.S. Fox-Rabinovich, B.D. Beake, J.L. Endrino, S.C. Veldhuis, R. Parkinson, L.S. Shuster, M.S. Migranov, Effect of mechanical properties measured at room and elevated

temperatures on the wear resistance of cutting tools with TiAlN and AlCrN coatings, Surface and Coatings Technology 200 (2006) 5738-5742.

[83] T. Y. Tsui, Y.-Ch. Joo, A new technique to measure through film thickness fracture toughness, Thin Solid Films 401 (2001) 203-210.

[84] B. R. Lawn, A. G. Evan, D. B. MARSHALL, Elastic/Plastic Indentation Damage in Ceramics: The Median/Radial Crack System, Journal of the American Ceramic Society 63 (1980) 574–581.

[85] G. M. Pharr , Measurement of mechanical properties by ultra-low load indentation, Materials Science and Engineering: A 253 (1998) 151-159.

[86] R. F. Cook, G. M. Pharr, Direct Observation and Analysis of Indentation Cracking in Glasses and Ceramics, Journal of the American Ceramic Society 73 (1990) 787–817.

[87] D. Broek, Elementary Engineering Fracture Mechanics, Kluwer Academic Publishers, Dordrecht, (1997).

[88] Z. Xia, W.A. Curtin, B.W. Sheldon , A new method to evaluate the fracture toughness of thin films, Acta Materialia 52 (2004) 3507-3517.

[89] Xiaodong Li, Dongfeng Diao, Bharat Bhushan, Fracture mechanisms of thin amorphous carbon films in nanoindentation, Acta Materialia 45 (1997) 4453-4461.

[90] Xiaodong Li, Bharat Bhushan, Measurement of fracture toughness of ultra-thin amorphous carbon films, Thin Solid Films 315 (1998) 214-221.

[91] J. Den Toonder, J. Malzbender, G. De With, R. Balkenende, Fracture Toughness and Adhesion Energy of Sol-gel Coatings on Glass, Journal of Materials Research 17 (2002) 224-233.

[92] X. Zhang, S. Zhang , Rethinking the role that the “step” in the load–displacement curves can play in measurement of fracture toughness for hard coatings, Thin Solid Films 520 (2012) 3423-3428.

[93] J.M. Jungk, B.L. Boyce, T.E. Buchheit, T.A. Friedmann, D. Yang, W.W. Gerberich, Indentation fracture toughness and acoustic energy release in tetrahedral amorphous carbon diamond-like thin films, Acta Materialia 54 (2006) 4043-4052.

[94] P. Wellner, O. Kraft, G. Dehm, J. Andersons, E. Arzt , Channel cracking of β-NiAl thin films on Si substrates, Acta Materialia 52 (2004) 2325-2336.

[95] D. Galvan, Y.T. Pei, J.Th.M. De Hosson , Deformation and failure mechanism of nano-composite coatings under nano-indentation, Surface and Coatings Technology 200 (2006) 6718-6726.

[96] A. Czyzniewski, Optimising deposition parameters of W-DLC coatings for tool materials of high speed steel and cemented carbide, Vacuum 86 (2012) 2140-2147.

[97] A. Czyżniewski, W. Gulbiński, G. Radnóczi, M. Szerencsi, M. Pancielejko, Microstructure and mechanical properties of W-C:H coatings deposited by pulsed reactive magnetron sputtering, Surface and Coatings Technology 205 (2011) 4471-4479.

[98] T.Y. Tsui, G.M. Pharr, W.C. Oliver, .S. Bhatia, R. L. White, S. Anders, A. Anders, I. G. Brown, Nanoindentation and nanoscratching of hard carbon coatings for magnetic disks, Materials Research Society Symposium Proceedings 383 (1995) 447–451.

[99] S. Kamiya, H. Kimura, M. Saka, H. Abé, A new method for measurement of the toughness of brittle thin films, Thin Solid Films 389 (2001) 180-186.

[100] Z. Jiang, F.X. Lu, W.Z. Tang, S.G. Wang, Y.M. Tong, T.B. Huang, J.M. Liu , Accurate measurement of fracture toughness of free standing diamond films by three-point bending tests with sharp pre-cracked specimens, Diamond and Related Materials 9 (2000) 1734-1738.

[101] G. Jaeger, I. Endler, M. Heilmaier, K. Bartsch, A. Leonhardt, A new method of determining strength and fracture toughness of thin hard coatings, Thin Solid Films 377–378 (2000) 382-388.

[102] D. K. Leung, M. Y. He, A. G. Evans, Cracking resistance of nanoscale layers and films, Journal of Materials Research 10 (1995) 1693-1699.

[103] G. Stoney, The tension of metallic films deposited by electrolysis, Proceedings of the Royal Society of London, A82 (1909) 172-175.

[104] S. R. Swanson, On the mechanics of microcracking in fiber composite laminates under combined stress, Journal of Engineering Materials and Technology 111 (1989) 145-149.

[105] J. Musil, J. Sklenka, R. Čerstvý, T. Suzuki, T. Mori, M. Takahashi, The effect of addition of Al in ZrO_2 thin film on its resistance to cracking, Surface and Coatings Technology 207 (2012) 355-360.

[106] T. Nosaka, M. Yoshitake, A. Okamoto, S. Ogawa, Y. Nakayama, Thermal decomposition of copper nitride thin films and dots formation by electron beam writing, Applied Surface Science 169–170 (2001) 358-361.

[107] J.H. Hsieh, P.C. Liu, C. Li, M.K. Cheng, S.Y. Chang , Mechanical properties of TaN-Cu nanocomposite thin films, Surface and Coatings Technology 202 (2008) 5530-5534.

[108] J. Musil, P. Zeman, H. Hrubý, P.H. Mayrhofer , ZrN/Cu nanocomposite film - a novel superhard material, Surface and Coatings Technology 120–121 (1999) 179-183.

[109] J. Musil, S. Miyake, Nanocomposite coatings with enhanced hardness, in: Novel materials processing by advanced electromagnetic energy sources, Elsevier Ltd., Amsterdam (2004) 345-356.

[110] P.B. Barna, M. Adamik , Fundamental structure forming phenomena of polycrystalline films and the structure zone models, Thin Solid Films 317 (1998) 27-33.

[111] Chun-Chin Chen, Franklin Chau-Nan Hong , Structure and properties of diamond-like carbon nanocomposite films containing copper nanoparticles, Applied Surface Science, 242 (2005) 261-269.

[112] Xiaohua Zhang, Daoxin Liu, Guohua Liu, Zhenya Wang, Bin Tang , Improvement of the fretting damage resistance of Ti-811 alloy by Cu/Ni multilayer films, Tribology International 44 (2011) 1488-1494.

[113] H. Hirakata, O. Nishijima, N. Fukuhara, T. Kondo, A. Yonezu, K. Minoshima , Size effect on fracture toughness of freestanding copper nano-films, Materials Science and Engineering: A 528 (2011) 8120-8127.

[114] G. A. Pankey, L. D. Sabath, Clinical Relevance of Bacteriostatic versus Bactericidal Mechanisms of Action in the Treatment of Gram-Positive Bacterial Infections, Clinical Infectious Diseases 38 (2004) 864–70.

[115] B. Kaoutar, C. Joly, F. L'He´riteau, F. Barbut, J. Robert et al., Journal of Hospital Infection 58 (2004) 268–275.

[116] C. F. Amábile-Cuevas, Multiple Drug Resistant Bacteria, Horizon Scientific Press, (2003).

[117] A. M. R. Fernando, S. McQueen, M. Sharland, Coping with MRSA, Current Paediatrics 15 (2005) 437–442.

[118] G. Poulakou, I. Katsarolis, I. Matthaiopoulou, S. Tsiodras, S. Kanavaki et al., Nationwide surveillance of Streptococcus pneumoniae in Greece: patterns of resistance and serotype epidemiology, International Journal of Antimicrobial Agents 30 (2007) 87–92.

[119] Z. Rahim, Ch. Nakajima, R. Raqib, K. Zaman, H. P. Endtz et al., Molecular mechanism of rifampicin and isoniazid resistance in Mycobacterium tuberculosis from Bangladesh, Tuberculosis 92 (2012) 529-534.

[120] F.F. Reinthaler, J. Posch, G. Feierl, G. Wüst, D. Haas, G. Ruckenbauer, F. Mascher, E. Marth, Antibiotic resistance of E. coli in sewage and sludge, Water Research 37 (2003) 1685–1690.

[121] G.G. Rao, F. Ojo, D. Kolokithas, Vancomycin-resistant Gram-positive cocci - risk factors for faecal carriage, Journal of Hospital Infection 35 (1997) 63-69.

[122] Heng-Li Huang, Yin-Yu Chang, Jui-Ching Weng, Ya-Chi Chen, Chih-Ho Lai, Tzong-Ming Shieh, Anti-bacterial performance of Zirconia coatings on Titanium implants, Thin Solid Films 528 (2013) 151-156.

[123] G. Borkow, J. Gabbay, Copper as a Biocidal Tool, Current Medicinal Chemistry 12 (2005) 2163-2175.

[124] G. Grass, Ch. Rensing, M. Solioz, Metallic Copper as an Antimicrobial Surface, Applied and Environmental Mcrobiology 77 (2011) 1541–1547.

[125] Jun Sung Kim, Eunye Kuk, Kyeong Nam Yu, Jong-Ho Kim, Sung Jin Park et al., Antimicrobial effects of silver nanoparticles, Nanomedicine: Nanotechnology, Biology, and Medicine 3 (2007) 95– 101.

[126] Y. Kikuchi, K. Sunada, T. Iyoda, K. Hashimoto, A. Fujishima, Photocatalytic bactericidal effect of TiO2 thin films: dynamic view of the active oxygen species responsible for the effect, Journal of Photochemistry and Photobiology A: Chemistry 106 (1997) 51–56.

[127] M. Bagheri, M. Beyermann, M. Dathe, Immobilization Reduces the Activity of Surface-Bound Cationic Antimicrobial Peptides with No Influence upon the Activity Spectrum, Antimicrobial Agents and Chemotherapy, 53 (2009) 1132–1141.

[128] Yong Chen, Qiuxia Han , Designing N-halamine based antibacterial surface on polymers: Fabrication, characterization, and biocidal functions, Applied Surface Science 257 (2011) 6034-6039.

[129] Hsin-I Chang, Ming-Syun Yang, Mong Liang, The synthesis, characterization and antibacterial activity of quaternized poly(2,6-dimethyl-1,4-phenylene oxide)s modified with ammonium and phosphonium salts, Reactive & Functional Polymers 70 (2010) 944–950.

[130] A. Muñoz-Bonilla, M. Fernández-García, Polymeric materials with antimicrobial activity, Progress in Polymer Science 37 (2012) 281-339.

[131] J.H. Hsieh, T.H. Yeh, C. Li, S.Y. Chang, C.H. Chiu, C.T. Huang , Mechanical properties and antibacterial behaviors of TaN–(Ag,Cu) nanocomposite thin films after annealing, Surface and Coatings Technology 228 (2013) S116-S119.

[132] J.H. Hsieh, T.H. Yeh, C. Li, C.H. Chiu, C.T. Huang, Antibacterial properties of TaN–(Ag,Cu) nanocomposite thin films, Vacuum 87 (2013) 160-163.

[133] I. Šlamborová, V. Zajícová, J. Karpíšková, P. Exnar, I. Stibor, New type of protective hybrid and nanocomposite hybrid coatings containing silver and copper with an excellent antibacterial effect especially against MRSA, Materials Science and Engineering: C 33 (2013) 265-273.

[134] L. Mai, D. Wang, S. Zhang, Y. Xie, Ch. Huang, Z. Zhang , Synthesis and bactericidal ability of Ag/TiO_2 composite films deposited on titanium plate, Applied Surface Science 257 (2010) 974-978.

[135] J. Musil, M. Louda, R. Cerstvy, P. Baroch, I. B. Ditta, A. Steele, H. A. Foster, Two-Functional Direct Current Sputtered Silver-Containing Titanium Dioxide Thin Films, Nanoscale Research Letters 4 (2009) 313–320.

[136] V. Ondok, J. Musil, M. Meissner, R. Čerstvý, K. Fajfrlík , Two-functional DC sputtered Cu-containing TiO_2 thin films, Journal of Photochemistry and Photobiology A: Chemistry 209 (2010) 158-162.

[137] International Organization for Standardization, Plastics-measurement of antibacterial activity on plastics surfaces, ISO 22196; 2007 standard, (2007).

[138] Te-Wei Chiu, Yung-Chin Yang, An-Chou Yeh, Yung-Po Wang, Yi-Wei Feng , Antibacterial property of $CuCrO_2$ thin films prepared by RF magnetron sputtering deposition, Vacuum 87 (2013) 174-177.

[139] Doo-Hoon Song, Soo-Hyuk Uhm, Sang-Bae Lee, Jeon-Geon Han, Kyoung-Nam Kim, Antimicrobial silver-containing titanium oxide nanocomposite coatings by a reactive magnetron sputtering, Thin Solid Films 519 (2011) 7079-7085.

[140] C. E. Santo, E. W. Lam, C. G. Elowsky, D. Quaranta, D. W. Domaille, C. J. Chang, G. Grass, Bacterial Killing by Dry Metallic Copper Surfaces, Applied Environmental Microbiology 77 (2011) 794-802.

[141] Heng-Li Huang, Yin-Yu Chang, Meng-Cheng Lai, Cai-Rong Lin, Chih-Ho Lai, Tzong-Ming Shieh, Antibacterial TaN-Ag coatings on titanium dental implants, Surface and Coatings Technology 205 (2010) 1636-1641.

[142] H.A. Foster, D.W. Sheel, P. Sheel, P. Evans, S. Varghese, N. Rutschke, H.M. Yates, Antimicrobial activity of titania/silver and titania/copper films prepared by CVD, Journal of Photochemistry and Photobiology A: Chemistry 216 (2010) 283-289.

[143] S.X. Jiang, W.F. Qin, R.H. Guo, L. Zhang, Surface functionalization of nanostructured silver-coated polyester fabric by magnetron sputtering, Surface and Coatings Technology 204 (2010) 3662-3667.

[144] M. Khan, S.D. Gittard, R.J. Narayan, D.M. Bubb, Antimicrobial testing, morphological characterization and surface potential mapping of silver-poly-(methyl methacrylate) nanocomposite films made through matrix-assisted pulsed laser deposition against S. aureus, Nano Life, 1 (2010) 145-152.

[145] Qing Ling Feng, Taik Nam Kim, Jing Wu, Eui Seo Park, Jong Ock Kim, Dae Young Lim, Fu Zhai Cui, Antibacterial effects of Ag-HAp thin films on alumina substrates, Thin Solid Films 335 (1998) 214-219.

[146] Z.G. Dan, H.W. Ni, B.F. Xu, J. Xiong, P.Y. Xiong, Microstructure and antibacterial properties of AISI 420 stainless steel implanted by copper ions, Thin Solid Films 492 (2005) 93-100.

[147] Yu-Chu Kuo, Jyh-Wei Lee, Chaur-Jeng Wang, Yu-Jie Chang, The effect of Cu content on the microstructures, mechanical and antibacterial properties of Cr–Cu–N nanocomposite coatings deposited by pulsed DC reactive magnetron sputtering, Surface and Coatings Technology 202 (2007) 854-860.

[148] P. Osorio-Vargas, R. Sanjines, C. Ruales, C. Castro, C. Pulgarin, A.-J. Rengifo-Herrera, J.-C. Lavanchy, J. Kiwi, Antimicrobial Cu-functionalized surfaces prepared by bipolar asymmetric DC-pulsed magnetron sputtering (DCP), Journal of Photochemistry and Photobiology A: Chemistry 220 (2011) 70-76.

[149] V. Stranak, H. Wulff, H. Rebl, C. Zietz, K. Arndt, R. Bogdanowicz, B. Nebe, R. Bader, A. Podbielski, Z. Hubicka, R. Hippler, Deposition of thin titanium–copper films with antimicrobial effect by advanced magnetron sputtering methods, Materials Science and Engineering: C 31 (2011) 1512-1519.

[150] P.C. Liu, J.H. Hsieh, C. Li, Y.K. Chang, C.C. Yang, Dissolution of Cu nanoparticles and antibacterial behaviors of TaN–Cu nanocomposite thin films, Thin Solid Films 517 (2009) 4956-4960.

[151] Yu-Hao Chan, Chung-Fang Huang, Keng-Liang Ou, Pei-Wen Peng, Mechanical properties and antibacterial activity of copper doped diamond-like carbon films, Surface and Coatings Technology 206 (2011) 1037-1040.

[152] X.B. Tian, Z.M. Wang, S.Q. Yang, Antibacterial copper-containing titanium nitride films produced by dual magnetron sputtering, Surface and Coatings Technology 201 (2007) 8606–8609.

[153] T. Sato, M. Taya, Copper-aided photosterilization of microbial cells on TiO_2 film under irradiation from a white light fluorescent lamp, Biochemical Engineering Journal 30 (2006) 199-204.

[154] Xiangyu Zhang, Xiaobo Huang, Yong Ma, Naiming Lin, Ailan Fan, Bin Tang, Bactericidal behavior of Cu-containing stainless steel surfaces, Applied Surface Science 258 (2012) 10058-10063.

[155] K. Jamuna-Thevi, S.A. Bakar, S. Ibrahim , N. Shahab, M.R.M. Toff, Quantification of silver ion release, in vitro cytotoxicity and antibacterial properties of nanostuctured Ag doped TiO2 coatings on stainless steel deposited by RF magnetron sputtering, Vacuum 86 (2011) 235-241.

[156] J.H. Hsieh, C.C. Tseng, Y.K. Chang, , S.Y. Chang, W. Wu, Antibacterial behavior of TaN–Ag nanocomposite thin films with and without annealing, Surface and Coatings Technology 202 (2008) 5586–5589.

[157] O. Baghriche, J. Kiwi, C. Pulgarin, R. Sanjinés, Antibacterial Ag–ZrN surfaces promoted by subnanometric ZrN-clusters deposited by reactive pulsed magnetron sputtering, Journal of Photochemistry and Photobiology A: Chemistry 229 (2012) 39–45.

[158] J.H. Hsieh, C.C. Chang, C. Li, S.J. Liu, Y.K. Chang, Effects of Ag contents on antibacterial behaviors of TaON–Ag nanocomposite thin films, Surface and Coatings Technology 205 (2010) S337–S340.

[159] Wen-Chien Lan, Shih-Fu Ou, Ming-Hong Lin, Keng-Liang Ou, Meng-Yuan Tsai, Development of silver-containing diamond-like carbon for biomedical applications. Part I: Microstructure characteristics, mechanical properties and antibacterial mechanisms, Ceramics International 39 (2013) 4099–4104.

[160] O. Baghriche, A.P. Ehiasarian, E. Kusiak-Nejman, C. Pulgarin, R. Sanjines, A.W. Morawski, J. Kiwi, High power impulse magnetron sputtering (HIPIMS) and traditional pulsed sputtering (DCMSP) Ag-surfaces leading to E. coli inactivation, Journal of Photochemistry and Photobiology A: Chemistry 227 (2012) 11– 17.

[161] M.C. Fung, D.L. Bowen, Silver Products for Medical Indications: Risk-Benefit Assessment, Clinical Toxicology, 34 (1996) 119- 126.

[162] D. Brandt, B. Park, M. Hoang, H.T. Jacobe, Argyria secondary to ingestion of homemade silver solution, Journal of the American Academy of Dermatology, 53 (2005) S105-S107.

[163] A. Dorsey, L. Ingerman, S. Swarts, Toxicological profile for copper, U.S. Department of health and human services, Agency for Toxic Substances and Disease Registry, Atlanta, (2004).

[164] J.J. Hostýnek, F. Dreher, H.I. Maibach, Human stratum corneum penetration by copper: In vivo study after occlusive and semi-occlusive application of the metal as powder, Food and Chemical Toxicology 44 (2006) 1539-1543.

[165] C. d'Arcangues, Worldwide use of intrauterine devices for contraception, Contraception 75 (2007) S2-S7.

[166] H.H.A. Dollwet, S.P. Schmidt, R.E. Seeman, Anti-inflammatory properties of copper implants in the rat paw edema: A preliminary study, Agents and Actions 11 (1981) 746-749.

[167] A.L. Casey, D. Adams, T.J. Karpanen, P.A. Lambert, B.D. Cookson, P. Nightingale, L. Miruszenko, R. Shillam, P. Christian, T.S.J. Elliott, Role of copper in reducing hospital environment contamination, Journal of Hospital Infection 74 (2010) 72-77.

[168] A. Mikolay, S. Huggett, L. Tikana, G. Grass, J. Braun, D.H. Nies, Survival of bacteria on metallic copper surfaces in a hospital trial, Applied Microbiology and Biotechnology 87 (2010) 1875–1879.

[169] Q. Like, L. Xikun, P. Yang, M. Weimin, Q. Guanming, S. Yanbin, Types, Performance and Application of AI_2O_3 System Ceramic Cutting Tool, Journal of Rare Earths 25 (2007) 322-326.

[170] S. Vuorinen, L. Karlsson, Phase transformation in chemically vapour-deposited κ-alumina, Thin Solid Films 214 (1992) 132-143.

[171] H.G. Prengel, W. Heinrich, G. Roder, K.H. Wendt, CVD coatings based on medium temperature CVD κ- and α-Al_2O_3, Surface and Coatings Technology 68–69 (1994) 217-220.

[172] B.Y. Man, L. Guzman, A. Miotello, M. Adami, Microstructure, oxidation and H_2-permeation resistance of TiAlN films deposited by DC magnetron sputtering technique, Surface and Coatings Technology 180–181 (2004) 9-14.

[173] A. Hatton, J.E. Nevelos, A.A. Nevelos, R.E. Banks, J. Fisher, E. Ingham, Alumina–alumina artificial hip joints. Part I: a histological analysis and characterisation of wear debris by laser capture microdissection of tissues retrieved at revision, Biomaterials 23 (2002) 3429-3440.

[174] I. Levin, D. Brandon, Metastable Alumina Polymorphs: Crystal Structures and Transition Sequences, Journal of the American Ceramic Society, 81 (1998) 1995–2012.

[175] V. Edlmayr, M. Moser, C. Walter, C. Mitterer, Thermal stability of sputtered Al_2O_3 coatings, Surface and Coatings Technology 204 (2010) 1576-1581.

[176] D.H. Trinh, K. Back, G. Pozina, H. Blomqvist, T. Selinder, M. Collin, I. Reineck, L. Hultman, H. Högberg, Phase transformation in κ- and γ-Al_2O_3 coatings on cutting tool inserts, Surface and Coatings Technology 203 (2009) 1682-1688.

[177] H. Bolt, F. Koch, J.L. Rodet, D. Karpov, S. Menzel, Al_2O_3 coatings deposited by filtered vacuum arc — characterization of high temperature properties, Surface and Coatings Technology 116–119 (1999) 956-962.

[178] O. Zywitzki, G. Hoetzsch, Influence of coating parameters on the structure and properties of Al_2O_3 layers reactively deposited by means of pulsed magnetron sputtering, Surface and Coatings Technology 86–87 (1996) 640-647.

[179] M. Sridharan, M. Sillassen, J. Bøttiger, J. Chevallier, H. Birkedal, Pulsed DC magnetron sputtered Al_2O_3 films and their hardness, Surface and Coatings Technology 202 (2007) 920-924.

[180] E. Wallin, T. I. Selinder, M. Elfwing, U. Helmersson, Synthesis of α-Al2O3 thin films using reactive high-power impulse magnetron sputtering, Europhysics Letters 82 (2008) 36002.

[181] W.H. Gitzen, Alumina as a Ceramic Material, Alcoa Research Laboratories, The American Ceramic Society, USA, (1970).

[182] B.D. Wirth, Crystal structures, http://iron.nuc.berkeley.edu/bdwirth/NE120/documents/Chap2.crystals.pdf, accessed 28/04/2010.

[183] P. Pirouz, B.F. Lawlor, T. Geipel, J.B. Bilde-Sørensen, A.H. Heuer, K.P.D. Lagerlöf, On Basal slip and basal twinning in sapphire (α-Al_2O_3)—II. A new model of basal twinning, Acta Materialia 44 (1996) 2153-2164.

[184] G. Gutiérrez, A. Taga, B. Johansson, Theoretical structure determination of γ-Al2O3, Physical review B 65 (2001) 012101.

[185] C. Loyola, E. Menéndez-Proupin, G. Gutiérrez, Atomistic study of vibrational properties of γ-Al2O3, Journal of Materials Science 45 (2010) 5094-5100.

[186] G. Paglia, A.L. Rohl, C.E. Buckley, J.D. Gale, Determination of the structure of γ-alumina from interatomic potential and first-principles calculations: The requirement of significant numbers of nonspinel positions to achieve an accurate structural model, Physical Review B 71 (2005) 224115.

[187] G. Paglia, C.E. Buckley, A.L. Rohl, B.A. Hunter, R.D. Hart, J.V. Hanna, L.T. Byrne, Tetragonal structure model for boehmite-derived γ-alumina, Physical Review B 68 (2003)144110.

[188] X. Krokidis, P. Raybaud, A.-E. Gobichon, B. Rebours, P. Euzen, H. Toulhoat, Theoretical study of the dehydration process of boehmite to γ-alumina, Journal of Physical Chemistry B 105 (2001) 5121-5130.

[189] W.Y. Ching, L. Ouyang, P. Rulis, H. Yao, Ab initio study of the physical properties of γ-Al_2O_3: Lattice dynamics, bulk properties, electronic structure, bonding, optical properties, and ELNES/XANES spectra, Physical Review B 78 (2008) 014106.

[190] P. Eklund, M. Sridharan, G. Singh, J. Bøttiger, Thermal stability and phase transformations of γ-/amorphous-Al_2O_3 thin films, Plasma Processes and Polymers 6 (2009) S907-S911.

[191] K. Bobzin, E. Lugscheider, M. Maes, C. Piñero, Relation of hardness and oxygen flow of Al_2O_3 coatings deposited by reactive bipolar pulsed magnetron sputtering, Thin Solid Films 494 (2006) 255-262.

[192] F. Fietzke, K. Goedicke, W. Hempel, The deposition of hard crystalline Al_2O_3 layers by means of bipolar pulsed magnetron sputtering, Surface and Coatings Technology 86–87 (1996) 657-663.

[193] J.M. Andersson, Z. Czigány, P. Jin, U. Helmersson, Microstructure of α-alumina thin films deposited at low temperatures on chromia template layers, Journal of Vacuum Science and Technology A: Vacuum, Surfaces and Films 22 (2004) 117-121.

[194] G. Balakrishnan, P. Kuppusami, S. Tripura Sundari, R. Thirumurugesan, V. Ganesan, E. Mohandas, D. Sastikumar, Structural and optical properties of γ-alumina thin films prepared by pulsed laser deposition Thin Solid Films 518 (2010) 3898-3902.

[195] R.H. French, Electronic band structure of Al_2O_3 with comparison to AlON and AlN, Journal of the American Ceramic Society 73 (1990) 477-489.

[196] P. Patnaik, Handbook of Inorganic Chemicals, The McGraw-Hill Companies Inc., USA, (2003).

[197] K. Wefers, Ch. Misra, Oxides and Hydrides of Alumina, Alcoa Technical Paper No. 19, Alcoa Research Laboratories, Aluminium Company of America, USA, (1987).

[198] Su Zhao, Jizhong Zhang, Duan Weng, Xiaodong Wu, A method to form well-adhered γ-Al_2O_3 layers on FeCrAl metallic supports, Surface and Coatings Technology 167 (2003) 97-105.

[199] J.M. McHale, A. Auroux, A.J. Perrotta, A. Navrotsky, Surface energies and thermodynamic phase stability in nanocrystalline aluminas, Science 277 (1997) 788-789.

[200] Jo-Yong Park, Yun-Jo Lee, Prashant R. Karandikar, Ki-Won Jun, Jong Wook Bae, Kyoung-Su Ha, Ru promoted cobalt catalyst on γ-Al_2O_3 support: Influence of pre-synthesized nanoparticles on Fischer–Tropsch reaction, Journal of Molecular Catalysis A: Chemical 344 (2011) 153-160.

[201] S. Ruppi, Deposition, microstructure and properties of texture-controlled CVD α-Al_2O_3 coatings, International Journal of Refractory Metals and Hard Materials 23 (2005) 306-316.

[202] R. Brill, F. Koch, J. Mazurelle, D. Levchuk, M. Balden, Y. Yamada-Takamura, H. Maier, H. Bolt, Crystal structure characterisation of filtered arc deposited alumina coatings: temperature and bias voltage, Surface and Coatings Technology 174–175 (2003) 606-610.

[203] J.M. Andersson, E. Wallin, U. Helmersson, U. Kreissig, E.P. Münger, Phase control of Al_2O_3 thin films grown at low temperatures, Thin Solid Films 513 (2006) 57-59.

[204] P. Eklund, M. Sridharan, M. Sillassen, J. Bøttiger, α-Cr_2O_3 template-texture effect on α-Al_2O_3 thin-film growth, Thin Solid Films 516 (2008) 7447-7450.

[205] P. Jin, S. Nakao, S.X. Wang, L.M. Wang, Localized epitaxial growth of α-Al2O3 thin films on Cr2O3 template by sputter deposition at low substrate temperature, Applied Physics Letters 82 (2003) 1024-1026.

[206] A. Aryasomayajula, S. Canovic, D. Bhat, M.H. Gordon, M. Halvarsson, Transmission electron microscopy and X-ray diffraction analysis of alumina coating by alternate-current inverted magnetron-sputtering technique, Thin Solid Films 516 (2007) 397-401.

[207] J. Ramm, M. Ante, T. Bachmann, B. Widrig, H. Brändle, M. Döbeli, Pulse enhanced electron emission (P3e™) arc evaporation and the synthesis of wear resistant Al–Cr–O coatings in corundum structure, Surface and Coatings Technology 202 (2007) 876-883.

[208] J. Ramm, M. Ante, H. Brändle, A. Neels, A. Dommann, M. Döbeli, Thermal stability of thin film corundum-type solid solutions of $(Al_{1-x}Cr_x)_2O_3$ synthesized under low-temperature non-equilibrium conditions, Advanced Engineering Materials 9 (2007) 604-608.

[209] K. Pedersen, J. Bøttiger, M. Sridharan, M. Sillassen, P. Eklund, Texture and microstructure of Cr_2O_3 and $(Cr,Al)_2O_3$ thin films deposited by reactive inductively coupled plasma magnetron sputtering, Thin Solid Films 518 (2010) 4294-4298.

[210] D. Diechle, M. Stueber, H. Leiste, S. Ulrich, V. Schier, Combinatorial approach to the growth of α-$(Al_{1-x},Cr_x)_2O_3$ solid solution strengthened thin films by reactive r.f. magnetron sputtering, Surface and Coatings Technology 204 (2010) 3258-3264.

[211] K. Jiang, D. Music, K. Sarakinos, J. M. Schneider, Ab initio study of effects of substitutional additives on the phase stability of γ –alumina, Journal of Physics: Condensed Matter 22 (2010) 505502.

[212] Ch. Täschner, B. Ljungberg, V. Alfredsson, I. Endler, A. Leonhardt, Deposition of hard crystalline Al_2O_3 coatings by bipolar pulsed d.c. PACVD, Surface and Coatings Technology 108–109 (1998) 257-264.

[213] K.T. Jacob, C.B. Alcock, Thermodynamics of $CuAlO_2$ and $CuAl_2O_4$, and Phase Equilibria in the System Cu_2O-CuO-Al_2O_3, Journal of The American Ceramic Society, 58 (1975) 192-195.

[214] H. Kawazoe, M. Yasukawa, H. Hyodo, M. Kurita, H. Yanagi, H. Hosono, P-type electrical conduction in transparent thin films of $CuAlO_2$, Nature 389 (1997) 939-942.

[215] L.C. Leu, D.P. Norton, G.E. Jellison Jr., V. Selvamanickam, X. Xiong, Optical and dielectric properties of $CuAl_2O_4$ films synthesized by solid-phase epitaxy, Thin Solid Films 515 (2007) 6938-6942.

[216] Ch.H. Ong, H. Gong, Effects of aluminum on the properties of p-type Cu–Al–O transparent oxide semiconductor prepared by reactive co-sputtering, Thin Solid Films 445 (2003) 299-303.

[217] J.H. Shy, B.H. Tseng, Characterization of $CuAlO_2$ thin film prepared by rapid thermal annealing of an Al_2O_3/Cu_2O/sapphire structure, Journal of Physics and Chemistry of Solids 66 (2005) 2123-2126.

[218] N. Tsuboi, Y. Itoh, J. Ogata, S. Kobayashi, H. Shimizu, K. Kato, F. Kaneko, Composition and Structure Control of Cu–Al–O Films Prepared by Reactive Sputtering and Annealing, Japanese Journal of Applied Physics 46 (2007) 351–355.

[219] M. Salavati-Niasari, F. Davar, M. Farhadi, Synthesis and characterization of spinel-type CuAl2O4 nanocrystalline by modified sol–gel method, Journal of Sol-Gel Science and Technology 51 (2009) 48–52.

[220] J. Yanyan, L. Jinggang, S. Xiaotao, N. Guiling, W. Chengyu, G. Xiumei, $CuAl_2O_4$ powder synthesis by sol-gel method and its photodegradation property under visible light irradiation, Journal of Sol-Gel Science and Technology 42 (2007) 41–45.

[221] Weizhong Lv, Bo Liu, Qi Qiu, Fang Wang, Zhongkuan Luo, Peixin Zhang, Shaohui Wei, Synthesis, characterization and photocatalytic properties of spinel $CuAl_2O_4$ nanoparticles by a sonochemical method, Journal of Alloys and Compounds 479 (2009) 480-483.

[222] O. Ilinich, W. Ruettinger, X. Liu, R. Farrauto, $Cu–Al_2O_3–CuAl_2O_4$ water–gas shift catalyst for hydrogen production in fuel cell applications: Mechanism of deactivation under start–stop operating conditions, Journal of Catalysis 247 (2007) 112-118.

[223] S. Sato, M. Iijima, T. Nakayama, T. Sodesawa, F. Nozaki, Vapor-Phase Dehydrocoupling of Methanol to Methyl Formate over $CuAl_2O_4$, Journal of Catalysis 169 (1997) 447-454.

[224] K. Lee, I. Song, G. Park, Preparation of $Bi_2Sr_2CaCu_2O_y$ films on alumina substrates with a $CuAl_2O_4$ buffer layer, Journal of Applied Physics 74 (1993) 1459-1461.

[225] G. Katz, Adhesion of copper films to aluminum oxide using a spinel structure interface, Thin Solid Films 33 (1976) 99-105.

[226] Ching-Yao Hu, Kaimin Shih, J. O. Leckie, Formation of copper aluminate spinel and cuprous aluminate delafossite to thermally stabilize simulated copper-laden sludge, Journal of Hazardous Materials 181 (2010) 399-404.

[227] JCPDS 33-0448 standard, International Centre for Diffraction Data, (1997).

[228] Materials Science International Team and Pierre Perrot, Chromium–Copper–Oxygen, in: G.. Effenberg, S. Ilyenko, Springer Materials - The Landolt-Börnstein Database, Springer-Verlag Berlin Heidelberg (2010).

[229] K.T. Jacob, G.M. Kale, G.N. K. Iyengar, Oxygen potentials, Gibbs' energies and phase relations in the Cu-Cr-O system, Journal of Materials Science 21 (1986) 2753-2758.

[230] F. Jlaiel, M. Amami, P. Strobel, A. B. Salah, Non-magnetic impurity doping effect on the magnetic state of p-type Al-doped delafossite oxide $CuCrO_2$, Central European Journal of Chemistry 9 (2011) 953-958.

[231] R. Nagarajan, N. Duan, M.K. Jayaraj, J. Li, K.A Vanaja, A. Yokochi, A. Draeseke, J. Tate, A.W. Sleight, p-Type conductivity in the delafossite structure, International Journal of Inorganic Materials 3 (2001) 265-270.

[232] W. Ketir, A. Bouguelia, M. Trari, NO_3^- removal with a new delafossite $CuCrO_2$ photocatalyst, Desalination 244 (2009) 144-152.

[233] W. Ketir, A. Bouguelia, M. Trari, Photocatalytic removal of M^{2+} (—Ni^{2+}, Cu^{2+}, Zn^{2+}, Cd^{2+}, Hg^{2+} and Ag^{+}) over new catalyst $CuCrO_2$, Journal of Hazardous Materials 158 (2008) 257-263.

[234] W. Li, H. Cheng, Synthesis and characterization of Cu-Cr-O nanocomposites, Journal of Central South University of Technology 14 (2007) 291-295.

[235] S. Luo, L. Li, K.F. Wang, S.Z. Li, X.W. Dong, Z.B. Yan, J.-M. Liu, Enhanced magnetic and ferroelectric properties of multiferroic $CuCrO_2$ by Ni-doping, Thin Solid Films 518 (2010) 50-53.

[236] A.C. Rastogi, S.H. Lim, S.B. Desu, Structure and optoelectronic properties of spray deposited Mg doped p-CuCrO2 semiconductor oxide thin films, Journal of applied physics 104 (2008) 023712.

[237] Te-Wei Chiu, Shao-Wei Tsai, Yung-Po Wang, Kai-Hung Hsu, Preparation of p-type conductive transparent $CuCrO_2$:Mg thin films by chemical solution deposition with two-step annealing, Ceramics International 38 (2012) S673-S676.

[238] G. Dong, M. Zhang, X. Zhao, H.Yan, Ch. Tian, Y. Ren, Improving the electrical conductivity of $CuCrO_2$ thin film by N doping, Applied Surface Science 256 (2010) 4121-4124.

[239] A. Fujishima, X. Zhang, Titanium dioxide photocatalysis: present situation and future approaches, Comptes Rendus Chimie 9 (2006) 750-760.

[240] S. Götzendörfer, Ch. Polenzky, S. Ulrich, P. Löbmann, Preparation of $CuAlO_2$ and $CuCrO_2$ thin films by sol–gel processing, Thin Solid Films 518 (2009) 1153-1156.

[241] Electronic Circuit Carriers Made from Advanced Ceramic Materials, http://www.ceramtec.com/substrates/ , accessed 21/10/2013.

[242] A.T. Tran, G. Pandraud, H. Schellevis, T. Alan, V. Aravindh, O. Wunnicke, P.M. Sarro, Fabrication of AlN slender piezoelectric cantilevers for highspeed MEMS actuations, Procedia Engineering 25 (2011) 673-676.

[243] J. Olivares, E. Iborra, M. Clement, L. Vergara, J. Sangrador, A. Sanz-Hervás, Piezoelectric actuation of microbridges using AlN, Sensors and Actuators A: Physical 123–124 (2005) 590-595.

[244] F. Stoppel, C. Schröder, F. Senger, B. Wagner, W. Benecke, AlN-based piezoelectric micropower generator for low ambient vibration energy harvesting, Procedia Engineering 25 (2011) 721-724.

[245] Ping-Feng Yang, Sheng-Rui Jian, Sean Wu, Yi-Shao Lai, Chung-Ting Wang, Rong-Sheng Chen, Structural and mechanical characteristics of (1 0 3) AlN thin films prepared by radio frequency magnetron sputtering, Applied Surface Science 255 (2009) 5984-5988.

[246] H. Takikawa, K. Kimura, R. Miyano, T. Sakakibara, A. Bendavid, P. J. Martin, A. Matsumuro, K. Tsutsumi, Effect of substrate bias on AlN thin film preparation in shielded reactive vacuum arc deposition, Thin Solid Films 386 (2001) 276-280.

[247] I.C. Oliveira, K.G. Grigorov, H.S. Maciel, M. Massi, C. Otani, High textured AlN thin films grown by RF magnetron sputtering; composition, structure, morphology and hardness, Vacuum 75 (2004) 331-338.

[248] Sheng-Rui Jian, G.-J. Chen, H.-G. Chen, Jason S.-C. Jang, Y.-Y. Liao, P.-F. Yang, Y.-S. Lai, M.-R. Chen, H.-L. Kao, J.-Y. Juang, Cross-sectional transmission electron microscopy studies for deformation behaviors of AlN thin films under Berkovich nanoindentation, Journal of Alloys and Compounds 504 (2010) S395-S398.

[249] H.O. Pierson, Handbook of refractory carbides and nitrides, Noyes Publications, New Jersey, (1996).

[250] JCPDS 25-1133 standard, International Centre for Diffraction Data, (1997).

[251] C. Ristoscu, C. Ducu, G. Socol, F. Craciunoiu, I.N. Mihailescu, Structural and optical characterization of AlN films grown by pulsed laser deposition, Applied Surface Science 248 (2005) 411-415.

[252] Min-Ho Park, Sang-Ho Kim, Thermal conductivity of AlN thin films deposited by RF magnetron sputtering, Materials Science in Semiconductor Processing 15 (2012) 6-10.

[253] Wurtzite crystal structure, http://en.wikipedia.org/wiki/Wurtzite_crystal_structure, accessed 9/8/2013.

[254] S. Mohri, T. Yoshitake, T. Hara, K. Nagayama, Growth of metastable cubic AlN by reactive pulsed laser deposition, Diamond and Related Materials 17 (2008) 1796-1799.

[255] J. Wang, W.L. Wang, P.D. Ding, Y.X. Yang, L. Fang, J. Esteve, M.C. Polo, G. Sanchez, Synthesis of cubic aluminum nitride by carbothermal nitridation reaction, Diamond and Related Materials 8 (1999) 1342-1344.

[256] JiaCai Kuang, ChangRui Zhang, XinGui Zhou, QiCheng Liu, Chang Ye, Formation and characterization of cubic AlN crystalline in a carbothermal reduction reaction, Materials Letters 59 (2005) 2006-2010.

[257] N. Kietipaisalsophon, W. Bunjongpru, W. Techitdheera, and J. Nukeaw, Structure properties of cubic-A1N grown by reactive gas-timing rf magnetron sputtering, IEEE lCIT 2002, 1365-1367.

[258] J. Zhu, D. Zhao, W.B. Luo, Y. Zhang, Y.R. Li, Epitaxial growth of cubic AlN films on $SrTiO_3$(1 0 0) substrates by pulsed laser deposition, Journal of Crystal Growth 310 (2008) 731-737.

[259] Yuechun Fu, Yao Zhang, Weijia Yang, Huan He, Xiaoming Shen, Surface evolution of NaCl-type cubic AlN films on MgO (100) substrates deposited by laser molecular beam epitaxy, Journal of Crystal Growth 343 (2012) 28-32.

[260] J. Musil, H. Hrubý, P. Zeman, H. Zeman, R. Čerstvý, P.H. Mayrhofer, C. Mitterer, Hard and superhard nanocomposite Al–Cu–N films prepared by magnetron sputtering, Surface and Coatings Technology 142–144 (2001) 603-609.

[261] J. Tian, K. Shobu, Hot-pressed AlN-Cu metal matrix composites and their thermal properties, Journal of Materials Science 39 (2004) 1309-1313.

[262] F.Y. Ran, M. Subramanian, M. Tanemura, Y. Hayashi, T. Hihara, Ferromagnetism in Cu-doped AlN films, Applied Physics Letters 95 (2009) 112111.

[263] F.-Y. Ran, M. Subramanian, M. Tanemura, Y. Hayashi, T. Hihara, Electron spin resonance (ESR) analysis of Cu-doped ZnO and AlN films, Physica B: Condensed Matter 405 (2010) 3952-3954.

[264] J. Musil, H. Zeman, J. Kasl, Relationship between structure and mechanical properties in hard Al–Si–Cu–N films prepared by magnetron sputtering, Thin Solid Films 413 (2002) 121-130.

[265] P. Zeman, R. Čerstvý, P.H. Mayrhofer, C. Mitterer, J. Musil, Structure and properties of hard and superhard Zr–Cu–N nanocomposite coatings, Materials Science and Engineering: A 289 (2000) 189-197.

[266] Operating instructions for RMP-10 Generator, Huettinger Electronic Sp z o.o., Zielonka, Poland, (2007).

[267] IAP-1010 User manual, EN Technologies Inc., Anyang, Korea, (2004).

[268] Dektak 8 Advanced Development Profiler Manual, Veeco Instruments Inc., Tucson, USA, (2004).

[269] M. Zecchino, T. Cunningham, Thin Film Stress Measurement Using Dektak Stylus Profilers, Veeco Instruments Inc., Tucson, USA, (2004).

[270] International Organization for Standardization, Metallic materials - Instrumented indentation test for hardness and materials parameters, ISO 14577-1:2002(E), (2002).

[271] Basics of X-ray Diffraction, Scintag, Inc., Cupertino, USA, (1999), http://epswww.unm.edu/xrd/xrdbasics.pdf accessed 21/10.2013.

[272] H. Bubert, H. Jenett, Surface and thin film analysis, Wiley VCH, Germany, (2003).

[273] Se Jin Ko, Kyung Ho Min, Young Do Kim, n-Hyung Moon, A study on the fabrication of Al_2O_3/Cu nanocomposite and its mechanical properties, Journal of Ceramic Processing Research 3 (2002) 192-194.

[274] D. Depla, S. Heirwegh, S. Mahieu, J. Haemers, R. De Gryse, Understanding the discharge voltage behavior during reactive sputtering of oxides, Journal of Applied Physics 101 (2007) 013301.

[275] http://resource.npl.co.uk/docs/science_technology/nanotechnology/sputter_yield_values /arsputtertable.pdf accessed 21/10/2013.

[276] J. Musil, J. Blažek, P. Zeman, Š. Prokšová, M. Šašek, R. Čerstvý, Thermal stability of alumina thin films containing γ-Al_2O_3 phase prepared by reactive magnetron sputtering, Applied Surface Science 257 (2010) 1058-1062.

[277] S. K. Misra, A. C. D. Chaklader, The System Copper Oxide-Alumina, Journal of The Americun Ceramic Society(1963) 509.

[278] A. R. West, Solid state chemistry and its applications, John Wiley & Sons Ltd., Chichester, UK, (1984).

[279] P. Vitanov, Tz. Babeva, Z. Alexieva, A. Harizanova, Z. Nenova, Optical properties of $(Al_2O_3)_x(TiO_2)_{1-x}$ films deposited by the sol–gel method, Vacuum 76 (2004) 219-222.

[280] C.C. Trapalis, P. Keivanidis, G. Kordas, M. Zaharescu, M. Crisan, A. Szatvanyi, M. Gartner, $TiO_2(Fe^{3+})$ nanostructured thin films with antibacterial properties, Thin Solid Films 433 (2003) 186-190.

[281] S. Kadlec, J. Čapek, J. Kousal, J. Vyskočil, Oxide Films Deposited by Reactive Bipolar High Power Impulse Magnetron Sputtering, oral presentation given at 19th International Vacuum Congress, Paris, France, (2013)

[282] Ruei-Sung Yu, Chung-Ming Wu, Characteristics of p-type transparent conductive $CuCrO_2$ thin films, Applied Surface Science 282 (2013) 92-97.

[283] Fei Luo, Xiaolu Pang, Kewei Gao, Huisheng Yang, Yanbin Wang, Role of deposition parameters on microstructure and mechanical properties of chromium oxide coatings, Surface and Coatings Technology 202 (2007) 58-62.

[284] G. Contoux, F. Cosset, A. Célérier, J. Machet, Deposition process study of chromium oxide thin filmsobtained by d.c. magnetron sputtering, Thin Solid Films 292 (1997) 75-84.

[285] H.C. Barshilia, K.S. Rajam, Growth and characterization of chromium oxide coatings prepared by pulsed-direct current reactive unbalanced magnetron sputtering, Applied Surface Science 255 (2008) 2925-2931.

[286] Linmao Qian, Ming Li, Zhongrong Zhou, Hui Yang, Xinyu Shi, Comparison of nano-indentation hardness to microhardness, Surface and Coatings Technology 195 (2005) 264-271.

[287] J.H. Hsieh, T.H. Yeh, C. Li, S.Y. Chang, C.H. Chiu, C.T. Huang, Mechanical properties and antibacterial behaviors of TaN–(Ag,Cu) nanocomposite thin films after annealing, Surface and Coatings Technology 228 (2013) S116-S119.

[288] J. Musil, H. Poláková, J. Šuna, J. Vlček, Effect of ion bombardment on properties of hard reactively sputtered Ti(Fe)N_x films, Surface and Coatings Technology 177–178 (2004) 289-298.

[289] H. Poláková, J. Musil, J. Vlček, J. Allaart, C. Mitterer, Structure-hardness relations in sputtered Ti–Al–V–N films, Thin Solid Films 444 (2003) 189-198.

Nomenclature

a	lattice parameter
A	number of colonies on the control sample (Si substrate)
B	number of colonies on the sample corresponding to the film tested
d	indentation depth of the diamond indenter into the film
d	mean crystallite size
$d_{\mathrm{s-t}}$	substrate-to-target distance
E	antibacterial efficiency
E^*	effective Young’s modulus
ε	film strain
f_{r}	repetition frequency of the magnetron power supply
f_{s}	repetition frequency of the substrate bias
ϕ_{Ar}	flow rates of Ar
ϕ_{O2}	flow rates of O_2
ϕ_{N2}	flow rates of N_2
H	indentation hardness
$h \equiv h_{\mathrm{f}}$	film thickness
h_{s}	substrate thickness
i_{s}	average substrate ion current density in the negative pulse
I_{d}	average cathode current in the pulse on time
k	extinction coefficient
λ	wavelength of electromagnetic radiation
L	load applied on the diamond indenter during instrumented indentation
n	index of refraction
p_{Ar}	partial pressure of Ar
P_d	average target power in the pulse on time
p_{N2}	partial pressure of N_2
p_{O2}	partial pressure of O_2
p_{T}	total discharge pressure
RT	room temperature
σ	film macrostress≡film residual stress
t	deposition time
t	contact time of the bacterial suspension with the thin film
τ	negative voltage pulse length≡pulse on time
$\tau_{\mathrm{Al/Cu}}$	negative voltage pulse length on the composed Al/Cu target
τ_{Al}	negative voltage pulse length on the compact Al target
T	pulse period
T	film transmitance
T_{a}	maximum annealing temperature
$T_{\lambda=550\mathrm{nm}}$	transmittance of the film/glass substrate system measured for the wavelength of $\lambda=550$ nm
U_{d}	average voltage between magnetron 1 and magnetron 2 in the pulse on time
U_{s}	magnitude of the negative voltage pulse applied to the substrate (substrate bias)
W_{e}	elastic recovery
W_{d}	average target power density in the pulse on time
$Ø_{\mathrm{fc}}$	diameter of the fixed cylinder used in the bending test
$Ø_{\mathrm{in}}$	inner diameter of the copper ring used for fixing the Cr or Al target

Author's list of publications

Referred journal papers:

[I] P.Zeman, Š. Zuzjaková, **J. Blažek**, R. Čerstvý, J. Musil, Thermal transformations in metastable alumina coatings prepared by magnetron sputtering, Surface and Coatings Technology, submitted for publication.

[II] J. Musil, **J. Blažek**, K. Fajfrlík, R. Čerstvý, Š. Prokšová, Antibacterial Cr–Cu–O films prepared by reactive magnetron sputtering, Applied Surface Science 276 (2013) 660–666.

[III] J. Houška, **J. Blažek**, J. Rezek, Š. Prokšová, Overview of optical properties of Al_2O_3 films prepared by various techniques, Thin Solid Films 520 (2012) 5405–5408.

[IV] **J. Blažek**, J. Musil, P. Stupka, R. Čerstvý , J. Houška, Properties of nanocrystalline Al–Cu–O films reactively sputtered by DC pulse dual magnetron, Applied Surface Science 258 (2011) 1762– 1767.

[V] J. Musil, **J. Blažek**, P. Zeman, Š. Prokšová, M. Šašek, R. Čerstvý, Thermal stability of alumina thin films containing γ-Al_2O_3 phase prepared by reactive magnetron sputtering, Applied Surface Science 257 (2010) 1058–1062.

Contributions at scientific conferences:

[I] J. Musil, **J. Blažek**, K. Fajfrlík, R. Čerstvý, Š. Prokšová, Antibacterial Cr-Cu-O thin films prepared by reactive magnetron sputtering, 19th International Vacuum Congress (IVC-19), 9.-13.9. 2013, Paris, France. (*oral presentation*)

[II] Š. Prokšová, P. Zeman, **J. Blažek**, R. Čerstvý, J. Musil, Thermal stability and transformations in magnetron sputtered Al-Cu-O films, 2nd Central and Eastern European Conference on Thermal Analysis and Calorimetry (CEEC-TAC2), 27.-30.8. 2013, Vilnius, Lithuania. (*co-author of oral presentation*)

[III] **J. Blažek**, J. Musil, P. Stupka, R. Čerstvý, J. Houška, Properties of nanocrystalline Al-Cu-O films reactively sputtered by dc pulse dual magnetron, 39th International Conference on Metallurgical Coatings and Thin Films (ICMCTF), 23.-27. 4. 2012, San Diego, CA, USA. (*oral presentation*)

[IV] P. Zeman, Š. Prokšová, **J. Blažek**, R. Čerstvý, J. Musil, Cu-dependent thermal transformations in hard Al-Cu-O coatings, 39th International Conference on Metallurgical Coatings and Thin Films (ICMCTF), 23.-27. 4. 2012, San Diego, CA, USA. (*co-author of oral presentation*)

[V] **J. Blažek**, J. Musil, P. Stupka, R. Čerstvý, J. Houška, Properties of nanocrystalline Al-Cu-O films reactively sputtered by dc pulse dual magnetron, 10th International konference on reactive spputter deposition (RSD), 8.-9.12. 2011, Linköping, Sweden. (*oral presentation*)

[VI] **J. Blažek**, R. Čerstvý, P.Stupka, J. Musil, Effect of Cu content on structure and mechanical properties of sputtered Al-Cu-O films**,** Potential and Applications of Thin Ceramic and Metal Coatings 2011 (PATCMC 2011), 6.-8.6. 2011, Plzeň, Czech Republic. (*oral presentation*)

[VII] **J. Blažek**, R. Čerstvý, P. Zeman, J. Musil, Crystallization and thermal stability of nanocrystalline γ-Al_2O_3 thin films prepared by reactive magnetron sputtering, 12th International Conference on Plasma Surface Engineering (PSE 2010), 13.-17.9. 2010, Garmisch-Partenkirchen, Germany. (*poster presentation*)

[VIII] **J. Blažek**, J. Musil, P. Zeman, R. Čerstvý, Š. Prokšová, M. Šašek, Influence of annealing time and temperature on thermal stability of magnetron sputtered Al_2O_3 films, Potential and Applications of Thin Ceramic and Metal Coatings 2011 (PATCMC 2011), 26.-28.5. 2010, Plzeň, Czech Republic. (*oral presentation*)

Annotation

At present the incorporation of additional element into a binary material system represents an efficient way to enhance physical and functional properties of thin films in various applications. This Ph.D. thesis investigates the effect of Cu content and other process parameters on structure, physical, mechanical and antibacterial properties of thin films prepared by pulsed reactive magnetron sputtering using a dual magnetron. Thin films of three different ternary systems containing Cu were investigated: (1) Al-Cu-O, (2) Cr-Cu-O and (3) Al-Cu-N.

The Al-Cu-O thin films were systematically studied in order to improve the mechanical properties and resistance to cracking of pure nanocomposite Al_2O_3 films containing nanocrystalline γ-Al_2O_3 phase. As the Cu content in the film increases from 0 at.% up to 16 at.% the strucure of the nanocrystals changes from γ-Al_2O_3 phase via $(Al_{8-2x},Cu_{3x})O_{12}$ solid solution to $CuAl_2O_4$ phase. These sructural changes are accompanied by increase of hardness, elastic recovery, H/E^* ratio and compressive macrostress reaching maximum values of $H\approx20$ GPa, $W_e\approx77$ %, $H/E^*\approx0.133$ and $\sigma\approx$-2 GPa, respectively. The nanocomposite Al-Cu-O films with >2 at.% of Cu also show enhanced resistance to cracking in the indentation test. Compared to pure Al_2O_3 films the nanocomposite Al-Cu-O films exhibt significantly higher mechanical properties as well as resistance to cracking.

The second part is focused on the effect of Cu content and phase composition on antibacterial and mechanical properties of Cr-Cu-O films. It was found that the antibacterial efficiency of the as-deposited Cr–Cu–O films increases with increasing Cu content. Effective inactivation of *E. coli* bacteria was achieved for amorphous films with Cu content >15 at.%. The antibacterial effect is strongly dependent on the phase composition of the film. The highest antibacterial efficiency is observed for amorphous as-deposited Cr-Cu-O films and for crystalline films with delafossite $CuCrO_2$ structure obtained by rapid thermal annealing to 700°C in N_2 atmosphere. The killing of *E. coli* bacteria by the Cr-Cu-O film requires no excitation by UV or visible light, operates both in the daylight as well as in the dark and can be accomplished by a very thin (≈70 nm) semitransparent film. The amorphous antibacterial Cr-Cu-O films exhibit hardness of ≈4 GPa and their mechanical properties are stable up to 500 °C.

The last study deals with designing a multifunctional hard antibacterial Al-Cu-N film resistant to cracking. The effect of various deposition parameters was investigated in order to find optimum deposition conditions enabling production of a multifunctional Al-Cu-N film. The obtained results indicate that the optimized film is characterized by Cu content ranging from ≈7.5 at.% to ≈11 at.% and by a very fine-grained nanocomposite structure composed of a mixture of nanocrystalline h-AlN and Cu phases. To achieve high hardness (up to ≈23 GPa) a sufficient energy needs to be delivered to the growing film e.g. in the form of subtrate bias, increased discharged current or reduced total pressure. The hard nanocomposite Al-Cu-N film is able to efficiently inactivate *E. coli* bacteria in the daylight as well as in the dark and the antibacterial efficiency generally increases with increasing Cu content. The hard nanocomposite Al-Cu-N films exhibit enhanced resistance to cracking in the indentation test. The resistance to cracking in bending increases with increasing magnitude of the compressive macrostress in the Al-Cu-N film, which can be controlled by the total pressure of the gas mixture. The multifunctional Al-Cu-N film can be prepared at a high deposition rate of $a_D\approx63.5$ nm/min.

Anotace

Přidávání dalšího prvku do materiálů na bázi binárních sloučenin představuje v současnosti jeden z možných způsobů, jakými lze docílit zlepšení fyzikálních, mechanických a funkčních vlastností tenkovrstevných materiálů v různých aplikacích. Tato disertační práce se zabývá vyšetřováním vlivu různých procesních parametrů zejména pak přidáváním mědi na strukturu, fyzikální, mechanické a antibakteriální vlastnosti tenkých vrstev připravených metodou pulzního reaktivního magnetronového naprašování s využitím duálního magnetronu. V práci jsou zkoumány tři různé ternární systémy obsahující měď: (1) Al-Cu-O, (2) Cr-Cu-O a (3) Al-Cu-N.

Vrstvy Al-Cu-O byly systematicky studovány s cílem zlepšit mechanické vlastnosti a odolnost proti vzniku trhlin nanokompozitních Al_2O_3 vrstev obsahujících nanokrystalickou fázi γ-Al_2O_3. Bylo zjištěno, že s rostoucím obsahem Cu ve vrstvách (z 0 at.% až do 16 at.%) se struktura nanokrystalů mění z γ-Al_2O_3 přes tuhý roztok $(Al_{8-2x},Cu_{3x})O_{12}$ až na $CuAl_2O_4$. Zmíněné změny struktury jsou doprovázeny nárůstem tvrdosti, elastické vratnosti, poměru H/E^* a kompresivního makropnutí, přičemž maximální dosažené hodnoty odpovídají $H\approx20$ GPa, $W_e\approx77$ %, $H/E^*\approx0.133$ a $\sigma\approx-2$ GPa. Nanokompoztní vrstvy Al-Cu-O s >2 at.% mědi také vykazují zvýšenou odolnost proti vzniku trhlin při indentačním testu. Ve srovnání s vrstvami čistého Al_2O_3 bylo u nanokompozitních vrstev Al-Cu-O dosaženo vyšších hodnot mechanických vlastností a zároveň i vyšší odolnosti proti vzniku trhlin.

Druhá část práce se zabývá vlivem obsahu mědi a fázového složení vrstev na bázi Cr-Cu-O na jejich antibakteriální a mechanické vlastnosti. Bylo zjištěno, že efektivita zabíjení bakterií *E. coli* se u nadeponovaných vrstev Cr-Cu-O zvyšuje s rostoucím obsahem mědi ve vrstvě. Výrazného antibakteriálního efektu bylo dosaženo v případě, že obsah mědi ve vrstvě byl >15 at.%. Antibakteriální efekt také silně závisí na fázovém složení. Nejvyšší antibakteriální efektivitu vykazovaly nadeponované vrstvy s amorfní strukturou a krystalické vrstvy se strukturou delafositu $CuCrO_2$ připravené rychlým teplotním ohřevem na 700 °C v dusíkové atmosféře. Pro zabíjení bakterií *E. coli* není nutné ozařovat vrstvu ani UV ani viditelným zářením, a vrstvy tedy vykazují antibakteriální efekt jak za denního světla tak ve tmě. Antibakteriálního efektu je dosaženo i v případě velmi tenkých (≈70 nm) semitransparentních vrstev. Amorfní antibakteriální vrstvy Cr-Cu-O mají tvrdost ≈4 GPa a jejich mechanické vlastnosti jsou stabilní do 500 °C.

Poslední studie je věnována vývoji multifunkční tvrdé antibakteriální vrstvy na bázi Al-Cu-N se zvýšenou odolností proti vzniku trhlin. Byl zkoumán vliv různých depozičních parametrů s cílem nalézt optimální podmínky pro přípravu takové multifunkční vrstvy. Bylo zjištěno, že optimalizovaná vrstva se vyznačuje obsahem mědi v rozsahu ≈7.5 at.% až ≈11 at.% a nanokompozitní strukturou složenou z hexagonálního h-AlN a kovové mědi, přičemž obě tyto fáze se vyskytují ve formě drobných nanokrystalů. Pro dosažení vysoké tvrdosti (až ≈23 GPa) je nutné do rostoucí vrstvy dodat dostatečné množství energie, čehož je možné docílit např. přivedením předpětí na substrát, zvýšením výbojového proudu nebo snížením celkového tlaku. Tvrdé nanokompozitní vrstvy na bázi Al-Cu-N jsou schopné efektivně zabíjet bakterie *E. coli* jak za denního světla tak ve tmě, přičemž antibakteriální efektivita se zvyšuje s rostoucím obsahem mědi ve vrstvě. Tyto tvrdé nanokompozitní vrstvy zároveň vykazují zvýšenou odolnost proti vzniku trhlin při indentačním testu. Odolnost proti vzniku trhlin v ohybovém testu roste s rostocím kompresivním makropnutím ve vrstvě, jehož hodnota může být regulována velikostí celkového tlaku při depozici. Takovéto multifunkční nanokompozitní vrstvy na bázi Al-Cu-N mohou být připraveny vysokou depoziční rychlosti ($a_D\approx63.5$ nm/min).